Characterization of the interface electronic structure of ultra-thin ferroelectric HfxZr1-xO2 films for low power, CMOS-compatible, non-volatile memories

Wassim Hamouda

To cite this version:

Wassim Hamouda. Characterization of the interface electronic structure of ultra-thin ferroelectric HfxZr1-xO2 films for low power, CMOS-compatible, non-volatile memories. Materials Science [cond-mat.mtrl-sci]. Université Paris-Saclay, 2022. English. NNT : 2022UPASP041 . tel-04010782

HAL Id: tel-04010782
https://theses.hal.science/tel-04010782

Submitted on 2 Mar 2023

Characterization of the interface electronic structure of ultra-thin ferroelectric $Hf_xZr_{1-x}O_2$ films for low power, CMOS-compatible, non-volatile memories

Caractérisation de la structure électronique d'interfaces des couches ultra-minces ferroélectriques $Hf_xZr_{1-x}O_2$ pour des mémoires non-volatiles à basse consommation d'énergie, CMOS-compatibles

Thèse de doctorat de l'université Paris-Saclay

École doctorale n°564 : physique en Île-de-France (PIF)
Spécialité de doctorat: Physique
Graduate School : Physique. Référent : Faculté des sciences d'Orsay

Thèse préparée dans l'unité de recherche SPEC (Université Paris-Saclay, CEA, CNRS), sous la direction de Dr Nick BARRETT

Thèse soutenue à Paris-Saclay, le 29 Avril 2022, par

Wassim HAMOUDA

Composition du jury

Marc BOCQUET Professeur, Aix-Marseille Université	Président
Martina MÜLLER Professeure, University of Konstanz	Rapporteur & Examinatrice
Florencio SÁNCHEZ Directeur de recherche, Institute of Materials Science of Barcelona	Rapporteur & Examinateur
Simon JEANNOT Ingénieur de recherche, STMicroelectronics Crolles, entreprise	Examinateur
Sylvia MATZEN Maîtresse de conférences, Université Paris-Saclay	Examinatrice
Nick BARRETT Docteur, Service de Physique de l'État Condensé	Directeur de thèse

THESE DE DOCTORAT
NNT : 2022UPASP041

Characterization of the interface electronic structure of ultra-thin ferroelectric $Hf_xZr_{1-x}O_2$ films for low power, CMOS-compatible, non-volatile memories

Thèse de doctorat de l'université Paris-Saclay

ÉCOLE DOCTORALE
Physique en
Île-de-France (PIF)

École doctorale n°564 : physique en Île-de-France (PIF)
Spécialité de doctorat: Physique
Graduate School : Physique. Référent: Faculté des sciences d'Orsay

Thèse préparée dans l'unité de recherche SPEC (Université Paris-Saclay, CEA, CNRS),
sous la direction de Dr Nick BARRETT

Thèse soutenue à Paris-Saclay, le 29 Avril 2022, par

Wassim HAMOUDA

Composition du jury

Marc BOCQUET Professeur, Aix-Marseille Université	Président
Martina MÜLLER Professeure, University of Konstanz	Rapporteur & Examinatrice
Florencio SÁNCHEZ Directeur de recherche, Institute of Materials Science of Barcelona	Rapporteur & Examinateur
Simon JEANNOT Ingénieur de recherche, STMicroelectronics Crolles, entreprise	Examinateur
Sylvia MATZEN Maîtresse de conférences, Université Paris-Saclay	Examinatrice
Nick BARRETT Docteur, Service de Physique de l'État Condensé	Directeur de thèse

Characterization of the interface electronic structure of ultra-thin ferroelectric $\mathrm{Hf}_x\mathrm{Zr}_{1-x}\mathrm{O}_2$ films for low power, CMOS-compatible, non-volatile memories

Thèse préparée dans l'unité de recherche:
Université Paris-Saclay, CEA, CNRS, SPEC, 91191, Gif-sur-Yvette, France

Commissariat à l'énergie atomique et aux énergies alternatives (CEA)
Direction de la recherche fondamentale (DRF)
Institut Rayonnement Matière de Saclay (IRAMIS)
Service de Physique de l'État Condensée (SPEC)
Laboratoire d'Étude des NanoStructures et Imagerie de Surface (LENSIS)
www.lensislab.com

sous la direction de :
Nick BARRETT

Abstract

Ferroelectric HfO_2-based thin films are promising candidates for high-density non-volatile memory technologies such as ferroelectric random access memory (FRAM) and ferroelectric field effect transistors (FeFETs). They can overcome the integration limitations associated with conventional perovskite ferroelectrics thanks to the low film thicknesses supporting ferroelectricity, conformal atomic layer deposition (ALD) and compatibility with state-of-the-art CMOS processing. Oxygen vacancies (V_O) are believed to play a significant role on the overall device performance made of these attractive systems. The role of these point defects is often discussed through theoretical calculations or by modelling approaches of experimental electrical measurements.

Using the high chemical and electronic sensitivity of photoemission-based spectroscopy techniques, the objective of this thesis is to investigate and correlate the optimized ferroelectric response in CMOS compatible $Hf_xZr_{1-x}O_2$-based capacitors with the variation of V_O densities and electronic band shifts. First, the electrode-ferroelectric interface chemistry and the effect of crystallization annealing temperature in TiN/$Hf_{0.5}Zr_{0.5}O_2$(HZO)/TiN and W/HZO/W capacitor stacks were investigated using X-ray photoelectron spectroscopy (XPS). With hard X-rays (HAXPES), using synchrotron radiation, more deeply buried HZO/TiN interfaces along with the effects of La doping were evaluated. In addition, special device design was made to allow HAXPES measurements with *in-situ* applied bias. TiN/La doped HZO/TiN and TiN/Ti/Si implanted HfO_2/TiN technologically relevant capacitors have been investigated combining the *in-situ* HAXPES analysis with electrical measurements.

The results reveal that TiN induces higher V_O concentration than W electrodes and lower Schottky barrier heights for electron (φ_{Bn}), due to the higher oxygen affinity of TiN. When annealing, the provided thermal energy is responsible of oxygen scavenging by the TiN top electrode, resulting in a negative V_O gradient going from the top to the bottom interface. The HAXPES analysis shows an oxygen scavenging mainly by the top electrode due to the passivation of the bottom electrode during the first steps of the growth process, impeding thus the latter from oxygen scavenging. The asymmetric defect distribution with TiN electrodes results in asymmetric electron trapping, giving rise to an imprint field. The use of W allowed the optimization of this effect. La doping in HZO showed that the negative charge induced by substituting Hf^{4+} by La^{3+} impurities is screened by positively charged oxygen vacancies. In oxygen-rich films, this leads to an increase of the overall V_O concentration. Using the Poole-Frenkel mechanism for charge transport, La was also found to decrease the trap energy level associated to V_O with respect to the conduction band. The analyzes on capacitors at different cycling stages showed that the wake-up behavior (increase of the ferroelectric response with field cycling) is mainly due to an increase of V_O concentration and the re-distribution more uniformly within the film. *In-situ* polarization switching was used to evaluate the values of φ_{Bn} in optimal capacitors and to derive the electrostatic potential within the ferroelectric. Finally, X-ray photoemission electron microscopy (X-PEEM) were further conducted for similar investigations on $\sim$20μm sized TiN/HZO/TiN capacitors. The V_O were found to migrate depending on the stored polarization state due to the internal field resulting from imperfectly screened polarization charges.

The work presents a new step towards understanding the sources and effects of V_O in HfO$_2$-based capacitors and highlights the potential of photoemission based techniques in providing qualitative and quantitative information needed for further optimization in the microelectronics research.

Keywords: Ferroelectricity, non-volatile memories, ferroelectric HfO$_2$, photoemission spectroscopy (XPS, HAXPES), oxygen vacancies, band alignment

Acknowledgments

I would like to thank Patrice ROCHE, head of the Service de Physique de l'Etat Condensé (SPEC) and François DAVIAUD, head of the Institut Rayonnement Matière de Saclay (IRAMIS) of the Atomic Energy Commission (CEA) for giving me the opportunity to work as a PhD student in a very motivating environment and a resourceful laboratory.

I am very grateful to Martina MÜLLER and Florencio SÁNCHEZ for agreeing to be my reading committee. I also thank the other members of my oral defense committee: Marc BOCQUET, Sylvia MATZEN and Simon JEANNOT.

I would like to thank my PhD Director Nick BARRETT, head of the Photoemission, Photodiffraction and Spectromicroscopy group, for providing me the opportunity to work on this project and expand my knowledge on so many topics. I would like to thank him along with Claire MATHIEU for the confidence they have placed in me for a very competitive position. I want to aknowledge all the commitment he brought during these three years and all the professional and scientific knowledge he taught me. I want to point out the excellent material conditions in which I worked, the numerous conferences and synchrotron beamtimes I went with him and thanks to his dedication. I also thank him for the corrections since day one on abstracts, papers, slides and in particular for the last months when he had to read the same manuscript again and again, always cheerfully.

I am in great debt of the others members of the group too: I warmly thank Christophe LUBIN for teaching and helping me so much through these years; I thank Ludovic TORTECH for the help with C-AFM and for all the fun he brought to the group and I wish them good luck for the rest of their journey. I also want to thank Grégoire, Myriam, Kerisha and Santiago who were the perfect co-PhD student, joyful, helpful, independent and challenging at the same time. Finally, I want to thank Alexandre, Nataliya, Sergey and Anthony former and current postdocs of the group. I whish all the best for all of them.

I would like to thank all the co-workers who helped me to conduct my experiments and understand my results. I thank Uwe SCHROEDER from NamLab; Laurent GRENOUILLET and Olivier RENAULt from CEA-LETI, Sylvia MATZEN and Thomas MAROUTIAN from C2N; Pierre-François ORFILA and Sébastien DEPLART from SPEC's NanoFab facility, Bertrand VILQUIN from Ecole Centrale de Lyon and Athanasios Dimoulas from NCSRD.

I would also like to acknowledge all the support I got from the synchrotron teams: Denis CEOLIN and Jean-Pascal RUEFF from SOLEIL; Shigenori UEDA and Yoshiyuki YAMASHITA from SPring8 and Onur MENTES and Andrea LOCATELLI from ELETTRA.

My deep personal gratitude goes to Anne BOOS, head of the RePSeM group (IPHC, Strasbourg) and director of my Master 2 internship for the chance she gave me to come to France in the first place and to my professor Nathalie VIART from Strasbourg University for the excellent course I had with her on functional oxides which strongly contributed to the orientation of my research.

The doctoral work has been financially supported by the 3ϵFERRO project which has received funding from the European Union's Horizon 2020 research and innovation programme under grant agreement No 780302 (www.3eferro.eu/).

Contents

Abstract i

Acknowledgments iii

Preface ix

1 Ferroelectricity **3**
- 1.1 Background . . . 3
  - 1.1.1 Generalities . . . 3
  - 1.1.2 Structural aspects . . . 6
  - 1.1.3 Hysteresis loop . . . 8
  - 1.1.4 Thermodynamics . . . 9
  - 1.1.5 Phonon dispersion . . . 10
- 1.2 The modern theory of polarization . . . 10
- 1.3 Boundary conditions . . . 12
  - 1.3.1 Depolarizing field . . . 12
  - 1.3.2 Screening mechanisms . . . 12
- 1.4 Metal/ferroelectric interface: the Schottky barrier . . . 15
  - 1.4.1 Schottky-Mott rule . . . 15
  - 1.4.2 Fermi level pinning . . . 16
  - 1.4.3 Addition of the ferroelectric polarization term . . . 18
- 1.5 Ferroelectric memory . . . 20

2 Ferroelectric hafnia **23**
- 2.1 Overview . . . 23
- 2.2 Bulk structure . . . 23
- 2.3 Thin film properties . . . 26
  - 2.3.1 High-k gate oxide . . . 26
  - 2.3.2 Ferroelectricity . . . 27
- 2.4 Ferroelectric hafnia-based devices . . . 32
  - 2.4.1 Ferroelectric random access memory (FRAM) . . . 32
  - 2.4.2 Ferroelectric field effect transistor (FeFET) . . . 33
  - 2.4.3 Ferroelectric tunnel junction (FTJ) . . . 34
  - 2.4.4 Reliability aspects . . . 35
- 2.5 Defects . . . 38
  - 2.5.1 Overview . . . 38
  - 2.5.2 Oxygen vacancies . . . 39
  - 2.5.3 Charge transport . . . 42

3 Experimental methods 45
3.1 Electrical measurements . . . 45
3.1.1 Dynamic Hysteresis measurements . . . 45
3.1.2 Capacitance and leakage current measurements . . . 47
3.1.3 Endurance cycling . . . 48
3.2 Photoelectron spectroscopy . . . 49
3.2.1 Overview . . . 49
3.2.2 The photoemission process . . . 49
3.2.3 Important features in XPS spectra . . . 55
3.3 Hard X-ray photoelectron spectroscopy . . . 60
3.3.1 Synchrotron radiation: relativistic effect . . . 61
3.3.2 Technical aspects . . . 62
3.3.3 HAXPES beamlines specifications . . . 64

4 Interface physical chemistry of $Hf_{0.5}Zr_{0.5}O_2$-based capacitors 67
4.1 Introduction . . . 67
4.2 TiN/$Hf_{0.5}Zr_{0.5}O_2$ interface . . . 68
4.2.1 Electrical characterization . . . 68
4.2.2 XPS analysis . . . 69
4.3 W/$Hf_{0.5}Zr_{0.5}O_2$ interface . . . 80
4.3.1 Electrical characterization . . . 80
4.3.2 XPS analysis . . . 81
4.4 Conclusions . . . 86

5 Effect of La doping and field cycling in La doped $Hf_{0.5}Zr_{0.5}O_2$ 87
5.1 Introduction . . . 87
5.2 Chemical and electronic implications of La doping in $Hf_{0.5}Zr_{0.5}O_2$ . . 88
5.2.1 XPS analysis . . . 88
5.2.2 Leakage current measurements . . . 92
5.3 Interface chemistry of HZLO-based capacitors . . . 95
5.3.1 Experimental . . . 95
5.3.2 Top *vs* bottom interface . . . 97
5.3.3 Oxygen vacancies . . . 99
5.4 HAXPES with applied bias . . . 102
5.4.1 Electrical characterization . . . 104
5.4.2 Effect of field cycling . . . 107
5.4.3 Polarization-dependent band diagram . . . 109
5.5 Conclusions . . . 111

6 Oxygen vacancy engineering in Si implanted HfO_2-based capacitors 113
6.1 Introduction . . . 113
6.2 Experimental . . . 114
6.3 Electrical characterization . . . 116
6.4 HAXPES results . . . 119
6.4.1 Effect of Ti scavenging layer on the as grown V_O distribution . 121
6.4.2 Effect of field cycling on V_O . . . 122
6.4.3 Polarization-dependent band diagram . . . 123

6.5 Conclusions 126

Conclusions & perspectives **127**

A Sample preparations and preliminary analyzes **131**
A.1 TiN/$Hf_{0.5}Zr_{0.5}O_2$/TiN capacitors 131
A.2 W/HZO/W capacitors 133
A.3 TiN/La doped HZO/TiN capacitors 133
A.4 TiN/Ti/Si implanted HfO_2/TiN capacitors 134

B Synchrotron-based X-PEEM experiments **135**

French summary **141**

Bibliography **163**

Preface

Ferroelectric materials exhibit a remanent polarization state that can be stored and reoriented using low power (electrically) in a non-volatile manner. They can therefore be used to encode boolean algebra and made the basis of a non-volatile memory (NVM). Ferroelectric *random access memory* (FRAM) has the highest endurance among all NVM candidates, low energy per bit and power consumption making the technology a good candidate to replace the standard Flash technology in embedded applications. However, the current FRAMs using perovskite oxides present serious problems with regard to the memory cell scaling, compatibility with Si processing, manufacturability and cost, inhibiting thus the development of the ferroelectric memory as a mainstream solution. New materials which overcome the shortcomings of the present day FRAMs are therefore sought for. Within the framework of the H2020 European project 3ϵFERRO, led by the CEA, we used ferroelectric HfO_2-based materials to develop a competitive and versatile FRAM technology for embedded NVM solutions. HfO_2 is already a key element in modern nanoelectronics as dielectric material thanks to its compatiblility with state-of-the-art Complementary Metal Oxide Semiconductor (CMOS) technology. In 2011, the discovery of a ferroelectric phase in HfO_2 placed the material on a completely different hierarchical level of importance as it became the element defining the device physics, renewing tremendous interest in FRAMs.

The PhD work reports on the interface chemical and electronic structure of optimized ferroelectric thin films made of HfO_2. In a capacitance or transistor structure, the interface is probably one of the major challenges for engineering hafnia thin films. Amorphous films are crystallized in the desired orthorhombic ferroelectric structure only after a high temperature annealing. $Hf_xZr_{1-x}O_2$ with $x = 0.5$ is considered so far as the most promising material for device integration thanks to its low crystallization temperature (400-500°C), fully compatible with the thermal limitations of back end of the line (BEOL) in advanced CMOS nodes. The PhD work focuses therefore on ferroelectric $Hf_{0.5}Zr_{0.5}O_2$ interfaces with electrodes. The main goal is to elucidate the role of oxygen vacancies on the reliability of these films. We combined electrical measurements and mainly X-ray photoemission spectroscopy techniques with *in-situ* biasing when necessary in order to evaluate the effect of electrode material, annealing temperature, doping, field cycling and polarization reversal on the oxygen vacancy concentration and profile in addition to the band alignments at interfaces. The thesis also highlights the potential of photoemission-based techniques in the semiconductor industry research.

The work was done at the French Atomic Energy Authority (CEA) in the Service de Physique de l'Etat Condensée (SPEC), part of the IRAMIS institute. It involved many close collaborations with the 3ϵFERRO consortium members. The samples analyzed are fabricated in NamLab (Dresden) and at CEA LETI (Grenoble). Photoemission spectroscopy with *in-situ* bias experiments have been conducted at different synchrotron facilities: the Japanese synchrotron SPring-8 on the BL15XU beamline, Synchrotron SOLEIL (France) on the GALAXIES beamline and in Sincrotrone Elettra (Italy) on the Nanospectroscopy beamline. Micro-fabrication processes have been conducted at the SPEC's NanoFab facility.

The dissertation comprises 6 chapters organized as follows:

Chapter 1 covers the different aspects behind the development of a permanent switchable electric polarization within a solid, i.e ferroelectricity, in addition to the metal/ferroelectric interface with a focus on the Schottky barrier height. The advantage of a ferroelectric memory is also discussed.

Chapter 2 is fully devoted to hafnia (HfO_2) and the root causes of ferroelectricity in this material. The chapter gives also a short review on the recent hafnia-based devices and the related reliability aspects. Finally, the chemistry and physics of oxygen vacancies along with their different origins and implications in the hafnia systems are reviewed.

Chapter 3 contains a description of the various experimental methods used to characterize the capacitor structures made from 3ϵFERRO partners. It is divided into two parts. The first part describes the different electrical measurement while the second part is devoted to the basis of photoemission spectroscopy techniques. The advantages of synchrotron radiation and a description of the synchrotron beamlines used are also presented.

Chapter 4 consists of a systematic investigation on the role of the electrode material on the interface physical chemistry of $Hf_{0.5}Zr_{0.5}O_2$-based capacitors. TiN and W electrodes were investigated, mainly by laboratory X-ray photoelectron spectroscopy (XPS).

Chapter 5 reports on the effect of La doping in $Hf_{0.5}Zr_{0.5}O_2$ capacitors. The chemical and electronic implications are discussed. Then, capacitors with an optimized La concentration have been used to study the effect of field cycling and polarization reversal using Hard X-ray photoelectron spectroscopy (HAXPES) with *in situ* applied bias. These measurements were performed at SPring-8.

Chapter 6 highlights oxygen vacancy engineering in technologically relevant Si implanted HfO_2 thin films in collaboration with CEA LETI. HAXPES measurements with *in-situ* bias were realized at SOLEIL to correlate controlled oxygen scavenging with endurance and electrical performance.

Finally, a general conclusion and discussion of perspectives, is followed by two appendices on sample preparation and on the latest experiments performed using X-ray photoemission electron microscopy (X-PEEM) at Elettra.

Chapter 1

Ferroelectricity

1.1 Background

1.1.1 Generalities

In 1921, using Rochelle salt (Sodium potassium tartrate tetrahydrate, ($C_4H_4KNaO_6 \cdot 4H_2O$), which owes its name to a historic town in France "La Rochelle", Valasek reported the first ever electrical hysteresis loop (shown in Fig. 1.1) and described the analogy with the hysteretic behavior of ferromagnetism[1]. A new class of material was thus called ferroelectric. Whereas ferromagnets exhibit a permanent magnetic moment that may be reoriented with a sufficiently strong magnetic field, the order parameter in ferroelectrics is a permanent electric dipole moment referred to as spontaneous electrical polarization in zero applied field that can be reoriented under a sufficiently strong electric field.

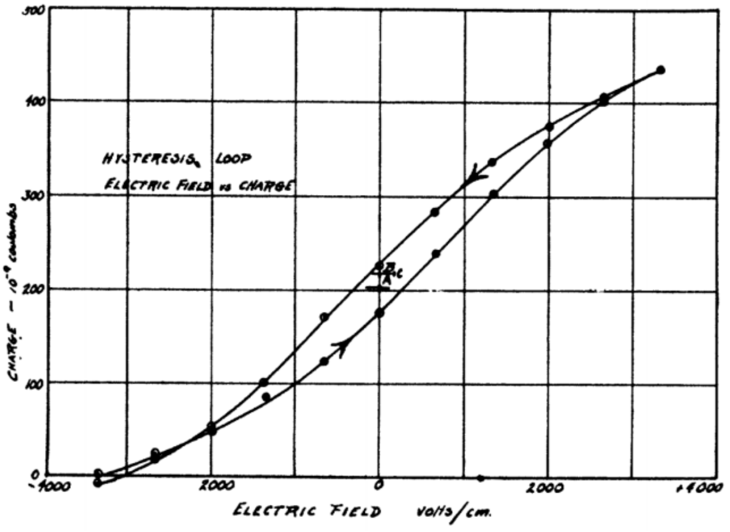

Figure 1.1: *The first ever electric hysteresis loop measured by Valasek on Rochelle Salt in 1921* (from ref.[1])

Ferroelectric materials show therefore an electric polarization hysteresis loop under applied electric field similar in shape to the magnetization loop of ferromagnetic materials under applied magnetic field (Fig. 1.1). The prefix ferro has nothing to do with the ferrous, i.e. iron content of the material, but was used to highlight the analogy of a physical parameter ordering under an external stimulus. Ferroelastics are the third known ferroic materials and are characterized by an elastic hysteresis behavior under mechanical stress. Ferroelasticity plays a major role in the mineralogical behavior of the earth's crust and mantle and it is the most common nonlinear effect in natural materials[2]. Recently, ferrotoroidicity, that is a uniform arrangement of toroidal magnetic vortices, has been actively discussed as the fourth ferroic order in addition to ferromagnetism, ferroelectricity, and ferroelasticity[3, 4].

After the first evidence of ferroelectricity in 1921, further ferroelectric materials were discovered such as KH_2PO_4 in 1935[5] and the first ferroelectric perovskite oxide $BaTiO_3$ by the end of the second world war in 1946[6]. The discovery of $BaTiO_3$ was the beginning of ferroelectric-based electronics era. The initial reports were in 1941 by the American Lava Corporation based on doping TiO_2 with BaO, which produced $BaTiO_3$ ceramic materials with enhanced dielectric permittivities (k>1100) (U.S. Patent No.2429588[7]). It was therefore since the beginning proposed as high-k medium in capacitor applications[7, 8, 9]. In a dielectric capacitor, the electric displacement field (D), which corresponds to the electrical flux density directly related to the stored energy (expressed in units of $C.m^{-2}$), is related to the electric field by the following expression:

$$D = \epsilon_0 E + P \tag{1.1}$$

Where ϵ_0 is the vacuum permittivity, E is the applied electric field and P is the electronic polarization of the dielectric due to the net dipole moments of the atomic nuclei and the electron cloud. The polarization is determined by the electric polarizability of the material (χ_e) as follows:

$$P = \epsilon_0 . \chi_e E \tag{1.2}$$

The displacement field can thus be written as:

$$D = \epsilon_0 E + \epsilon_0 . \chi_e . E = \epsilon_0 (1 + \chi_e) E = \epsilon E \tag{1.3}$$

This gives the relative permittivity ϵ_r, also called the dielectric constant k, of the material:

$$\epsilon_r = \frac{\epsilon}{\epsilon_0} = 1 + \chi_e \tag{1.4}$$

The capacitance C is an important parameter, defining the stored charge ($Q = CV$). It is related to the relative permitivity (ϵ_r), the film thickness (d) and the electrode area (A) in a parallel plate capacitor as follows:

$$C = \frac{\epsilon_0 \epsilon_r A}{d} \tag{1.5}$$

In a ferroelectric material, an ionic-based electric dipole moment is further produced within the material. The sum of the dipoles lead to a macroscopic spontaneous electric polarization (P$_s$) which adds a switching term to the displacement field as follows:

$$D = \epsilon_0 \epsilon_r E + P_s \tag{1.6}$$

Hippel *et al*[6] and others attributed after the high polarizability observed with BaTiO$_3$ to its ferroelectric nature and its additional P$_s$. Since then, investigations on BaTiO$_3$ and similar ferroelectric perovskites have pushed forward the theoretical and experimental knowledge on ferroelectrics. Ferroelectric materials exhibit also pyroelectric and piezoelectric properties. Pyroelectricty is the ability to turn thermal energy in electricity owing to the emergence of electric polarization by time-dependent temperature variation. The generated pyroeletric current can be expressed as follows[10]:

$$I_{pyr} = \frac{dQ}{dt} = pA(\frac{dT}{dt}) \tag{1.7}$$

Where Q is the pyroelectric charge, p is the pyroeletric coefficient, A is the electrode surface area and $\frac{dT}{dt}$ is the rate of temperature change. The effect is largely used in power generation, thermal energy harvesting, ultra-violet (UV) and infrared (IR) light sensing and imaging, in addition to electrochemical applications including hydrogen generation and wastewater treatment[11]. Piezoelectricity, on the other hand, represents the ability to develop an electric displacement field under an homogenous applied mechanical stress (σ). Thermodynamically, all piezoelectric materials exhibit in addition the so-called converse piezoelectric effect which is defined by a strain (S) manifestation under applied electric field. The piezoelectric coupling can be described by a linear relationship between a first rank tensor (vector) D or E and the second rank tensors σ or S as shown by the following expressions[12]:

$$\begin{aligned} D_k &= d_{kij}\sigma_{ij} \\ S_{ij} &= d_{kij}E_k \end{aligned} \tag{1.8}$$

Where d_{kij} are third rank tensors called the coupling coefficients with $i, j, k = 1, 2, 3$. In practise, both the piezoelectric and the converse piezoelectric effects are generally quantified using the reduced matrix form d_{km}, where k denotes the componenets of D or E in the cartesian reference (x_1, x_2, x_3) and m defines the applied mechanical stress or the generated strain. m= $1, 2$ or 3 correspond to the normal stress or strain along x_1, x_2, x_3 and $4, 5$ and 6 values for shear stresses or deformations[13]. d_{33} for instance is very useful to evaluate piezoelectric materials since it corresponds to a polarization induced parallel to the direction of the applied mechanical stress or equivalently a strain parallel to the applied field direction. Piezoresponse force microscopy (PFM) presents an imporant experimental tool in evaluating ferroelectrics thanks to its piezoelectric coupling and in particularly d_{33}. Furthermore, it should be noted that the electric polarization can be developed in all dielectric materials by the application of a strain gradient (inhomogenous), the so-called flexoelectricty [14]. Although discovered in the late 1960s[15], the field lay relatively dormant until the early 2000s thanks to a series of reports[14] showing that materials with high ϵ_r, could have rather large flexoelectric coefficients, sufficiently large to make micro- and nano-electric mechanical system (MEMS/NEMS) devices without the need of piezoelectric materials like the widely used lead zirconate titanate ($PbZr_{1-x}Ti_xO_3$)[16].

1.1.2 Structural aspects

Many oxides having the chemical formula ABO_3 adopt the perovskite structure. Originally, the structure owes its name to Perovsky, a russian mineralogist (also minister) who attributed the name to the crystal structure of calcium titanate ($CaTiO_3$)[17]. Perovskite oxides exhibit many interesting properties such as ferroelectricity ($BaTiO_3$, $PbTiO_3$), ferroelasticity ($CaTiO_3$) or even multiferroicity where at least two ferroic orders exist in the same material ($BiFeO_3$, $EuTiO_3$). Giving the relative simplicity of the structure, it is generally used to illustrate the basic structural aspects behind the development of P_s. Figure. 1.2 shows the ideal cubic perovskite structure. The B cations (generally transition metals) are placed in the bcc position. The A cations are placed at the corners and the oxygen in the fcc position, forming an oxygen octahedron around the bcc B-type cations.

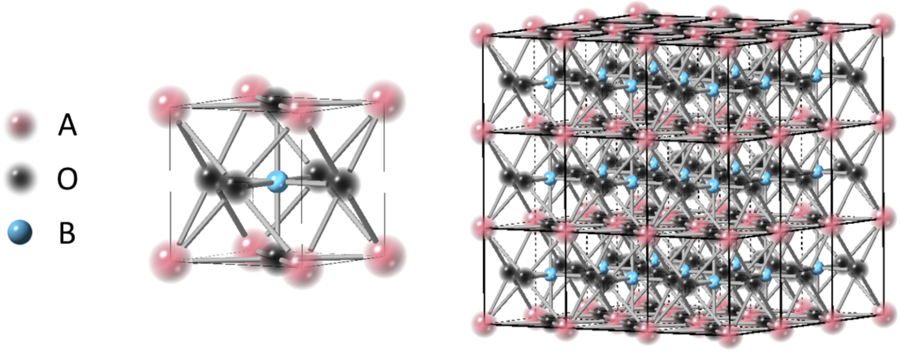

Figure 1.2: *ABO_3 ideal cubic perovskite structure*

The stability of such structure is determined by the cation sizes and can be evaluated using the Goldschmidt factor t:

$$t = \frac{r_A + r_O}{\sqrt{2}(r_B + r_O)} \tag{1.9}$$

The structure is energetically favorable only if t$\sim$1. If A is small (t<1), rotation and tilting of the oxygen octahedral will be favored to minimize the total energy. This, for instance, is at the origin of ferroelasticity in $CaTiO_3$. When t>1 (the B atom is too small), the structure however will develop a ferroelectric distortion and this is the case with $BaTiO_3$[17].

The evolution of the crystal phase of $BaTiO_3$ as a function of temperature is shown in Fig. 1.3. Decreasing the temperature leads to a structural phase transition from a high symmetry cubic phase called paraelectric to low temperature, lower symmetry ferroelectric phases due to the off-centering of the Ti cation in the oxygen octahedron along certain axes. In fact, this breaks the centrosymmetry within the unit cell and leads to a net electric dipole moment due to the imbalance of the distribution of ions charges. $BaTiO_3$ exhibits three such ferroelectric phases: tetragonal (278K to 393K), orthorhombic (183 K to 278 K) and a rhombohedral phase (up to 183K)[17]. In each case, the Ti is off-centered, following the <001>, <011> and <111> directions, respectively. Due to long-range Coulomb interactions between the dipole moments of the unit cells, a macroscopic electric polarization will occur along the off-centering axis, called the polar axis. This off-centering may also lead to different hybridization between the *d* orbitals of the transition B metal (3*d* with Ti) and the O2*p* orbitals of oxygen which may induce modification on the bulk properties of the material such as the band gap [17, 18].

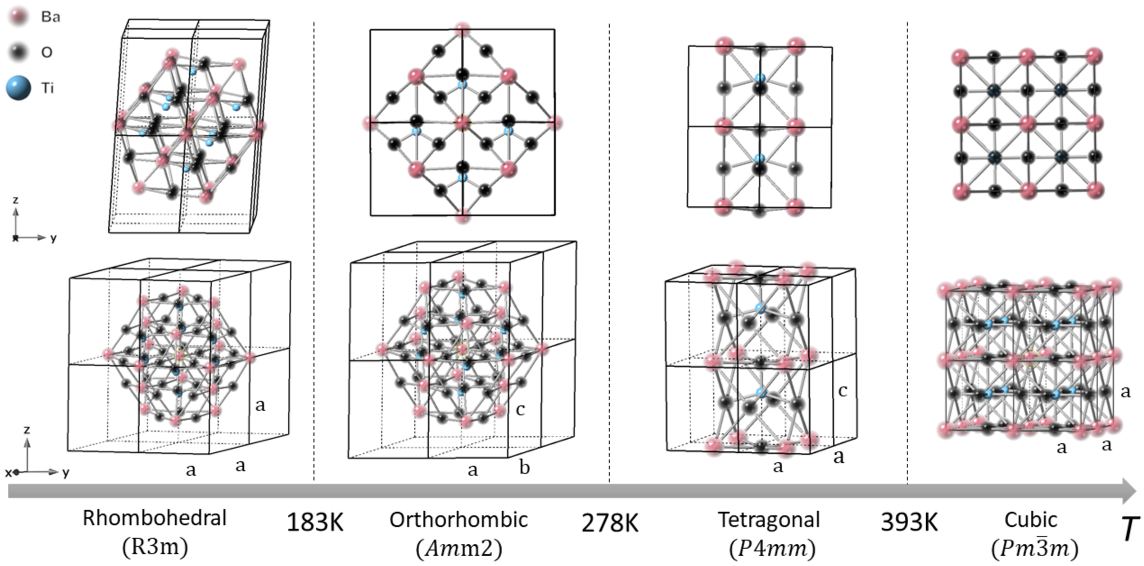

Figure 1.3: *$BaTiO_3$ crystal structure evolution with temperature using data from ref.[19] and CrystalMaker software. The Ti cation is off-centered following <001>, <011> and <111> directions with respect to the paraelectric cubic position, giving rise to a tetragonal, orthorhombic and rhombohedral ferroelectric phases, respectively. Space groups are also given. They combine translations with point symmetry operations*

As shown in Fig. 1.3, the emergence of polarization is therefore accompanied by a symmetry-breaking from a higher-symmetry centrosymmetric phase to a lower symmetry polar non-centrosymmetric phases[17]. Of the 32 crystal known point groups, only 21 are non-centrosymmetric. Piezoelectricity is permitted in 20. However, due to the lack of inversion symmetry, certain piezoelectric materials do not possess a unique polar axis and, therefore, stable polarization. Only 10 can be considered for pyroelectricity. Ferroelectricity is defined as a crystal property where the permanent dipole can be reoriented with an electric field. There is therefore no structural evidence of difference between pyroelectrics and ferroelectrics, only the switching ability allows to differentiate ferroelectrics[20].

1.1.3 Hysteresis loop

To evaluate the ferroelectric behavior of a material, the hysteresis loop of the polarization as a function of the applied field, which presents the defining feature in the electrical response of a ferroelectric, is measured. A hysteresis loop is generated by plotting the ferroelectric polarization as a function of voltage or electric field, commonly denoted as a $P - V$ or $P - E$ plot, respectively (Fig. 1.4). Obtaining P as a function of E gives key information such as remanent and saturation polarization (P_r , P_s), i.e. the polarization at zero field and the maximum polarization or the coercive field (E_C), the field required to switch the polarization. P_r and E_c are determined by:

$$P_r = \frac{\mid P_r^+ \mid + \mid P_r^- \mid}{2} \tag{1.10}$$

$$E_c = \frac{V_c}{d} = \frac{\mid V_c^+ \mid + \mid V_c^- \mid}{2d} = \frac{\mid E_c^+ \mid + \mid E_c^- \mid}{2} \tag{1.11}$$

Where P_r^+ and P_r^- are the antiparallel positive and negative remanent polarization, V_c^+ (E_c^+) and V_c^- (E_c^-) represent the positive and negative coercive voltages (fields) and d is the ferroelectric film thickness. E_c is a key characteristic as it permits to know the electric field at which the volume averaged electric dipoles, i.e. the macroscopic polarization, changes sign. Thus, at E_c, P_r=0 and the applied electric field needed to fully flip the polarization vector must be higher than E_c.

Experimentally, there is no direct electrical measurement of the polarization vector itself. However, the switching of the polarization vector leads to a current flow at E_c called the switching current. The time integration of this current allows to deduce, knowing the capacitor area, the polarization (see Section. 3.1).

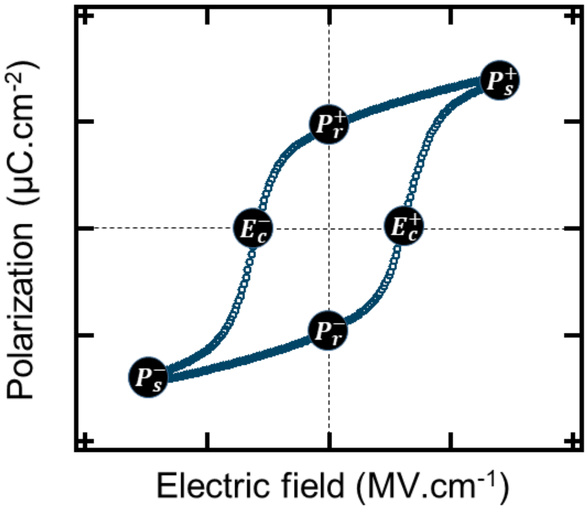

Figure 1.4: *Typical electric polarization - field hysteresis loop (P-E) identifying the positive and negative saturation (P_s^+ and P_s^-) and remanent polarization (P_r^+ and P_r^-) values as well as the positive and negative coercive fields (E_c^+ and E_c^-). In this thesis, we adopted the units commonly used in device physics*

1.1.4 Thermodynamics

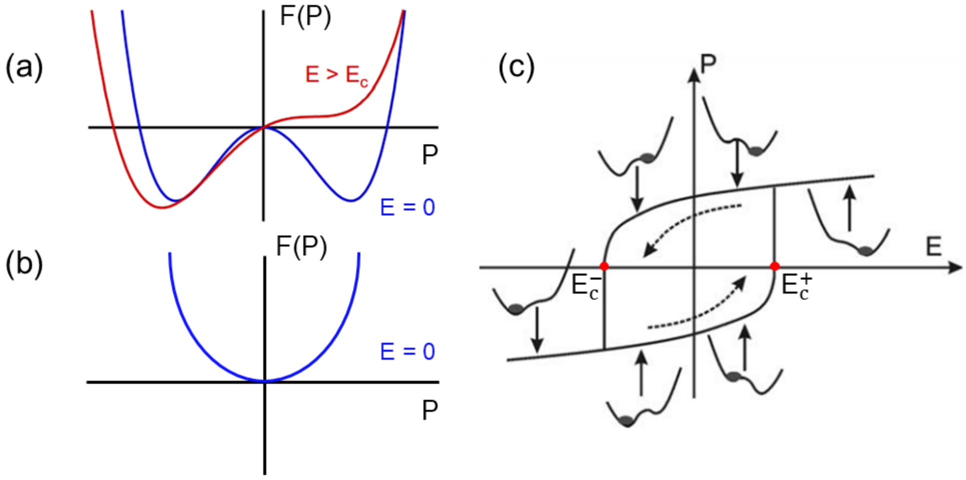

Figure 1.5: *Free energy as a function of electric polarization in (a) ferroelectric (double well) (b) paraelectric (single well) and (c) the evolution of the free energy under applied electric field for a ferroelectric (adapted from ref.[17])*

Understanding structural phase transitions through thermodynamics approach was first given by Lev Landau, Nobel prize in physics in 1962. Landau theory is a phenomenological approach using symmetry based arguments for macroscopic entities used to analyze the behavior of a system near a phase transition involving a change of symmetry[21]. In 1949, Devonshire was the first to apply this theory to ferroelectrics[22]. The phases are characterized by an order parameter (polarization) which is zero in a high-symmetry phase (cubic in the case of $BaTiO_3$) and continuously change to a finite value in the low-symmetry phase. Thermodynamically, the theory defines a ferroelectric material by a double potential well in the free energy of at least one set of ions (Fig. 1.5a). A paraelectric material on the contrary shows only a single parabolic well (Fig. 1.5b). An electric field higher than E_c will switch the polarization from one ground state to the other (Fig. 1.5c). Landau-Devonshire theory is a displacive model (cation off-centering). In the order-disorder model[23], ions progressively acquire enough kinetic energy with increasing temperature ($k_B T$) to hop back and forth between the two sides of the potential double well and the average position is midway between the two polar states. However, most ferroelectrics are shown to be displacive without any dominating kind of quantum mechanical tunneling between the double-well minima as in an order-disorder system. Most of ferroelectrics are therefore very well described using Landau-Devonshire theory[17]. Indeed, the development of free energy as a function of different variables (temperature, strain, electric field) allowed outsanding results about the transition energy, the Curie temperature, i.e the transition temperature from a paraelectric to a ferroelectric phase and other properties of many ferroelectrics. However, it should be noted that the theory fails to describe systems of reduced size when the macroscopic averaging of the order parameter is no longer possible.

1.1.5 Phonon dispersion

Crystallography considerations show the necessary symmetries to support ferroelectricity while thermodynamics outline the free energy landscape allowing the development of P$_S$. However, these two approaches do not highlight the local mechanisms of atomic displacement. The first step towards a microscopic approach was introduced in 1960 by Cochran who described ferroelectricity in terms of phonons, i.e crystal lattice modes of vibrations[24]. Considering a 1D linear chain of O-Ti-O atoms along the polar axis in BaTiO$_3$ (see the tetragonal phase in Fig. 1.3), the displacement dynamics of titanium atom out of its equilibrium position (oxygen octahedral center) can be described using classical Newtonian physics:

$$\mu\frac{\delta^2 x}{\delta^2 t} = -Rx + Ax \tag{1.12}$$

R describes the restoring force due to the short-range Coulombic interaction between anions and cations while A describes the destabilizing force due to the long range coulombic forces (dipole-dipole coupling). μ is the reduced mass of the Ti - O unit. The existence of ferroelectricity depends on the competition between these forces. Acoustic modes of phonons are coherent movement of all atoms of the lattice out of their equilibrium position. They cannot therefore contribute to the emergence of ferroelectricity. However, optical modes consisting of out-of-phase cation/anion movement do play a role. Indeed, Cochran showed that the freezing of the transverse optical (TO) mode can stabilize ferroelectricity[24]. The frequency of the TO mode creating relative ionic displacement is expressed as follows:

$$\mu\omega^2(TO) = R - \frac{4\pi(\epsilon_{opt}+2)(Zq^2)}{3V(T)} \tag{1.13}$$

Where V(T) is the unit cell volume as a function of temperature (increases by increasing temperature), Z is the effective charge of the mode and ϵ_{opt} is the optical permitivitty. At high temperature (high symmetry phase), the restoring forces R are maximized and the system is paraelectric. However , decreasing temperature leads to V(T) decrease which results in softening and freezing of the TO mode (it progressively goes to zero until it disappears at the transition temperature). Decreasing further the temperature allow the long range forces A to become dominant and the system becomes ferroelectric.

1.2 The modern theory of polarization

So far, the electric polarization is defined as a macroscopic quantity describing the integrated contributions of localized permanent dipoles. However, in finite crystalline solids, this definition fails to unambiguously describe a bulk polarization P_{bulk} (surface vs bulk polarization, choice of the unit cell). In addition, the electronic polarization in a crystal has a periodic but continuous charge distribution, which cannot be unambiguously partitioned into localized contributions.

In typical ferroelectric oxides, this is also the case as the bonding has a mixed ionic/covalent character, with a sizeable fraction of the electronic charge being shared among ions in a delocalized manner[25]. Therefore, the electric polarization cannot be regarded as the sum of localized dipoles. For these reasons, Resta, King-Smith and Vanderbilt developed in the early 1990s a solution to tackle this fundamental issue on the microscopic scale, known as the *modern theory of polarization*[25]. The theory is based on calculating rather the polarization difference using the time-integrated accumulated adiabatic current occurring as a crystal is modified or deformed and takes into account the quantum nature of electrons. Focusing on the current (as it is experimentally measured) instead of the charge was therefore crucial to an unambiguous definition. The polarization difference ΔP is simulated between two states of the crystal that are connected by an adiabatic process with a dimensionless adiabatic time parameter, λ. This parameter varies continuously and the transition from the initial (centrosymmetric for example at λ=0) to the final state (ferroelectric at λ=1) is achieved by stimulus applications (atomic displacement for instance). The change in polarization is expressed as follows[25]:

$$\Delta P = \int_0^1 d\lambda \frac{dP}{d\lambda} \tag{1.14}$$

where $\frac{\mathrm{d}P}{\mathrm{d}\lambda}$ is the rate of the polarization change. At this point, one needs the adiabatic electronic current that flows through the crystal while the perturbation is switched on. Within a quantum-mechanical description, currents are closely related to the phase of the Bloch wavefunction[25]. In addition, the electrons in the crystal in this case are interacting with an external apparatus (to measure the current). This interaction gives rise to a certain quantum phase in the electronic Bloch wavefunction called Berry phase, whose observable effects constitute the macroscopic polarization difference ΔP. By definition, a general parametric Hamiltonian allows one to deal with a part of a larger system as if it was isolated. However, the interaction of a non-isolated quantum system with the rest of its "universe" (circuit for instance) results in the quantum Berry phase[26]. For this reason, the theory is also called *Berry phase theory of polarization* since the polarization is expressed in the form of that phase.

One of the most interesting implications of the theory is the concept of dynamical charges of atoms also called Born effective charge or infrared charge. As already mentioned, the covalent character in perosvkite oxides, which is mainly due to the hybridization of 2*p* oxygen orbitals with the 4*d* or 5*d* orbitals of the B cation, prevents unambiguous attribution of electronic charge to an atom[27, 28]. Thus, a dynamical charge is at the heart of a modern theory of polarization and models the changes in the atom polarization induced by an infinitesimal atomic displacements. In periodic systems, a dynamical charge tensor $Z^{\star}_{s,\alpha\beta}$ measures (linear approximation) the macroscopic polarization per unit cell created in the α direction induced by a sublattice displacement μ_s of atoms in β direction at zero electric field as follows[28]:

$$Z^{\star}_{s,\alpha\beta} = \frac{\Omega}{e} \frac{\delta P_\alpha}{\delta \mu_{s,\beta}} \tag{1.15}$$

Where Ω is the unit cell volume. Applying the Berry phase formalism on perovskite oxides leads to outstanding results. In $BaTiO_3$, dynamical charges are much higher than the static charge calculated from an ionic picture. For Ti^{4+}, Ba^{2+} and O^{2-}, the calculated dynamical charges are +7.25, +2.77 and -2.15 (or -5.71 depending on its chemical environment), respectively[28].

First-principles based effective Hamiltonian techniques based on Berry phase formalism are therefore very useful to calculate experimentally-accessible quantities such as piezoelectric coefficients, spontaneous polarization and dynamical charges. However, common limitations of *ab-initio* techniques such as the limited-cluster size and the impossibility to monitor non-equilibrium phenomena prevent it from accurately describing phase transition, for instance. Along with the Landau-Devonshire theory, which allows to find the energy minima as a function of the degrees of freedom of the system, the combination of both theories, in addition to the huge advances of the experimental and crystal growth techniques, have provided a much more detailed and accurate picture to the physics of ferroelectrics.

1.3 Boundary conditions

1.3.1 Depolarizing field

The depolarizing field (E_{dep}) is a fundamental part of ferroelectricity in finite materials. In thin film system, an out-of-plane component (vector n) of the ferroelectric polarization (P) induces a surface charge density ($\sigma_{polar} = P.n$). These charges generate an electric field E_{dep} that acts against the ferroelectric polarization as shown in Fig. 1.6:

$$E_{dep} = -\frac{P}{\epsilon\epsilon_0} \tag{1.16}$$

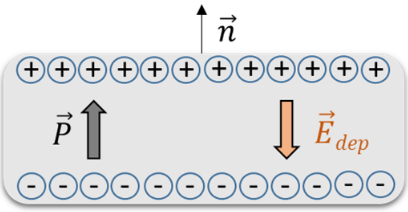

Figure 1.6: *Schematic of the depolarizing field E_{dep} inside a ferroelectric thin film due to unscreened polariation charges $\sigma_{polar} = P.n$. If E_{dep} is not screened, it can destabilize the ferroelectric stack*

It appears therefore that the electrical boundary condition, i.e. the screening of the polarization charges is a fundamental property of stabilizing the polarization when decreasing the film thickness.

1.3.2 Screening mechanisms

Putting a ferroelectric film in a circuit with two electrodes is a straightforward way to bring free charges that can screen the polarization charges. This will be treated separately in section. 1.4 devoted to the metal/ferroelectric interface. In uncapped thin films, other screening mechanisms have to be considered which can be classified into three groups. This is schematically shown in Fig. 1.7.

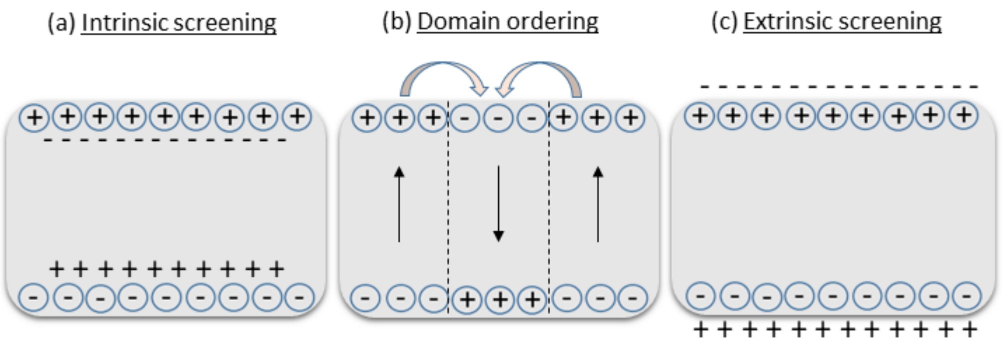

Figure 1.7: *Different mechanisms for screening the polarization charges in a finite thin film. (a) Intrinsic screening by free carriers and defects (b) domain ordering and (c) extrinsic screening mechanisms*

Intrinsic screening

Within a ferroelectric film, intrinsic screening is possible by mean of mobile charges (Fig. 1.7a). In many perovskite oxides, vacuum annealing at sufficiently high temperature generates two free electrons and one double positively charged oxygen vacancy via the following reaction: $O_O \rightarrow V_O^{\cdot\cdot}$ + $\frac{1}{2}$ O_2(g) + 2e$'$. These free carriers and charged point defects can screen the polarization charges reducing thus the magnitude of E$_{dep}$, which results in higher stable polarization value. However, these charges may also pin the polarization state in one direction and they are at the origin of internal fields causing different reliability issues in a ferroelectric capacitor such as imprint and polarization retention loss. This will be further developed in Chapter 2.

Domain organization

Domain organization is a very important natural screening mechanism (Fig. 1.7b). Depending on several internal and external parameters (temperature, strain, defects, history of the sample…), the dipoles rearrange themselves to minimize the energy of the system by forming domains separated by domain walls. The simplest case is the formation of domains with alternating antiparallel polarization. In such a case, the stray field from a domain screens the depolarizing field in adjacent domains and *vice-versa*. This domain organization can explain the ferroelectric stability of very thin films (Fig. 1.7b). However, domain walls are formed only when the energy gain by the domain formation is higher than the energy cost of the wall. The Kittel law (originally derived from ferromagnetic systems) for a thin film states that the energy gained by forming domains scales with volume, while the domain wall energy cost scales with area. This gives the famous square root dependence of the domain width (w) as a function of the film thickness (d) [29]:

$$w = \sqrt{\frac{\sigma}{U}}d \tag{1.17}$$

Where U is the volume energy density of the domain and σ the surface energy density of the wall per unit area. For tetragonal perovskites such as the room-temperature ferroelectric phase in $BaTiO_3$, two kinds of ferroelectric domains can nucleate: 180° domains with polarizations antiparallel to each other, which minimize depolarizing fields, and 90° domains with polarizations orthogonal to each other, which minimize strain via the formation of the so-called twin walls observed in ferroelastics[30]. They are also called c- and a-domains respectively by analogy to the long c-axis and shorter a-axis of the tetragonal lattice (P_s is always aligned along the long axis). While a transverse electric field is unable to switch in-plane domains, under energetically favorable conditions, an a-domain may be converted to a c-domain in what is called ferroelastic switching or 90° domain switching. Figure. 1.8 provides an illustration of 180° and 90° domain switching.

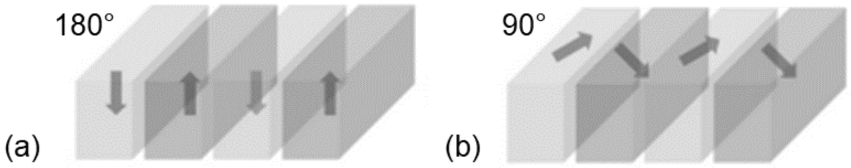

Figure 1.8: *Illustration of (a) 180° and (b) 90° domain ordering*

Extrinsic screening

Finally, extrinsic screening by the mean of adsorbates provides another tool for screening (Fig.1.7c). Different studies have indeed highlighted the role of adsorbents on stabilizing ferroelectricity or even the ability to induce domain switching. Shin *et al*[31] have studied the role of H_2O exposure on a $BaTiO_3$ bare films and showed that large exposures resulted in surface hydroxylation, formation of surface oxygen vacancies and even the reversal of the polarization direction at high exposure. Kelvin probe force microscopy (KPFM) and low energy electron miscroscopy (LEEM) techniques (surface potential sensitive techniques), have also shown that the sign of the surface charges have rather an oppposite sign to that of the expected polarization charges[32, 33, 34, 35]. These observations suggest that surface screening with adsorbates is a universal feature of oxide surfaces in air, and great care should be taken in the interpretation of the results. Recently, first-principle calculations have demonstrated the ability of adsorbates in engineering the polarization and coercive field values in technologically relevant ferroelectric films. The authors investigated the role of surface functionalization by hydroxyl (-OH) and fluorine (-F) groups and showed that the control of these adsorbates can be harnessed to stabilize preferred crystallographic orientations providing an additional tool to optimize the ferroelectric response[36].

1.4 Metal/ferroelectric interface: the Schottky barrier

The most important property of a metal-ferroelectric interface related to its electrical characteristics is the Schottky barrier height (SBH). It represents the potential barrier for free carrier transport formed when a metal is brought in contact with a ferroelectric. So far, ferroelectrics have been regarded as perfect insulators. This approach has been successful in explaining the basic properties like phase transition but totally fails in explaining charge transport mechanisms or other properties involving internal mobile charges. They can therefore be treated as wide band gap semiconductors[37, 38]. Figure. 1.9 shows a schematic of the energy band diagram of a semiconductor in direct contact with a metal electrode. The SBH for electrons and holes transport are denoted respectively as φ_{Bn} and φ_{Bp}. φ_{Bn} is defined as the potential energy difference between the conduction band minimum (CBM) of the semiconductor and the Fermi level (E_F) while φ_{Bp} is the energy difference between valence band maximum (VBM) and E_F. The sum of these two quantities is therefore equal to the band gap energy of the semiconductor (E_g=φ_{Bn}+φ_{Bp}). The insulating properties are guaranteed by the wide E_g at E_F where propagation of carriers is forbidden.

Φ is the work function. It represents the strength of the potential barrier that prevent valence electrons from escaping the sample. It is equal to the potential difference between a potential immediately outside the surface called vaccum level E_0 and the electrochemical potential of the material E_F. E_0 (thus Φ) depends on the orientation, the structure or even the contamination of the solid surface and can therefore vary from a sample to another. Φ plays an important role in all phenomena dealing with the escape of electrons from a solid (photo, thermionic, or field emission) or with the transfer of electrons between two materials (contact potential)[39]. The electron affinity (χ_s) and the ionization potential energy (I_s) of the semiconductor represent, respectively, the energy difference between E_0 and the CBM and between E_0 and the VBM.

1.4.1 Schottky-Mott rule

The first attempt to describe the band alignment of a metal/semiconductor junction goes back to the end of thirties when the Schottky-Mott rule was firstly reported [40, 41]. The model assumes no charge transfer occuring during the formation of the interface and the alignment depends only on the electronic properties of the two bulk materials. The vacuum level E_0 of both materials is aligned and the E_F of the metal is continuous through the interface and remains its original value with respect to E_0 within the bulk of the semiconductor[42]. Actually, the E_F position of the semiconductor when isolated was lowered once in contact with the metal by an amount called the contact potential which is equal to the work function difference between the two materials (E_0 is thus aligned). The adjustment occurs through band bending of semiconductor bands due to formation of a space charge region (not shown in Fig. 1.9). According to this phenomenological model, φ_{Bn}= Φ_m - χ_s and φ_{Bp}= I_s - Φ_m (Fig. 1.9). However, experimental results have proved the invalidity of this approach. In fact, it was found that the actual SBHs are much less dependent on Φ_m[43]. It appeared that charge transfer and the presence of interface states are responsible for the presence of dipoles at the interface which in turn modify the band alignment. This phenomenon is called Fermi level pinning.

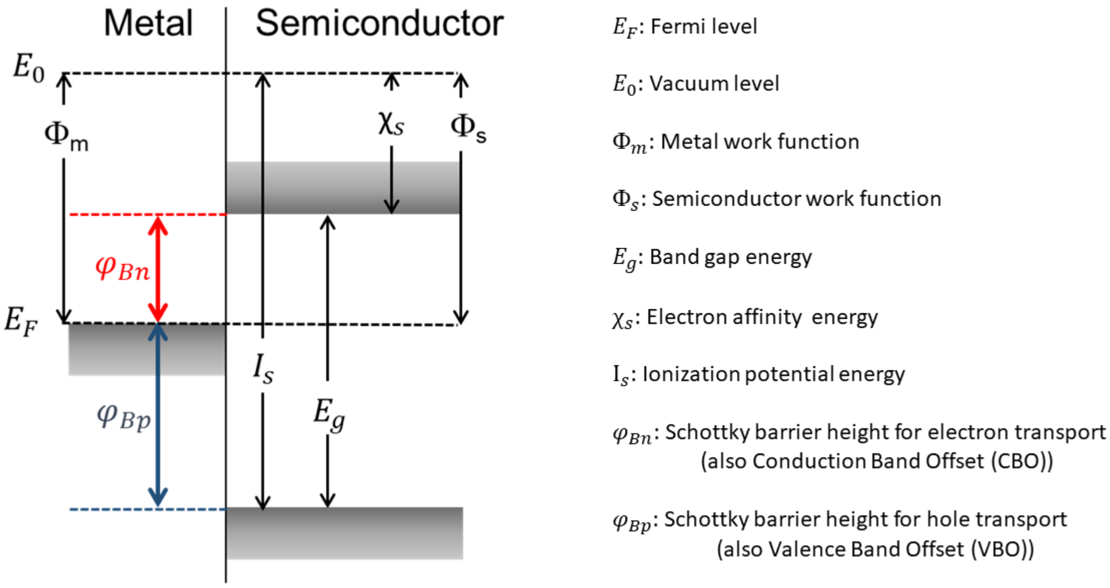

Figure 1.9: *Metal/Semiconductor interface band alignement diagram*

1.4.2 Fermi level pinning

The discrepancy between the experimental data and the Schottky-Mott rule led Bardeen[44] in 1947 to conceive an new approach incorporating the role of surface states in the semiconductor side. In this picture, E_F of the semiconductor is pinned by these surface states to its original charge neutrality level (E_{CNL}) and the work function difference between the two materials is rather compensated by an exchange of charges. The factor S=$\frac{\delta\varphi_{Bn}}{\delta\Phi_m}$ is used to quantify this Fermi level pinning phenomenon. S is equal to 1 for the Schottky-Mott limit where φ_{Bn} depends only on the Φ_m while the Bardeen's limit corresponds to $S = 0$ (only the surface states are considered). Figure. 1.10 compares the measured φ_{Bn} as a function of different metals work function in contact with n-type doped Si using the theoretical Schottky-Mott and Bardeen's models[45]. The limits $S = 0$ and $S = 1$ are also given. As shown in Fig. 1.10, most materials fall between these two limits. In 1965, Hein suggested that the surface states which pin E_F are mainly metal induced gap states (MIGS) due to the evanescence of the electrons wave function inside the semiconductor upon the chemical bond formation[46]. Originally, these MIGS were estimated basing on the covalency/ionicity of the bonding with higher MIGS for higher covalency. Later on, better correlations with the experimental results were reported when considering S in terms of the optical dielectric permittivity (S = $\frac{1}{1+0.1(\epsilon_{opt}-1)^2}$)[47].

In 1965, Cowley-Sze succeeded in developping a phenomenological model providing the first quantitative synthesis of the two previous limits, i.e the dependence on the work function of the metal and the presence of surface states[48]. In this approach the free charges in the electrode and the surface states are treated

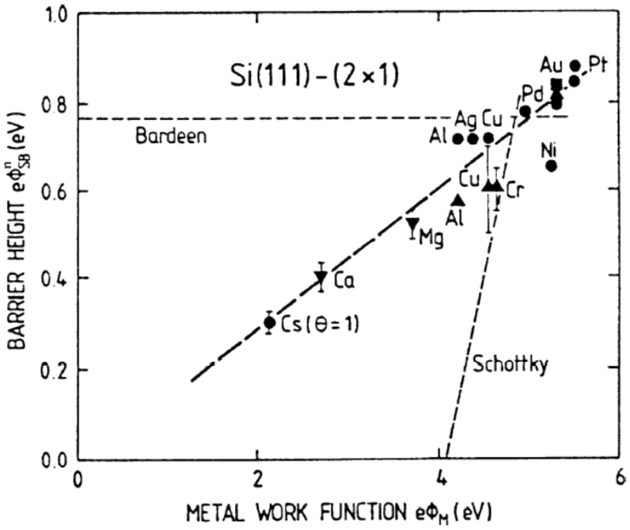

Figure 1.10: *Experimental dependence of φ_{Bn} on Φ_m of different metals in contact with n-type Si(111). The Schottky-Mott ($S = 1$) and Bardeen limits ($S = 0$) are also shown. (from ref.[48])*

separated by an interface layer of thickness δ which takes into account both the Thomas-Fermi screening length by the metal free charges and the penetration of the MIGS. A detailled band diagram is shown in Fig. 1.11. The first quantity of interest is the energy separation between the VBM and E_{CNL} for a given semiconductor surface φ_0. As already mentioned, E_{CNL} tends to pin the semiconductor Fermi level to it before the metal contact. Above this level, the states are acceptor type and below are donors. Consequently, when the final E_F of the electrode/semiconductor system coincides with E_{CNL}, the net interface-trap charge (Q_{is}) is zero. In Fig. 1.11 for instance, E_{CNL} lies below E_F. This leads to a negative interface trap charge (acceptor sites filled) which can be calculated as follows:

$$Q_{is} = -qD_{it}(E_F - E_{CNL}) = -qD_{it}(E_g - \varphi_{Bn} - \varphi_0) \tag{1.18}$$

Where D_{it} is the total interface charge density. Q_{SC} is the space charge density in the semiconductor depletion region at thermal equilibrium given by:

$$Q_{sc} = qN_D W \tag{1.19}$$

Where N_D is the density of ionized donors (n-type semiconductor) and W is the depletion layer width. The total surface charge density on the semiconductor surface is given by the sum of equations 1.18 and 1.19. This results in an equal amount of opposite charges on the metal surface:

$$Q_m = -(Q_{is} + Q_{sc}) \tag{1.20}$$

In order to retrieve the SBH, let's first consider the potential drop Δ across the interfacial layer:

$$\Delta = \Phi_m - \chi_s - \varphi_{Bn} \tag{1.21}$$

This potential drop can also be calculated using Gauss law as follows:

$$\Delta = -\frac{\delta Q_m}{\epsilon_i} \tag{1.22}$$

With ϵ_i is the dielectric permitivitty of the interface layer. Using the above equations allows finally to express φ_{Bn} as follows[48]:

$$\varphi_{Bn} = \gamma(\Phi_m - \chi_s) + (1-\gamma)(E_g - \varphi_0) - \Delta\varphi \tag{1.23}$$

with

$$\gamma = \frac{\epsilon_i}{\epsilon_i + q^2\delta D_{it}}. \tag{1.24}$$

When $D_{it} \to \infty$, then $\gamma \to 0$ and φ_{Bn} is completely independent of Φ_m. E_F is pinned at E_{CNL} and $\varphi_{Bn} = E_g - \varphi_0$. However, if D_{it} is 0, we found the schottky limit and the SBH is given by $\varphi_{Bn} = \Phi_m - \chi_s$. $\Delta\varphi$ corresponds to the lowering of φ_{Bn} by image force in an applied electric field (coulombic attraction between the metal charges and Q_{is}) which is typically $\Delta\varphi$ <10 meV and usually neglected[48, 42].

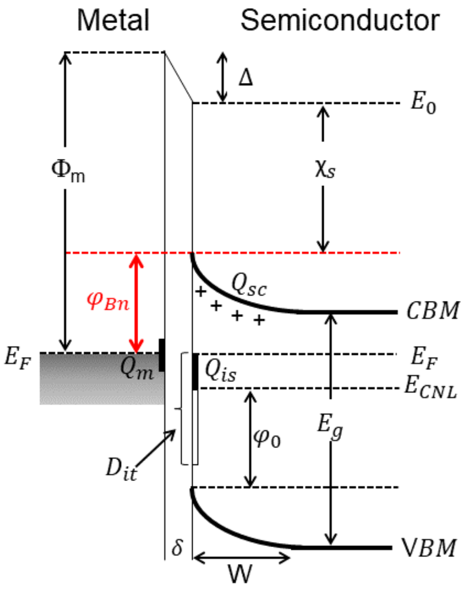

E_{CNL}: Charge neutrality level of the semiconductor

Δ: Potential drop across the interface layer

δ: Thickness of the interface layer

W: Depletion layer thickness within the semiconductor

Q_{sc}: Space charge density in the semiconductor

D_{it}: Total interface trap charge density

Q_{is}: Charged Interface traps (negatively charged acceptors)

Q_m: Surface charge density on the metal side

Figure 1.11: *Detailed energy-band diagram of a metal/n-type semiconductor contact with an interfacial layer (reproduced from ref.[48])*

1.4.3 Addition of the ferroelectric polarization term

Ferroelectric materials entail an additional degree of freedom, the macroscopic polarization P, which is absent in the non-polar semiconductor case. It is natural then to expect that the above picture of the band offset may need to be extended. Indeed, the observed SBHs can be compared to the predictions based on the theory of metal-semiconductor junctions extended to ferroelectric materials by Pintilie *et al*[38]. From this formalism, the theoretical magnitude of φ_{Bn} change due to the ferroelectric polarization in comparison to a semiconductor or similarly a paraelectric material can be derived from the Schottky thermionic emission model for charge transport and is given by[38, 49]:

$$\varphi_{Bn}(FE) - \varphi_{Bn}(sem) = \sqrt{\frac{eP}{4\pi\epsilon_r\epsilon_{opt}\epsilon_0^2}} \tag{1.25}$$

In addition, in the case of metal-ferroelectric interfaces, the interfacial dipole becomes explicitly dependent on the magnitude and direction of the polarization. This is due to the imperfect screening of the polarization charges due to the presence of a thin interfacial layer with a lower local permittivity, or some other mechanism that produces a spatial separation from the free screening charges of the electrode and the polarization charges[18]. In all cases, λ_{eff}, an effective screening length, takes into account the overall effects regardless of their microscopic nature including electronic and chemical bonding effects. The voltage drop associated with the interfacial layer can be written as:

$$\Delta V = \frac{P}{\epsilon_0}\lambda_{eff} \tag{1.26}$$

The associated depolarizing field is given by:

$$E_{dep} = -2\frac{\Delta V}{d} = -2\frac{P}{d\epsilon_0}\lambda_{eff} \tag{1.27}$$

Where d is the ferroelectric film thickness. Stengel *et al*[18] stated that the capacitance density of the interfacial layer is the most important parameter and is uniquely defined by λ_{eff}. Figure. 1.12 shows a short-circuited ferroelectric capacitor in a polarized configuration within the imperfect-screening model.

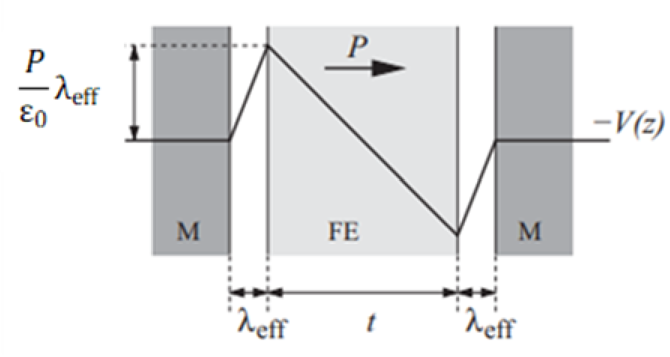

Figure 1.12: *Schematic representation of a symmetric, short-circuited ferroelectric capacitor in a polarized configuration within the imperfect-screening model (from ref.[18])*

Interestingly, it can be shown that the effective screening length (λ_{eff}) can be accessible via the change of SBH upon polarization reversal as follows:

$$e\Delta\varphi_{Bn} = \frac{e}{\epsilon_0} 2\lambda_{eff} P \tag{1.28}$$

Table 1.1: *Estimation of the change in φ_{Bn} of typical ferroelectric perovskites upon polarization reversal. P_S is the bulk spontaneous polarization of the ferroelectric and λ_{eff} is the effective screening length*

Interface	P_S (C.m^{-2})	$\Delta\varphi_{Bn}$ (eV)	λ_{eff} (Å)
$BaTiO_3/SrRuO_3$	0.39	1.8	0.20
$PbTiO_3/SrRuO_3$	0.75	2.6	0.15

Table. 1.1 gives the change in φ_{Bn} in typical ferroelectric perovskites BaTiO_3 and $PbTiO_3$ with $SrRuO_3$ oxide electrodes upon polarization reversal and the corresponding λ_{eff}[50]. The results indicate that $\Delta\varphi_{Bn}$ can be rather large of the order of 1–2 eV using oxide electrodes. However, different experimental results have shown that using noble metal electrodes allows a much better screening leading to shorter λ_{eff} and lower $\Delta\varphi_{Bn}$ [51, 52].

1.5 Ferroelectric memory

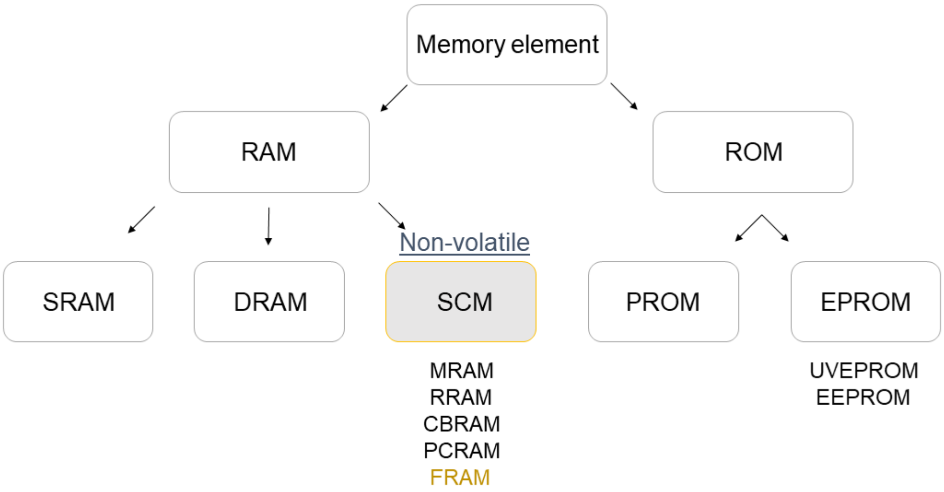

Figure 1.13: *(a) Primary memory classification, including some recent emerging memory technologies*

Memory elements can be divided into two groups as shown in Fig. 1.13: Random Access and Read Only memories referred to as RAM and ROM, respectively. The principle of this classifiction is that ROMs are non-volatile, i.e., data does not disappear when power is lost. As the name suggests, ROM can only be read by the processor and no write operations are possible. The basic limitation encountered with the first programmable ROM (PROM) is that once it is programmed (physically), it cannot be changed or altered. This limitation has been overcame by Erasable Programmable ROM (EPROM) where the stored state can be erased and reprogammed allowing multiple operations. This can be done with ultra violet (UV) light exposure making UV Erasable Programmable ROM (UVEPROM) or electrically making EEPROM.

Random access memory (RAM) allows data to be read and written but are volatile. The read and write operations are performed in the same amount of time irrespective of the physical location of the data, thus the name random access. It is the fastest memory available and hence the most expensive. They can be divided into static and dynamic RAMs referred to as SRAM and DRAM, respectively. A typical SRAM layout consists in a flip-flop circuit used to store a single bit of information and consists of six transistors per cell. DRAM uses 1 transistor-1 capacitor (1T-1C) and the stored information is governed by the charging/discharging of the capacitor (see Section. 2.3.1 for further information on transistors). Flash technology combines both ROM and RAM aspects as it is based on EEPROM principle and is able to perform non-volatile write operations. The basic element consists of a transistor with a floating gate. Memories can be characterized by the latency, i.e a measure of the time it takes for the data requested by the central processing unit (CPU) to be returned to it. This parameter varies with application as well as the architecture of the processor and memory. In general, DRAM has a latency in the 15 to 100 ns range while Flash has latencies in the 80 to 120 μs. The gap between the latencies is therefore one of the targets for Storage Class Memory (SCM), a new class of memory under developement which are by the contrary to DRAM, non-volatile. Flash at the present is the standard NVM element used embedded in microcontroller units (MCUs). This is mainly because of the high density, manufacturability and low cost technology. However, it suffers from low latency, high power, low endurance and vulnerability to radiation (see Tab. 1.2). The MCU with embedded non-volatile memory (eNVM) is for instance at the heart of emergent Internet of Things (IoT) devices. eNVM have the task of pre-computing the data to reduce heavy loading of the processor. Most of the power is consumed during the time the MCU is inactive so eNVM can be used to realize a “normally off” MCU drastically cutting power consumption. SCM technologies exploiting different physical phenomena including magnetic, resistive, conductive bridge or phase change RAMs present latencies close to DRAM and are considered potential candidates for replacing Flash in eNVM applications.

In this context, ferroelectric materials are particularly attractive. Two remanent polarization states can be written with low power (electrically) in a non-volatile manner. They can therefore be used to encode boolean algebra and form the basis of a NVM cell. The write speed and the energy efficiency outperform existing Flash memories. Figure. 1.14 shows a schematic of 1T-1C ferroelectric RAM (FRAM) and its basic operation. It is similar to DRAM as it consists of one transistor and one capacitor (1T-1C). However, in FRAM a ferroelectric material replaces the dielectric layer used in DRAM capacitors[53].

The ferroelectric is connected to a plate line (PL) and a bit line (BL) via a standard transistor. The BL hold a reference capacitor. To write a logic state, the word line (WL) is selected meaning that the transistor is on. Then a positive voltage V_{cc} (higher than E_c) is applied between BL and PL (top and bottom electrodes of the ferroelectric capcitor, respectively). Writing "0" is accomplished by making BL at V_{CC} while grounding PL , whereas "1" state is written by making PL= V_{CC} and BL = 0V. Reading operation is ensured by putting BL at 0V and pulsing the PL by

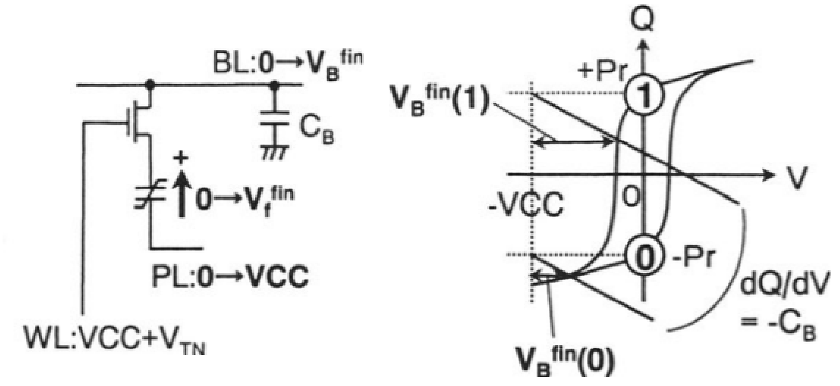

Figure 1.14: *(a) Schematic of 1T-1C FRAM write operation (from ref.[53])*

V_{CC}. If the "1" state was stored, no switching occurs resulting in very low current flowing through the transistor toward the reference capacitor (mainly dielectric current). However, if "0" was stored, polarization will switch inducing high current to flow. This therefore results in a destruction of the originally written information (switched). Due to this destructive read property, FRAM capacitors must be rewritten after each reading operation. For this reason, ferroelectric materials require a high cycling endurance before breakdown. FRAM can also be employed in a 2 transistor-2 capacitor (2T-2C) cell. 1T-1C takes less space (footprint) on a wafer and thus could be used to achieve high densities. However, destructive read can lead to fast degradation and early memory failure. 2T-2C architecture provides a more reliable memory circuit for commercial applications although this comes at the cost of the storage density[42, 54].

Table. 1.2 summarizes the key characteristics of FRAM technologies, with respect to FLASH and the emerging SCM technologies[55]. Despite the several advantages of FRAM as the very low power consumption, ns switching and high endurance, the commercialization of FRAMs has until now always been limited to niche markets. This is mainly due to the limitations imposed by state of the art perovskites (Pb(Zr,Ti)O_3 (PZT) and $SrBi_3Ta_2O_9$ (SBT)). The main limitations include contamination (Pb and Bi) and device scalability[56]. However, the discovery of ferroelectricity in HfO_2 materials has revived the interest in ferroelectric NVMs. Apart from the fact that it is already well known to the semiconductor industry as a high-k dielectric and fully compatible with state of the art Si technology, the advantage is the high device scalability potentially thanks to the very low film thickness needed to maintain a high polarization values, to make competitive memory and logic devices. Ferroelectricty in hafnia-based materials is the main topic of this thesis and will now be introduced.

Table 1.2: *Benchmark table of FRAM with other NVM technologies (from.[55])*

	FLASH	MRAM	PCM	RRAM	FRAM (PZT)	FRAM (HfO_2)
Programming power	∼200pJ/bit	∼20pJ/bit	∼300pJ/bit	∼100pJ/bit	∼10fJ/bit	∼10fJ/bit
Write speed	20μs	20ns	10-100ns	10-100ns	<100ns	14ns@2.5V
Endurance	10^5-10^6	10^6-10^{15}	10^8	10^5-10^6	>10^{15}	>10^{11}
Retention	>125°C	85°-215°C	165°C	>125°C	125°C	85°C
Process flow	Complex	Medium	Medium	Simple	Simple	Simple
Scalability	Bad	Medium	High	High	Poor	High (3D)

Chapter 2

Ferroelectric hafnia

2.1 Overview

Hafnium (Hf) is a group IV transition metal element in the periodic table with an atomic number Z=72 ([Xe] $4f^{14}5d^{2}6s^{2}$). It was identified for the first time in 1922[57]. It forms a stable binary oxide called hafnium oxide (HfO_2), also denoted (as hafnium dioxide or) hafnia. Due to the similar chemical and structural properties to zirconium (Zr:[Kr] $4d^{2}5s^{2}$), the two elements are difficult to separate and often found alloyed in nature, with Zr being the more abundant element[57].

Historically, hafnia has been used in the nuclear industry due to its large neutron absorption coefficient[58]. In addition, thanks to its large bulk modulus ($\sim$ 250 GPa), high melting point ($\sim$ 2800°C), high chemical stability and low thermal conductivity ($\sim$ 1.5 W/mK), it has always been considered as a refractory material of choice[58, 59, 60]. Nowadays, amorphous HfO_2 is widely used in the semiconductor industry thanks to its high dielectric constant (k $\sim$ 20)[61], large band gap ($E_g \sim$ 6 eV)[62] and thermal stability[58]. Due to the continuous need of scaling, i.e. shrinking device dimensions, it has become a material of choice as dielectric in state of the art complementary metal oxide semiconductor (CMOS) processing to overcome the excessive increase of tunneling leakage currents when scaling down the original SiO_2 dielectric (k $\sim$ 4)[63]. Tremendous effort has been undertaken essentially by the mean of doping and interface engineering in order to achieve higher permittivity crystal phases and to allow further optimization of the device stability, e.g. for PMOS and NMOS logic[64, 65, 66].

After several years of intense studies, ferroelectric behavior was uncovered in 2007 by researchers at the DRAM manufacturer Qimonda and first published in 2011 using a suitable combination of doping and annealing conditions[67]. The finding was a breakthrough as it has completely renewed the interest of ferroelectric non-volatile memories, which were so far confined to niche applications because of scaling, CMOS compatibility and reliability issues related to common ferroelectric perovskites[56].

2.2 Bulk structure

Figure. 2.1a shows the phase diagram of hafnium oxide. HfO_2 is obtained by adding 67 at% oxygen (O) to Hf[20]. At ambient conditions, the most stable crystal structure is a monoclinic fluorite-type crystal structure (space group P2_1/*c*)[60, 20]. It is a polymorphic distortion of the cubic fluorite structure named after the mineral CaF_2. In the cubic fluorite structure, cations occupy the corners and faces of a cube and anions on the eight tetrahedral interstitial sites. The monoclinic distortion consists of $\sim$9° shearing of the unit cell and a sevenfold oxygen coordination around the Hf^{4+} ions with four O^{2-} at the base of the cube, one at an upper corner, and two at the midpoints of the cube. At ambient pressure, Fig. 2.1a shows that two high temperature polymorphs can be found: a tetragonal (P4_2/*nmc*) above 1800°C and the cubic (F*m*$\overline{3}$*m*) phase above 2600°[20]. The monoclinic, tetragonal and cubic hafnia phases are generally denotes as α-HfO_2, β-HfO_2 and γ-HfO_2, respectively. In the following, they will be referred as m, t and c-phases.

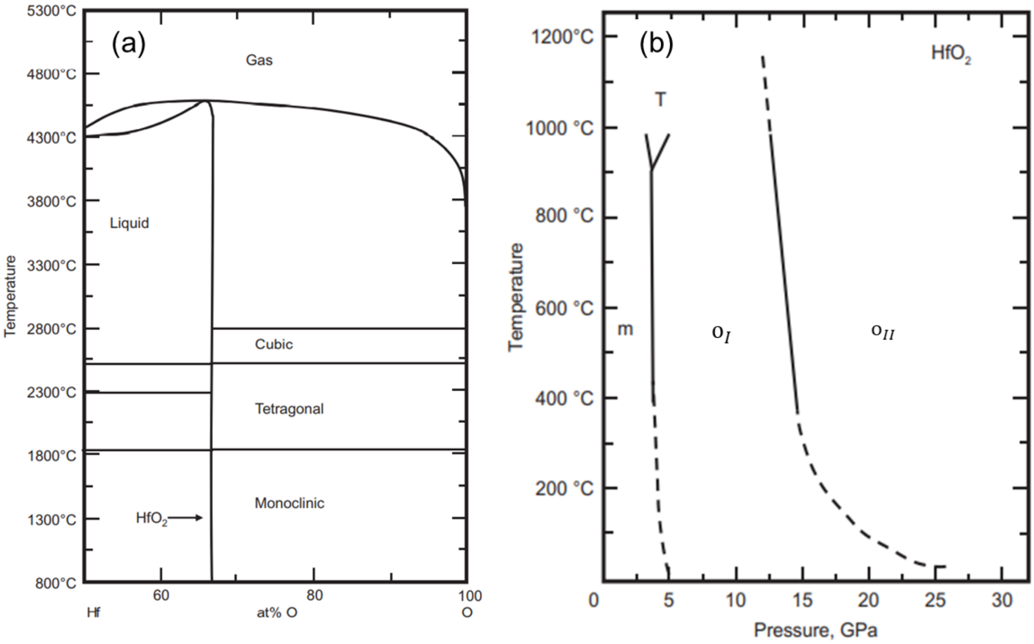

Figure 2.1: *Hafnia temperature phase diagrams as a function of (a) oxygen content and (b) pressure (from ref.[20])*

Figure. 2.1b shows the phase diagram of bulk hafnia as a function of pressure. Under increased pressure, hafnia exhibits two orthorhombic polymorphs denoted as o_I and o_{II}. This occurs respectively at around 5 and 26 GPa although different transition pressures values can be found in literature[20]. Space groups are also not a subject of agreement. P*bca*[68, 69] and P*bcm*[70, 71] spaces groups were reported for the o_I phase while P*nma*[72, 73] and P*mnb*[74] were attributed to the o_{II} phase. All these phases are centrosymmetric and cannot therefore exhibit ferroelectricity. The reported crystal parameters along with the band gap energy (E_g) and the dielectric permittivity values corresponding to the temperature polymorphs are summarized in Tab. 2.1[75, 76, 61]. E_g corresponds to the energy difference between the filled oxygen 2*p* orbitals and the unfilled Hf 5*d* states.

Table. 2.1 shows that the t-phase is characterized by a higher k value relative to the room temperature m-phase. This phase is therefore particularly interesting in term of high-k dielectric applications. Size effects and doping have

Table 2.1: *Crystal parameters, band gap (E_g) and dielectric constant (k) values of hafnia polymorphs*

Phase	a (nm)	b (nm)	c (nm)	E_g (eV)	k
Monoclinic	0.511	0.516	0.529	5.8	16-18
Tetragonal	0.505	0.505	0.512	6.4	70
Cubic	0.585	0.585	0.585	6	29

been widely used to attempt the stabilization of both t and c-phases at lower temperatures. The size effect on the crystal phase was firstly reported in zirconia (ZrO_2) nanocrystallites by Garvie *et al*[77]. Experiments on hafnia nanotubes, nanorods and thin films (∼10 nm) were all found to exhibit a significant decrease of the transition temperatures[78, 79, 80]. For instance, HfO_2 nanorods show a tetragonal phase transition at 600°C, which is significantly lower than the conventional transformation at 1800°C[79]. Doping is also used to modify the phase diagram energetics. Si doping (5 - 10 mol%) for example highly stabilizes the t-phase[64, 81, 82]. With zirconia, HfO_2 is completely miscible and forms a solid solution, which can be expressed as $Hf_xZr_{1-x}O_2$[83]. Figure. 2.2 shows the phase diagram of $Hf_xZr_{1-x}O_2$[20].

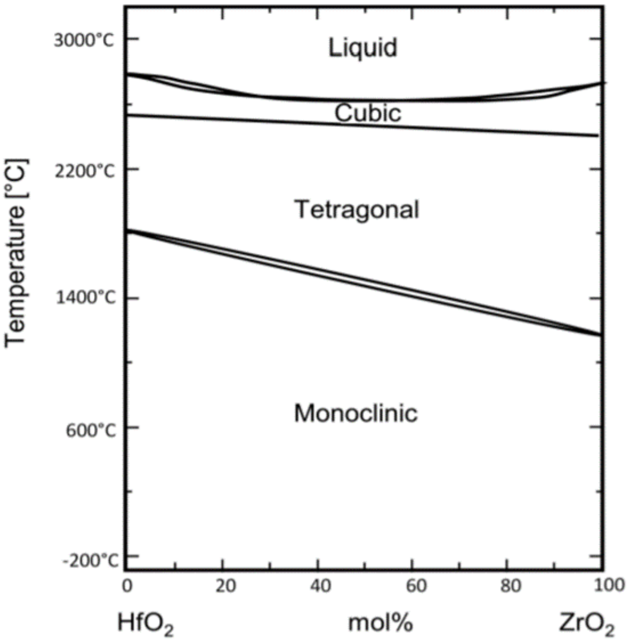

Figure 2.2: *Phase diagram of $Hf_xZr_{1-x}O_2$ (from ref.[20])*

The phase transition temperatures decrease with increasing Zr content. HfO_2, ZrO_2 and $Hf_xZr_{1-x}O_2$ have been therefore studied with a variety of doping compounds. The most common are MgO and Yb_2O_3[58]. While studying the crystal structure of Mg-doped ZrO_2 (Mg:ZrO_2) at low temperatures and under hydrostatic pressure, Kisi *et al*[84] was the first to notice the existence of a polar o-phase of space group P*ca*2_1 originating from a tetragonal phase. As it will be shown, this behavior was finally attributed to explain the ferroelectricity in HfO_2.

2.3 Thin film properties

2.3.1 High-k gate oxide

Figure. 2.3a shows a schematic of the basic princicple of a Metal Oxide Semiconductor Field Effect Transistor (MOSFET), the standard switching element in nowadays digital technology. It is a four-terminal device having gate (G), Body (B), Source (S) and Drain (D) terminals and consists in metal, dielectric oxide and doped Si semiconductor (MOS) capacitor-like stack. In NMOS, the regions below the source and drain are highly n-type doped and the substrate is p-type. The opposite with PMOS transistors. In the enhancement mode of a NMOS (PMOS), a positive (negative) voltage applied to the metal gate induces electrons (holes) accumulation at the dielectric oxide interfcae. These charges form a channel of a width controllable by the voltage magnitude. A bias applied between the source and drain allows current to flow through the channel to the drain terminal. The presence or absence of drain current defines thus the physical mechanism of the switchable logic state between 0 and 1. Advanced CMOS logic uses both NMOS and PMOS functionalities and the shrinking of transistors dimensions enables nowadays hundreds of millions to be placed on a single chip.

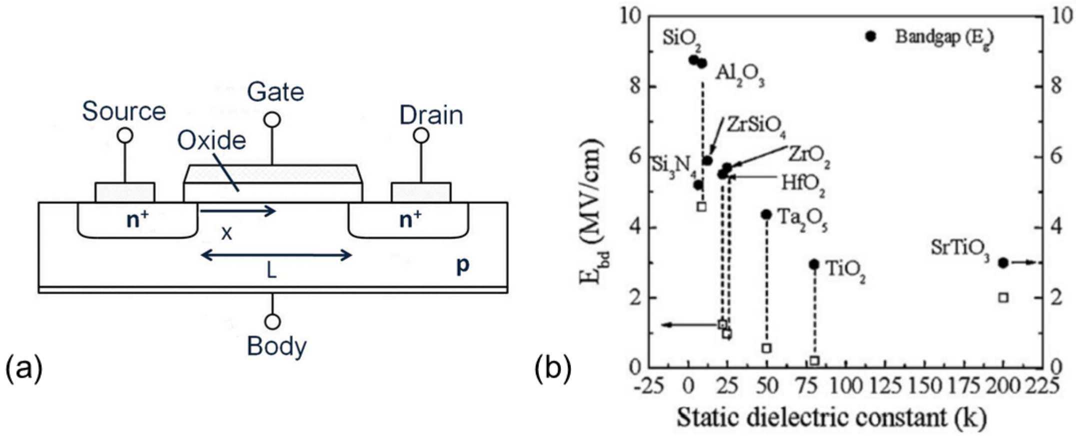

Figure 2.3: *(a) Schematic of an n-type MOSFET (b) Band gap (E_g) and electrical breakdown field (E_{bd}) versus dielectric constant (k) for MOSFET high-k candidates (from ref.[85])*

By the beginning of the 21^{st} century, further scaling following Moore's law, replacing the original SiO_2 oxide used in MOSFETs became urgent[76]. This is due to the low k value (k=4) and to the excessive tunneling currents when decreasing the film thickness (d) which increases exponentially as d decreases. A higher k material was therefore sought for[63, 85, 86, 87]. High-k materials enable thicker films which prevents tunneling currents while maintaining the equivalent oxide thickness (EOT) defined as $EOT = \epsilon_{SiO_2}\frac{t_{high-k}}{\epsilon_{high-k}}$ (in nm). Several high-k candidates have therefore been intensively studied in terms of high k value in addition to the band gap energy E_g and the breakdown field E_{bd}. E_{bd} represents the field at which the insulating property of the dielectric is broken and the film become conducting. Figure. 2.3b shows that higher dielectric constant could only be obtained at the cost of smaller E_g and E_{bd}[85]. Interfacial reactions with the metal and the semiconductor in addition to the subsequent band alignments were also major concerns[85, 88, 86, 87]. A balance between all these properties have rapidly placed hafnia and zirconia as viable candidates to replace SiO_2. However, due to its higher thermal stability, hafnia was preferred[85, 89]. In 2007, Intel led the first incorporation of hafnia into semiconductor commercial production. Atomic layer deposited HfO_2 thin films have been used for the first time in 45 nm CMOS node[90]. Since that, and despite all the progress, Hf-based dielectrics have remained unchallenged in advanced CMOS nodes.

2.3.2 Ferroelectricity

Si doped HfO_2

As already mentioned, Kisi *et al* were the first to report the presence of the polar o-phase P$ca2_1$ in Mg:ZrO_2 stabilized from a t-phase[84]. This was forgotten until Böscke *et al*[67] rediscovered this structure in 10 nm thick Si-doped HfO_2 films in 2011. A few years previously, Böscke was working on k value engineering in hafnia thin films at the Qimonda company for DRAM applications. It was found that improvements can be obtained by Si doping or by using a capping TiN electrode during annealing[91]. It was this research work that enabled the discovery of ferroelectricity in HfO_2 as the first report combined Si-doping and a post-metallization anneal (PMA) with a capping TiN electrode. Figure. 2.4a shows the Grazing Incidence X-ray Diffraction (GIXRD) data from the original report. A capping electrode was required to suppress monoclinic $(111)_m$ and $(-111)_m$ reflections (predominant in the uncapped case) and to induce an orthorhombic symmetry. Indeed, the triplet reflections at $2\vartheta \sim 83^\circ$ corresponds to a polar o-phase basing on the similarities with the diffraction pattern of the Mg:ZrO_2 reported by Kisi *et al*[84]. This allowed attributing the emergence of ferroelectricity to the stabilization of a polar o-phase with space group P$ca2_1$.

In this original work, the Si content was also crucial to obtain ferroelectricity (Fig. 2.4b). Si doping was used to destabilize the m- over the t-phase favoring a controlled crystallization in the presence of a capping electrode. The optimal Si content was 3.6 mol%. Increasing Si led to antiferroelectric (AFE) behavior due to higher stabilization of the t-phase[67].

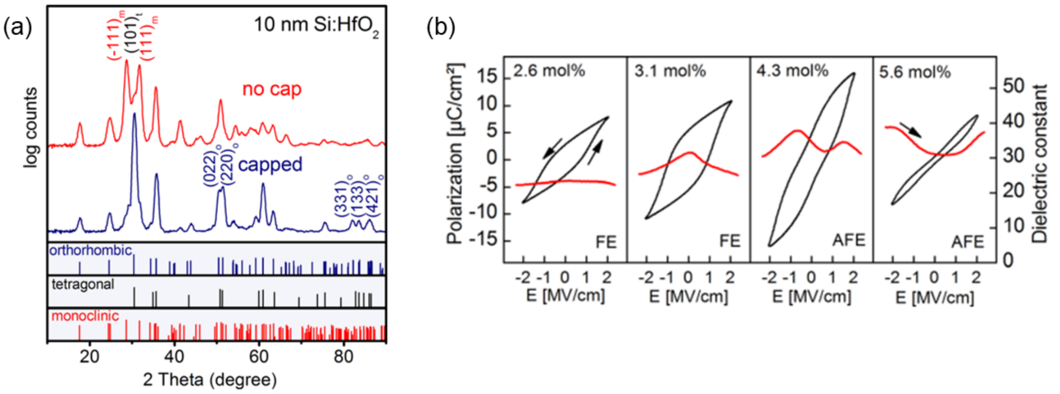

Figure 2.4: *(a) Grazing incidence x-ray diffraction pattern of two Si-doped HfO_2 thin films crystallized with and without top electrode capping (b) Polarization and capacitance measurements as a function of Si content (from ref.[67])*

$\mathbf{Hf_{0.5}Zr_{0.5}O_2}$

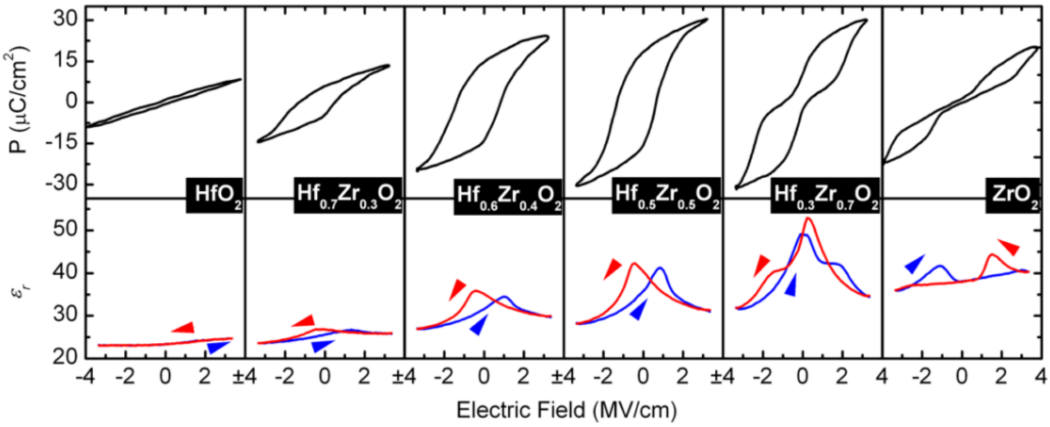

Figure 2.5: *Polarization (P) and dielectric permittivity (ϵ_r) as a function of electric field measured for $Hf_xZr_{1-x}O_2$ thin films with x ranging from 0 to 1 (from ref.[92])*

In the same year, Müller *et al*[93] reported ferroelectricity in the $Hf_{0.5}Zr_{0.5}O_2$ (HZO) solid solution. Given the vast semiconductor industry experience with hafnia and zirconia in high-k dielectric applications, $Hf_xZr_{1-x}O_2$ ferroelectric thin films were considered promising candidates for memory technologies. The crystallization temperature of HZO (T_{PMA}=450°C)[93] is also considerably lower than with Si:HfO_2 (HSO) (T_{PMA} =1000°C)[67] which allow ferroelectricity at lower annealing temperatures. This has a major importance in view of integration in CMOS technology. CMOS processing includes a front end of line (FEOL) first step at which the components of the integrated circuit are fabricated directly on the wafer via advanced lithography tools. This is followed by a back end of line (BEOL) step to allow device interconnection via a metallization process. The thermal budget used in standard BEOL technology is 450°C[94, 95, 96]. Thanks to its compatibility with these thermal limitations, HZO is regarded as the most promising material for device integration. Figure. 2.5 shows also that, similarly to HSO, $Hf_xZr_{1-x}O_2$ exhibits different electrical response depending on the Zr content[92]. Pure ZrO_2 is antiferroelectric which has been demonstrated to be associated to a predominantly t-phase[92]. This highlights the role of Zr and Si content in tailoring the capacitor properties allowing a wide window of possible functionalities of these materials.

Effect of capping electrode

The two original reports of ferroelectricty with HSO and HZO showed that the mechanical constant imposed by the electrode plays a significant role in achieving the polar o-phase. This is known as the capping effect where the desired polar o-phase is promoted when the crystallization annealing is performed after capping with a top electrode[67, 93, 97].

Electrodes used with hafnia include common metals (W[99], Mo[100], Ni[98], Pt[101]), metal nitrides (TiN[67, 93], TaN[102]) and metal oxides ($La_{0.7}Sr_{0.3}MnO_3$ (LSMO) [103]). Significant efforts have been made to elucidate the role of top and bottom electrode (TE and BE) materials in terms of the induced mechanical

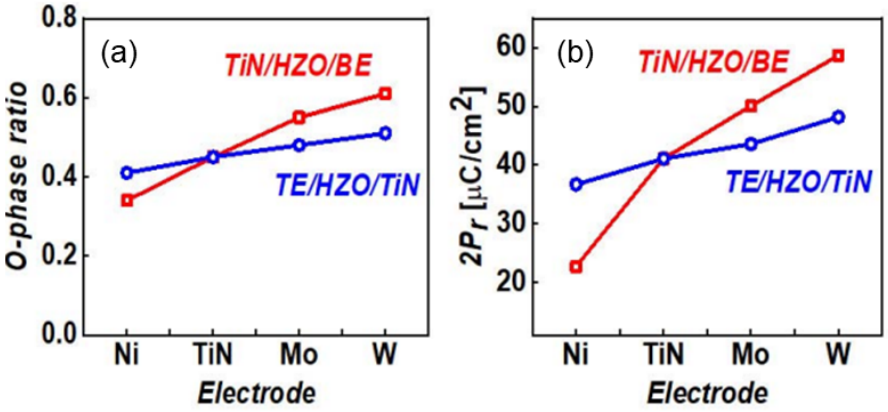

Figure 2.6: *(a) o-phase ratio with respect to the m- and t-phases and (b) 2P_r values as a function of the used top and bottom electrodes (from ref.[98])*

stress during the process of annealing and the resulting phase composition. Lee *et al*[98] conducted a systematic study by analyzing different electrode materials presenting different thermal expansion coefficients (TEC). With Ni, TiN, Mo and W, TEC values are 13, 9.4, 5, and 4.5$\times$10^{-6}/°C, respectively[98]. By varying the top (TE/HZO/TiN) and bottom electrodes (TiN/HZO/BE), the obtained results are shown in Fig. 2.6. The results indicate that smaller the TEC , the o-phase is higher with respect to the m- and t-phases. This results in higher P$_r$ values (Fig. 2.6b). The capping effect is a mechanical stress occuring when crystallization of amorphous hafnia is induced by temperature annealing. First, a nucleation in a metastable t-phase occurs. Then, during cooling, an in-plane tensile strain is provided by the electrode due to the small TEC. This inhibits the shearing of the unit cell (which would favour going back to monoclinic) and allows a transformation into the polar o-phase. This is schematically summarized in Fig. 2.7. Electrodes with small TEC values are therefore beneficial to induce higher tensile strain during cooling favoring ferroelectricty. In this context, tungsten (W) seems a very promising electrode material[104]. Another aspect related to electrodes is the interface with the ferroelectric. This will be detailed in section. 2.5.2 along with the role of oxygen vacancies.

Epitaxial film growth by Pulsed Layer Deposition (PLD) allows to obtain highly ordered films as the growth follows the substrate orientation. The lattice mismatch between the film and substrate induce a strain which highly defines the film crystallinity and its orientation. Different semiconductor and electrode oxides implying in-plane tensile strain have been reported to induce ferroelectricity in HfO$_2$ originated from the same polar o-phase. Epitaxial ferroelectric hafnia films have shown higher orthorombic fraction than their ALD-grown counterpart films in spite of the fact that in both cases these systems still polycrystalline. The epitaxy approach has also made possible the observation of ferroelectricty in polar phases other than the o-phase P*ca*2$_1$. In 2018, Wei *et al* reported 34μC.cm^{-2} P$_r$ value in epitaxial HZO-grown on (001)-oriented La$_{0.7}$Sr$_{0.3}$MnO$_3$ (LSMO)/SrTiO$_3$ (STO) substrate originating from a different polar structure, a rhombohedral phase (r-phase) with space group R3*m*[103]. A review on epitaxial ferroelectric HfO$_2$ films with the recent advancements can be found in the work of Fina *et al*[105].

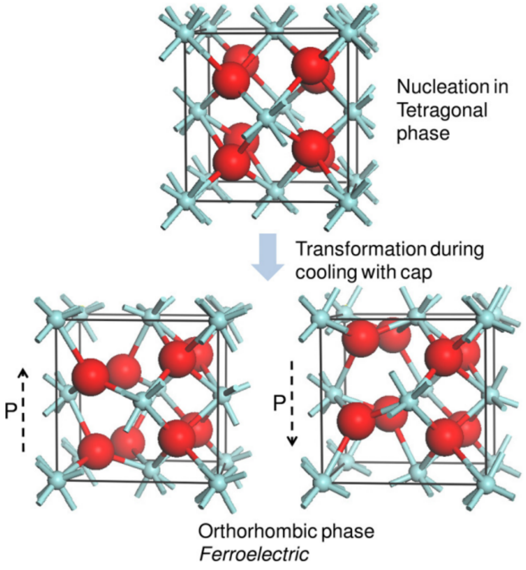

Figure 2.7: *Schematic of the polar o-phase stabilization in hafnia. At higher temperature nucleation occurs in the t-phase which on cooling tranforms into the non-centrosymmetric o-phase. The dashed black arrows indicate the polarization direction (from ref.[67])*

Effect of annealing

The as-deposited hafnia films are amorphous after the growth process. A crystallization annealing is therefore needed. The capping effect requires that crystallization be performed after top electrode deposition. This is why the term post-metallization annealing (PMA) is commonly used. Different annealing techniques and atmospheres have been investigated. The most common PMA technique is the rapid thermal annealing (RTA) in N_2 atmosphere. The operation involves rapid heating from ambient to approximately 450–1000°C. When the temperature is reached, the sample is held for a few seconds before cooling down. An alternative technique to the standard RTA which is very promising in CMOS processing, is the so-called nanosecond laser annealing (NLA). An UV laser pulse exposure leads to a shorter absorption depth in the sample, while the nanosecond duration limits the heat diffusion towards embedded structures. The heat confinement is therefore more controlled rendering the technique very beneficial for hafnia-based devices integration in BEOL technology[106, 96]. Annealing temperature (typically from 450 to 1000°C), duration (few seconds to minutes) as well the atmosphere (inert (N_2), oxidizing (O_2) or reducing (forming gas (N_2 + H_2)) were all found to tune the ferroelectricity window in HfO_2 and HZO films[107, 104, 108].

Effect of doping

Substantial efforts have been conducted to understand the role of doping in hafnia-based capacitors. In addition to the original isovalent elements Si^{4+} and Zr^{4+}, various aliovalent cations such as Y^{3+}[109], Al^{3+}[110], Gd^{3+}[111], Sr^{2+}[112], and La^{3+}[113] have been reported to induce ferroelectricity in HfO_2 thin films. In addition to the valence state, depending on the element size and its concentration, different P_r values can be obtained[114]. Figure. 2.8a shows the evolution of P_r with different dopants as a function of their concentration. Doping with lanthanum (La) allowed so far the highest P_r value ($\sim 50\mu$C.cm^{-2}) in HfO_2 films. In addition, it was also found to be an excellent leverage to increase the P_r value and cycling endurance before breakdown occurence in the BEOL-compatible HZO thin films (Fig. 2.8b)[115].

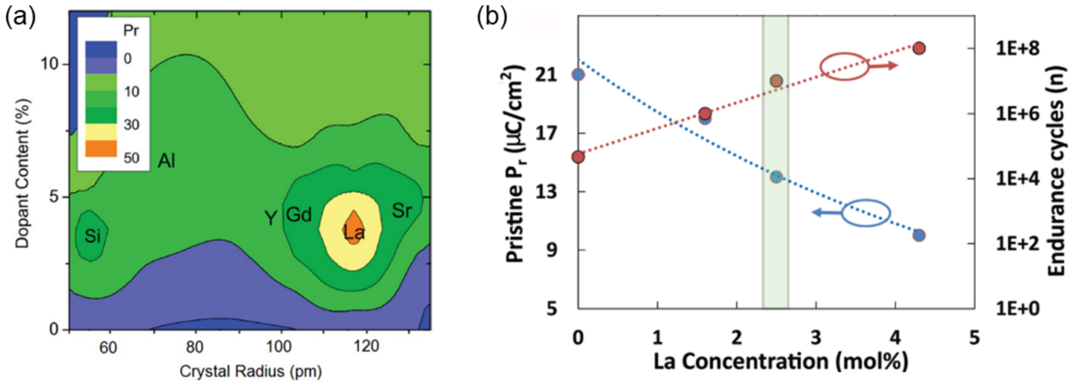

Figure 2.8: *(a) Contour plot of P_r as a function of dopant size and its content (from ref.[113]) (b) effect of La doping on P_r value and cycling endurance in BEOL-compatible HZO thin films (from ref.[115])*

The role of oxygen deficiency

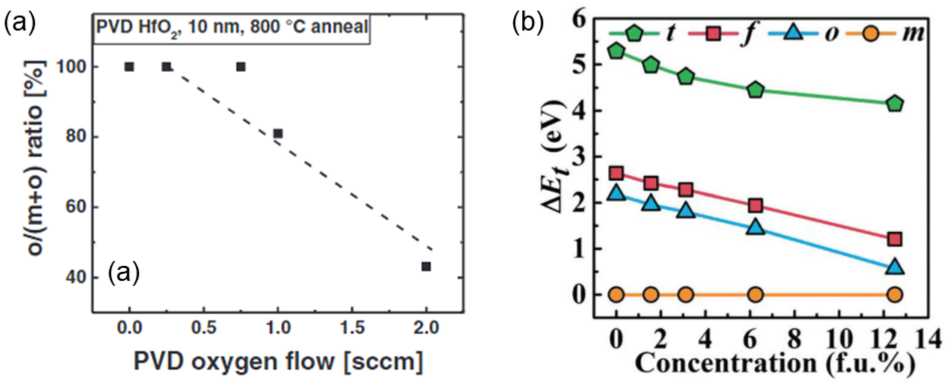

Figure 2.9: *(a) Influence of the oxygen flow on the ferroelectric o-phase fraction in thin HfO_2 films made by physical vapor deposition (from ref.[116]) (b) DFT calculations showing the impact of increasing oxygen vacancy concentration on the energies of the non polar m-, t- and o-phases and on the polar ferroelectric o-phase denoted f (from ref.[117])*

In fact, ferroelectric behavior was also observed in undoped films. Mittmann *et al*[116] attributed the emergence of ferroelectricity in undoped HfO_2 to the role of oxygen vacancies (V_O). Figure. 2.9a shows the reported orthorombic fraction with respect to the m-phase in 10nm thin HfO_2 films. Increasing the oxygen flow leads to a m-phase stabilization over the desired polar phase. It was concluded that the defect concentration determines the nucleation phase of the as-deposited film influencing thus the later phase transitions during annealing and cooling. Oxygen-deficient layers are therefore believed to be favorable to stabilize the polar o-phase. In oxygen-rich films (higher oxygen sccm), the m-phase is favored (Fig. 2.8a)[116]. Experimental and therotical reports have proven the positive impact of V$_O$ in stabilizing the ferroelectric phase in both doped and undoped films. Figure. 2.9b shows density functional theory (DFT) results on the energy of formation of the competing phases relative to the m-phase as a function of V$_O$ concentration. The results clearly indicate the favorable structural implication of oxygen vacancies.

To summarize, except for the specific case of epitaxial films where a rhombohedral structure can be stabilized, the structural origin of the unexpected ferroelectricity in HfO$_2$ is the formation of the non-centrosymmetric o-phase with a space group P*ca2*$_1$. The crystallization is induced by high temperature annealing with a nucleation in a metastable t-phase. During cooling, an in-plane tensile stress provides the necessary mechanical stress to induce the ferroelectric phase. The combination of the capping effect along with annealing, doping, size and defects are the root causes for ferroelectricity in hafnia-based thin films. The deposition technique is not limited to ALD and PLD. Various other techniques such as physical vapor deposition (PVD)[118, 119], chemical vapor deposition (CVD)[120], chemical solution deposition (CSD)[121] have also been reported.

2.4 Ferroelectric hafnia-based devices

In addition to FRAM, different logic concepts based on the ferroelectric switching have gained a lot of interest thanks to the discovery of ferroelectricity in hafnia thin films. These include notably Ferroelectric Field Effect Transistors (FeFETs) and Ferroelectric Tunnel Junction (FTJs), in addition to emerging concepts such as negative capacitance (NC) and neuromorphic computing. These promising technologies amplified the research to go beyond the von-Neumann computing in which logic and memory elements are physically separated. Ferroelectric NVM elements have been already reported incorporated into computational units as NV-logic or computational tasks being conducted within the memory arrays (Logic-in-Memory, LiM)[122].

2.4.1 Ferroelectric random access memory (FRAM)

FRAM using perovskite based ferroelectrics has reached its scaling limit at 130 nm node[123]. However, thanks to the low film thickness allowed with ferroelectric hafnia and mature ALD capability, 3 dimensional integration became possible paving the way toward more scaled and denser chips. High aspect ratio FRAM capacitors have been already demonstrated using ALD-grown Al:HfO$_2$[124]. Figure. 2.10a shows the reported transmission electron microscopy (TEM) micrograph and the measured P-E loop of the deep trench capacitor array proving the concept of 3D integration. This allowed a P_r value of 150 μC.cm^{-2} comprable to only 14 μC.cm^{-2} with a planar geometry.

Furthermore, hafnia thin films also demonstrated the BEOL compatibility. Figure. 2.10b shows an optical microscope image of the 64 kbit 1T-1C FRAM test chip reported by Sony based on HZO films capped with TiN electrodes (at T<450°C)[95]. The 3D capability and the BEOL compatibility using hafnia are practical solutions to obtain higher density FRAM arrays. However, for real commercialization, the solder reflow compatibility, in which the pre-programmed chips have to be resistant to the packaging temperature of typically 260°C, has to be taken into account. Recently, this has also been proved by the 3ϵFERRO consortium using BEOL-compatible 16kbit FRAMs based on TiN/HSO/TiN capacitors. François *et al* showed that these 1T-1C devices are capable of withstanding three successive surface mount technology (SMT) temperature stresses of 260°C for 30 s without any bit failure for both memory states[125].

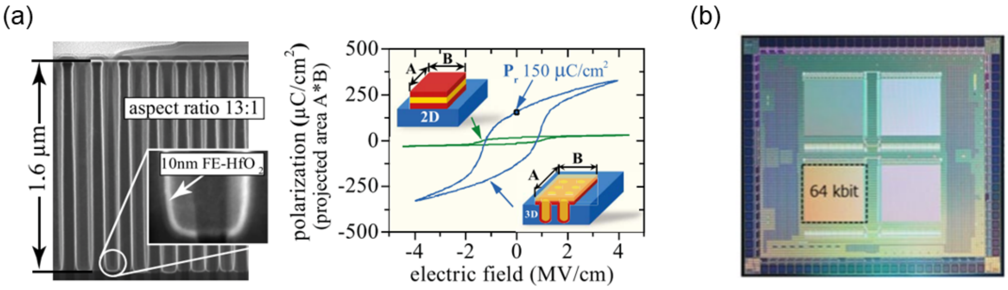

Figure 2.10: *(a) Transmission electron microscopy cross section of Al:HfO$_2$–based trench capacitor array and P-E hysteresis loops from this 3D gemotry and from a planar one. 3D capacitors allow a P_r of 150 μC.cm^{-2} while with planar 2D-capacitors, P_r = 14 μC.cm^{-2} (b) Optical microscope image of the Sony 64-kbit 1T-1C FRAM test chip (from ref.[124, 95, 125])*

2.4.2 Ferroelectric field effect transistor (FeFET)

A ferroelectric field effect transistor consists of a standard MOSFET (as shown Fig. 2.3a) with the high k gate dielectric replaced by a ferroelectric material. The transistor channel current is thus directly controlled by the non-volatile polarization charge. It is therefore a non-volatile transistor in which the binary logic states are encoded in the threshold voltage of the transistor[126]. The original stack used for a FeFET operation, consisting in a ferroelectric in direct contact with the semiconductor channel (MFS) suffers from several drawbacks as the inter-diffusion of elements between the ferroelectric and the channel. Therefore, various FeFET concepts have been proposed. In MFIS stack, an interface layer is added to act as a diffusion barrier. However, such insulator layer will introduce an additional capacitance in series to the ferroelectric and consumes an additional voltage drop. The screening of the polarization charges becomes also less efficient resulting in E_{dep} increase. The MFMIS stack design adds an additional floating metal layer between the ferroelectric and the insulator. This allows different capacitance matching as compared to MFIS, reducing thus E_{dep} significantly. However, high charge injection into the floating gate may overscreen the polarization charges and invalidate the FeFET operation. This becomes particularly critical over cycling, as the charges become harder to remove from the floating gate and tend to accumulate with cycling[126]. Beyond these planar configurations, different FeFET geometries can also be used. Vertical (3D)[127], recess-gate[128], gate-all-around (GAA)[129] and FinFET[130] structures have all been reported using ferroelectric hafnia thin films.

Negative capacitance is another concept using a ferroelectric layer in the gate stack of a transistor. The principle was first proposed in 2008 by Salahuddin *et* *al*[131]. The principle is predicted from the Landau-Devonshire theory, where in the free energy landscape, a transient negative capacitance regime during the switching takes place. When $V = 0V$, the free energy is symmetric and the ferroelectric is at its minimum energy corresponding to a given polarization state with an energy barrier separating the two states. When the bias is increased, the landscape is tilted up from the stored state side due to the stabilization of the opposite state (see Fig. 1.5). At $V = V_C$, the barrier vanishes and the polarization passes through a negative slope regime until it reaches the other energy minimum. Finally, when the voltage is turned off, the barrier re-emerge and the landscape is again symmetric. The effect was always thought to be just transient. However, by the combination of very thin ferroelectric hafnia film and an appropriate dielectric layer in series to the ferroelectric, different reports claim the possibility to control this effect. The idea behind this phenomenon is to use it for the amplification of the vertical electric field applied to the transistor, allowing in turn to overcome the fundamental limitation of the sub-threshold swing of 60 mV/dec at room temperature, also known as the Boltzmann tyranny. Many experiments have consistently proven transient NCFET[132, 133]. A breakthrough has recently occurred when GlobalFoundries demonstrated NCFET-based circuits using HSO films in state of th art 14 nm FinFET technology[134]. This demonstrated, for the first time, a NC-based device fully compatible with the existing CMOS fabrication processes.

2.4.3 Ferroelectric tunnel junction (FTJ)

In 1971, Esaki *et al* was the first to formulate the idea of a ferroelectric tunnel junction (FTJ). At that time, it was called a polar switch[135]. In 2005, Zhuravlev *et al* experimentally demonstrated the concept[136]. When using an ultra-thin ferroelectric film between two electrodes (below 5nm), the polarization direction allows to manipulate the quantum mechanical tunneling current (resistance), non-destructively. The effect is called tunneling electroresistance effect (TER). When the polarization is switched, the electrostatic potential profile across the junction is modulated due to imperfect screening of the polarization charges at interfaces leading to a resistance change[137]. The critical requirement of this technology is a sizeable tunneling electroresistance (TER) effect that is a relatively high resistance change between ON and OFF states. The ferroelectric film needs therefore to be sufficiently thin to allow current tunneling with conserving the ferroelectric properties. In this context, ferroelectric hafnia maintain a high P_r values at very low film thickness, providing a high potential for further FTJ developement. Salahuddin *et al* used 1 nm thick HZO films and demonstrated promising results in term of ON/OFF current ratio[138]. Using a theoretical approach, Lee *et al* reported a quite astonishing results stating that hafnia can even be a scale free material in which ferroelectric dipoles can be stabilized in half of a single unit cell (3Å) without being disrupted by external effects[139]. FTJs based on ferroelectric hafnia showed high potential in both energy-efficient NVMs but also in artificial neural network computing.

Neuromorphic computing draws inspiration from the organization and function of the human brain. The idea is to overcome the performance limitations of the actual technologies and architectures. The main building blocks to reproduce in a neuromorphic system are neurons and their interconnections, called synapses. In this context, NVM elements, essentially FeFETs and FTJs have been recognized as suitable candidates to mimic the synaptic behavior and the development of neuromorphic hardwares, thanks to their rich physical properties and CMOS compatibility.

2.4.4 Reliability aspects

Field cycling behavior

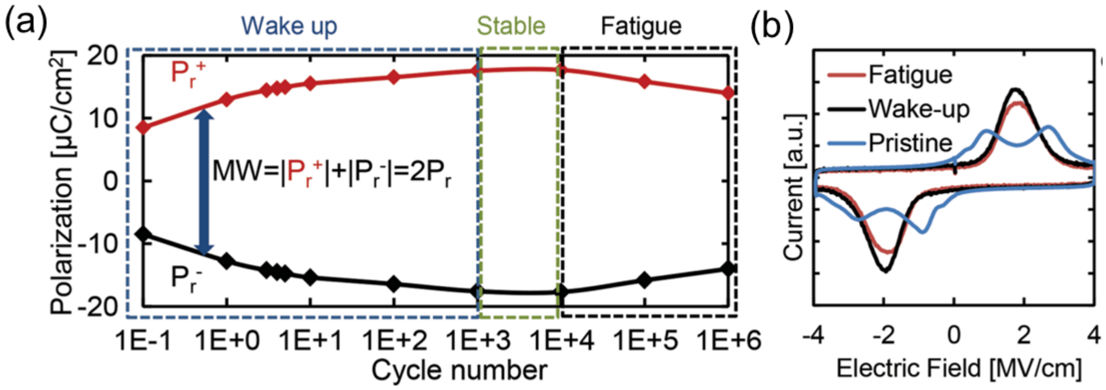

Figure 2.11: *(a) Field cycling behavior of Sr doped HfO_2-based capaciors and (b) the current response at the pristine, woken-up and fatigue stages (from ref.[140])*

The technological breakthrough of ferroelectric hafnia systems is however still hindered by the high coercive field of $E_c \sim 1 - 1.5 MV.cm^{-1}$ which requires a high operation voltage. Within the lifetime of a capacitor made of almost all hafnia materials (doped or undoped), two critical stages can be identified: wake-up and fatigue. During wake-up, the memory window MW (defined as $MW = \mid P_r^+ \mid + \mid P_r^- \mid = 2P_r$), increases with cycling, whereas in the fatigue stage the MW closes. In the pristine state, i.e before cycling, the device shows two current peaks in both positive and negative bias regions. This results in a pinched hysteresis loop with reduced P_r values. After a certain number of cycles, these peaks merge to a single peak with higher intensity occuring at the expected E_c and the P-E loop is depinched with higher MW. The device enters thus its optimal regime (optimal MW). Figure. 2.11 shows the field cycling behavior of the MW and the switching current peaks in the case of Sr doped HfO_2 thin films capped with TiN electrodes[140]. The wake-up would mean that an external cycling of all capacitors or the integration of a suitable periphery providing this cycling on the chip is necessary, which is not necessarly the most practical conditions. This phenomenon is also present when dealing with ferroelectric perovskites where it is often called deaging. In conventional perovkite-based FRAMs, the number of wake-up cycles needed is 10^3 cycles which is negligible with respect to the total number of cycles where the material is optimal ($10^{13} - 10^{15}$)[123]. In addition to the high wake-up cycles needed with hafnia (up to 10^6), a fatigue stage characterized by a reduction of the number of switchable domais leading to a decrease of the MW occurs well before conventional perovskites. Further cycling causes a dielectric breakdown marking the end of the device lifetime. The endurance of hafnia-based capacitors needs therefore to be sufficiently high to have an optimal regime competing with existing and emergent NVMs. The best field cycling endurance reported so far are in the range of $10^9 - 10^{11}$[141, 56, 55].

Many reports have shown that in the pristine state, an internal field is present and is at the origin of the switching current peak splitting. After wake-up, the internal field vanishes and one single switching peak is observed[142]. Combining experimental and computational techniques, Pešic *et al* suggested that the most plausible mechanism behind the wake-up phenomenon is the more uniform redistribution of charged oxygen vacancies[140]. The dependency of the number of wake-up cycles needed, on the frequency and the amplitude of the switching pulses hints also toward the mobility of mobile charged species. In addition, cycling at enhanced temperatures or annealing at higher PMA temperatures strongly reduce the number of wake-up cycles required. These observations corroborate the role of charge contribution to the wake-up problem[141]. Before cycling, an asymmetric profile of the vacancies creates an internal field, which depending on its sign, can lower or increase the field needed to switch a given polarization state over the other. Sufficiently high internal fields may even overcome E_c resulting in the so-called back-switching. Adding to that, oxygen vacancies are known to pin the domain walls and domain seeds inhibiting thus the switching[143]. Uniform redistribution due to bipolar cycling reduces the internal field and the degree of pinning causing an overall improvement. Internal fields stem also from E_{dep} due to imperfect screening of the polarization charges or due to the polycrystallinity nature of the material. Non-polar crystallites were suggested to induce depolarizing fields within the film[115].

Furthermore, a field cycling-induced phase transition mechanism for wake-up is also highly possible. Using impedance spectroscopy and STEM, Grimley *et al* identified experimentally regions with different dielectric and conductive properties as a function of cycling[144]. The results showed a decrease of the m-phase and an increase of the o-phase within the bulk regions in addition to a significant decrease of a defect rich t-phase fraction at electrode interfaces on cycling. Oxygen vacancies were found to minimize the energy of the desired o-phase. Their redistribution may then alter the structure locally in different portions across the film thickness increasing thus the number of ferroelectric crystallites which can participate in the switching process. Finally, besides the wake-up, an insufficient lifetime of the device is another critical problem. This was also attributed to a significant increase of the amount of oxygen vancancies which induce a strong pinning of the domain walls reducing thus the MW until breakdown occurs due to a high number of conduction paths.

Imprint

The second major factor limiting the adoption of hafnia-based NVMs is the ferroelectric imprint. Imprint manifests itself as a shift of the hysteresis loop along the voltage axis (Fig.2.12)[53]. The positive and negative coercive voltages are thus not symmetric which mean that imprint is just the measure of the internal field magnitude and is therefore closely linked as discussed to the wake-up problem. It is a major issue for memory operation as it may leads to a bit read failure while larger operation voltage to reach the stored states results in high stress and poor endurance. When a polarization state is stored, asymmetric charge distribution may induce an asymmetric charge trapping between top and bottom interfaces resulting in different effective screening of the polarization charges, strengthening one state at the expense of the other. This leads to an imprint field. The activation energies (E_a) of this phenomenaon can be evaluated thermally by measuring the temperature and time dependence of the coercive field shifts for each stored polarization state. This is performed generally with a woken-up capacitor to ensure a maximum of symmetry before monitoring the change of E_c. From the obtained Arrhenius plots one can measure E_a of the involved mechanism. Value of $\sim$1eV have been reported in HZO films hinting toward charge trapping, most likely electrons at positively charged oxygen vacancies sites, as the most likely mechanism for imprint[145, 146].

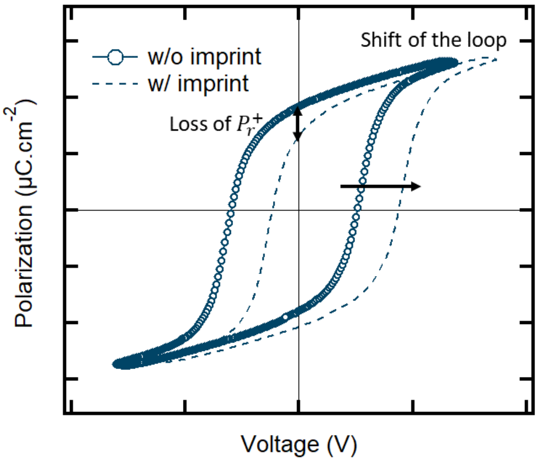

Figure 2.12: *The imprint is defined a shift in the hysteresis loop along the voltage axis. The magnitude is given by* $V_{imprint} = \frac{|V_c^+|-|V_c|}{-2}$

Data retention

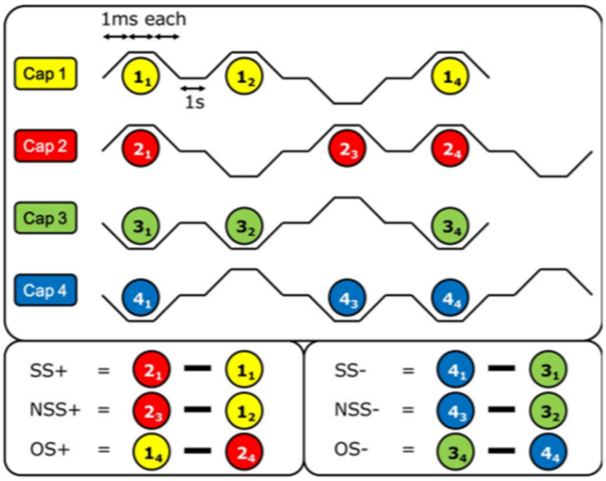

Figure 2.13: *Polarization retention measurements procedure involving 4 capacitors to allow evaluation of the NSS, SS and OS states (from ref.[147])*

The ability to retain the stored information for a certain amount of time at given temperature is also an important characteristic defining NVM. As shown in Fig. 2.12, a polarization loss and imprint can be closely related[148]. For retention tests, four capacitors are required. The device is then baked at a certain temperature. For automative applications for example, this is evaluated at 150°C. For consumer electronics at 85°C[149]. After baking, the retention behavior of a capacitor can be different depending on the previous state. Accordingly, the same stored state (SS), new same state (NSS), and opposite state (OS) retention tests are evaluated. The procedure is summarized in Fig.2.13[123, 147]. Severe retention loss, especially in the case of the opposite state, essential for FRAM operation, is reported for different HfO_2-based capacitors, including HZO[149].

2.5 Defects

2.5.1 Overview

Understanding the origin and the role of defects is crucial for reliability improvement of ferroelectric devices. The main defects encountered with hafnia thin films are point defects such as oxygen vacancies (V_O), carbon (C), nitrogen (N), and hydrogen (H). C, N and H are residual impurities mostly observed in ALD-grown films. They are related to the oxide organic precursors ($Hf[(Zr)N(CH_3)(C_2H_5)]_4$ (TEMA-Hf(Zr)), $Hf(Zr)N(CH_3)_2]_4$ (TDMA-Hf(Zr)), and $CpHf(Zr)[N(CH3)_2]_3$), the common nitride electrodes (TiN, TaN) and the annealing conditions. In ALD-grown HZO films, Kim *et al*[150] reported the effect of the deposition temperature on the C and N concentrations. At low deposition temperature (180°C), these impurities were proposed to be at the origin of t-phase stabilization. Optimal conditions with higher o-phase fraction were only obtained at higher deposition temperature of 280°C corresponding to a significant decrease of these defects concentrations. C and N were also reported to decrease the grain size of the crystallites, affecting thus the energy balance between the competing polymorphs[151]. Since both are present in the organic ligands of the metal precursors, higher deposition temperatures is therefore needed to minimize their concentration. When annealing, inter-diffusion of elements can occur. This is in particularly the case with N diffusion toward the ferroelectric film from the most commonly used nitride electrodes (TiN and TaN)[152, 102]. H is another impurity found in hafnia films incorporated at interstitial positions and reported to alter the ferroelectric properties[151]. In TiN/HZO/TiN capacitors, Park *et al* examined the conduction mechanisms and reported the presence of a trap level estimated from the temperature-dependent examination at $\sim$0.2 eV below conduction band minimum attributed by the authors to the presence of interstitial H[153].

However, V_O are considered as the most decisive defect in fluorite-structure oxides. O insertials are usually not considered due to the close packed nature of the fluorite-like structures. Grain boundaries and domain walls are known to be the most energetically favorable location of V_O accumulation[143]. Acting as electronic traps, they have already been widely studied in standard MOSFETs. In ferroelectric hafnia, they present so far one of the most studied topics as they largely define the electrical properties, including the ferroelectric and the charge transport properties[154, 155].

2.5.2 Oxygen vacancies

An oxygen vacancy (V_O) refers to the absence of an oxygen atom in the lattice. The Kröger-Vink notation follows the scheme M_S^C, where M can be a chemical element (O, Hf, La etc.,), a charge (e or h), a vacancy V or an interstitial i; S indicates the lattice site and C corresponds to the electronic charge, either positive (·), negative (′) or neutral (nothing or x). The oxygen exchange between the vapor and the crystal is governed following Eq. 2.1:

$$O_O \rightarrow V_O + \frac{1}{2}O_2(g) \tag{2.1}$$

Where O_o is the oxygen ion in the oxygen site and V_O is a neutral oxygen vacancy when the two excess electrons are localized on the vacancy site. As schematically shown in Fig.2.14, when the free electrons are delocalized, the vacancy site is double positively charged ($V_O^{\cdot\cdot}$). This can be described using Eq. 2.2:

$$O_O \rightarrow V_O^{\cdot\cdot} + \frac{1}{2}O_2(g) + 2e^{'} \tag{2.2}$$

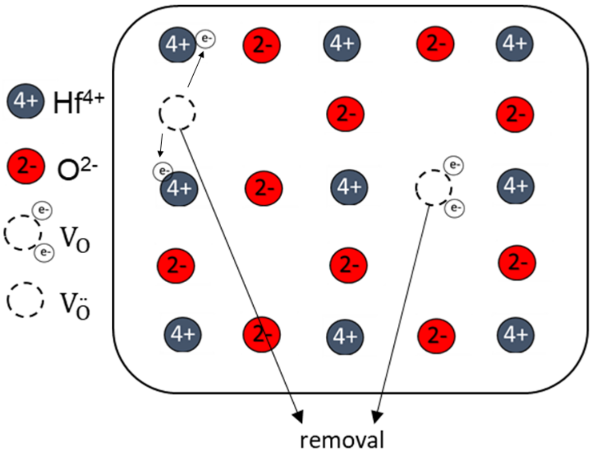

Figure 2.14: *Schematic of a neutral (V_O) and double positively charged oxygen vacancy ($V_O^{\cdot\cdot}$) in HfO$_2$*

Depending on the number of the localized electrons (trapped), V_O can adopt 5 different charge states with different energy levels within the band gap of HfO$_2$. Despite the spread values depending on the experimental and theoretical methods adopted (DFT, photo-luminescence, spectroscopic ellipsometry, positron annihilation spectroscopy, UV and X-ray photoelectron spectroscopy and electron spin resonance), the energy levels calculated by Tse *et al*[156] gives an overall agreement between the reported results[157, 155]. Using DFT, Tse *et al* calculated the corresponding energy positions of the different charged vacancies. Figure. 2.15 shows the reported energy diagram[156]. The neutral and positive states (0,+ and 2+) introduce one gap state each. The neutral state, occupied by two electrons, creates a single level located at ∼3.8 eV above the valence band. The presence of this defect slightly modifies the position of the surrounding Hf atoms (Hf-Hf bond length increases from 3.54Å to 3.59Å). In the case of positively charged vacancy, the surrounding Hf ions undergo higher repulsion, which leads to a widening of the Hf atoms distances to 3.74Å and 3.90Å in the case of $V_{\dot{O}}$ and $V_{\ddot{O}}$, respectively. This higher relaxation of the structure modifies the defect level position towards shallower levels reported to be between ~4.5 ($V_{\dot{O}}$) and ~5.2 eV ($V_{\ddot{O}}$) from the valence band. V_O were also reported to be negatively charged. The extra localized electron(s) relative to a neutral case, cause a distortion of the local symmetry. This distortion results in the appearance of a second level in the band gap located at ~5 eV above the valence band in the case of $V_O^{'}$ and at ~5.5 eV in the case of $V_O^{''}$. The band gap energy used in this calculation was 5.6eV[156].

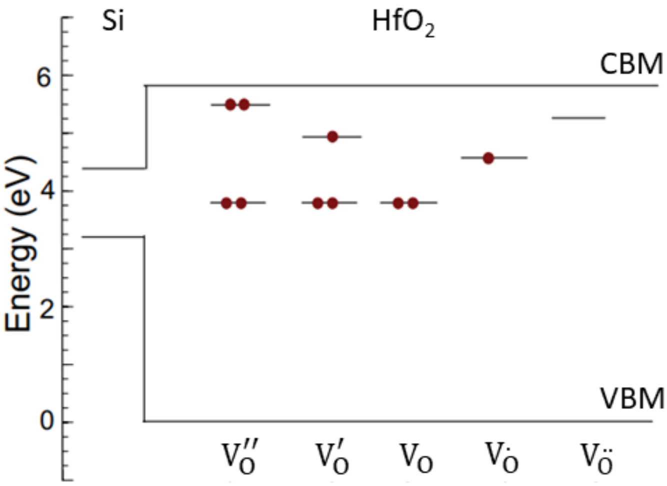

Figure 2.15: *Oxygen vacancies induced gap states energy levels in HfO$_2$. The energy diagram also show the band alignment with Si (from ref.[156])*

$V_{\ddot{O}}$ were originally evoked to explain threshold voltage shifts when replacing SiO$_2$ by HfO$_2$ as gate dielectric in MOSFETs[42]. In a TiN/HfO$_2$/SiO$_2$ typical MOSFET stack, it is unlikely for an oxygen to leave the lattice because it presents the highest oxygen affinity. Due to the lower Gibbs free energy of HfO$_2$ relative to SiO$_2$ and TiO$_2$, oxygen diffusion is unlikely, i.e, the free Gibbs energy of V_O formation in HfO$_2$ in such system is positive (Equation. 2.1). The oxygen diffusion towards TiN or Si can be expressed by Eq. 2.3 and 2.4, respectively:

$$O_O + \frac{1}{2}Ti \rightarrow V_{\ddot{O}} + \frac{1}{2}TiO_2 + 2e^{'} \tag{2.3}$$

$$O_O + \frac{1}{2}Si \rightarrow V_{\ddot{O}} + \frac{1}{2}SiO_2 + 2e^{'} \tag{2.4}$$

However, several mechanisms can lower the enthalpy of Hf reduction ($\Delta G = \Delta H - T\Delta S$). Let's consider first the following Eq. 2.5 and 2.6 which are exothermic ($\Delta G < 0$):

$$\frac{1}{2}Ti + \frac{1}{2}O_2 \rightarrow \frac{1}{2}TiO_2 \tag{2.5}$$

$$V_O \rightarrow V_O^{\cdot\cdot} + 2e^{'} \tag{2.6}$$

The oxidation of TiN alone, although exothermic, is not enough to allow the vacancy formation. In fact, $G_{2.1} + G_{2.5} > 0$ (Eqs. 2.1 and 2.5). It is therefore the two electrons release by the vacancy following Eq. 2.6 which make the whole process exothermic ($G_{2.1} + G_{2.5} + G_{2.6} < 0$).

According to Takeuchi *et al*[158], the energy gain is possible regarding the conduction band of Si relative to E_F (also shown in Fig. 2.15). The transport of O into Si promotes two electrons to the conduction band. The promoted electrons then fall into available lower-energy states: the unoccupied oxygen vacancy levels in HfO_2 or the conduction band of Si. The electron transfer results in a dipole at the oxide/Si interface pinning E_F towards higher energies. The O transport continues until the electrostatic dipole energy balances the effective reaction energy. Interfacial silicate layer are thus thermodynamically driven. In contrast, Ge channels do not form interfacial layers because of the larger $\Delta G_{2.5}$ for GeO_2 formation[158]. However, high annealing temperatures are performed to crystallize the HfO_2 films into the polar phase after the top electrode deposition. The energy gained from this annealing step is also believed to be the main driving energy lacking to the vacancy formation. The stability of HfO_2 at the top electrode interface can be therefore evaluated on a thermodynamical basis. Takeuchi *et al* measured the effective reaction energy (E_{eff}) needed for oxygen diffusion towards the most common metal electrodes using the work function values of these metals and the enthalpies of the corresponding oxides formation. Table. 2.2 summarizes the reported results[158].

Table 2.2: *Estimated effective reaction enthalpy for oxygen transfer from HfO_2 to metal gate electrode (from ref.[158])*

metal	Φ_m (eV)	E_{eff} (eV)
Al	4.06	-2.75 (Al_2O_3)
Co	5.00	0.65 (CoO)
Cr	4.50	-0.31 (CrO_2)
Cu	4.48	0.34 (CuO)
Mo	4.95	-0.24 (MoO_3)
Ni	5.04	-1.14 (Ni_2O_3)
Pd	5.22	1.19 (PdO)
Ru	4.71	1.00 (RuO_2)
Ta	4.15	-1.11 (Ta_2O_5)
Ti	4.33	-1.94 (TiO_2)
W	4.55	-0.32 (WO_2)

As shown from Tab. 2.2, most of the elements exhibit negative E_{eff}. Therefore, hafnia systematically suffer from oxygen scavenging[86]. Pd is known to be chemically inert resulting in positive E_{eff}. The results also show that Co, Mo and W appear to be promising candidates to avoid severe scavenging effects at interfaces relative to Ti (TiN) and Ta (TaN) electrodes. The formation of interface layers results in a voltage drop. In ferroelectric hafnia, voltage drops in addition to the high coercive fields can result in very high fields needed to flip the polarization ($\sim$3.5 MV.cm^{-1}) which is higher than 50% of E_{bd} ($\sim$5-6 MV.cm^{-1})[159]. Extensive effort to understand and control oxygen scavenging allowed the exploitation of this effect in the development of a new class of NVM called resistive random access memory (ReRAM). By controlling the formation/rupture of nano-filaments based on charged V_O, the presence of conductivity or no is used as a switch[160].

Doping can also be used to modulate the V_O concentration. In fact, in large band gap ionic crystals such HfO$_2$, impurity ions are electrically compensated by point defects rather than by electronic carriers[161]. Because these impurities are often highly soluble, they can produce very large concentrations of charge-compensating oxygen vacancies. La for instance is a trivalent dopant ion playing the role of an acceptor with a relatively deep trap position within the band gap of HfO$_2$ films. La^{3+} substitution of Hf^{4+} or Zr^{4+} corresponds to a negative charge which must be screened and positively charged oxygen vacancies ($V_O^{\cdot\cdot}$) are the most likely source of such screening charges[161]. Although one report states that the formation energy of neutral V_O actually increases in the vicinity of La dopants[162], it is generally accepted that the $V_O^{\cdot\cdot}$ concentration increases on acceptor doping[163, 161]. Doping n-type HZO films with La would lower E_F to a mid-position resulting in leakage current reduction. HZO doped with 2.3 mol La% doping allowed to obtain one of the most promising results in term of endurance and polarization values. The optimization were mainly attributed to leakagae current reduction. However, a larger number of wake-up cycles was found needed compared to the undoped HZO case[115].

To summarize, HfO$_2$ and ZrO$_2$ are vulnerable to reduction, forming oxygen vacancies with high concentrations in the range of $10^{18} - 10^{22} cm^{-3}$. Doped and undoped ferroelectric hafnia films were found similarly oxygen deficient, making these films n-type[157, 164, 155, 154]. In terms of device performance, V_O can play both negative (wake-up, imprint, retention) and positive roles (o-phase stabilization) and the concentration may be modulated depending on the growth technique, the choice of the oxygen precursor and its dose/exposure time, annealing conditions, reactions at interfaces with electrodes or on doping. In addition, V$_O$ are also responsible of charge transport in HfO$_2$[157].

2.5.3 Charge transport

A key problem in the physics of hafnia materials is the identification of the charge transport mechanism. In many applications, such in ferroelectric memories, a critical property is a low leakage current in applied electric fields. In HfO$_2$-based thin films, V_O were found to be directly associated with the charge transport. Different mechanisms have been reported to model the measured currents including interface-limited mechanisms like the Schottky thermionic emission or Fowler-Nordheim tunneling and bulk-limited mechanisms as the Poole-Frenkel (PF) conduction. In HfO$_2$ dielectrics, the PF was found to allow the best qualitative agreements with the experimental results[157]. The PF effect describes the ability of a trapped electron to be excited to the conduction band in the presence of an electric field thanks to the lowering of the trap level energy (ΔE) by the latter (Fig. 2.16). The effect can be regarded as the SBH image force lowering effect. The barrier reduction of the trap level is however twice larger than the Schottky effect[165]. In hafnia films, the PF was found to give a more accurate qualitative description than the interface-limited Schottky case. The PF mechanism emission is shown in Eq. 2.7:

$$J_{PF} \propto E.exp(-\frac{e}{k_BT}[E_T - (\frac{e}{\pi\epsilon_0\epsilon_{opt}})^{1/2}E^{1/2}]) \tag{2.7}$$

Where e is the elementary charge, k_B is the Boltzmann constant and ϵ_0, ϵ_{opt} are the vacuum and the film's optical permittivity. E_T is the trap energy. Using the characteristic PF-plot, i.e., $(logJ_{PF}/E)$vs$E^{1/2}$, a straight line should fit the leakage current curve at different fixed temperatures with the correct slope, $S_{PF} = \frac{e}{k_BT}(\frac{e}{\pi\epsilon_0\epsilon_{opt}})^{1/2}$. Park *et al* investigated the impact of annealing atmosphere (N_2, H_2 and FGA) on the leakage current in HZO films. By examining different transport mechanisms, it was found that the best accordance with experimental results is achieved using the PF emission model. The authors report the existence of shallow trap levels for all the samples at ~0.2eV below the conduction band assigned to the presence of interstitial H impurities[107]. Using the same mechanism, Khakimov *et al* reported also trap energies at ~0.2 and ~0.1 eV with 400 and 600°C annealing temperature but were attributed to $V_O^{\cdot\cdot}$. They showed that annealing at higher temperatures resulted in the decrease of the trap energy increasing thus the trap ionization probability and the leakage density. This was used to explain the decrease of endurance with higher annealing temperatures[166].

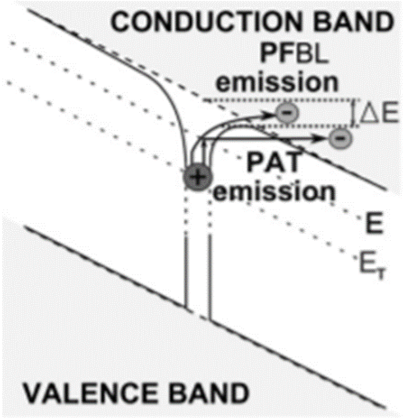

Figure 2.16: *Poole-Frenkel barrier height lowering (PFBL) and phonon-assisted tunneling (PAT) for an electron emissions from a donor deep level (from ref.[167])*

However, the PF mechanism is not capable to provide a qualitative adequate description to the experimental data. According to Gritsenko *et al*, in hafnia films, this can be achieved only by using the so-called phonon assisted tunneling between traps mechanism (PAT)[157]. The model assumes that delocalized charges can be captured even by neutral defects. In PF, only charged defects are considered and the electrostatic interaction between the electron in the conduction band and the charged trap allows the electron to be captured and transported across the film. In this PAT model, the conduction is controlled by the rate of the phonon-assisted ionization of the traps (Fig. 2.16). Since the typical phonon energies are much smaller than the trap ionization energies, this imply a large number of phonons and small distances between the traps[157].

In HZO ferroelectric films, Islamov *et al* used the following parameters to obtain the best accordance with the experimental results: $N \sim 10^{19} - 10^{20} cm^{-3}$, $E_T = 1.25eV$, $E_{opt} = 2.5eV$ and $m\star = 0.8m_0$. It was found with photoluminescence analysis, that the thermal and optical trap energies coincide with gap states level induced by V_O. This allowed to confirm that V_O provide traps for charge transport in hafnia. The authors analyzed also the field cycling of HZO as shown in Fig. 2.17. At the pristine state, the largest distance between the nearest traps was obtained ($2.17nm$ and $N = 9.7 \times 10^{19} cm^{-3}$). After 10^4 cycles, the current increases due to the generation of more vacancies ($N = 1 \times 10^{20} cm^{-3}$). After 10^8 cycles, the highest leakage current is observed corresponding to the highest trap concentration and the most close configuration between the traps ($1.6nm$ and N reaches $2.4 \times 10^{20} cm^{-3}$). V$_O$ engineering approaches seems therefore to be the best instrument to further optimize hafnia-based ferroelectric films, providing it can be reproducibly controlled[168, 169].

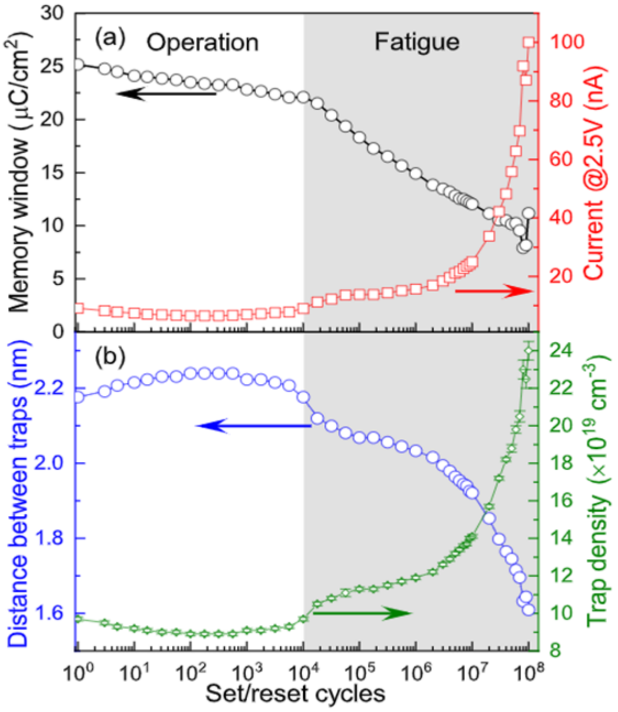

Figure 2.17: *Evolution of the memory window, distance between traps and leakage density as a function of field cycling in HZO-based capacitors using the phonon assisted tunneling between traps model (from ref.[168])*

Chapter 3

Experimental methods

3.1 Electrical measurements

3.1.1 Dynamic Hysteresis measurements

The classic setup to measure the P-E loop is the Sawyer-Tower circuit[170] shown in Fig. 3.1a. It consists of a linear reference capacitor (C$_{ref}$) in series with a ferroelectric capacitor (C$_F$). The principle is based on charge conservation; when a AC voltage is applied, the identical amount of charge is displaced in both devices. The measured voltage across C$_{ref}$ denoted V_{ref}, will be thus directly proportional to the charge Q_F that move in or out of the ferroelectric capacitor as a result of the applied voltage. The ferroelectric polarization can be calculated, knowing the electrode area (A), as:

$$P = \frac{Q_F}{A} = \frac{V_{ref}C_{ref}}{A} \tag{3.1}$$

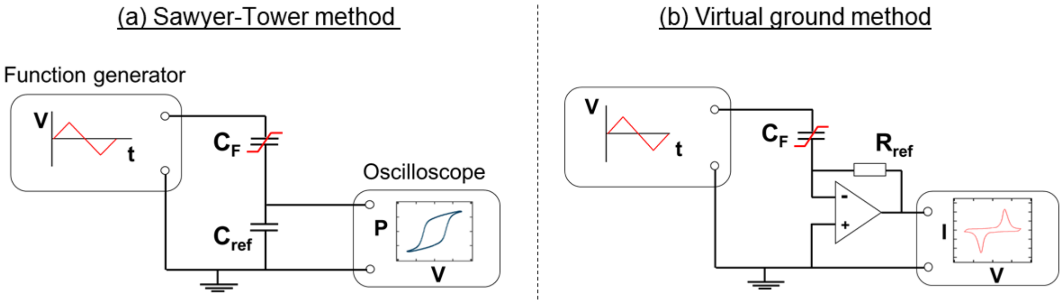

Figure 3.1: *Common setups for hysteresis measurements: (a) the original Sawyer-Tower and (b) the virtual ground method*

The AC voltage (triangular) pulses are used in order to ascertain the ferroelectric behaviour of the studied sample[171]. In this thesis, the dynamic hysteresis measurement (DHM) technique was used to extract the P-E loops using an Aixacct 1000 TF analyzer. This commercial test system uses a variation of the Sawyer-Tower circuit, the so-called virtual ground method (Fig. 3.1b). In this case, the reference capacitor is replaced by a reference resistor in series and the principle rely on measuring the displacement current via the voltage drop over the resistor instead of directly measuring the charge[171]. As shown in Fig. 3.1b, the resistor is also placed over an inverting amplifier. The signal from the ferroelectric capacitor is simultaneously fed to the inverting input and the output via the resistor. The inverting input must be pulled to the ground level, so that the output voltage yields $V = -IR$, where I is the displacement current. Both electrodes are therefore virtually at the same ground potential during the measurement thus the name virtual ground. The main advantages of this technique are the elimination of the parasitic capacitance and voltage losses on the reference capacitor frequently encountered with the Sawyer-Tower set-up.

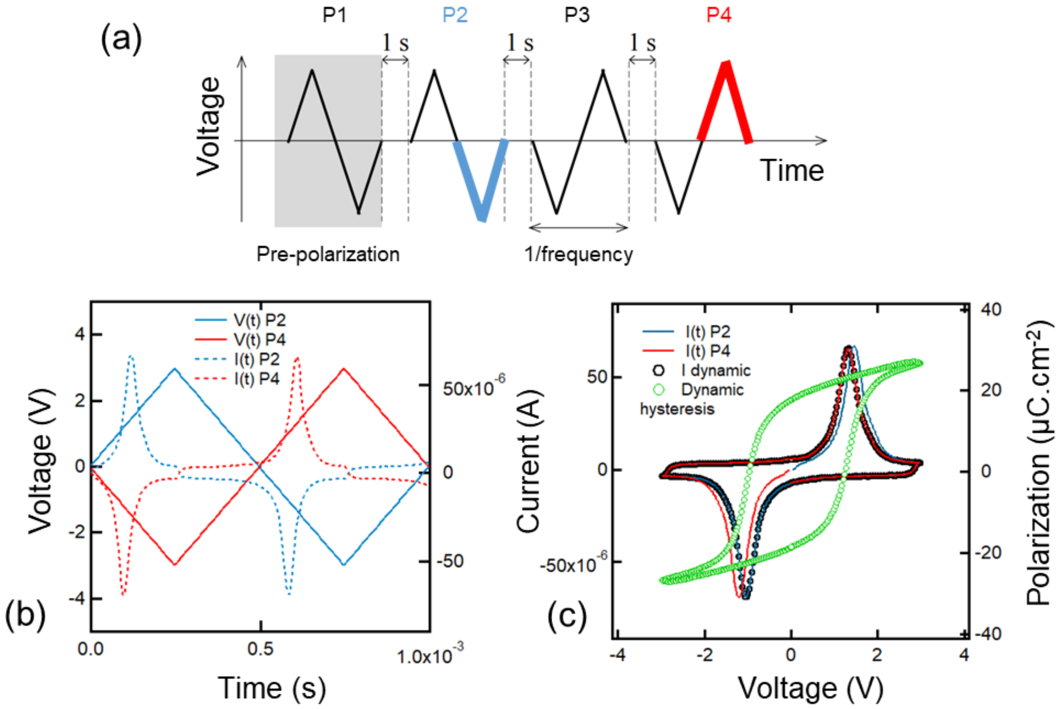

Figure 3.2: *(a) The four triangular voltage pulses used for dynamic hysteresis measurement (DHM) (b)* $I(t)$ *response (in dotted lines) to the second (P2) and fourth (P4)* $V(t)$ *cycles (c) I-V showing the dynamic current obtained from the second half of the current generated from P2 and P4 as shown in (a). The data are from a TiN/La doped HZO/TiN capacitor using pulses of* ± *3V at 1kHz frequency*

Figure. 3.2a shows the test sequence used for typical dynamic hysteresis measurement. It is composed of four bipolar triangular pulses separated by a relaxation time of 1s. The first is a pre-polarization pulse as the initial state of the ferroelectric is unknown. The second leads to the same polarization direction as the preset pulse (P_{up} when the pulse is applied to the top electrode) while the last two lead to the opposite direction. Figure. 3.2b gives the time response of the current generated by the second (P2) and the fourth pulse (P4). It shows the presence of two current peaks occuring in the positive and negative bias direction which correspond to the ferroelectric switching. The horizontal current background corresponds to the dielectric contribution. For a given capacitance, the dielectric current ($i(t)_{dielectric}$) is:

$$i(t)_{dielectric} = C\frac{dv(t)}{dt} \tag{3.2}$$

The dynamic hysteresis loop is obtained by time-integrating the dynamic current resulting from the second halfs of P2 and P4 as shown in Fig. 3.2c. All hysteresis measurements during this thesis were performed at a frequency of 1kHz.

Similar pulsed measurements have been developed in order to suppress the dielectric and leakage contributions from the measured I(t) response[172, 173]. The often used methodology is the P.U.N.D technique which refers to the Positive - Up - Negative - Down train of pulses depicted in Fig. 3.3. Similarly, an initial polarization state is stored using a first preset pulse followed by a PUND pulse train. The difference in this case is that the pulses are unipolar. The ferroelectric charge (the time-integrated switching current) is thus obtained by subtracting the non-switching charges (Q_U and Q_D) from the overall contribution (Q_P and Q_N) since in the Up and Down pulses no switching occurs.

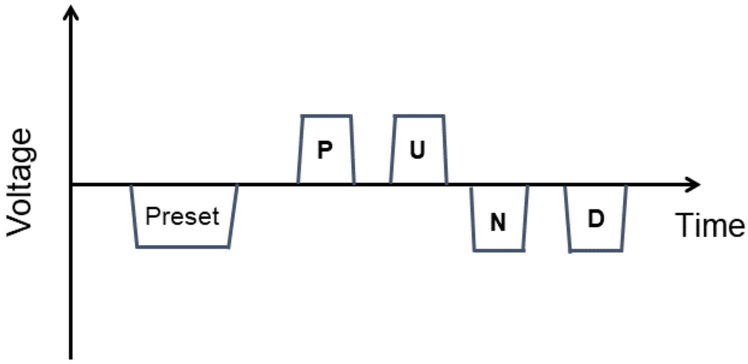

Figure 3.3: *Positive-Up-Negative-Down voltage pulses sequence used in the PUND technique for extracting the ferroelectric switching charge*

3.1.2 Capacitance and leakage current measurements

Ferroelectrics exhibit nonlinear capacitance-voltage response due to domain switching. The capacitance measurement is based on superimposing a small AC signal to a DC bias. An LCR meter is used and measures for each DC voltage step the capacitance at a fixed AC amplitude and frequency. When the coercive voltage is approached, the material exhibits a very high permittivity and consequently a very high capacitance. This happens twice in a ferroelectric material resulting in butterfly-like loop as shown in Fig. 3.4a. The AC signal frequency can be chosen depending on the intended application, but generally 1 kHz to 100 kHz are used while the AC amplitudes are in the 50 mV range. When the thickness of the ferroelectric material is known, it is common to use this technique in order to extract valuable information such as E_c, ϵ_r which gives an indication of predominant crystal phase or even the presence of space charge effects[174, 38].

Measuring leakage current through a ferroelectric capacitor is also of a great interest as it provides valuable information on the charge transport mechanisms. It can also be used to qualitatively evaluate the charge injection at a given interface subjected to forward and reverse bias conditions. Figure. 3.4b shows a typical $J-V$ curve evaluated using a DC applied bias at room temperature, where J represents the current density (the current divided by the electrode area). It is also widespread to evaluate the J-V response at different temperatures to analyze the different transport mechanisms. Small capacitor areas are however needed to avoid leaky devices showing an ohmic response due to high number of conduction paths. In this work, we have used $100 \times 100 \mu m^2$ capacitors.

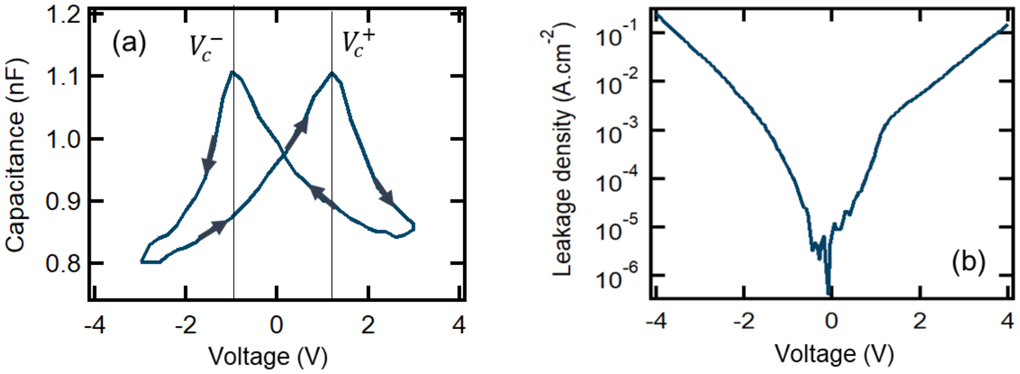

Figure 3.4: *(a) $C - V$ using 50mV AC amplitude and 1kHz frequency and (b) $J - V$ response of $100 \times 100 \mu m^2$ TiN/La:HZO/TiN capacitors for a DC bias range between -4 and 4V applied to the top electrode while keeping the bottom TiN grounded*

3.1.3 Endurance cycling

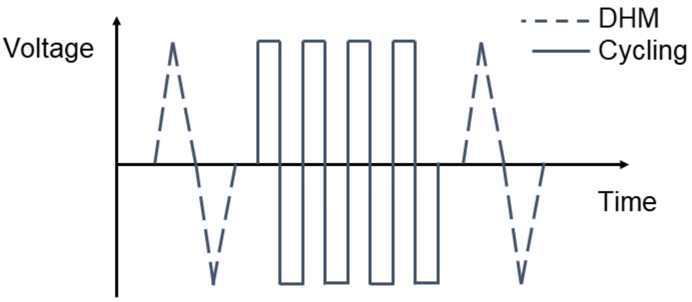

Figure 3.5: *Pulse sequence during an endurance test. A DHM is first performed followed by a number of bipolar rectangular pulses reresenting the number of cycles. A final DHM is used to obtain the P_r value at that point of cycling. The DHM follows the 4 pulse train shown in Fig. 3.2a*

Endurance cycling measures the lifetime of a ferroelectric capacitor, i.e. the number of write cycles before device failure. Such test is needed to evaluate the potential of new materials for use as memory devices. Symmetrical bipolar rectangular pulses are applied. Each periodic bipolar pulse represents a cycle. Rectangular waveform closely resembles memory circuit operation and is therefore generally used when evaluating the endurance of a ferroelectric for NVM applications (Fig. 3.5)[171]. After a certain number of cycles, a measurement of interest such as DHM, $C - V$, or $J - V$ is performed in order to evaluate the device response at that cycling stage. One should keep in mind that when such a low-frequency measurement (the slow sweeping DC voltage in $C - V$ and $J - V$ scans) alternates with the high-frequency during cycling typically at 100kHz, the ferroelectric behavior is influenced by the relatively long exposure time (1s per point in $J - V$) and a new capacitor is generally needed for a new cycling measurement.

3.2 Photoelectron spectroscopy

3.2.1 Overview

Photoelectron spectroscopy (PES) is a non-destructive, quantitative technique, which gives information on the chemical and the electronic state of a sample. The principle is based on the photoelectric effect where absorption of incident photons with sufficient energy ejects electrons from core and valence energy levels to energies high enough for them to escape the sample. The emitted electrons are thus called photoelectrons. Based on this phenomenon, several experimental techniques have been developed to resolve the kinetic energy (X-ray Photoelectron Spectroscopy, XPS)[175], the wavevector and take-off angle (Angle Resolved PhotoElectron Spectroscopy, ARPES[176] and X-ray Photoelectron Diffraction, XPD[177, 178]), position, energy and wave-vector (PhotoElectron Emission Microscopy, PEEM and k-PEEM)[179] or even time of emission (Time resolved XPS, Tr-XPS)[180] of the photoelectrons. These techniques are widely used in materials science, solid state and surface physics, in both laboratory and synchrotron facilities.

With XPS, the main technique used in this thesis, the photon irradiation is made with X-rays. Photoelectrons travel through the material until reaching the surface then leaves the sample with a certain kinetic energy E_k. An electron energy analyzer is then used to detect and filter in energy the photoelectrons to obtain an XPS spectrum, i.e, photoelectron intensity as a function of its kinetic energy or equivalently (as it will be shown) its binding energy E_B ($I = f(E_B)$).

Historically, the photoelectric effect was discovered by Frank and Hertz in 1887[181] before Albert Einstein (Nobel prize of 1921) gave the theoretical basis in one of his three famous papers he published in 1905[182]. X-rays were discovered in 1895 by Röntgen (Nobel Prize of 1901) and the photoelectric effect was firstly adapted to X-rays by Thomson and Lenard (Nobel Prize of 1905)[183]. The experimental breakthrough came in 1967 when Siegbahn *et al* studied the energy levels of core electrons in atoms using X-rays excitation and called the technique Electron Spectroscopy for Chemical Analysis (ESCA). Curiously, the work was also the first demonstration of the use of high energy X-rays which allowed much later the development of the Hard X-ray Photoelectron Spectroscopy (HAXPES) technique with the advent of the 3rd generation synchrotron sources[184, 185].

3.2.2 The photoemission process

The photoelectric effect

During the photoemission process, X-rays penetrate nanometers to micrometers into the bulk and are absorbed by atoms leading to photoelectron emission.

From energy conservation, the initial state consists of the photon energy $h\nu$ and an atom with N electrons of total energy $E(N)$. This results in a final state composed of the atom with $N-1$ electrons of energy $E^*(N-1)$ and a free electron in vacuum with a kinetic energy E_k:

$$h\nu + E(N) = E^*(N-1) + E_k \tag{3.3}$$

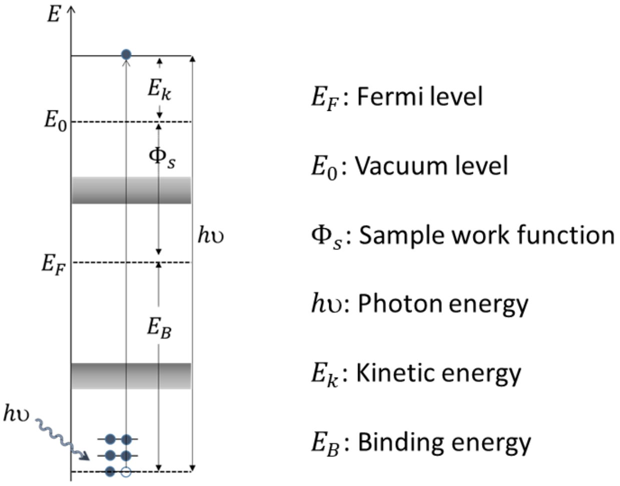

Figure 3.6: *Schematic of the photoemission process. $h\nu$ absorption leads to the emission of an electron from core level energies with a kinetic energy E_K. $h\nu$ needs to be higher than the binding energy of the electron (E_B) plus the sample work function (Φ_s) to allow the electron escaping the sample*

h is Plank's constant and ν the photon frequency. Assuming that E_k is measured with respect to E_F, the relationship between the kinetic and binding energy (E_B) of the photoelectron is:

$$h\nu = E_B + E_k \tag{3.4}$$

In order to escape the sample, the incident photon energy hν, transferred to the electrons, needs to be higher than its E_B plus the work function of the sample Φ_s. For a metal, Φ equals the minimum photon energy at which photoemission can occur[39]. The photoelectric effect (Fig. 3.5) is therefore given by the following equation :

$$h\nu = E_B + E_k + \Phi_s \tag{3.5}$$

Photoionization

An electron in an atomic subshell nl excited by photon absorption has a certain probability called the photoionization cross-section, σ_{nl} (where n and l are the principal and orbital quantum numbers, respectively). The value depends on the atom, the considered core level electron and the incident photon energy. In XPS experiments, the subshell differential photoionization cross-section can be approximated for the solid angle Ω and the atomic subshell nl by[186, 187]:

$$\frac{d\sigma_{nl}}{d\Omega} = \frac{\sigma_{nl}}{4\pi}(1 \pm \frac{\beta_{nl}}{2}(3cos^2\gamma - 1) \tag{3.6}$$

Where β_{nl} is an energy dependent asymmetry parameter of the atomic subshell nl. The $\pm$ in the parentheses is used to differenciate polarized ($+$) (as in the case with synchrotron light) and unpolarized ($-$) photon sources. γ is the angle between the photon direction and the polarization vector (when polarized) or the angle between photons and photoelectrons (when unpolarized). For elastic collisions, the modified photoionization cross-section is given by[188]:

$$\frac{d\sigma_{nl}}{d\Omega}_{elastic} = \frac{\sigma_{nl}}{4\pi} Q_{nl}(1 \pm \frac{\beta_{eff}}{4}(3cos^2\gamma - 1) \tag{3.7}$$

Where Q_{nl} and β_{eff} are correction parameters to account the decrease of the angular anisotropy of photoemission due to elastic collisions. Figure . 3.7 shows the evolution of σ in units of megaBarns for Hf 4*f* and Zr 3*d* core levels as a function of the photon energy. At $h\nu$=1486.7eV, the energy of Al Kα X-rays used in this thesis, the values are σ_{Hf4f}= 0.11Mb and σ_{Zr3d}= 0.09Mb.

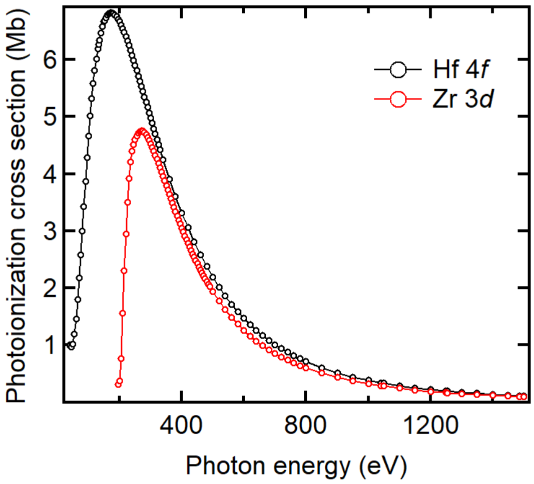

Figure 3.7: *Atomic subshell photoionization cross-sections of Hf 4f and Zr 3d core-levels (values from ref.[187])*

Path of the excited electron through the material

After photoexcitation, photoelectrons travel in the bulk toward the surface with or without loss of energy. Photoelectrons travelling to the surface without loss of energy compose the elastic peak of the spectrum while the others, which underwent at least one inelastic collision event, make up the secondary electron background. Sufficient inelastic scattering effects may also reduce the E_k of the photoelectron in a manner that it will not escape the sample surface (Fig. 3.8a). The attenuation of the elastic peak with the travelled distance is quantified by the inelastic mean free path (IMFP), λ, which describes the exponential attenuation of the photoelectron intensity with depth:

$$I(d) = I_0 exp(\frac{-d}{\lambda cos\vartheta}) \tag{3.8}$$

With d is the probing depth, $I(d)$ is the measured intensity coming from a depth d, I_0 is the theoretical intensity without attenuation and ϑ is the emission angle of the photoelectron (the angle between the electron analyzer and the normal to sample surface). Integrating Eq. 3.8 from 0 to a depth of $\lambda cos\vartheta$ leads to 63%

of the total intensity without attenuation. Accordingly, 86% and 95% of the total signal comes from probing depths of $d = 2\lambda cos\vartheta$ and $d = 3\lambda cos\vartheta$. This means that the vast majority of the electrons composing the elastic peak come from depth $\leqslant 3\lambda$. For this reason, the probing depth in XPS experiments is generally assumed to be $3\lambda cos\vartheta$.

λ is a measure of the average distance that a photoelectron travels before losing energy via an inelastic collision. The value depends on the material, the element and the electron kinetic energy (equivalently the photon energy) and can be evaluated via the Tanuma, Penn and Powell formula(TPP-2M)[189]:

$$\lambda = \frac{E_k}{E_p^2[\beta ln(\gamma E_k) - (\frac{C}{E_k}) + (\frac{D}{E_k^2})} \tag{3.9}$$

Where E_k is the electron kinetic energy (in eV), E_p is the free electron plasmon energy (in eV) and β, γ, C and D are parameters given by:

$$\beta = -0.0216 + 0.944(E_p^2 + E_g^2)^{-0.5} + 7.39 \times 10^{-4}\rho \tag{3.10}$$

$$\gamma = 1.191\rho^{-0.5}; C = 1.97 - 0.91U; D = 53.4 - 20.8U \tag{3.11}$$

$$U = \frac{N_v \rho}{M} = \frac{E_p^2}{829.4} \tag{3.12}$$

Where E_g is the band gap (in eV), ρ is the density (in g.cm^{-3}), N_v is the number of valence electrons per atom or molecule and M is the atomic or molecular weight (in g.mol^{-1}). The λ values can be calculated following Eq. 3.9 using the available free QUASES-IMFP-TPP2M software with an estimated accuracy of 10-20% (www.quases.com).

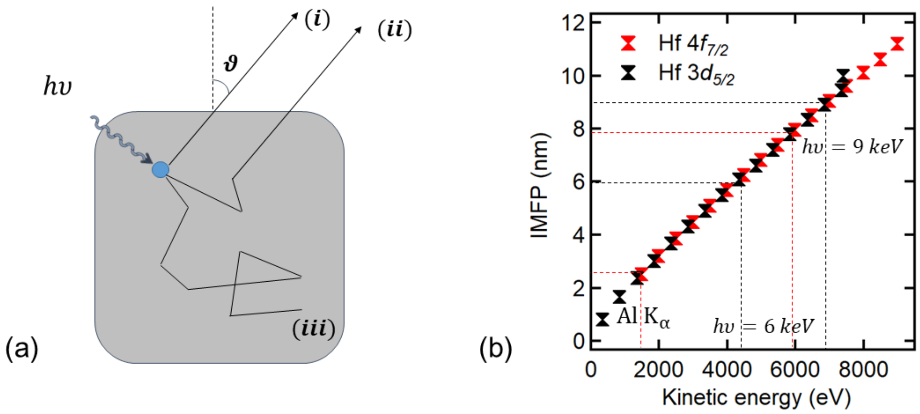

Figure 3.8: *(a) Scattering processes involved in photoemission: (i) primary (elastic) electron, (ii) secondary (inelastic) electrons and (iii) reabsorbed electrons (b) λ values of Hf 4f and Hf 3d core levels for photon energies up to 10 keV calculated using the QUASES-IMFP-TPP2M software*

For HZO, E_g=5.6eV, ρ=6.15 g.cm^{-3}, N_v=16 and M=166 g.mol^{-1}. Figure. 3.8b shows the calculated Hf 4*f* and Hf 3*d* electrons IMFP's from HZO under different excitation energies. With soft X-rays like Al Kα, λ_{Hf4f} through HZO is 2.5± 0.5nm. The same value is obtained through a metallic TiN layer taking E_g=0eV, ρ=5.4 g.cm^{-3}, N_v=9 and M=61 g.mol^{-1}. The small λ values obtained with laboratory X-ray sources explain why it is a surface sensitive technique. To probe deeper in a material, higher λ are needed and this can be achieved by increasing E_k through exciting the same electronic level with higher X-rays energies. Synchrotron light sources provide high energy X-rays (several keV) called hard X-rays making buried interfaces under realistic electrode thicknesses ($\sim$20nm) accessible (Fig. 3.8b).

Photoelectron detection

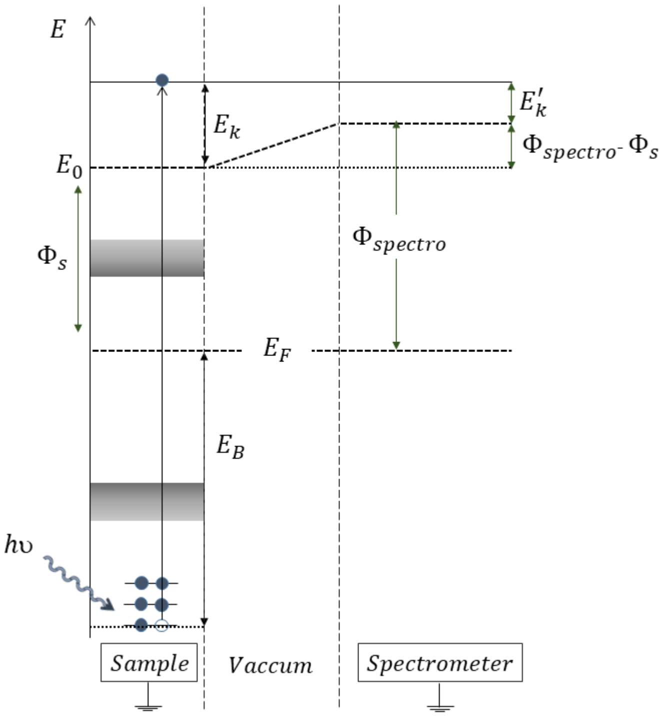

Figure 3.9: *Energy alignment of a sample connected to the spectrometer with a good ohmic contact (both have the same Fermi energy E_F. E_F of the spectrometer of work function $\Phi_{spectro}$ has to be calibrated to obtain the correct binding energy E_B of a photoelectron emitted from a sample of work function Φ_s with a kinetic energy E_K*

After passing the vacuum level, ultra-high vacuum ($\sim 10^{-10}$ mbar) environment is used to ensure a negligible additional loss of the electron energy until reaching the electron analyzer. Figure. 3.9 illustrates the methodology used to extract E_B of a photoelectron. First, the sample and spectrometer Fermi levels are assumed aligned thanks to a good ohmic contact. The real measured kinetic energy denoted $E_k^{'}$ depends on the work function of the spectrometer (Φ_{sp}). The latter can be determined by measuring the E_F position using a gold or silver reference sample. E_k can thus be written as:

$$E_k = E_k^{'} + (\Phi_{spectro} - \Phi_s) \tag{3.13}$$

However, this implies the knowledge of the work function values of each sample. To overcome this issue, E_F of the spectrometer is chosen as a reference and the energy conservation allows to obtain E_B as follows:

$$E_B = h\nu - (E_k^{'} + \Phi_{spectro}) \tag{3.14}$$

If the sample is insulating, the electric connection between the sample and the spectrometer can be insufficient and charging effects may occur due to unfilled holes decelerating photoelectrons and shifting thus the entire spectra towards lower E_k, i.e. higher E_B.

The electron analyzer used in this thesis is an Argus-128 hemispherical analyzer (ScientaOmicron). First, it consist of an electrostatic input lenses with 30mm working distance used to collect, focus and adjust the electrons energy at the entrance slit (of width W) of the analyzer. Five different in-lens aperatures can be selected manually in order to define the desired analysis area. Then, electrons pass through an hemispherical deflector (180°) of mean radius R_0 (=124mm) which is composed of two concentric hemispherical electrodes (of radius R_1 and R_2) kept at different potentials, creating a radial electric field ($\Delta V = V_2 - V_1$). Finally, electrons are detected using a 128 channel detector composed of micro-channel plate electron multipliers (MCP), a stripe anode array and 128 discriminators (Fig. 3.10). In order to complete the path along the hemispherical deflector, the photoelectron needs to have a kinetic energy called the pass energy E_{pass} given by:

$$E_{pass} = e\Delta V \frac{R_1 R_2}{R_1^2 - R_2^2} \tag{3.15}$$

Photoelectrons having high or lower energy than E_{pass} will hit the hemispheres and will not be detected. The system acts therefore as a narrow band pass energy filter which is described by Gaussian distribution. The energy resolution of the analyzer ΔE_a with an angular acceptance angle α of the entrance slit can be expressed as follows:

$$\Delta E_a = E_{pass}(\frac{W}{2R_0} + \alpha^2) \tag{3.16}$$

All core level XPS spectra shown in this thesis were recorded using $Epass = 20eV$ and an aperture of $10mm^2$ and $\alpha = \pm 3.1°$. This gives an energy resolution of 90meV. In addition, the linewidth of a monochromatic X-ray line is ΔE_X $\sim$ 250meV. This therefore gives an overall experimental energy resolution of $\sim$ $0.3eV$. Monochromatic Al Kα X-ray lines are obtained using a quartz (1,0,$\bar{1}$,0) crystal with 2d spacing of 0.851nm, an order of diffraction n=1 and an Bragg angle of 78.52°. However, the overall energy resolution ΔE_{tot} of a given core level line as measured by the full width at half maximum (FWHM) can be expressed as follows:

$$\Delta E_{tot} = \sqrt{(2\Gamma)^2 + (\Delta E_x)^2 + (\Delta E_a)^2} \tag{3.17}$$

Where 2Γ is the intrinsic energy resolution of the photoionized state which has a Lorentzian shape. Actually, an electron in a ground state with a long lifetime has a precise defined energy. However, when the electron passes to an excited state, the remaining core hole has a short lifetime Δt. According to Heisenberg uncertainty principle, the latter cannot be defined precisely giving an inherent uncertainty in its energy. This explains the widening of the FWHM of the observed photoemission peaks. The intrinsic energy resolution is given by:

$$\Delta E_{intrinsic} = 2\Gamma \sim \frac{h}{2\pi}\Delta t^{-1} \tag{3.18}$$

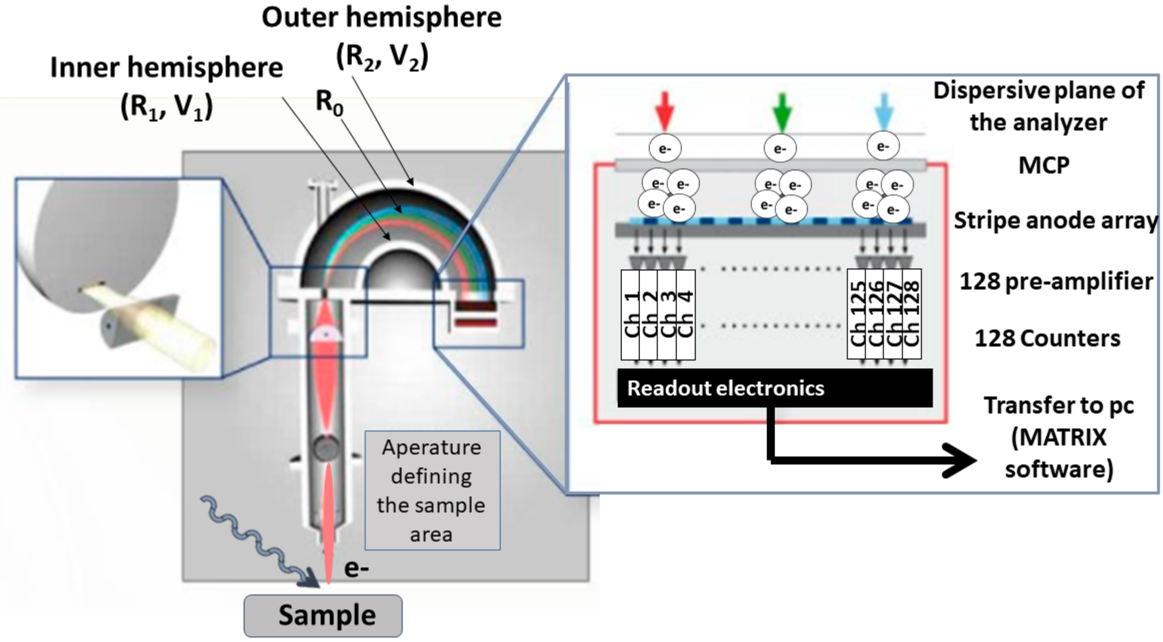

Figure 3.10: *Hemispherical electron energy analyzer operation schematic (adapted from www.scientaomicron.com)*

3.2.3 Important features in XPS spectra

Secondary electron background

Inelastically scattered electrons are called secondary electrons (SE) and form the background observed in XPS spectra. This is generally discarded using an adequate subtracting procedure in order to ensure that it meets the data at the limits of the energy interval defining a given elastic peak. The most commun types of background subtraction procedures are the simple linear background (straight line), the Shirley or the Tougaard models. The Shirley method used in this thesis considers that the background intensity at a given E_B is proportional to the intensity of the total peak area above at lower binding energies values than E_B (i.e. higher E_k). It goes up in proportion to the total intensity below the elastic peak value. Contrary to the linear shape, it therefore considers that the more electrons are excited by the photoemission process, the more can be inelastically scattered. Therefore, each main line induces a broadened step in the background intensity. The Shirley background accurately allow the correction of this phenomenon.

$$BG(E_B) = \frac{\int_{E_B}^{E_{B,min}} I(E).dE}{\int_{E_{B,max}}^{E_{B,min}} I(E).dE} \tag{3.19}$$

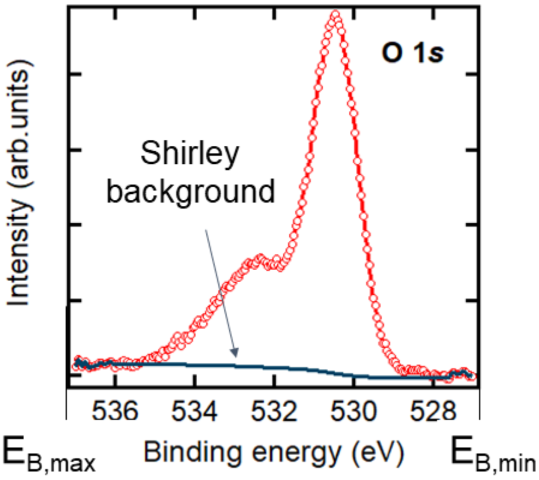

Figure 3.11: *O 1s core level spectrum from bare HZO showing the Shirley background substraction methodology*

Primary electron peak line shape

As already discussed, the shape of the elastic peaks is a convolution of the intrinsic shape of the photoionized state (Lorentzian shape) with a Gaussian broadening taking into account the thermal and the instrumental broadening (analyzer, X-ray source). For most of the oxide compounds, the elastic peaks are symmetric in shape and are therefore modeled with a pseudo-Voight functions, a Lorentzian convoluted by a Gaussian function. The line shape used for oxide peaks in this thesis is the pseudo-Voight Gaussian Lorentzian product form (GL) given by Eq. 3.20. F, E and m represent the FWHM, the energy at maximum intensity and m is the percentage of the Lorentzian contribution with m=1 for pure Lorentzian and m=0 for pure Gaussian. However, with metals, the excitation of conduction electrons causes energy losses intrinsic to the emitting atom and the core-level shape presents a typical asymmetry. Metal peaks are therefore generally modeled with Doniach-Sunjic functions given by Eq. 3.21 with α being an asymmetry parameter[190].

$$GL(x, F, E, m) = h \times exp[-4ln2(1-m)\frac{(x-E)^2}{F^2}] \times \frac{1}{1+4m\frac{(x-E)^2}{F^2}} \tag{3.20}$$

$$DS(x, F, E, \alpha) = \frac{cos[\frac{\pi x}{2} + (1-\alpha)tan^{-1}(\frac{x-E}{F})]}{[F^2 + (x-E)^2]^{1-\alpha/2}} \tag{3.21}$$

Spin orbit splitting

Figure. 3.12 shows that Hf 4*f* core level spectrum is present as a doublet. In fact, an electron having an orbital quantum number $l > 0$, possess an orbital angular momentum by virtue of its motion around the nucleus, in addition to its intrinsic spin angular momentum. Interaction between spin and orbital angular momentum of the electron interact and give rise to shifts and splitting of the lines. This interaction is called spin-orbit coupling ($\vec{J} = \vec{L} + \vec{S}$). The quantum number J has values between and $\mid l - s \mid$ and $l + s$. So, the electrons of an orbital f ($l = 3$) can have J values of $\frac{5}{2}$ and $\frac{7}{2}$. The relative intensity of the components of the doublet depends on the decay of the J state and is given by the $2J + 1$. For 4*f* electrons, the intensity ratio between the $\frac{5}{2}$ and $\frac{7}{2}$ components is 0.75. The energy separation depends on the spin-orbit coupling strength. In Hf 4*f*, $\Delta E_{5/2-7/2}$ = 1.7 eV.

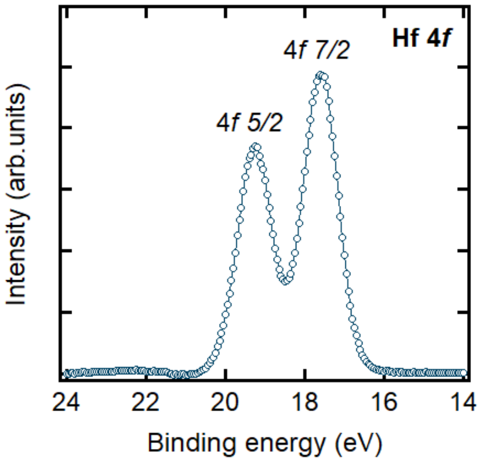

Figure 3.12: *Hf 4f core level spectrum showing the spin orbit splitting in $\frac{7}{2}$ and $\frac{5}{2}$ components*

Binding energy shift

The binding energy of a photoelectron may vary depending on the chemical environment of the emitting atom. The effect is called chemical shift and manifests itself as a difference in E_B between two electrons emitted from an identical atom but located in two non-equivalent chemical environments ($\Delta E_B = E_{B2} - E_{B1}$). The overall shift can be written as the sum of three contributions[191]:

$$\Delta E_B = \Delta\varepsilon + \Delta E_R + \Delta E_F \tag{3.22}$$

First, $\Delta\varepsilon$ is the chemical shift which translates the modification in the potential felt by the photoelectron due to the change in the valence electrons of the emitting atom. For instance, a 4*f* electron emitted from fully oxidized Hf^{4+} will have a higher binding energy ($\sim$17.5eV) than metallic Hf^{0} ($\sim$14.5eV). Contrary to the metal, the Hf has lost 4 electrons in the oxide environment. It feels therefore a higher attractive field from the nucleus and thus higher binding energy (Fig. 3.13).

The second term ΔE_R represents the relaxation energy of the photo-ionized state which results from the N-1 remaining electrons which tend to screen the remaining core hole.

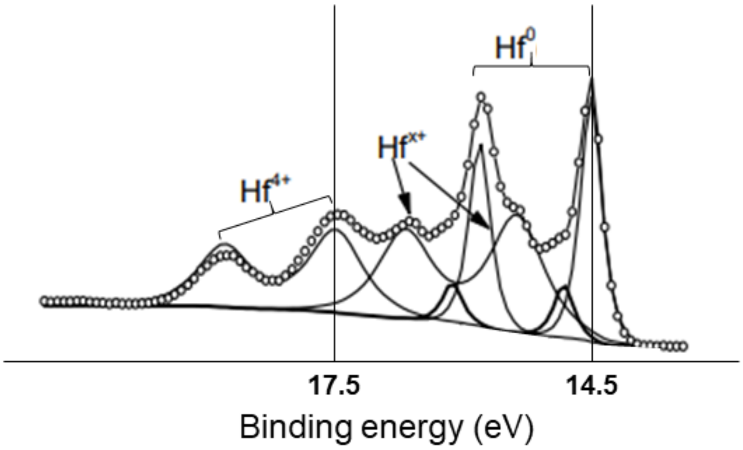

Figure 3.13: *Hf 4f core level spectrum showing the impact of the oxidation state on the effective binding energy. Oxidation (reduction) leads to higher (lower)* E_B *(from ref.[192])*

The last term ΔE_F is particularly important when studying buried interfaces. For instance, band bending at the surface or interfaces induces an internal electric field in the ferroelectric, rigidly shifting all of the electronic levels with respect to E_F. Since the energy separation between a core level and the valence band maximum is constant in the absence of chemical changes, this results in a rigid energy shift of the whole electronic structure. The magnitude of the shift depends on the distance from that interface, i.e. the distance over which the bands bend and these shifts are important to retrieve the true band offsets at a given interface.

Angle Resolved XPS measurements (AR-XPS)

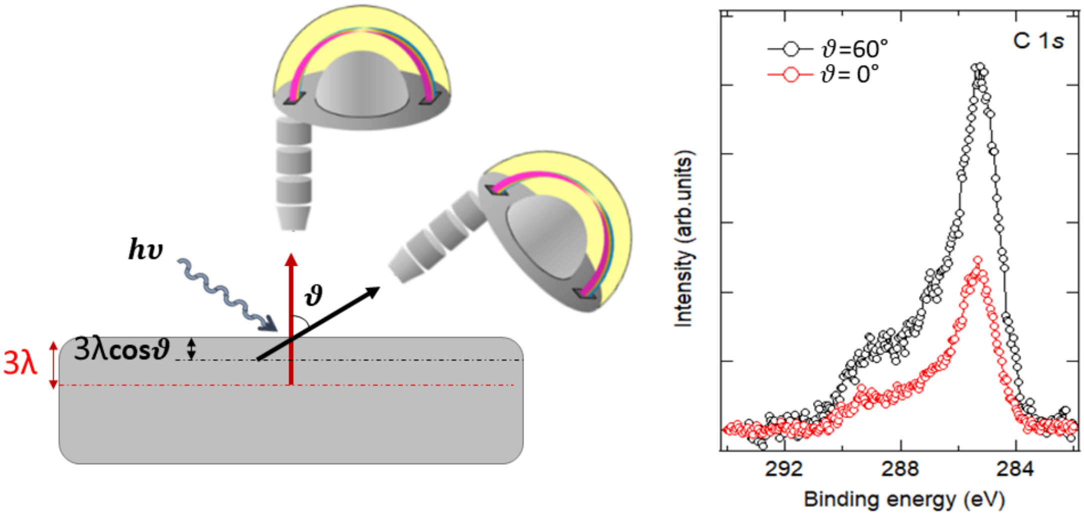

Figure 3.14: *Principle of probing depth modulation by using different emission angles. C 1s core level spectrum excited with Al Kα X-rays from bare HZO film. Recording at two different emission angles (0 and 60°) allow to modulate the probing depth within the maximum 3λ depth. The emission angle is the angle between the analyzer axis and the sample surface normal*

Angle Resolved XPS measurements (AR-XPS) allows to retrieve the depth distribution of chemical states within the 3λ depth by varying the emission angle of the experiment which adds further flexibility to laboratory XPS. Figure. 3.14 highlights the angular dependence of C 1*s* core level spectrum recorded from bare HZO film. Recording at different emission angles (0° and 60°) allow to modulate the probing depth within the maximum 3λ depth (the emission angle is the angle between the analyzer axis and the sample surface normal). The presence of carbon is due to surface contamination due to contact with air. Comparison of the spectra at two different angles ($\vartheta = 0°$ more bulk sensitive) and ($\vartheta = 60°$ more surface sensitive) confirm that the carbon is rather at the surface than in the bulk of the film (the intensity increases at $\vartheta = 60°$). Using $\lambda_{C1s,HZO}$ ~2.3nm, the probing depth ($3\lambda cos\vartheta$) are ~7 and and ~3.5nm. However, as it can be noticed, using laboratory based X-ray sources, the technique is still very surface sensitive as it is limited to the 3λ depth.

Depth profiling XPS

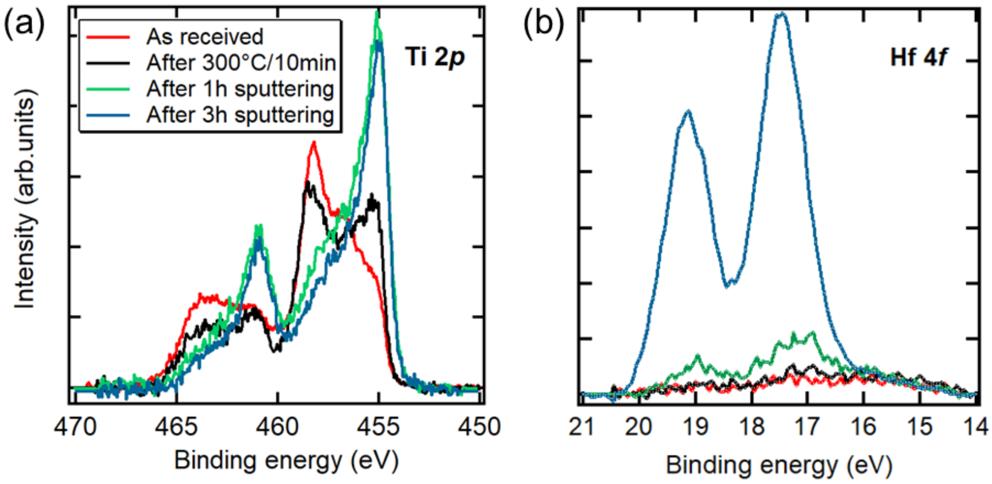

Figure 3.15: *Depth profiling XPS analysis on 10nm TiN/HZO. (a) Ti 2p and (b) Hf 4f spectra as a function of the total sputtering time using 500eV Ar$^+$ ions*

Depth profiling XPS is used to determine the profile of chemical states over depths greater than the 3λ limited sensitivity of AR-XPS. When analyzing a film under a realistic top electrode thickness (~10-20 nm), the conventional XPS or AR-XPS techniques do not allow the visualization of the ferroelectric core level photoelectrons underneath (3λ ~7.5 nm in the case of Hf 4*f*). The depth profiling is a destructive approach that allows accessing wider depths by successive ionic abrasion. This is achieved using ion beam etching (sputtering) combined with core level XPS spectra recording as a function of the etching time. However, the ion beam can alter the chemical state of the element (mainly reduction). In order to minimize ion beam reduction, a very low ion energy can be used although this also reduces the sputtering rate. In addition, the etching of the overlayer is generally stopped before achieving the material of interest (ferroelectric or the interface). In this thesis, depth profiling was performed using low Ar$^+$ ion beam of 500eV and at an angle of 45°. The measured ionic current on the sample holder are in the range of 10μA. Ions are accelerated to the sample surface to remove very slowly the first atomic layers by energy transfer. The rate depends on the material to be etched and a reference sample with a known thickness is needed to calculate the sputtering rate. An example of a depth profiling XPS analysis performed on a HZO film capped with 10nm TiN top electrode is shown in Fig. 3.15. With increased sputtering time, the Ti 2*p* signal decreases in intensity and the peak shape changes (Fig. 3.15a). The high binding energy component is ascribed to oxidized Ti surface which is gradually attenuated as sputtering proceeds to reveal the metallic TiN. At the same time, as the electrode thickness is reduced, the Hf 4*f* signal from the underlying HZO appears. This allow to retrieve the chemical state of Ti over the 10nm thickness, allowing after a total sputtering time of 3hrs to record the Hf 4*f* signal with good SN ratio (Fig. 3.15b).

3.3 Hard X-ray photoelectron spectroscopy

Hard X-ray photoelectron spectroscopy (HAXPES) uses high energy X-rays (>2keV) mainly generated by a synchrotron, although laboratory-based HAXPES equipments are also available[193]. However, brighter light, tunable energy and better resolutions are best obtained on a synchrotron beamline. The technique is quite popular in the field of solid state physics and used by several groups around the world[194]. The use of high energy has several advantages compared to soft X-rays and VUV. On the one hand, regardless of the nature of the irradiated sample (solid, gas, liquid), hard X-rays can be used to ionize deeper, highly localized electron shells. On the other hand, producing higher kinetic energy electrons allows their mean free path to be increased (see Fig. 3.8b). Using HAXPES, it is possible to probe materials down to depths about 10 times greater than with standard photoemission performed in the soft x-ray regime, which opens the way for the study of buried interfaces, as well as that of the mobility of ions in liquid solutions[195]. In condensed matter, this makes the technique a perfect choice for instance to analyze the chemical and electronic state of buried interfaces in realistic microelectronic devices[196]. However, it should be kept in mind that higher IMFP and therefore a greater depth of analysis would give just the integrated response from the whole analyzed depth. In addition, at the same time, the photoionization cross section decreases significantly with increasing photon energy ((Fig. 3.7). Furthermore, the resolving power of high kinetic energy electron analyzers becomes lower than at a lower energy. This must therefore be compensated using for instance larger acceptance angles of the analyzer and higher photon flux. The photon energy has also to be carefully chosen to obtain the best compromise between depth sensistivity and signal strength[194]. Table. 3.1 shows the evolution of the λ and σ values of Hf 3$d_{5/2}$ electrons using different photon energies[189, 187, 197].

Table 3.1: *λ and σ values of the Hf 3$d_{5/2}$ electrons at different excitation energies*

$h\nu$ (keV)	λ (nm)	σ (Mb)
2	0.9±0.2	0.85
5	4.9±0.9	0.13
8	8.5±1.7	0.16×10^{-3}

3.3.1 Synchrotron radiation: relativistic effect

The principle of synchrotron radiation is based on accelerating electrons on a curved trajectory at nearly the speed of light (c) to emit an electromagnetic radiation by Lorentz force called synchrotron light. The electron energy E of mass m travelling with a velocity v can be expressed using the Einstein formula of special relativity:

$$E = \frac{mc^2}{\sqrt{1-\beta^2}} = \gamma mc^2 \tag{3.23}$$

where mc^2 is the rest mass energy ($\sim$511 keV for an electron), $\beta = \frac{v}{c}$ and $\gamma = \frac{1}{\sqrt{1-\beta^2}}$ is the Lorentz factor. When $\beta \ll 1$ (γ slightly higher than 1), the situation corresponds to the classical limit where the energy is the sum of the rest energy and the kinetic energy. However, when $\beta \approx 1$ ($\gamma \gg 1$), the relativistic limit is achieved. The transition energy between the two limits is simply the rest mass energy mc^2. For instance, at $E = 1GeV$, $\gamma = 1955$ and $\beta \simeq 1-(1/2\gamma^2) = 1-0.125\times 10^{-6}$. v is therfore very close to c (slightly lower). When such a relativistic electron is forced to change the direction of its motion under the effect of magnetic field which is perpendicular to the plane of its motion, it emit light tangential to the orbit called synchrotron radiation as shown in Fig. 3.17. The acceleration is given by Lorentz equation[198]:

$$\frac{dp}{dt} = e(E + \frac{v \times B}{c}) \tag{3.24}$$

Where p, e are the momentum and charge of the electron and E and B are the electric and magnetic fields. A non-relativistic electron will emit a radiation called cyclotron emission which does not depend on the electron speed. The synchrotron radiation is therefore a relativistic emission. The first relativistic property is the vertical half-opening angle of the radiation which is given by $\psi = \gamma^{-1}$. At 1GeV, this gives $\psi \approx 0.5$mrad$\approx 0.029°$. The synchrotron radiation is therefore very collimated allowing high flux on small areas. The second relativistic effect is the Doppler shift of the emitted frequency for a given observer. The ν_+ blue and red ν_- shifted frequencies are given by:

$$\nu_+ = \nu_0 \frac{1}{1-\beta} \approx \nu_0 . 2\gamma^2 \tag{3.25}$$

$$\nu_- = \nu_0(1-\beta) \approx \nu_0 . \frac{1}{2\gamma^2} \tag{3.26}$$

This means that the forward lobe of the emitted pattern (w.r.t the observer and which is mainly used in synchroton) will undergo a boost in its frequency by $2\gamma^2$ and will carry a more higher power ($\gamma \gg 1$). The power radiated along a circular orbit of radius R is given by the Schwinger equation[199]:

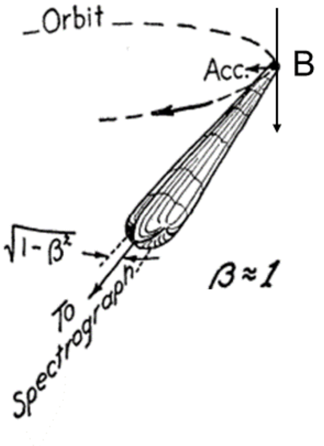

Figure 3.16: *Radiation pattern emitted from a relativstic electron ($\beta = \frac{v}{c} \approx 1$ in circular orbit due to magnetic field B perpendicular to orbit plane (from ref.[200])*

$$P_e = \frac{2}{3}\frac{e^2 c}{R^2}\gamma^4 \tag{3.27}$$

The spectral distribution of the radiation extends from the X-ray to the infrared region and is characterized by a critical wavelength, λ_c (given in Eq. 3.28), which divides the distribution into two parts of equal radiated power: 50% of the total power is radiated at λ higher than λ_c and 50% at wavelengths lower than λ_c.

$$\lambda_c = \frac{4}{3}\pi R \gamma^{-3} \tag{3.28}$$

3.3.2 Technical aspects

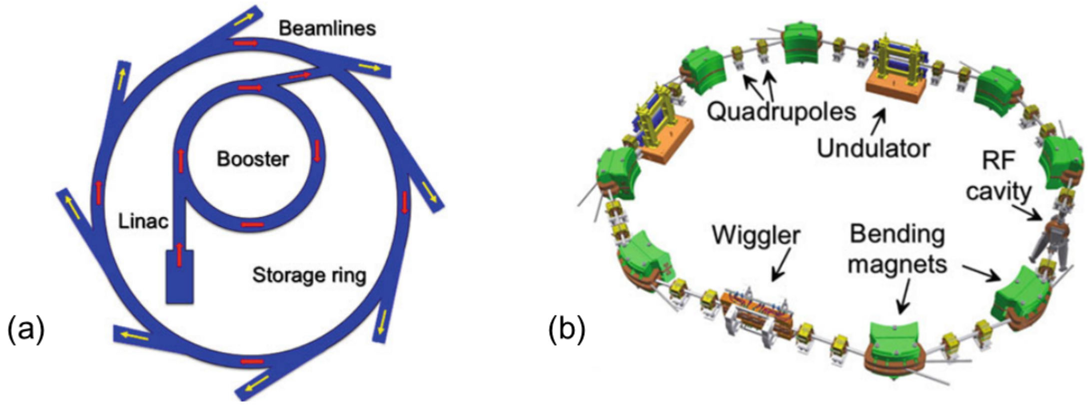

Figure 3.17: *Planar view of a typical synchrotron facaility consisting of a linear accelrator (Linac), a booster, the storage ring and bemalines (b) principal components in a storage ring (from ref.[198])*

Figure. 3.17 shows a planar view of a typical synchrotron facility. The electrons are first created and accelerated in a linear accelerator (Linac) typically to the MeV range. An energy booster is then used to achieve the desired energy

(GeV). Finally, the electrons are injected into a final circular accelerator called the storage ring used to keep the electrons at a stable velocity and force them to follow the circular path by the mean of magnetic field in quasi-stationnary situation. At each deviation, they loose part of the energy by emitting synchrotron radiation through beamlines. The energy loss is fully regained thanks to the radiofrequency (RF) cavities (generally placed in one of the straight sections of the storage ring) oscillating at the synchrotron frequency. For the circular trajectory, it is ensured by the presence of bending magnets which provide the needed magnetic field B (few Tesla). In the so-called second generation synchrotrons, the radiation is mainly produced by bending magnets. However, due to the collimation of the synchroton radiation only in the vertical direction with high angular distribution in the horizontal plane ($\gg \psi$), the optimization of the magnetic structures was needed. The use of insertion devices, like wigglers and undulators, placed in straight sections of the storage ring made afterwards possible the realization of third generation sources[198].

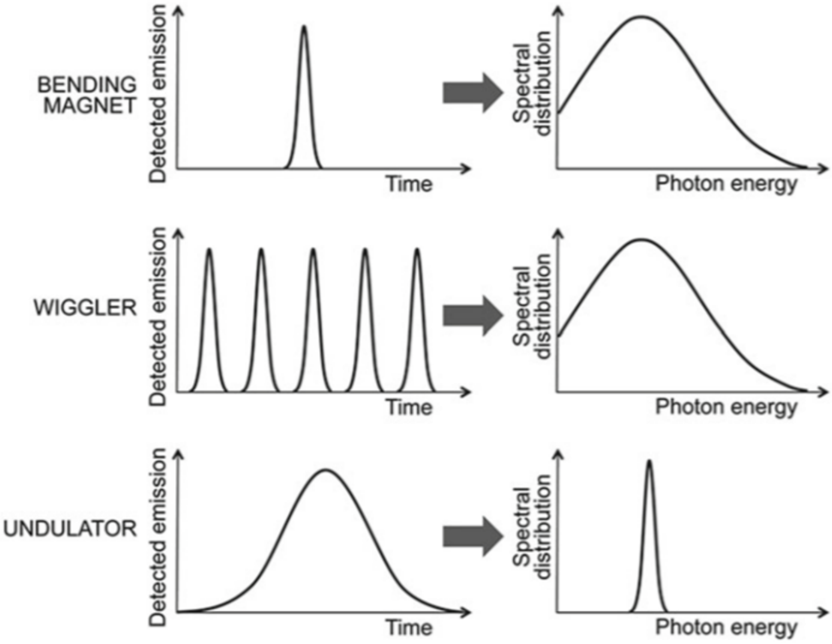

Figure 3.18: *Time emission and sepctral distribution of synchrotron radiation produced by different magnetic structures including bending magnets, wigglers and undulators (from ref.[201])*

Insertion devices are a periodic array of magnets with alternating polarity of the magnetic field. The electrons will therefore oscillate (perpendicular to its motion) and emit synchrotron radiation during each individual wiggle. This allows to increase the critical energy achieved by the bending magnet thanks to the smaller bending radius and the possible higher magnetic fields extending thus the spectral range of the storage ring. The difference between a wiggler and an undulator is α, the wiggling angle of the electron within the device. In wigglers, it is higher than the natural emission angle ψ angle and no interference occurs between the generated photons. However, in undulators α is very close to ψ and constructive interference occurs and the bandwidth narrows. Figure. 3.18 shows the time emission and the spectral distribution of the three discussed magnetic structures.

The amplitudes of radiation by each individual period of the undulator add up coherently and the intensity increases with N^2 while it increases with only as $2N$ in a wiggler. The gap of insertion devices can be altered to change the radius of the deviation and hence the critical wavelength following Eq. 3.28.

3.3.3 HAXPES beamlines specifications

BL15XU/SPring-8

Part of the synchrotron experiments during this thesis were performed at the Japanese synchrotron SPring-8 (see chapter. 5) which refers to *Super Photon Ring – 8 GeV*. Due to the high ring energy, it is one of the largest synchrotron radiation facilities in the world. The facility comprises 57 beamlines and HAXPES measurements were conducted on the BL15XU beamline.

Figure. 3.19 shows a schematic of the BL15XU layout[202]. First, X-rays with energies ranging from 2 to 10keV are obtained by revolver-type undulator. After, a front-end slit, a double crystal monochromator (DCM) with liquid-nitrogen cooling is used. The DCM is equipped with Si(111) and Si(311) crystals which can be easily selected through an horizontal motion normal to X-rays. A channel-cut monochromator (a high resolution monochromator (HRM)) is also installed after the DCM for high-energy-resolution HAXPES experiments. It is equipped with three channel-cut crystals of Si(111), Si(220), and Si(311) with different available reflections. The electron analyzer used is VG Scienta R4000 (scientaomicron) and the total energy resolution is better than 250 meV. The X-ray beam spot size on the sample is 30 and 35 μm in vertical and horizontal directions, respectively[202].

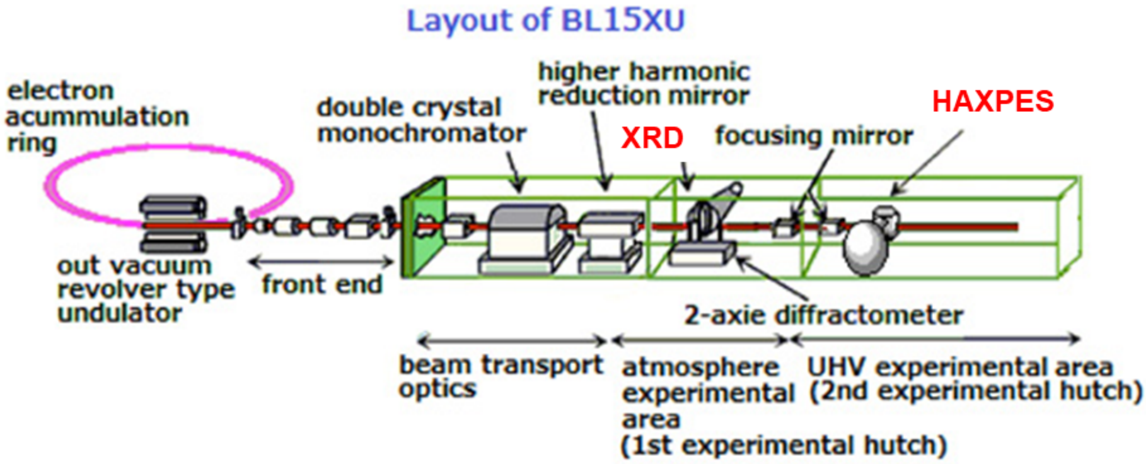

Figure 3.19: *Schematic of the BL15XU end station layout (from ref.[202])*

GALAXIES/Soleil

The HAXPES experiments discussed in chapter. 6 were performed at the GALAXIES beamline in the French synchrotron radiation facility, Soleil. The synchrotron name Soleil refers to *Source Optimisée de Lumière d'Energie Intermédiaire du Lure*. It comprises 29 beamlines and the nominal ring energy is 2.75GeV.

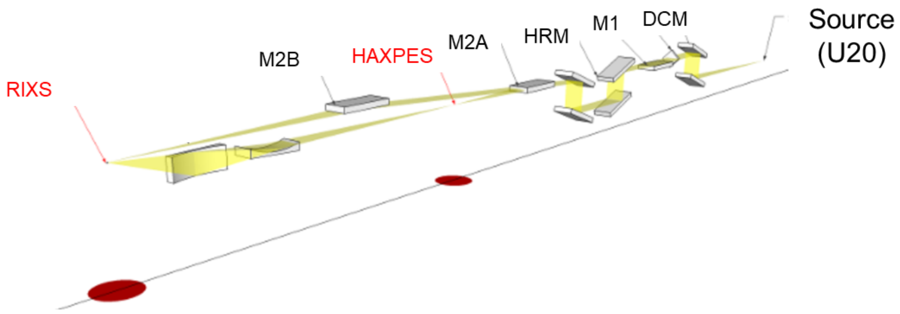

Figure 3.20: *Schematic of the GALAXIES end station layout (from ref.[203])*

The GALAXIES beamline is dedicated to resonant inelastic X-ray scattering (RIXS) and HAXPES experiments (Fig. 3.20). For HAXPES, the X-ray source consists of an U20 undulator (20mm period, 98 periods, 0.96 Tesla maximum magnetic field at a minimum gap of 5.5mm)[203]. The beamline is designed to provide X-ray beam energies in the 2.4–12keV spectral range and the beam spot size is 20 and 80 μm in vertical and horizontal directions, respectively. Similarly to BL15XU, the main optical components consist of a liquid nitrogen-cooled DCM followed by a HRM which can hold a different range of silicon crystals, both symmetric and asymmetric, in order to achieve the required energy resolution. The energy resolutions as a function of the photon energy and the selected monochromators are given in Fig. 3.21a. Eletron detection is ensured using a EW4000VG Scienta hemispherical analyzer situated at 90° relative to X-ray direction (Fig. 3.21b)[203].

Both SPring-8 BL15XU and Soleil GALAXIES offer the possibility of *operando* experiments, under bias.

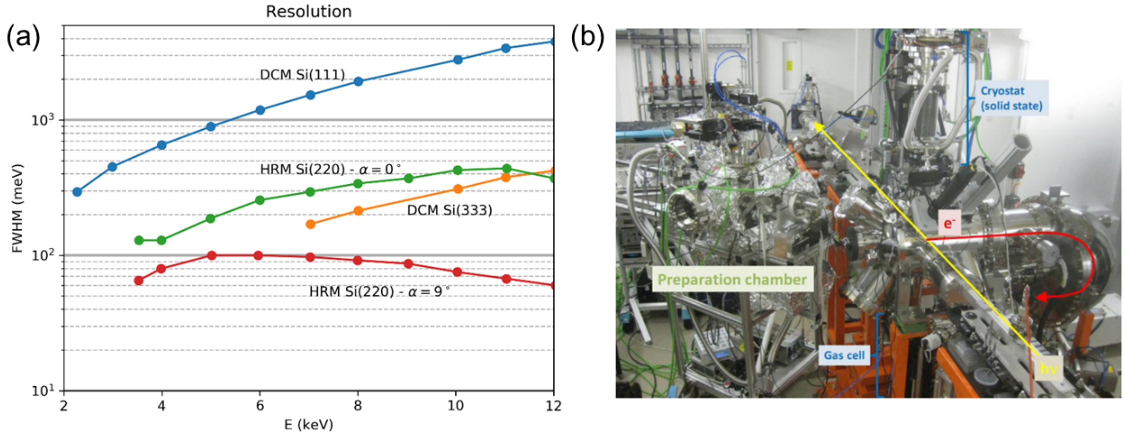

Figure 3.21: *a) Energy resolution as a function of photon energy using the different monochromators and (b) a photograph image from the GALAXIES beamline experimental hutch (from ref.[203])*

Chapter 4

Interface physical chemistry of $Hf_{0.5}Zr_{0.5}O_2$-based capacitors

4.1 Introduction

The electrode/ferroelectric interface and the crystallization annealing temperature appear to play a key role in the device performance. The electrode may chemically interact with the ferroelectric film oxidizing the electrode material at the interface and creating an oxygen depleted layer in the oxide.

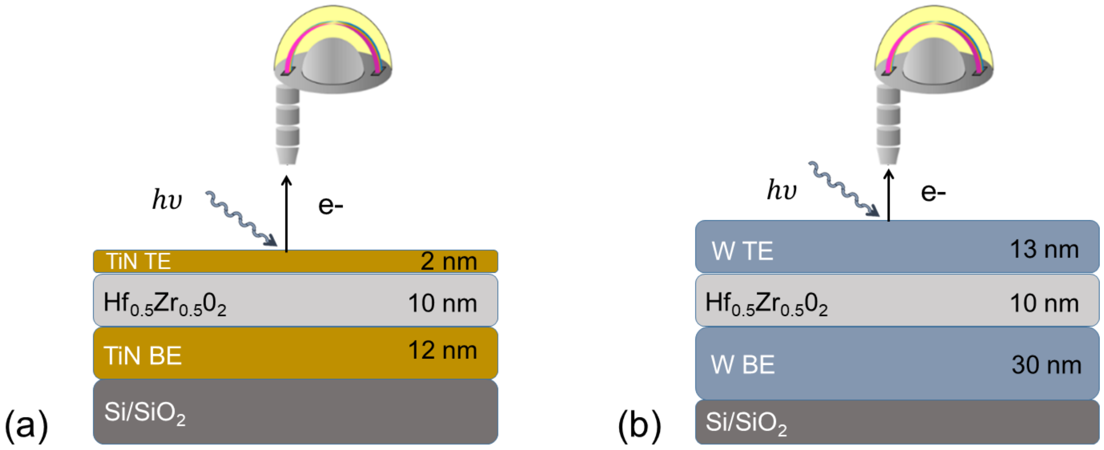

Figure 4.1: *Schematic of the analyzed samples with laboratory XPS (a) TiN(2 nm)/HZO(10 nm)/TiN(12 nm) and (b) W(13 nm)/HZO(10 nm)/W(30 nm) on Si substrates*

In this chapter, we present a combinatorial analysis using electrical measurements and laboratory XPS to characterize the interface physical chemistry of pristine ferroelectric $Hf_{0.5}Zr_{0.5}O_2$ (HZO) thin films with TiN and W electrodes. First, we will discuss the TiN/HZO interface, which is the most common used electrode material in microelectronics giving its high effectiveness from mass production perspective. The chemistry of the electrode material at the interface is first investigated. Then, the V_O concentration and the band alignement at the interface along with the effect of increasing annealing temperature are discussed. After, the results obtained using W electrode instead of TiN are presented. Tungsten presents lower TEC than TiN (4.5×10^6 *vs* 9.5×10^6 /°C for TiN) and can thus induce a higher o-phase as shown in section. 2.3.2. The Gibbs free energies of titanium and tungsten oxidation are also different with higher oxygen affinity for TiN. The two electrode are, therefore, believed to induce different chemical and electronic behaviors at the interface with the as-deposited HZO films. The effetcs on the pristine hysteresis loops are also presented. The analyzed samples in this chapter were provided by NamLab and the different aspects related to the preparation (film growth, electrodes, annealing) are summarized in Appendix. A. They consist of TiN(2 nm)/HZO(10 nm)/TiN(12 nm) and W(13 nm)/HZO(10 nm)/W(30 nm) capacitor structures grown on Si substrates (Fig. 4.1).

4.2 TiN/Hf$_{0.5}$Zr$_{0.5}$O$_2$ interface

4.2.1 Electrical characterization

Figure. 4.2 shows the endurance characteristic of the TiN/HZO/TiN stack highlighting the evolution of the memory window (MW) as a function of cycling. Using $\pm$3V at 100kHz cycling pulses, the device shows a breakdown after 10^7 cycles. The I-E and P-E curves obtained from pristine (1st cycle) and after 10^5 cycles states are given in Fig. 4.3a and b, respectively.

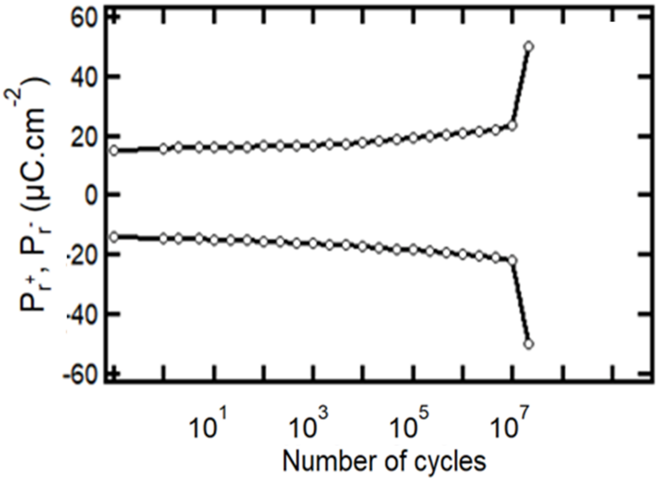

Figure 4.2: *Endurance plot showing the evolution of the memory window ($2P_r$) as a function of field cycling using rectangular cycling pulses of $\pm$3V/100kHz*

The pristine sample is characterized by double current peaks as shown in Fig. 4.3a, resulting in a pinched hysteresis loop (Fig. 4.3b). After 10^5 cycles, the double peaks merge to a single switching current peak with higher intensity, accompanied by an opening of the hysteresis loop and an increase of the MW from 34 to 40 μC.cm^{-2}, characteristic of a wake-up behavior. For the as-grown capacitor, a coercive field of 0.89 MV.cm^{-1} was extracted from the P–E curve, increasing to 1.07 MV.cm^{-1} after cycling. These high E_C are typical for ferroelectric hafnia materials[56]. The pristine capacitor shows also that the hysteresis loop is asymmetric toward negative fields. The unpoled capacitor exhibits an imprint field magnitude of -95 kV.cm^{-1}, pointing toward the top interface. After cycling, the magnitude of the imprint decreases to -15 kV/cm. Given these significant differences in electrical characteristics between the pristine and woken-up states, it indeed appears that the defect chemistry near the interfaces plays an important role.

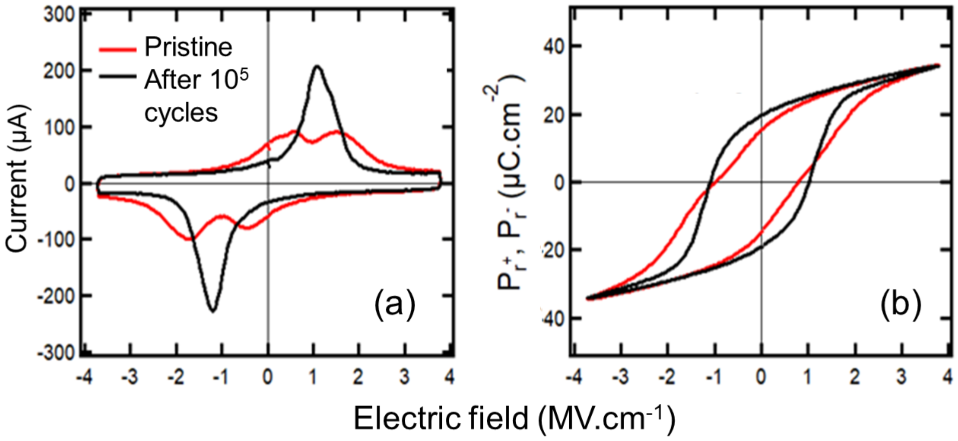

Figure 4.3: *(a) Switching current vs electric field (I-E) and (b) polarization vs electric field (P-E) recorded using DHM (±3V/1kHz) from pristine and woken-up (after 10^5 cycles) TiN/HZO/TiN capacitors*

4.2.2 XPS analysis

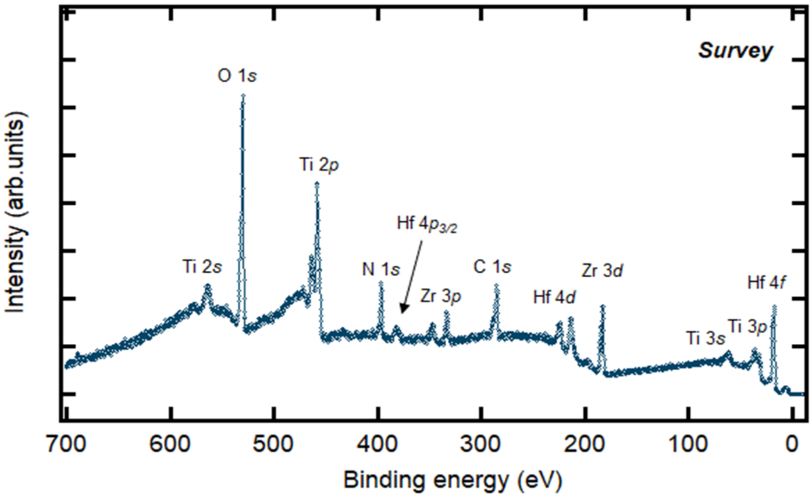

Figure 4.4: *Survey spectrum from the as-grown TiN(2nm)/HZO/TiN sample*

In order to get more insight into the origin of this asymmetry, XPS was used to evaluate the physical chemistry of the top interface. Prior to that, Conductive Atomic Force Microscopy (C-AFM) was used to qualify the uniformity of the used 2 nm TiN top electrode (TE). In fact, it is essential to verify that there are no pinholes and that the XPS will indeed probe only one single, buried interface between HZO and the TE. As shown in Appendix. A, C-AFM have confirmed that the electrode is rather continuous and uniform above the HZO film.

The survey spectrum recorded from the as-deposited capacitor is shown in Fig. 4.4. All the expected core levels are present together with some C contamination, which may stem from surface contamination or from incomplete removal of the precursors-related organic ligands during annealing. No other contamination is present. Table. 4.1 gives the measured E_B, FWHM and the corresponding peak areas of the main elements, in addition to the IMFP values assumed equal in HZO and TiN ($\lambda_{HZO,TiN}$). The E_B calibration was made using the C 1*s* emission at 285 eV. Using the peak area values and the ionization cross sections (σ), the concentration of Hf and Zr and the corresponding ratio was evaluated using the following equation:

$$\frac{Hf}{Hf+Zr}(\%) \propto \frac{\frac{I_{Hf}}{\lambda_{Hf}\sigma_{Hf}}}{\frac{I_{Hf}}{\lambda_{Hf}\sigma_{Hf}}+\frac{I_{Zr}}{\lambda_{Zr}\sigma_{Zr}}} \times 100 \tag{4.1}$$

Where I_i is the area of the peak. The σ values are taken from Fig. 3.7 as σ_{Hf4f}= 0.11Mb and σ_{Zr3d}= 0.09Mb. We measured 49 and 51% for Hf and Zr, respectively, giving a ratio of almost 1 as expected for $Hf_{0.5}Zr_{0.5}O_2$ stoichiometry.

Table 4.1: Binding energy (E_B), *full width at half maximum (FWHM), peak area and inelastic mean free path (λ) values of the main photoelectron lines*

	Hf 4*f*	Zr 3*d*	Ti 2*p*	N 1*s*	O 1*s*	C 1*s*
E_B (eV)	17.58 ($\frac{7}{2}$)	182.40 ($\frac{5}{2}$)	458.6 ($\frac{3}{2}$)	397.10	531.80	285.00
FWHM (eV)	1.05	1.00	2.13	1.43	1.50	1.80
Area	1923	1564	4860	980	5272	1415
$\lambda_{HZO,TiN}$ (nm)	2.5	2.3	1.9	2.0	1.8	2.2

Interface chemistry of the electrode material

Figure. 4.5 compares the N 1*s* spectra from the 2 nm TiN TE as a function of the emission angle (ϑ). Analysis of these spectra reveals two main peaks: the peak at 397.1 eV is assigned to N^{3-} in metallic TiN environment ($Ti^{3+}N^{3-}$) while the second peak observed at the lower binding energy (396.1 eV) indicates, given the electronegativities of Ti and O, the formation of an oxynitride phase $TiO_{2-\delta}N_y$. The E_B values and the 1eV energy difference between the two components is in very good agreement with previous studies on TiN oxidation using laboratory XPS[204, 205]. The higher energy peaks shaded in gray (397.7 eV and 399.3 eV) are related to molecular nitrogen species, which are inherent features characteristic of TiN and other transition-metal nitride surfaces. They are always present at approximately the same energy positions but their exact assignment remains ambiguous[205]. The peak shown in red at 402.8 eV can be unequivocally related to molecular nitrogen N_2, known as a result of TiN oxidation. The peaks were fitted using GL(30) line shapes except for the metallic component fitted using DS line shape with an asymmetry parameter α=0.05. By constraining the FWMH to 1.3 for TiN and 1.6 eV for the rest of the peaks and by constraining the area of the grey peaks, the results reveal that the relative intensity of the two main peaks depends on the probing depth of the analysis. In fact, the $TiO_\varsigma N_y$ intensity becomes lower with respect to that from the TiN phase with decreasing the probing depth (increasing the emission angle) and is, therefore, attributed to a presence rather at the interface with HZO than the surface of the electrode.

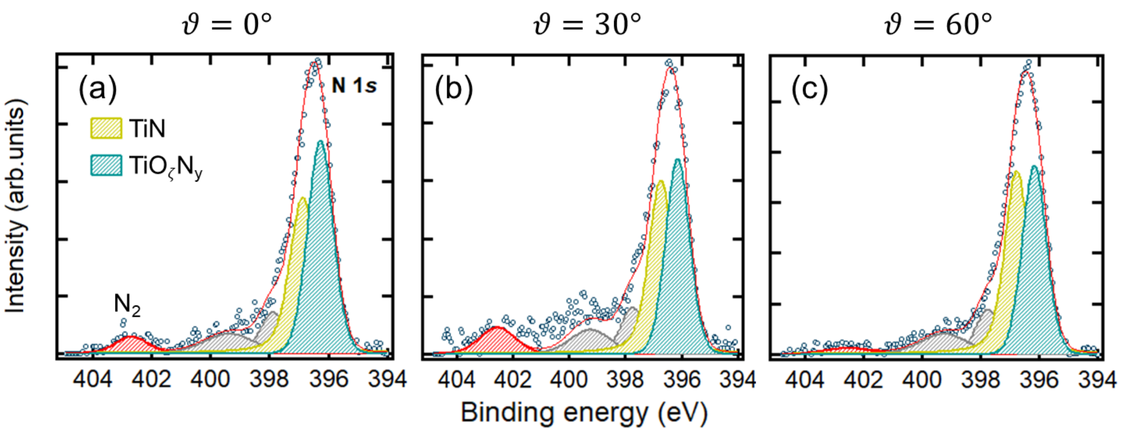

Figure 4.5: *(a) N 1s core level of the TiN TE at normal emission (b) at 30°, and (c) at 60°*

In order to get more insights into the physical chemistry at the interface, the Ti 2*p* core level has been investigated as a function of Ar^+ ion sputtering time. Using low ion energy of 500eV and an ionic current of $\sim 10\mu$A, the etch rate was calculated on a similar sample to be 0.8±0.5 nm.hr^{-1}. First, the as received Ti 2*p* spectrum is shown in Fig. 4.6a. It can be fitted with three spin–orbit split components. The first one located at the lowest binding energy (455.5 eV) is attributed to metallic TiN. The energy separation between Ti 2$p_{3/2}$ and N 1*s* lines, ΔE, is characteristic of the TiN chemistry and reflects its stoichiometry. The energy splitting ΔE in our case is 58.4 eV, in good agreement with that observed for nearly stoichiometric TiN[204, 205]. The two additional components, one at 1 eV from the metallic component as found with N 1*s* (at E_B=456.5 eV), points to the formation of an oxynitride phase $TiO_\zeta N_y$. The second, at 458.5 eV, corresponds to a Ti$^{\sim 4+}$ chemical state in a $TiO_{2-\delta}$ environment, with δ tending towards 0. A fully oxidized Ti corresponding to TiO_2 phase is generally observed with Ti 2$p_{3/2}$ emission at higher E_B values reported between 459 and 460 eV[206]. Table. 4.2 summarizes the fitting parameters and the measured peak area corresponding to each component.

Table 4.2: *Ti 2$p_{3/2}$ fitting parameters and and results*

	Line shape	BE(eV)	FWHM (eV)	Area
TiN	DS(α=0.05)	455.5	1.3	642
$TiO_\zeta N_y$	GL(30)	465.5	1.6	662
$TiO_{2-\delta}$	GL(30)	458.5	1.6	2113

Figure. 4.6b shows the evolution of the components percentage after 15 and 30min etching time. First, etching leads to a decrease of the intensity of the $TiO_{2-\delta}$ peak relative to TiN, confirming that the $TiO_{2-\delta}$ phase is present at the surface as suggested by C-AFM (see Appendix. A). Second, the results reveal that the oxynitride component, like the metallic TiN, increases in intensity relative to $TiO_{2-\delta}$ with increasing sputtering time. This confirms that the $TiO_\zeta N_y$ signal comes from the interface with HZO, in agreement with the angle-dependent measurements using N 1*s*. The Ti 2*p* and N 1*s* results point therefore to the presence of an oxidized $TiO_\zeta N_y$ layer at the interface.

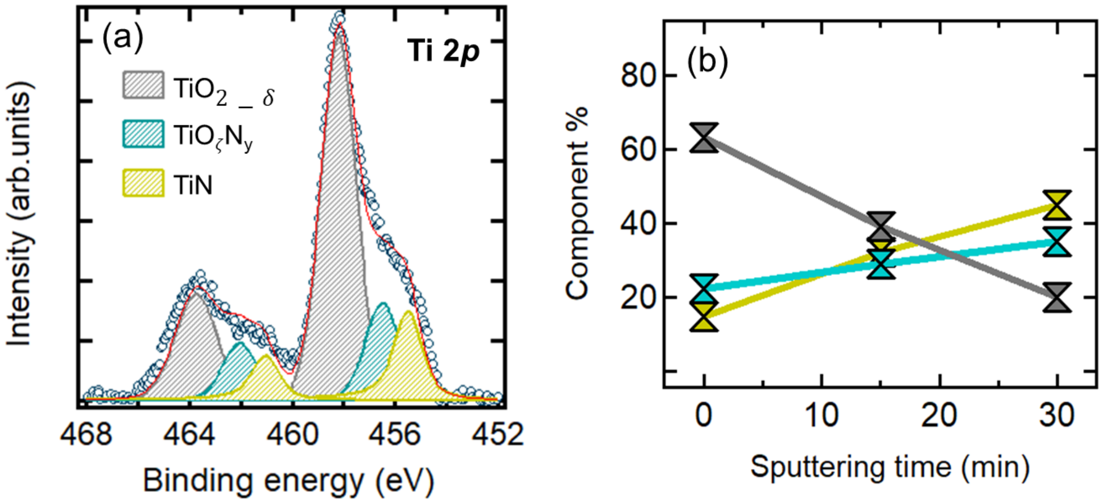

Figure 4.6: *(a) Ti 2p core level spectrum acquired at normal emission before sputtering and (b) the evolution of the TiN, $TiO_\zeta N_y$ and $TiO_{2-\delta}$ percentages (shown in a) after 15 and 30min Ar$^+$ sputtering (E_{Ar^+}=500eV)*

Using the photoelectron attenuation function and a layer-by-layer model of the stack, we calculate the thickness of the interfacial layer x as follows[207]: First, the peak area intensity from TiN and the oxynitride are given by:

$$I_{TiN} = 1 - exp(\frac{-d_{TiN}}{\lambda_{TiN}}) \tag{4.2}$$

$$I_{TiO_\zeta N_y} = exp(\frac{-d_{TiN}}{\lambda_{TiN}})(1 - exp(\frac{-x}{\lambda_{TiON}})) \tag{4.3}$$

Dividing the measured intensities (($I_{TiN}/I_{TiO_\zeta N_y}$), the thickness of the interface layer can be expressed as follows:

$$d_{TiO_\zeta N_y} = x = \lambda_{Ti} ln(\frac{Sexp^{\frac{t}{\lambda_{Ti}}} + 1}{S+1}) \tag{4.4}$$

With t is the top electrode thickness ($t = x + d_{TiN}$), λ_{Ti} is the inelastic mean free path of Ti 2*p* photoelectrons assumed equal through both layers with a value of 1.9 nm and $S = (I_{TiN} + I_{TiO_{2-\delta}})/I_{TiO_\zeta N_y}$. Taking the values after 30min sputtering, t=1.6 nm and S= 1.63 (from Fig. 4.6b), this leads to an interface layer thickness of 1.1±0.5 nm. A 1.5 nm oxidized layer at the top interface was also reported using Energy Dispersive X-Ray (EDX) elemental profiling along similar TiN(12 nm thick)/HZO/TiN/Si stack [208]. Lenser *et al* showed that similar oxidation at the interface occurs using Ti electrodes and that the oxidized interfacial layer becomes thicker when increasing the TE thickness[209]. This may explain the lower value obtained in this work giving the thin used TE (∼2nm).

In order to elucidate the origin of this oxidized layer at the interface, Hf 4*f* core level spectra were analyzed.

Oxygen vacancy concentration

The Hf 4*f* core level spectra were recorded as a function of the emission angle. Figure. 4.7a shows the spectrum acquired at normal emission. It is dominated by a spin–orbit splitting of ΔE=1.7eV with Hf 4$f_{7/2}$ at E_B = 17.6 eV. The value is in accordance with reported values for stochiometric HfO_2[210]. The singlet at higher E_B (22.6 eV) belongs to O 2*s* emission, while that at lower E_B is attributed to the N 2*s* from the TE (at 15.9 eV). The E_B values are in good agreement with reported values on similar TiN/HZO/TiN stack[211]. By changing the emission angle to 30° and 60° (Figs. 4.7b and c), increasing the sensitivity to the interface with respect to the bulk HZO film, we can see the emergence of an additional doublet at lower E_B, situated at 0.8 eV with respect to the stoichiometric HZO peak. From electronegativity arguments, this component is attributed to reduced Hf. By comparison with the literature, we deduce that the reduced Hf at the interface has a 3+ oxidation state[192, 210, 212]. In order to be able to compare these spectra, GL(30) line shapes were used for all emission lines with specific constrains summarized in Tab. 4.3. Thus, the only free parameter is the relative intensity of the Hf^{4+} and Hf^{3+}.

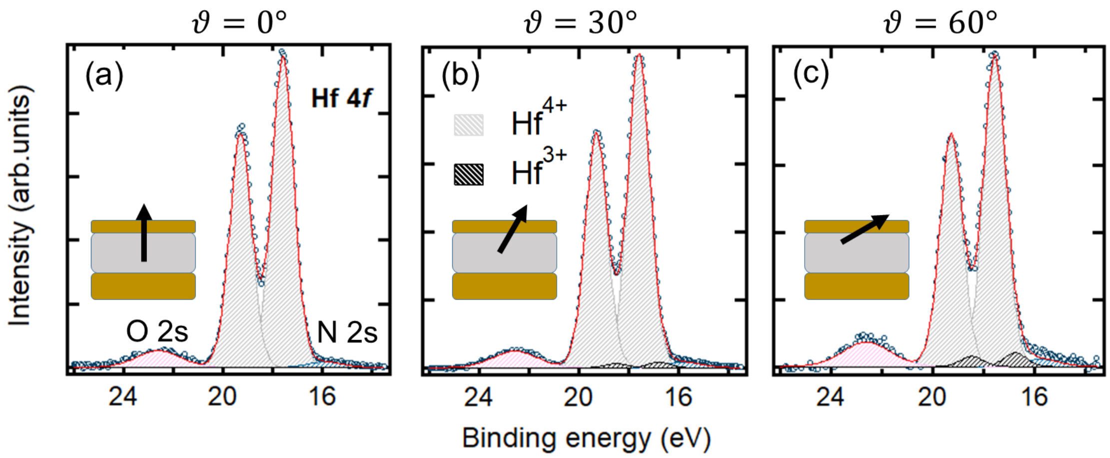

Figure 4.7: *(a) Hf 4f core level at normal emission, (b) 30° and (c) 60° emission angle*

Table 4.3: *Hf 4$f_{7/2}$ fitting constrains*

	BE(eV)	FWHM (eV)	Area
(A) Hf^{4+} ($\frac{7}{2}$)	17.6	1.05	
Hf^{4+} ($\frac{5}{2}$)	A+1.7	A×1	A×0.75
(B) Hf^{3+} ($\frac{7}{2}$)	A-0.8	A×1	
Hf^{3+} ($\frac{5}{2}$)	B+1.7	A×1	B×0.75
N 2*s*	A-1.7	1.8	A×0.03
O 2*s*	A+5	2.2	

Table. 4.4 gives the obtained $\frac{I(Hf^{3+})}{I(Hf^{4+})+I(Hf^{3+})}$ ratios. We suggest that oxygen vacancies created as a result of oxygen scavenging by the TE (oxygen movement toward the TE), which may in turn explain the oxidation of the latter at the interace as observed earlier, is the most likely source of electrons which can reduce interfacial Hf atoms. Since a Hf atom of valence state 3+ hosts one free electron,

we can estimate the oxygen deficiency concentration from the measured reduced hafnium amount. Taking into account that V_O releases two electrons and given the $\frac{1}{4}$ ratio between Hf and O atoms in HfZrO_4 molecule, the vacancy concentration, which account thus for $V_O^{\cdot\cdot}$, can be given by $V_O^{\cdot\cdot} \sim \frac{I(Hf^{3+})}{I(Hf^{4+})+I(Hf^{3+})} \times \frac{1}{8}$. The derived $V_O^{\cdot\cdot}$ concentrations in percentage and volumic density as a function of the emission angle are also included in Tab. 4.4.

Table 4.4: *Hf 4f fitting results*

	$\frac{I(Hf^{3+})}{I(Hf^{4+})+I(Hf^{3+})}$	$\sim V_O^{\cdot\cdot}$ (%)	$\sim V_O^{\cdot\cdot}(cm^{-3})$
$\vartheta = 0°$	-	-	-
$\vartheta = 30°$	2.8± 0.3	0.35	1.5×10^{20}
$\vartheta = 60°$	5.68± 0.5	0.71	3.1×10^{20}

The probing depth within the HZO film of these angular XPS measurements was determined using the photoelectron attenuation function as follows. First, we define the position of the interface with respect to the surface as z_0. The integrated intensity of Hf 4*f* can be expressed as follows:

$$I_{Hf} = \int_{z_0}^{\infty} exp(\frac{-z}{\lambda cos\vartheta}) = -\lambda cos\vartheta.exp(\frac{-z_0}{\lambda cos\vartheta}) \tag{4.5}$$

We then define a characteristic probing depth, z_c, as the depth to which the integrated Hf intensity is half of the total signal.

$$I_{Hf} = \int_{z_0}^{z_c} exp(\frac{-z}{\lambda cos\vartheta}) = -0.5\lambda cos\vartheta.exp(\frac{-z_0}{\lambda cos\vartheta}) \tag{4.6}$$

Equation.4.6 allows then to express z_c as a function of the emission angle ϑ :

$$z_c = \lambda cos\vartheta ln(2) + z_0 \tag{4.7}$$

Figure. 4.8 shows the obtained evolution of $V_O^{\cdot\cdot}$ within HZO in contact with a TiN electrode. The data point corresponding to a sample depth of 8 nm were extracted from Hf spectra recorded at normal emission after a complete chemical etching of the 2 nm TE (see Appendix.A). The $V_O^{\cdot\cdot}$ concentration shows a maximum (~0.71%) at the first nanometers of HZO and then decreases sharply going into the film. $V_O^{\cdot\cdot}$, therefore, accumulate at the top interface at the pristine state, giving rise to a non-uniform defect distribution along the stack. We suggest that at the bottom interface, the TiN electrode is passivated, i.e impeding oxygen scavenging (this will be experimentally investigated in chapter. 5 using HAXPES analysis on similar stack). However, the top electrode is not passivated. As a result, it can scavenge oxygen from HZO leading to the formation of an oxynitride phase and the accumulation of $V_O^{\cdot\cdot}$ and reduced Hf at the interface. This gives a strong negative V_O gradient going from the top to the bottom interface. We suggest that asymmetric electron trapping at more available $V_O^{\cdot\cdot}$ sites near the top interface is at the origin of the imprint field pointing toward the TE observed in the pristine hysteresis loop. In addition, $V_O^{\cdot\cdot}$ and the subsequent electron trapping may result in significant domain wall pinning which may explain the reduced pristine MW. Given the negative asymmetry in the P-V curve and the negative $V_O^{\cdot\cdot}$ profile from the top to the bottom interface, electron trapping by $V_O^{\cdot\cdot}$ is the most likely origin of the imprint and the pinned domains at the pristine state. The $V_O^{\cdot\cdot}$ concentration found here are higher than the values reported by Fengler *et al* for $V_O^{\cdot}$ and $V_O^{\cdot\cdot}$ (0.26% and 0.1%, respectively) using thermally stimulated currents measurements (TSDCs)[145]. The difference might stem from the fact that immobile oxygen vacancies are undetected with the TSDC method. Only mobile charged defects can be measured. With respect to the XPS measurements, TSDC may, therefore, underestimate the total vacancy concentration. Using the same technique, the same authors suggested also that both imprint and wake-up are indeed closely linked to a higher oxygen vacancy concentration near the top interface[213].

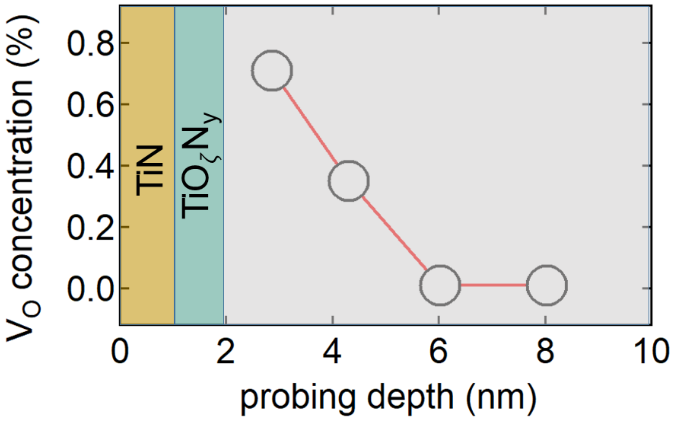

Figure 4.8: *V_O concentration percentage as a function of the probing depth in 10 nm HZO films with 2 nm TiN TE. The measured ∼1 nm thick $TiO_\zeta N_y$ interface layer is also shown*

Effect of annealing

As already discussed in section. 2.5.2, the thermal energy provided when annealing at relatively high temperatures is believed to be at the origin of the observed oxygen scavenging by the TE and the accumulation of $V_O^{\cdot\cdot}$ near the interface. In order to verify this, we investigated a similar stack with 2nm TiN TE which underwent a rapid thermal annealing at higher temperature of 1000°C. With respect to the discussed 600°C RTA sample, the XPS analysis reveal that the Hf 4*f* and Zr 3*d* spectra are rigidally shifted by 220 meV toward higher E_B values as shown in Fig. 4.9. This rigid band shift is characteristic of further n-type doping of the film.

Figure. 4.10 shows the fitted Ti 2*p* and Hf 4*f* core level spectra recorded, respectively, at 0° and 60° emission angles. This represents the most interface sensitive configurations for both.

Comparison with the results obtained with T$_{RTA}$=600°C shown in Fig. 4.6a and 4.7a indicate that annealing at 1000°C results in an increase of both the $TiO_\zeta N_y$ with respect to the metallic component and the $V_O^{\cdot\cdot}$ concentration. The $TiO_\zeta N_y$ phase percentage increases from 21% to 26% and the $V_O^{\cdot\cdot}$ concentration increases from ∼0.71 to 0.9%. The increase of $V_O^{\cdot\cdot}$ is in agreement with the electronic band

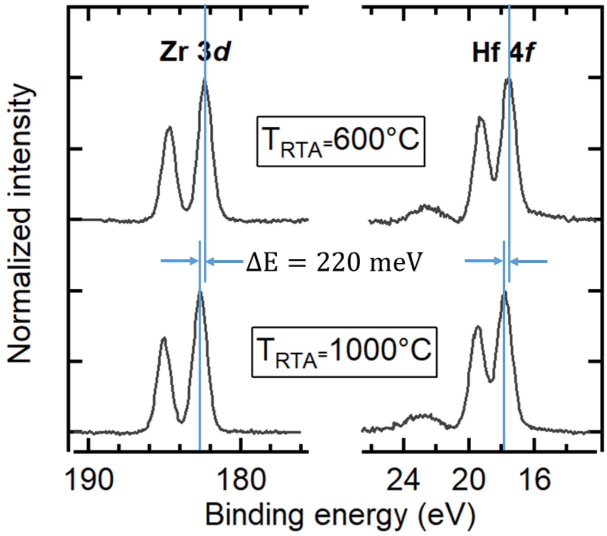

Figure 4.9: *Hf 4f and Zr 3d core level spectra acquired at 60° emission angle with the rapid thermal annealing at T=600°C and 1000°C*

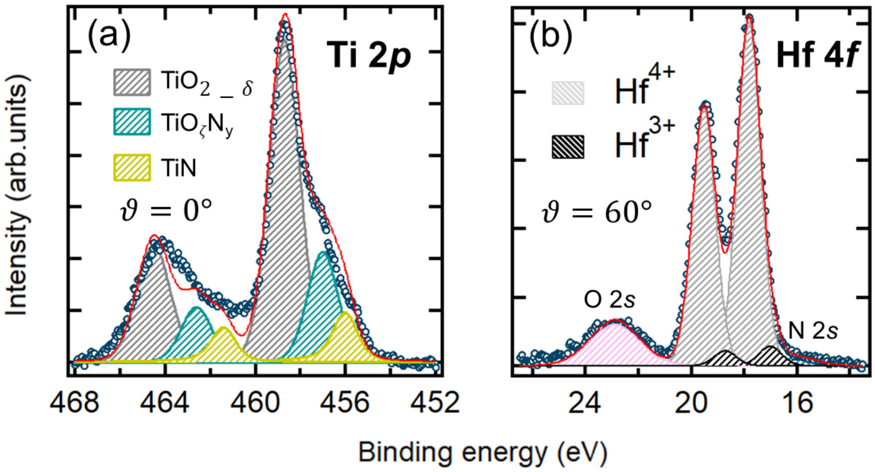

Figure 4.10: *(a) Ti 2p at ϑ=0° and Hf 4f at ϑ=60° from the capacitor annealed at T_{RTA}=1000°C*

shift characteristic of further n-type doping. In addition, the results clearly indicate the link between the $TiO_\zeta N_y$ layer and the oxygen deficiency at the interface and that oxygen scavenging is indeed promoted by thermal energy provided upon the annealing step to crystallize the films.

Interface electronic structure

We have calculated the φ_{Bn} at the top TiN/HZO interface following the method of Kraut *et al*[214] summarized in Fig.4.11.

First, the valence band offset (φ_{Bp}) at the interface can be evaluated using the following equation:

$$\varphi_{Bp} = (E_{B,Ti2p} - E_F)_{TiN_{reference}} - (E_{B,Hf4f} - VBM)_{HZO_{reference}} - (E_{B,Ti2p} - E_{B,Hf4f})_{TiN/HZO_{interface}} \quad (4.8)$$

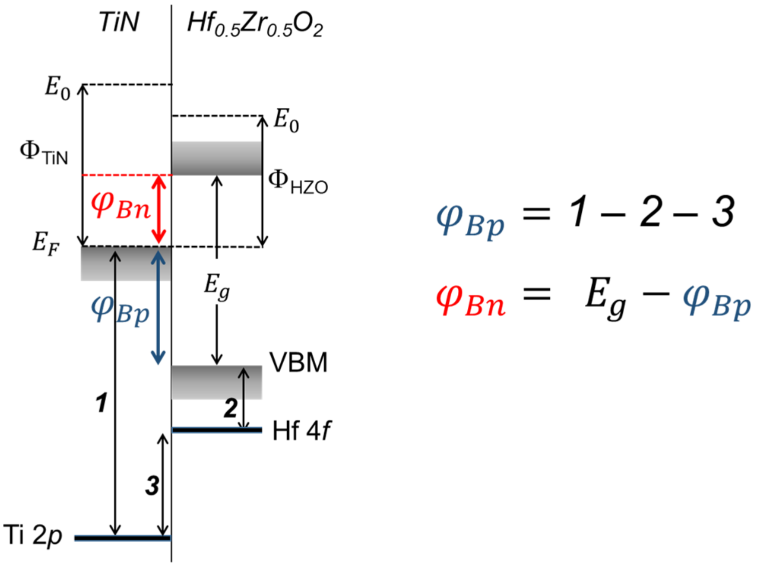

Figure 4.11: *Schematic of the determination methodology of φ_{Bn} using the Kraut method*[214]

Since the Ti 2*p* binding energy is referenced to the E_F, which is set to zero in the experiment, the φ_{Bp} can be calculated following:

$$\varphi_{Bp} = E_{B,Hf4fTiN/HZO_{interface}} - (E_{B,Hf4f} - VBM)_{HZO_{reference}} \tag{4.9}$$

The difference between the band gap energy (E_g) and φ_{Bp} allows then to obtain φ_{Bn}. For the VBM and work functions values (Φ), ultra-violet photoelectron spectroscopy (UPS) was used. Figure. 4.12a shows a typical UPS spectrum acquired from bare HZO after complete removal of the TiN TE using standard cleaning 1 followed by HF chemical etching treatments (see Appendix. A). This illustrates the relationship between the width of the spectrum and the work function value of the analyzed sample. Φ can be obtained via the following expression:

$$\Phi = h\nu + E_{cut-off} - E_F \tag{4.10}$$

Where $E_{cut-off}$ is due to inelastically scattered electrons which have just enough energy to reach the vacuum level E_0. The Fermi level at high kinetic energies represents, however, the most energetic electrons excited from a metallic sample reference. This was checked using a silver (Ag) reference sample shown in Fig. 4.12b. The measurements were performed at -7V in order to shift the entire spectra from HZO toward higher E_k values allowing thus the visualization of the cut-off edge by the analyzer.

The actual position of the inelastic cut-offs from bare HZO and 10nm thick TiN film were measured accordingly and using the energy corresponding to the half maximum of the intensity as shown in Fig. 4.13a and b, respectively. The energies were found to be 10.9 and 11 eV with HZO and TiN, respectively. These values correspond to 3.9 and 4 eV by substractiong the applied bias. Equation.4.10 is then used to determine the Φ values. We measured Φ_{HZO}=3.86 and Φ_{TiN}=3.96 eV. However, the obtained Φ value with TiN is much lower than the expected

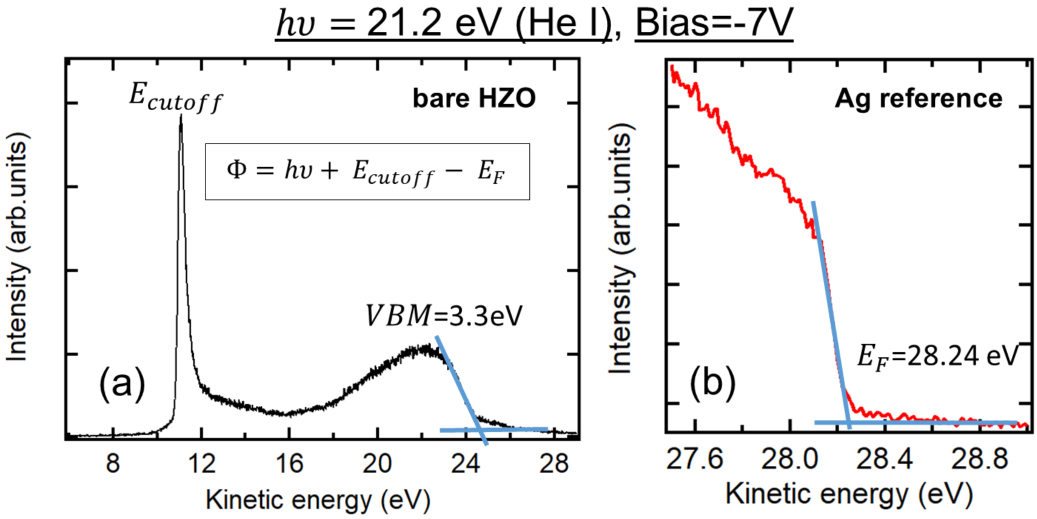

Figure 4.12: *(a) UPS spectrum recorded from bare HZO after the removal of the TE using SC1 + HF chemical etching and (b)* E_F *calibration using a silver reference sample using* $h\nu$*=21.2 eV (He I) and a bias of -7V for both*

value, which is usually reported to be around 4.6–4.7 eV[215]. These results point to the presence of an oxidized $TiO_{2-\delta}$ layer at the surface of the electrode formed due to contact with air as found with the Ti 2*p* XPS analysis.

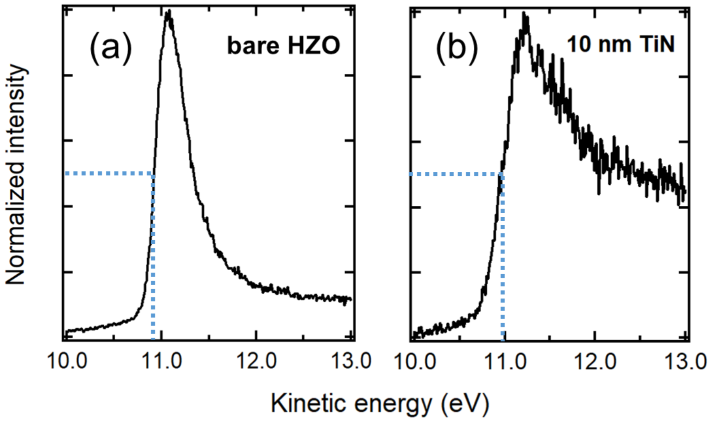

Figure 4.13: *Cut-off edges recorded from (a) bare HZO and (b) from TiN TE surface using* $h\nu$*=21.2 eV (He I) and a bias of -7V*

Similar investigation can be performed using PEEM (see Appendix.B.1 for further information on PEEM). In this case, the sample was illuminated with a Hg source ($h\nu$=4.9 eV), and a series of images are taken by varying the kinetic energy across the photoemission threshold, calibrated with respect to the Fermi level of the sample (E - E_F). This provides a set of images depicting the emission intensity I(x, y, E-E_F). Then, for each pixel I(x, y), the local work function (Φ) is calculated by an error function fit to the photoemission threshold leading edge. In this way, a 2D work function map is obtained over the field of view (FoV). For a FoV of 84.6 μm, Fig. 4.14a shows the obtained 2D Φ map from the as received 2nm TiN electrode. The corresponding histogram of the PEEM work function shows a narrow distribution and a peak value of 4.03 eV (Fig. 4.14c) which is close the value obtained with UPS. In Fig. 4.14b, the work function map was acquired after Ar$^+$ ion beam etching for 30 min (corresponding to the removal of 0.4 nm), followed by annealing at 400°C for 10 min. After this treatment, the Φ value is still uniform but increases to 4.86 eV (4.14d), much closer to the usual value for metallic TiN. The Ar$^+$ ion etch has therefore removed the top TiO$_{2-\delta}$ layer. In conclusion, the Φ values with HZO and TiN are 3.86 and 4.86 eV, respectively.

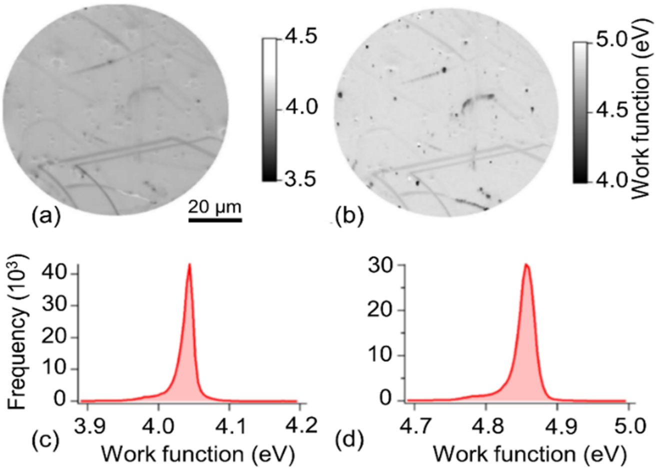

Figure 4.14: *(a) work function map of the TiN surface for a FoV = 84.6 μm, (b) work function map after Ar$^+$ sputtering for 30 min at 0.5 kV and heating at 400°C for 10 min to remove the top TiO$_{(2-\delta)}$ layer, and (c) and (d) histograms of the work function values corresponding to the maps (a) and (b), respectively*

The VBM was derived by linear extrapolation of the leading edge to the kinetic energy axis giving a value of 3.3 eV (Fig. 4.12a). From the bare HZO film, the energy separation between Hf 4$f_{7/2}$ emission and the VBM is 17.35 eV. Thus, from the energy positions extracted from the XPS, UPS and PEEM results, one can derive the electronic structure of the interface. The φ_{Bp} were found to be 3.55 and 3.77 eV for 600°C and 1000°C annealing temperatures, respectively. E_g was determined from the O 1*s* core level as the energy difference between the secondary electron background and E_B of the main peak centered at 531.8 eV (Fig.4.15a). The measured value of 5.6 eV value is in very good agreement with reported values using reflected electron energy loss spectroscopy (REELS)[208].

We calculated a schottky barrier height for electrons (φ_{Bn}) at the top interface in TiN/HZO/TiN capacitors as 2.05 and 1.83 eV for capacitors annealed at 600°C and 100°C, respectively. The results are in accordance with high oxygen vacancy at the interface with T$_{RTA}$=1000°C, which would reduce the potential energy for electron injection. Lomenzo *et al* found that the leakage current densities measured with Si:HfO$_2$ capacitors at annealing temperatures of 700°C, 800°C, and 900°C were 10^{-4}, 10^{-3}, and 10^{-2} (A.cm^{-2}), respectively. As a consequence, a decrease of endurance is observed[108]. The decrease of φ_{Bn} is qualitatively consistent with an increase of injected charges and higher leakage current. The degraded endurance observed with samples annealed at higher temperatures is therefore due to higher $V_{\ddot{O}}$ concentration present in the pristine state which in turn lower φ_{Bn} and induce high conduction paths resulting in an earlier dielectric breakdown.

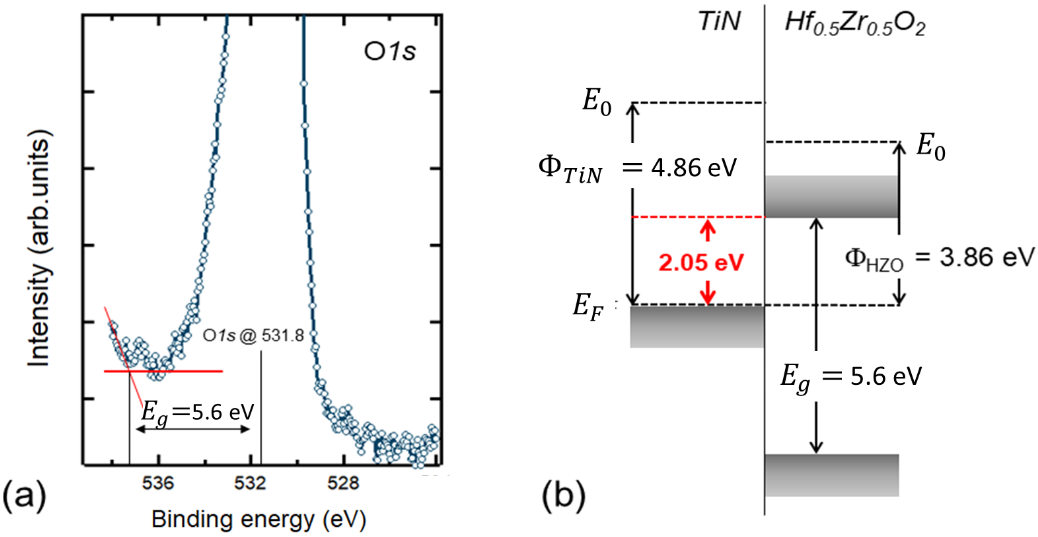

Figure 4.15: *(a) O 1s XPS spectrum used to extract the band gap energy and (b) schematic diagram of the band offset at the TiN/HZO top interface with T_{RTA}=600°C*

4.3 W/$Hf_{0.5}Zr_{0.5}O_2$ interface

4.3.1 Electrical characterization

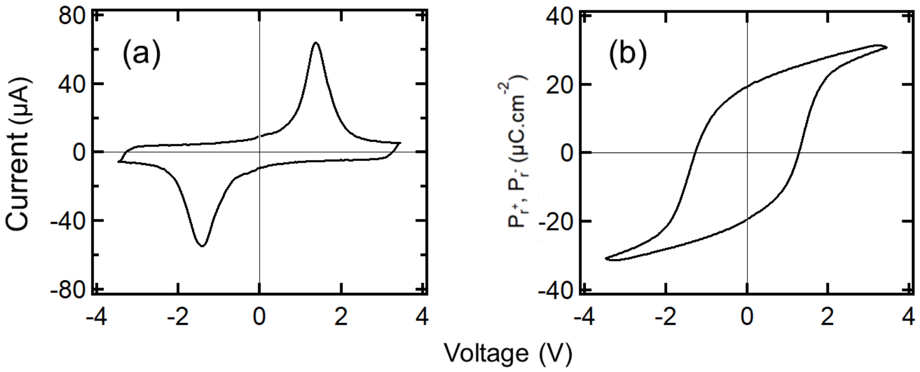

Figure 4.16: *(a) Switching current vs voltage (I-V) and (b) polarization vs voltage (P-V) recorded using DHM (±3V/1kHz) from a pristine W/HZO/W capacitor*

Figure.4.16 shows the I-V and P-V electrical response from W/HZO/W pristine capacitors. Interestingly, the current curve do not show the splitting behavior observed with TiN electrodes. In addition, the hysteresis loop is symmetric with an equal value for the positive and negative coercie voltages giving a mean E_C value of 1.1 MV.cm^{-1}. It appears therefore that W may indeed induce a different interfacial chemical and electronic properties compared to TiN which may explain the observed optimization of the pristine ferroelectric response. By investigating TiN/HZO/TiN and W/HZO/W capacitors, Keshir *et al* reported similar behavior, i.e tungsten electrodes highly decreases the domain pinning for as-grown capacitors and the hysteresis loop is fully depinched[99].

4.3.2 XPS analysis

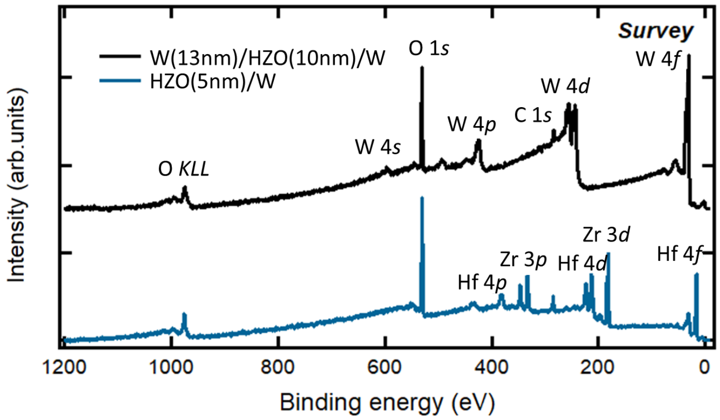

Figure 4.17: *Survey spectra from the as received W(13nm)/HZO(10nm/W capacitor and the HZO(10nm)/W samples*

Figure. 4.17 shows the survey spectra recorded from the as received W/HZO/W capacitor and from a bare HZO with W bottom electrode. These samples are used to investigate separately the top and bottom interfaces (see Appendix. A for further information). The HZO elements from the capacitor structure (black curve in Fig. 4.17) are actually highly attenuated through the 13nm top electrode. Only the W core level photoelectrons are reachable by the detector. The sample was thus subjected to a total sputtering time of 5 hours to reveal the top interface chemistry with better statistics. With an etch rate of 2.2±0.5 nm.hr^{-1}, calibrated separately on similar sample, this corresponds to a total 11 nm tungsten etching.

Interface chemistry of the top electrode material

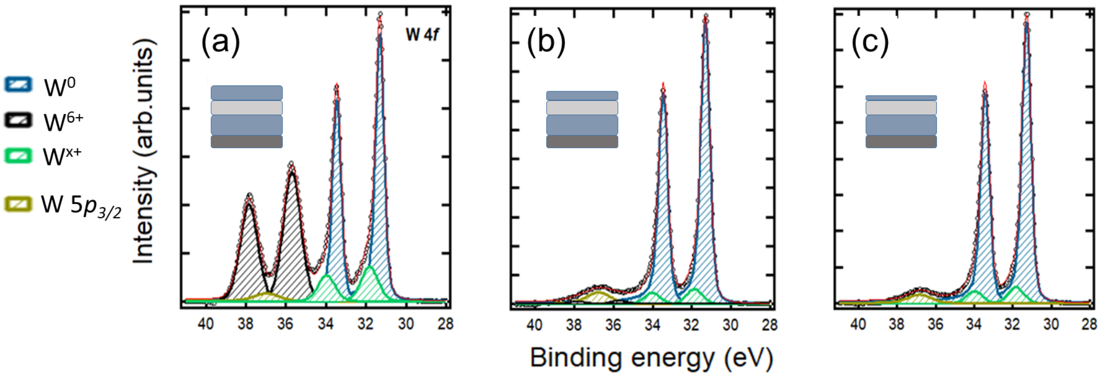

Figure 4.18: *(a) W 4f core level spectra from the as received capacitor (b) after 1hr and (c) after 5hrs sputtering at* E_{Ar^+}*=500eV*

Figure. 4.18 compares the W 4*f* spectra recorded as a function of the sputtering time. First, Fig. 4.18a shows the XPS spectrum recorded from the as received capacitor (before sputtering). The spectrum was fitted into three peak doublets with a spin–orbit splitting $E_{5/2\text{-}7/2}$= 2.1±0.1 eV. The first doublet situated at $E_{B,7/2}$=31.3 eV is attributed to pure metallic tungsten (W^0)[206]. DS line shape with α=0.05 and FWHM of 0.55 eV were used. The two additional components, one at E_B = 31.8 eV points to the formation of a tungsten sub-oxide phase (WO_x), and the second, at 35.7 eV, corresponds to a W^{6+} chemical state in a WO_3 environment[216, 217]. The oxide peaks were modeled using GL(30) lines with a FWHM of 1 eV. The component situated at E_B=37 eV (in yellow color) is attributed to W 5$p_{3/2}$. Figure. 4.18b and c show the evolution of the W 4*f* spectra after 1 and 5 hrs sputtering. This corresponds to an etched thickness of 2.2 and 11 nm, respectively. First, the W^{6+} peak area dropped to almost zero after just 1hr of sputtering. This confirms that the WO_3 phase is at the surface of the electrode similarly to the $TiO_{2-\delta}$ observed with TiN, most probably due to contact with air. The etching has therefore removed this surface layer or reduced it to W^{x+} state. The W 4$f_{7/2}$ peak of W^{x+} is related to the shape of the curve in the range between 31.6 eV and 32.2 eV. It should be an intermediate state between W^{4+} and W^0 (W^{3+}, W^{2+} or W^{1+}) oxidation states[216, 218]. When fitting this range with the same asymmetric parameters of the pure metallic W, the W^{x+} peak centered at 31.8 eV is still present after 5hrs sputtring.

Figure. 4.19 shows the W 4*d* core level spectrum recorded through the remaining top electrode after 5hrs sputtering. In order to analyze the interface chemistry, we use the W 4*d*. This is due to the fact that when analyzing samples without a top electrode to investigate the bottom interface, there will be a superposition between Zr 4*p* (E_B $\sim$ 30 eV) and W 4*f* lines. The analyses of W 4*f* core level spectra were used to exactly assign the tungsten components at the interface and to fit the W 4*d* spectrum accordingly. The spectrum can thus be fitted, similarly to the W 4*f*, into two spin-orbit doublets with a metallic (W^0) contribution at $E_{B3/2}$=255.5 eV and W^{x+} ions in WO_x environment at $E_{B3/2}$=259.8 eV[218, 206]. The WO_x area percentage is $\sim$ 1%, i.e close to the XPS sensitivity limit. With respect to the 2 nm thick remaining TE, this fraction of ångström suggests a very clean and sharp interface between HZO and the top electrode. Whereas with TiN top electrode, we measured $\sim$1 nm oxynitride interfacial layer. This may be explained by the Gibbs free energy which is lower for titanium oxide formation (ΔG_{WO_x}) $\sim$ -500kJ/mol and $\Delta G_{TiO_x \sim}$ -750kJ/mol). When annealing, oxygen scavenging by the TiN electrode is, therefore, energetically more favorable.

Interface chemistry of the bottom electrode material

To check the effect of the annealing treatment and the oxidation degree of the bottom electrode on the interfacial defect chemistry, three HZO/W samples without a top electrode are prepared. The first one was annealed in N_2 atmosphere at 600°C for 20s, a second one witout annealing and a third one subjected to 2 min oxygen plasma exposure before the ferroelectric film deposition. Figure. 4.20a-c show, respectively, the corresponding W 4$d_{3/2}$ XPS spectra. Relative to the top electrode spectrum, the results indicate an additional component at higher binding energy (264.5 eV) corresponding to W^{6+} contribution and an overall higher oxidation than the top electrode. Table. 4.5 summarizes the fitted results of the top and bottom interfaces.

First, the bottom electrode presents, in all cases, higher oxidation at the interface than the top electrode. We can see that the metallic contribution decreased from 99 (top interface) to 5% (bottom interface with annealing). Similar observation was reported by Keshir *et al*[99]. Comparing the oxides contribution from

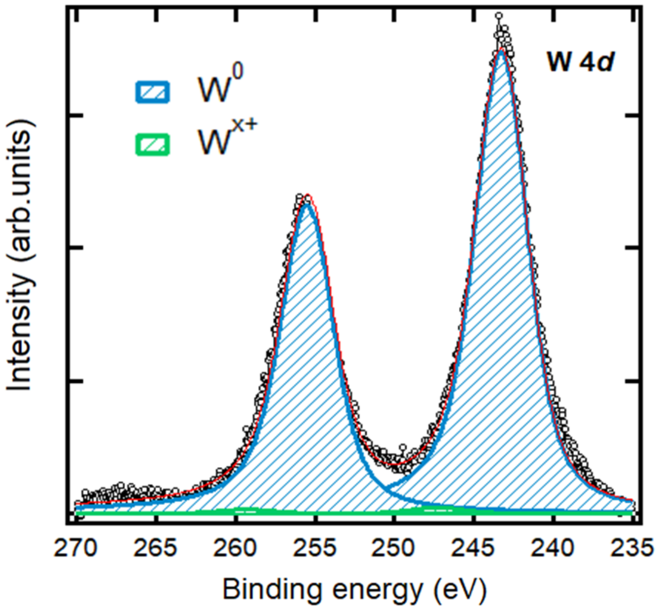

Figure 4.19: *W 4d core level spectrum recorded after 5hr Ar$^+$ sputtering at normal emission*

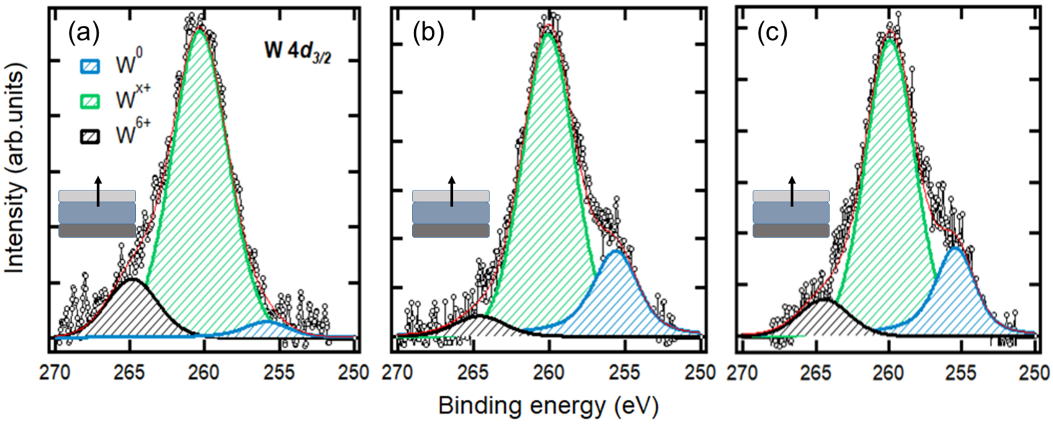

Figure 4.20: *W 4$d_{3/2}$ core level spectra recorded from bare HZO films in contact with a bottom W electrode (a) annealed at 600°C (b) w/o annealing and (c) w/o annealing but subjected to 2min oxygen plasma exposure*

HZO/W samples with and without annealing shows an increased contribution of the oxides with the annealed sample. The annealing has therefore significantly increased the oxidation of the electrode at the interface. The sample with 2 min oxygen plasma exposure showed, however, a very slight increase of the oxides components relative to the one without annealing. The IMFP of W 4$d_{3/2}$ through HZO is ~2.5 nm. Giving the 5nm HZO thickness, the analyzed thickness of the bottom electrodes at normal emission is ~2.5 nm. The annealed sample shows therefore that almost 95% of the tungsten analyzed bottom electrode area is in oxides environment (WO$_x$ and WO$_3$). This fully oxidized 2.5 nm layer is in contrast to the almost perfectly sharp metal/ferroelectric top interface. In order to get more insights on the implications of different oxidation degree of the electrodes, the oxygen vacancy concentration was evaluated using the Hf 4*f* core level spectra.

Table 4.5: *W $4d_{3/2}$ fitting results (components area in %)*

Component	W/HZO/W	HZO/W (annealed)	HZO/W (w/o anneal)	HZO/W (with 2min O_2 exposure)
W^0	99	5.1	26	24.2
W^{x+}	1	80.9	69.5	67.4
W^{6+}	-	14	4.5	8.4

Oxygen vacancy concentration

Figure. 4.21 shows the fitted Hf $4f$ spectra from the discussed W/HZO/W and HZO/W samples. The peaks were modeled with GL30 line shapes with a fixed FWHM at 1.05 eV and an energy separation between the two oxidation states (Hf^{4+} and Hf^{3+}) of 0.8eV, i.e the same parameters used for the TiN/HZO analyzes. The fitting results are presented in Tab. 4.6 along with the results obtained from the TiN/HZO interface.

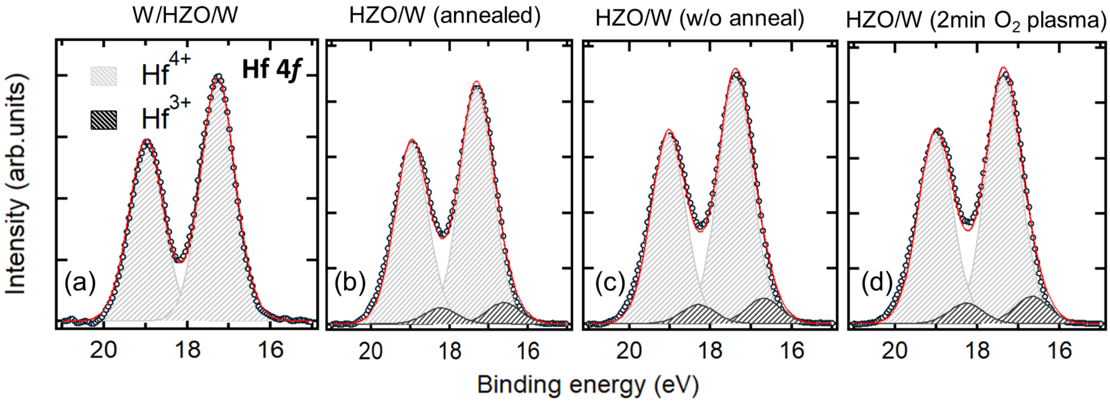

Figure 4.21: *Hf 4f core level spectra recorded from the capacitor after 5hrs sputtering, (b) from bare HZO film in contact with a bottom W electrode annealed at 600°C (c) HZO/W without annealing and (d) HZO/W without annealing but the electrode was subjected to 2min oxygen plasma exposure before HZO deposition*

Table 4.6: *Hf 4f fitting results and the derived oxygen deficiency concentration at the top interface in TiN/HZO/TiN and W/HZO/W capacitors and at the bottom interface using the discussed HZO/W samples*

	$\frac{I(Hf^{3+})}{I(Hf^{4+})+I(Hf^{3+})}$	$\sim V_O^{\cdot\cdot}$ (%)	$\sim V_O^{\cdot\cdot}(cm^{-3})$
MFM (TiN)	5.68 ± 0.5	0.71	3.1×10^{20}
MFM (W)	-	-	-
HZO/W (annealed)	8.3 ± 0.6	1.02	4.5×10^{20}
HZO/W (w/o anneal)	9.3 ± 0.6	1.16	5.1×10^{20}
HZO/W (with 2min O_2 exposure)	9.9 ± 0.6	1.25	5.4×10^{20}

First, the results from the W/HZO/W capacitor reveal that the V_O concentration at the top interface is under the detection limit. This is in agreement with the absence of oxygen scavenging with the W top electrode. However, a higher V_O concentration is present near the bottom interfaces. This may explain the higher oxidation observed with the bottom electrode with respect to the top W electrode. In this case, the higher V_O concentration is the result of oxygen scavenging mainly by the bottom electrode when annealing. However, oxygen scavenging by W should be energetically unfavorable in adjacent to HfO_2, as observed with the top electrode. Indeed, the samples which did not underwent any annealing show a similar and even higher V_O concentration with respect to the annealed one. The oxygen deficiency might therefore stem from the first steps of the ALD process. The oxygen supply oxidizes the electrode material at the interface at the beginning of the HZO deposition, leading to the strong oxidation of the bottom electrode material and an oxygen deficient layer at the bottom interface. When annealing, the V_O may redistribute which can explain the slightly lower V_O density with respect to the non-annealed samples. With TiN electrodes, we suggest the same scenario. However, giving, the higher oxygen affinity with Ti, the oxygen scavenging by the top electrode leads to higher V_O at the top interface with respect to the genarated vacancy at the bottom interface during the first ALD steps. The leakage current from pristine W/HZO/W capacitor shown in Fig. 4.22 indicates that leakage is higher at positive voltages applied to the top electrode (bottom electrode injection). This is also consistent with higher V_O amount near the bottom interface which would decrease the SBH for electrons with respect to the top interface. However, further investigations are needed to get more insights on the origin of the observed oxygen deficiency at the bottom interface.

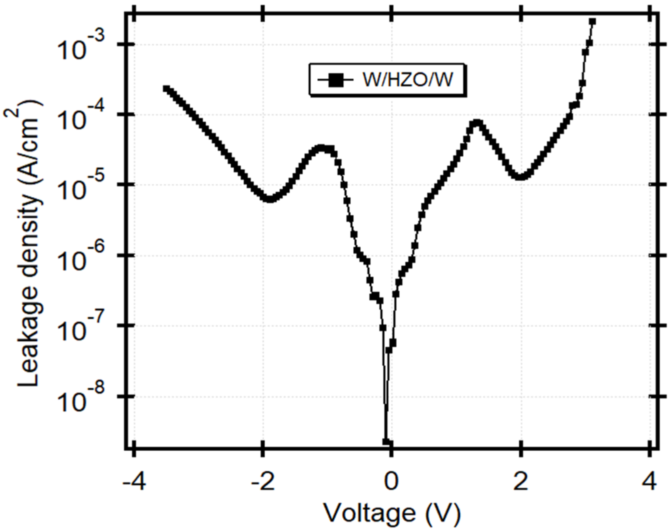

Figure 4.22: *DC Leakage current through pristine W/HZO/W capacitor*

Finally, we have further measured the φ_{Bn} at the W/HZO top interface using the same methodology adopted with TiN. Taking the same band gap energy of 5.6eV, an energy separation between the Hf 4f emission and the VBM from bare films to be 17.35 eV, we calculated a value of 2.3eV. Taking a work function value of W from literature (Φ_W=4.60 eV), the band diagram at the top W/HZO is presented in Fig. 4.23. With respect to the TiN/HZO interface, the decrease of V_O concentration has therefore increased the SBH by almost 300 meV. By investigating TiN, W and Pt electrodes, it was reported that a W/HZO/Pt stack (with Pt being the bottom electrode) showed the best results in term of memory window and wake-up. The optimization was reported to be mainly linked to the suppression of oxygen scavenging by the TiN top and W bottom electrodes[99].

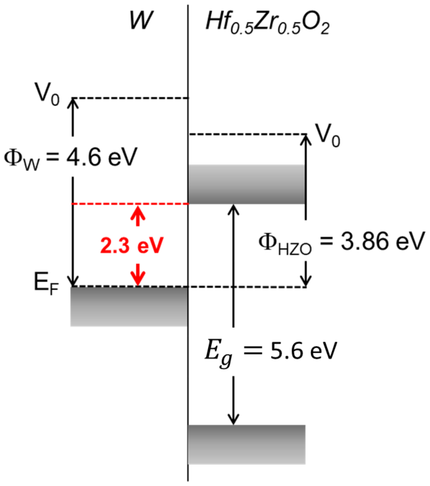

Figure 4.23: *Band alignement at the top interface in W/HZO/W capacitors*

4.4 Conclusions

In conclusion, ferroelectric $\mathrm{Hf}_{0.5}\mathrm{Zr}_{0.5}\mathrm{0}_{0.5}$ thin films with TiN electrodes showed an asymmetric ferroelectric characteristics at the pristine state due to the existence of an imprint field. Electric field cycling increased the remanent polarization and reduced the magnitude of the imprint. The chemical behavior of the top TiN/HZO interface was analyzed using XPS. The results revealed the presence of $\sim$1 nm thick oxynitride interfacial layer and an accumulation of reduced Hf caused by oxygen scavenging by the top electrode. The oxygen vacancy concentration reaches 0.71% at the first nm of the HZO layer and decreases sharply going to the bottom interface. Electron trapping by V_O is higher at the top interface, causing an imprint proposed to be the origin of the wake-up behavior. The effect of the annealing temperature was also studied. A decrease of the Schottky barrier height for electrons was observed from 2.05 to 1.83 eV when increasing the annealing temperature from 600°C to 1000°C, due to the generation of additional V_O at the top interface.

With W electrodes, the top interface chemistry revealed a cleaner and sharper interface. This is due to the higher Gibbs free energy of tungsten oxide formation, preventing thus oxygen scavenging and the formation of an interface layer. This results in significantly lower oxygen vacancy concentration at the top interface relative to the TiN electrode. Consequently, the SBH increased from 2.05 to 2.3 eV and the pristine hysteresis loop shows no evidence for imprint. The analysis of the bottom W electrodes revealed, however, a higher electrode oxidation and higher V_O concentrations. The difference may stem from the effect of the first ALD deposition steps, oxidizing the bottom electrode and leaving an oxygen-deficient film near the interface.

Chapter 5

Effect of La doping and field cycling in La doped Hf$_{0.5}$Zr$_{0.5}$O$_2$

5.1 Introduction

As already mentioned in section. 2.3.2, doping with La has proven to be an excellent tool to optimize the ferroelectric response in HfO$_2$ and HZO thin films. However, despite a higher endurance, La:HZO (HZLO) shows a significant wake-up behavior with respect to the undoped case as shown in Fig. 5.1. With 3 MV.cm^{-1} cycling field, undoped HZO shows a breakdown after 10^7 cycles while 2.3 mol% La doped films still operational after 10^9 cycles with a negligible fatigue behavior. On the other side, the pristine memory window (MW) drops from 29 to 15 μC.cm^{-2} when adding La. 5$\times$10^6 cycles are needed for HZLO to reach its optimal MW of 36 μC.cm^{-2}.

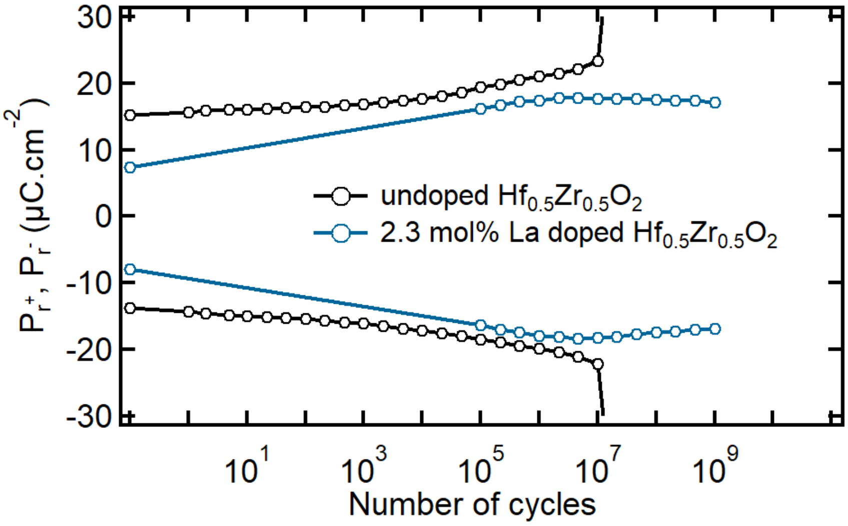

Figure 5.1: *Endurance plot showing the evolution of the MW as a function of field cycling in TiN/undoped Hf$_{0.5}$Zr$_{0.5}$O$_2$/TiN and TiN/2.3 mol% La doped Hf$_{0.5}$Zr$_{0.5}$O$_2$/TiN capacitors using cycling pulses of* $\pm 3V/100kHz$

Mehmood *et al*[115] investigated the effect of varying La content on the structural and ferroelectric properties. La was found to reinforce the nonpolar t-phase resulting in increased E_{dep} within the bulk of the film. This was reported to explain the higher wake-up cycles. The improvements in endurance have been, however, assigned to the decrease of leakage current when increasing La. The authors also showed that the optimal ferroelectric response (in term of P_r, endurance, imprint and retention loss) was obtained with 2.3 mol% La.

In this chapter, we combine XPS, HAXPES and electrical measurements to investigate the chemical and electronic implications of La doping and the origin of the enhanced wake-up behavior in TiN/HZLO/TiN capacitors. The chapter is thus divided into 3 parts. The first part is devoted to elucidate the intrinsic chemical and electronic modifications induced by varying La content in pristine bare HZO thin films. 0, 2.2, 3.4 and 5.8 mol% La concentrations were used and analyzed using laboratory XPS and leakage current measurements. In the second part, HAXPES was used to obtain a better insight on the interface physical chemistry by using realistic top electrode thickness, exploiting thus the advantages of hard X-rays to probe more deeply buried interfaces. In addition, a specific sample design was used for a separate top and bottom interface analysis. The same synchrotron compaign was also exploited to further check the effects of La doping and annealing temperatures. Two La content of 1.7 and 2.7 mol% and two RTA temperatures of 600 and 800°C were used. Finally, the last part is dedicated to the effects of cycling and polarization reversal investigated using HAXPES with *in-situ* bias. An original device gemotry was made using standard micro-fabrication tools in order to match with all the technical requirements of such experiment. All the analyzed samples are provided by NamLab and are desribed in Appendix. A.

5.2 Chemical and electronic implications of La doping in $Hf_{0.5}Zr_{0.5}O_2$

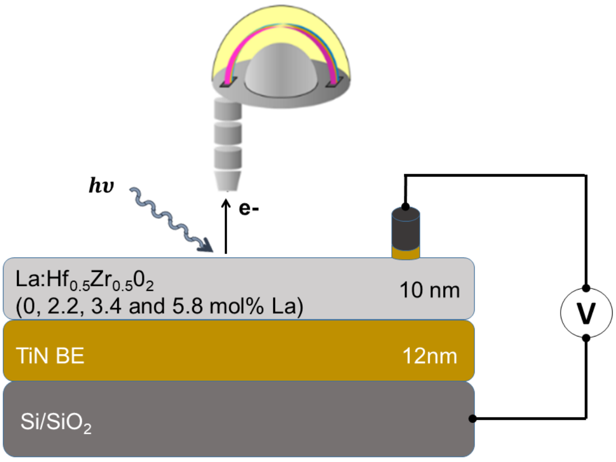

Figure 5.2: *Schematic of the samples designed for XPS and leakage measurements to evaluate the effects of 0, 2.2, 3.4 and 5.8 mol% La in 10nm ALD-grown $Hf_{0.5}Zr_{0.5}O_2$ films*

5.2.1 XPS analysis

The survey spectra recorded from the different samples are shown in Fig. 5.3a. All the expected core levels are present at binding energies in agreement with reported values[206]. The spectra are almost identical for all dopants apart from the specific dopant core level lines as shown by the La 4$p_{3/2}$ in Fig. 5.3b. The intensity increases with doping, confirming the nominal differences between the samples. The line shapes, however, do not change with doping.

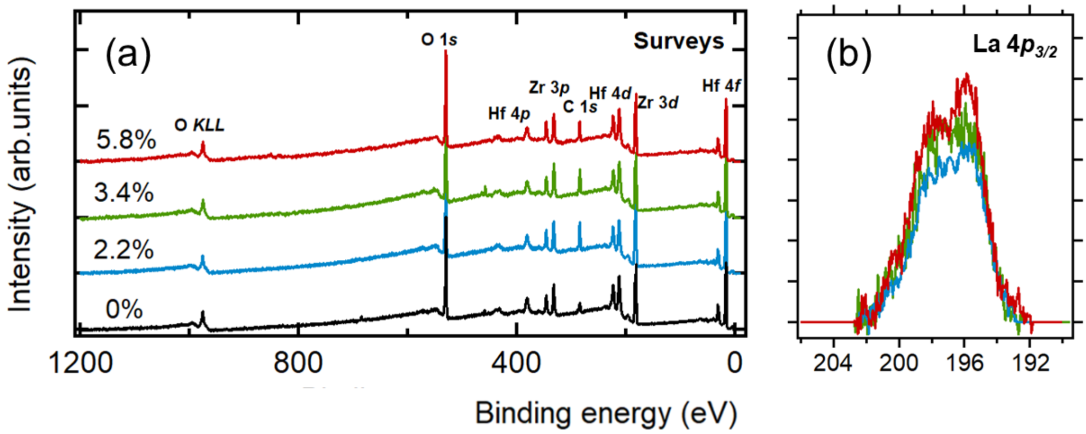

Figure 5.3: *(a) Surveys recorded from the different samples and (b) the corresponding La 4*$p_{3/2}$ *spectra*

Core level shift

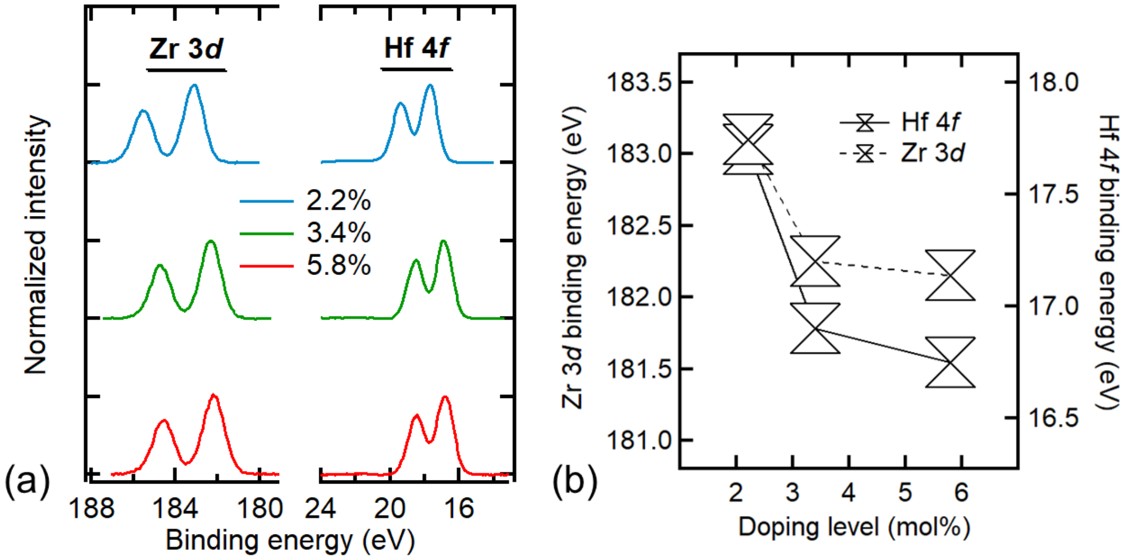

Figure 5.4: *(a) Hf 4f and Zr 3d core level spectra recorded from 2.2, 3.4 and 5.8 mol% La doped HZO films (b) La doping induced core level shifts of Hf 4*$f_{7/2}$ *and Zr 3*$d_{5/2}$

By calibrating the binding energy with respect to the C 1*s* emission at 285 eV, shifts in the Hf 4*f* and Zr 3*d* core levels are, however, detected when increasing La. This is shown in Fig. 5.4a. The lines shift toward lower E_B values with higher La. Table.5.1 gives the relative binding energies shifts with respect to the 2.2mol% La.

Table 5.1: *Hf 4f$_{7/2}$ and Zr 3d$_{5/2}$ lines shifts as a function of La doping*

	Δ BE$_{Hf4f}$	Δ BE$_{Zr3d}$	$\Delta\varphi_{Bn}$
2.2%	0.00	0.00	0.00
3.4%	0.80	0.75	0.80
5.8%	0.95	0.85	0.95

The shifts are consistent with a rigid band shift characteristic of doping, also observable in Zr 3*p* and Hf 4*d* spectra (not shown). The small shift difference between the two core levels (shown in Tab. 5.1) may be related to different dynamic charges of the cations[27]. The upward band bending is characteristic of an acceptor doping and the bending reaches a maximum of 0.95 eV for 5.8mol% La with respect to 2.2%. This imply a shift of E_F to a mid-position relative to the n-type undoped HZO position as shown in chapter. 4, resulting in an increase of φ_{Bn} (Tab.5.1). La cations have one valence electron less than Hf. Hence, they can be mainly found in the charge state of -1 while occupying a Hf site. They would therefore not agglomerate due to the repulsive force. They can however screen positively charged oxygen vacancies, $V_O^{\cdot\cdot}$ (mutual screening). Several DFT calculations have indeed shown that ionically compensated defect (2La$_{Hf}$)V_O), where two La atoms screen one $V_O^{\cdot\cdot}$ following this equation: La$_2$O$_3$ $\rightarrow$ 2La$'_{Hf}$+ 3O$_O$ + $V_O^{\cdot\cdot}$, are energetically favorable in hafnia thin films with La impurities[219, 220]. However, one would wonder if these vacancies are already present in the film or are new generated ones due to the negative charge incorporation. The downward shifting of E_F suggest that these vacancies are already present in the film and screened by La.

Oxygen vacancies

To further investigate the effects of La doping, the V_O concentration was evaluated using hafnium reduction signature in Hf 4*f* spectra. Two different emission angles of 0° and 60° corresponding, respectively, to probing depths of 7.5±0.4 and 3.75±0.2 nm were used. Figure. 5.5 shows the fitted Hf 4*f* spectra using the same parameters adopted in chapter. 4. The spectra show two components; the main one at high E_B (grey color) assigned to Hf^{4+} in stoichiometric HZO and a low E_B component, shifted by 0.8 eV with respect to the main peak corresponding to Hf^{3+}. Fitting procedure was performed using GL(30) line shapes and by constraining FWHM at 1.05eV . Table. 5.2 summarizes the obtained Hf^{3+}/(Hf^{3+} + Hf^{4+}) intensity ratios (n) and the corresponding V_O concentration (derived as n/8) in percentage and volume density.

Table 5.2: *Hf 4f$_{7/2}$ and Zr 3d$_{5/2}$ lines shifts as a function of La doping*

	$\vartheta = 0°$			$\vartheta = 60°$		
	$\frac{I(Hf^{3+})}{I(tot)}$	$\sim V_O$(%)	$\sim V_O$(cm^{-3})	$\frac{I(Hf^{3+})}{I(tot)}$	$\sim V_O$(%)	$\sim V_O$(cm^{-3})
0%	5.5 ± 0.4	0.69	3×10^{20}	5.8 ± 0.4	0.72	3.2×10^{20}
2.2%	4.2 ± 0.4	0.52	2.3×10^{20}	6 ± 0.7	0.75	3.3×10^{20}
3.4%	1 ± 0.4	0.125	5×10^{19}	8.1 ± 0.5	1.02	4.5×10^{20}
5.8%	-	-	-	11.5 ± 0.5	1.44	6.3×10^{20}

The trends are opposite when varying the probing depth. The results suggest an increase of V_O with doping near the surface region and a lowering when analyzes are deeper in the film. The band bending as already suggested is due to a compensation of V_O. This would reduce charge trapping for instance but doesn't involve a lowering of the trap concenrtation. The V_O decrease in the bulk can therefore be related to the extra oxygen atoms supplied by La_2O_3 layers during the growth. A higher number of La_2O_3 layers is needed to achieve the desired doping level which may explain the decrease of V_O. On the other hand, the increase of V_O at the surface also seems to follow the increase of La suggesting the generation of new vacancies to screen the additionnal negative La impurities. In addition, at the surface, E_B shift toward higher energies with increasing La suggesting rather an n-type doping (Fig. 5.5e-h). We suggest therefore that the effect of La on V_O depends on the initial defective state of the film and the chemical environment of the added La within the stack. In addition, the oxidant character nature of SC1 used to remove the TEs may be behind a reduction of the V_O amount at the surface. Thus, La in this case will act as a source of new V_O generation and the resulting doping is n-type. In the bulk, La will just screen the existing V_O and the extra oxygen atoms provided by the La_2O_3 layers allow the decrease of the overall defect concentration.

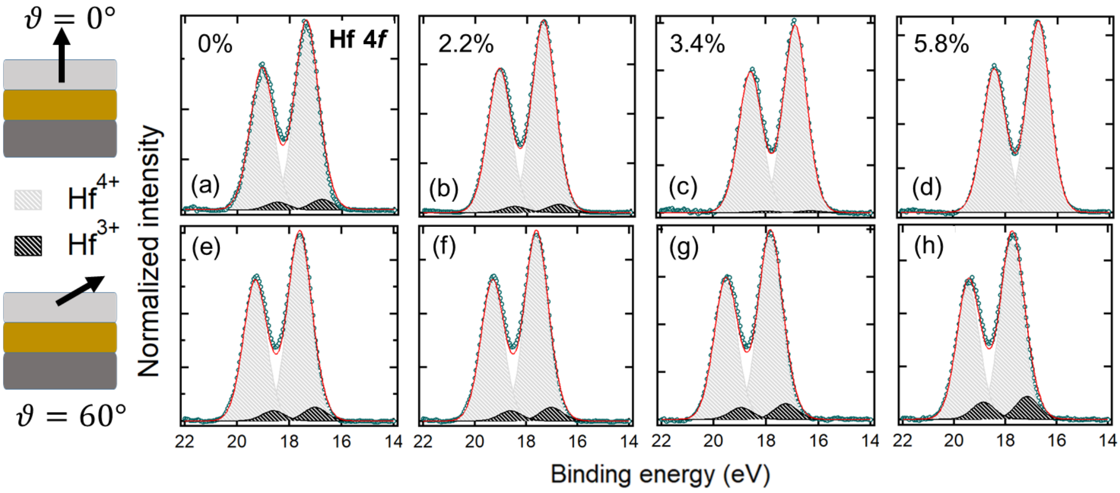

Figure 5.5: *Best fit to the Hf 4f spectra (a,b,c,d) at $\vartheta = 0°$ and (e,f,g,h) at $\vartheta = 60°$ from 0, 2.2, 3.4 and 5.8mol% La doped $Hf_{0.5}Zr_{0.5}O_2$ bare films, respectively*

According to the methodology used by Sunding *et al*[221], the La 4$p_{3/2}$ spectra can be used to evaluate the chemical environment of La across the film thickness. Figure. 5.6 shows the recorded spectra from the highest La film (5.8mol%) at 0 and 60° emission angles. La has an empty 4*f* orbital but charge transfer from coordinated ligands can occur resulting in an electron occupancy. They can therefore be fitted into three peaks: A main peak corresponding to the final state without charge transfer (presence of a core hole ($4f^0$) and two satellite peaks corresponding to the final state with charge transfer ($4f^1$). These contributions to the spectra, called shake-up satellites, are attributed to the process in which the electron density shifts from filled O 2*p* (of a given ligand) to empty La 4*f* levels. This results in two stallite peaks to account for the bonding ($4f^1$ bonding) and antibonding ($4f^1$ antibonding) hybridization. Interestingly, the energy splitting between these contributions and the main peak reflect the hybridization strength and can be used to evaluate the nature of the ligand [221, 222]. GL(40) and FWHM of 2.9eV were used to model the three contributions while the area of the two satellite peaks was held equal. In order to obtain the best fits to the experimental spectra (minimizing the residual standard deviation), the energy splitting was varied and the best conditions used in Fig. 5.6 are given in Tab. 5.3.

Table 5.3: *La 4p$_{3/2}$ fitting results*

	$\vartheta = 0°$			$\vartheta = 60°$		
	BE(eV)	FWHM (eV)	Area	BE(eV)	FWHM (eV)	Area
4f^0	196.4	2.9	272	196.2	2.9	71
4f^1 antibonding	197.9	-	117	198.7	-	22
4f^1 bonding	200.5	-	117	200.1	-	22

The energy splitting of 1.5 and 4.1 eV from 4f^1 antibonding and 4f^1 bonding with respect to the main peak obtained at 0° are characteristic of La$_2$O$_3$ environment. However, these energy splitting values do no allow the best fit of the data recorded at 60°. In this case, 2.5 and 3.9eV were used, respectively. According to Sunding *et al*[221], this would correspond better to La(OH)$_3$ environment. The results confirm therefore a different environment for La within the HZO depth which may explain the different implications of La on the V_O concentrations within the film.

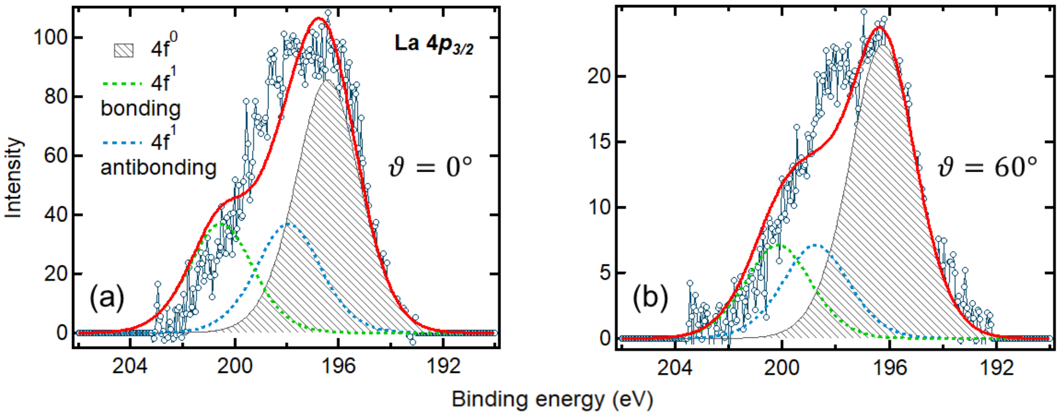

Figure 5.6: *La 4p$_{3/2}$ spectra recorded from 5.8mol% La doped HZO films at 0° and 60° emission angles*

5.2.2 Leakage current measurements

Figure. 5.7 shows the leakage current density (J) from the undoped, 2.2 and 5.8mol% La samples for a bias range of ±3V applied to the TEs. A decrease of J when increasing La can be noticed as observed by Mehmood *et al*[115]. Table. 5.4 gives the measured values at ±1 and ±2V.

As already stressed in chapter. 2, the Poole-Frenkel mechanism is capable of providing qualitatively adequate description to the experimental data and allows the extraction of the trap energy level governing the charge transport. Leakage

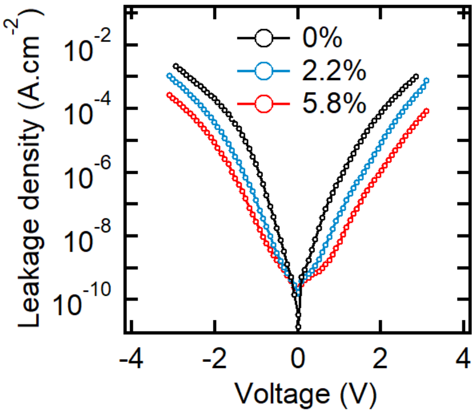

Figure 5.7: *Leakage current density of undoped, 2.2 and 5.8 mol% La doped HZO-based capacitors*

Table 5.4: *Leakage current density (J) values at ±1 and ±2V applied to TEs from 0, 2.2 and 5.8mol% La doped HZO capacitors*

	1V	2V	-1V	-2V
0%	6.1×10^{-7}	7.8×10^{-5}	1.8×10^{-6}	2.1×10^{-4}
2.2%	5.1×10^{-8}	8.6×10^{-6}	1.4×10^{-7}	3.7×10^{-5}
5.8%	6.7×10^{-9}	1.2×10^{-6}	2.9×10^{-8}	8.6×10^{-6}

measurements were further performed within a temperature range of 25°C to 125°C. These measurements were done by NamLab. The $JvsE$ and the characteristic PF plot $ln(J/E)$vs$E^{1/2}$ are shown in Fig. 5.8 (see section. 2.5.3 for the PF equation).

According to Fig. 5.8d, e and f, the curves show a linear relationship to the PF characteristic plot. The slope (S_{PF}) and intercept (y_0) values obtained from the linear fits are summarized in Tab. 5.5. S_{PF} can be expressed using the following equation:

$$S_{PF} = \frac{e^{3/2}}{k_B T\sqrt{\pi\epsilon_r\epsilon_{opt}\epsilon_0}} \tag{5.1}$$

Table 5.5: *Results from the leakage densities fitted with the Poole-Frenkel mechanism*

	La mol%					
	5.8%		2.2%		0%	
T(°C)	S_{PF}	y_0	S_{PF}	y_0	S_{PF}	y_0
25	11.02	-29.9	10.75	-28.6	10.43	-26.6
50	10.52	-28.6	10.65	-27.9	10.02	-23.5
75	10.28	-27.8	10.32	-27.1	9.37	-22.1
100	10.51	-27.9	10.18	-26.5	9.87	-21.0
125	11.92	-29.6	11.31	-28.2	9.65	-23.2

Using ϵ_r=33[223] in Eq. 5.1 and the measured S_{PF} in Tab. 5.5, the obtained optical permitivitty ϵ_{opt} value from the different samples is in the range of 4 - 6,

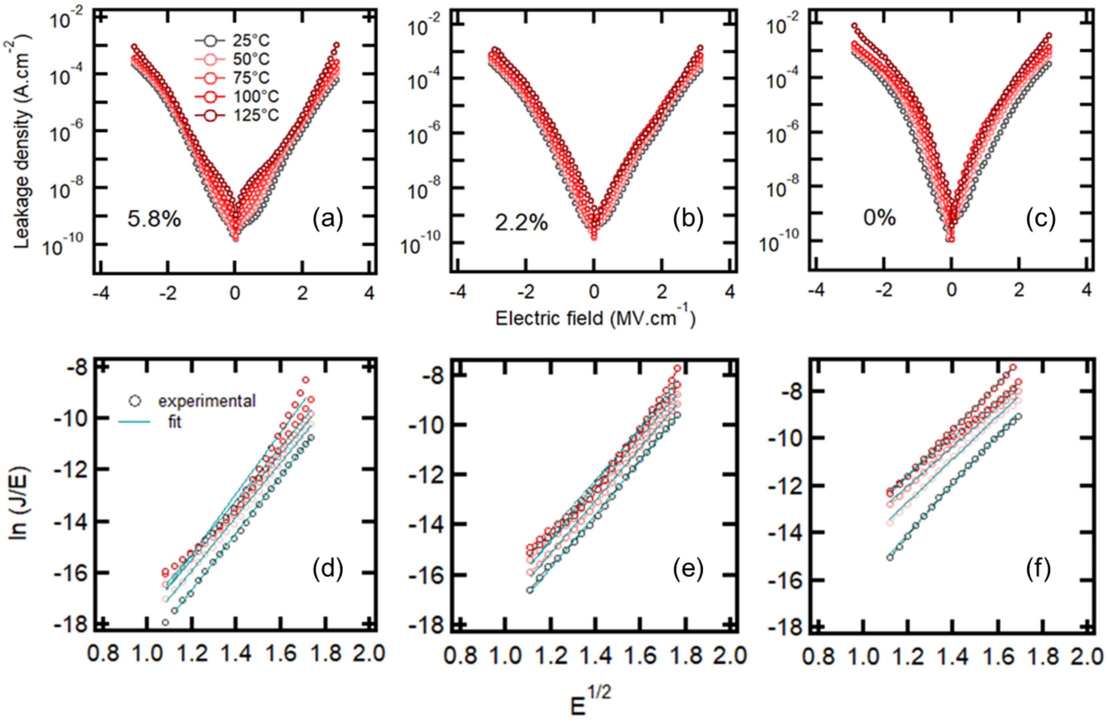

Figure 5.8: *The $JvsE$ and $ln(J/E)$vs$E^{1/2}$ curves for 0, 2.2 and 5.8 mol% La doped HZO capacitors at temperatures ranging from 25 to 125°C*

which corresponds to the refractive index of 2 - 2.5 ($\epsilon_{opt} \sim n^2$, where n is the refractive index of the material) reported for HfO_2 and ZrO_2[224]. This therefore confirm the validity of the use of the PF model to extract the trap energies[165]. The trap energy level (E_T) in the discussed samples were extracted using the Arrhenius plots shown in Fig. 5.9. E_T is thus determined using the slopes of the Arrhenius plots (S'_{PF}) as shown in the following expression:

$$E_T = 1000 \times \frac{S'_{PF} k_B}{e} \tag{5.2}$$

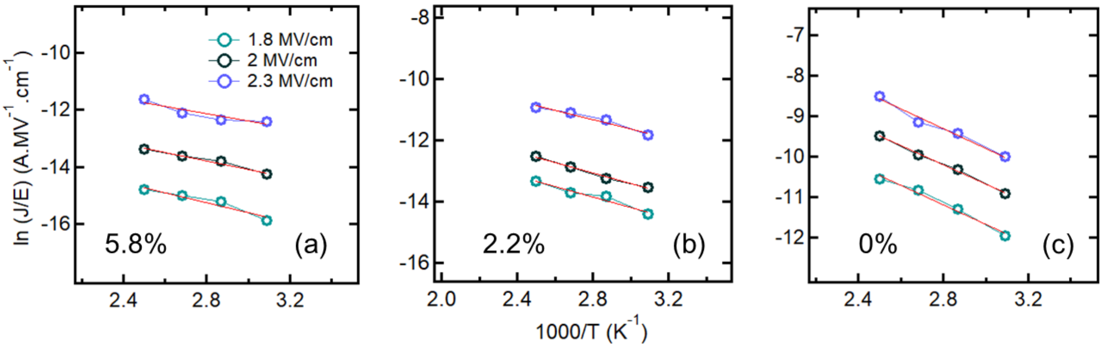

Figure 5.9: *Arrhenius plots of the Poole-Frenkel emission for TiN/HZLO/TiN capacitors with of (a) 5.8 (b) 2.2 and (c) 0 mol% La content*

The obtained slopes from Fig. 5.9a, b and c are, respectively, 1.6, 1.8 and 2.4. Using Eq. 5.2, this gives a trap energy level of 0.14, 0.16 and 0.21±0.02eV with

5.8, 2.2 and 0mol% La, respectively. First, these values are close to the trap levels of $V_O^{\cdot\cdot}$ (see section. 2.5.2). However, this indicates that increasing La leads to the decrease of the energy level with respect to the conduction band minimum. It canno't therefore explain the reduction of leakage current when increasing La. We suggest therefore that the observed decrease of the leakage is probably due to the screening of $V_O^{\cdot\cdot}$ by La which may inhibit the capture of electrons by the traps or due due to the decrease of the $V_O^{\cdot\cdot}$ amount thanks to the extra oxygens provided by the La_2O_3 layers.

5.3 Interface chemistry of HZLO-based capacitors

5.3.1 Experimental

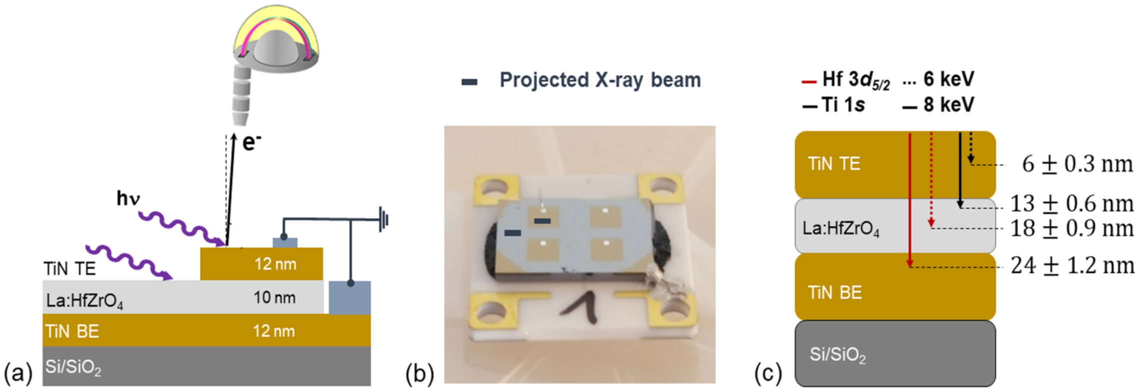

Figure 5.10: *(a) Schematic and (b) an image of the designed sample for HAXPES analysis. (c) Sampling depths of Ti1s (arrows in black) and Hf3d$_{5/2}$ (in red) photoelectrons at $h\nu = 8$ and $6keV$ (solid and dotted lines, respectively)*

To study the top and bottom interface separately, 2×2 mm^2 TiN top electrodes were patterned using a KLOE Dilase 650 laser lithography (λ=375nm). Lift-off (TE electrode removal) was done through reactive ion etching (RIE Plassys MG200) using CF_4(20 sccm)/Ar(10 sccm) plasma at a pressure of 5×10^{-2} mbar. For 12nm thick TE, the etching time is 90s. Thicker (100 nm) 300×300 μm^2 Al pads were then deposited on the capacitors by electron beam evaporation to enable wire bonding to the sample holder. The connection to the BE was made by hard breakdown of one of the capacitors (E_{bd} = 6MV.cm^{-1}). The top and bottom electrodes were grounded during the analysis to avoid charging effects under hard X-rays. The samples were then introduced in the ultrahigh vacuum ($\sim10^{-8}$ Pa) chamber of the HAXPES setup of the BL15XU beamline (see section. 3.3.3). Grazing x-ray incidence at 5° was used to promote the photoemission signal. The 400×30 μm^2 projected beam size is then either centered onto a single capacitor (top interface) or directed onto the bare film (bottom interface) using the precision sample manipulator (Fig. 5.10b). HAXPES measurements were carried out at room temperature using two photon energies, 6 and 8 keV. The emission angle was 5° and the overall energy resolution was 235 meV for both energies, verified by the Fermi cutoff of a Au sample reference. The IMFPs of Ti 1*s* and Hf 3d$_{5/2}$ (λ_{Ti1s}, $\lambda_{Hf3d5/2}$) are assumed to be the same in HZLO and TiN for a given kinetic energy. The sampling depths are 6±0.3 (13±0.6) nm and 18±0.9 (24±1.2) nm at 6 (8) keV photon energy, for Ti 1*s* and Hf 3*d* photoelectrons, respectively. At 8 keV, the Ti 1*s* core level is, therefore, sensitive to the top interface of the TiN/HZLO/TiN stack, whereas the Hf 3*d* core level is sensitive to the entire film thickness (Fig. 5.10c).

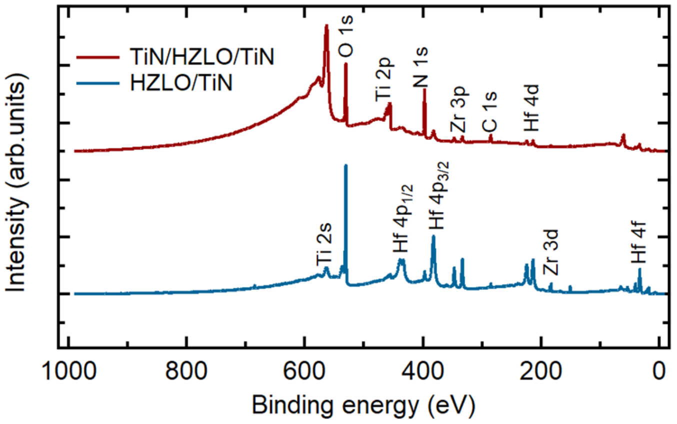

Figure 5.11: *Survey spectra corresponding to the 2.7 mol% La capacitor recorded at* $h\nu = 8keV$ *through the TE (upper spectrum) and from the bare film (lower spectrum)*

The survey spectra through the TE (TiN/HZLO/TiN) and from the bare film (HZLO/TiN) are shown in Fig. 5.11. All the expected core levels are present together with some C surface contamination, which does not influence the interface chemistry. No other contamination is present. The leakage current of both capacitors together with the result obtained using an undoped film are shown in Fig. 5.12a. Increasing La doping leads to lower leakage current as already observed over the complete bias range (±4V). Figure. 5.12a shows the La 3$d_{5/2}$ core level spectra recorded for bare films at 8 keV. The La content derived from the core level intensities is 1.7 and 2.7% La content, in good agreement with the nominal doping levels. The corresponding dopant densities are 1.8 and $2.8 \times 10^{20} cm^{-3}$, respectively. The La 3$d_{5/2}$ spectra for both samples consist of a main peak at ∼840 eV and the corresponding shake-up satellite at higher E_B. The energy difference is 5.2 and 5 eV for 1.7 and 2.7mol% La, respectively.

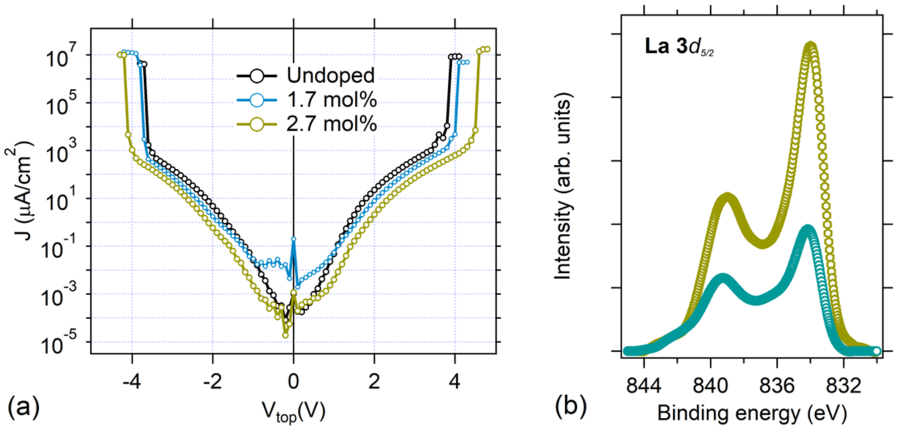

Figure 5.12: *(a) Leakage current density of HZLO capacitors. (b) La 3*$d_{5/2}$ *core level spectra recorded at* $8keV$

5.3.2 Top *vs* bottom interface

The Ti 1*s* core level spectra of the TE are shown in Figs. 5.13a and b. The spectra are fitted with three components. The first, at the lowest binding energy (4965.5 eV), is due to metallic TiN. The component at 4966.5 eV points to the formation of an oxynitride phase ($TiO_{\varsigma}N_y$) and at 4968.2 eV to the Ti$^{\sim4+}$ chemical state in a $TiO_{2-\delta}$ phase, with $2-\delta$ close to 2. The 1 and 3 eV shifts of the sub-oxides with respect to the metallic component and the line shapes are the same used to fit the Ti 2*p* spectra dicussed in chapter. 4. The E_B values are also in good agreement with previous HAXPES studies[225, 226]. Table. 5.6 summarizes the fitting parameters and the components percentages.

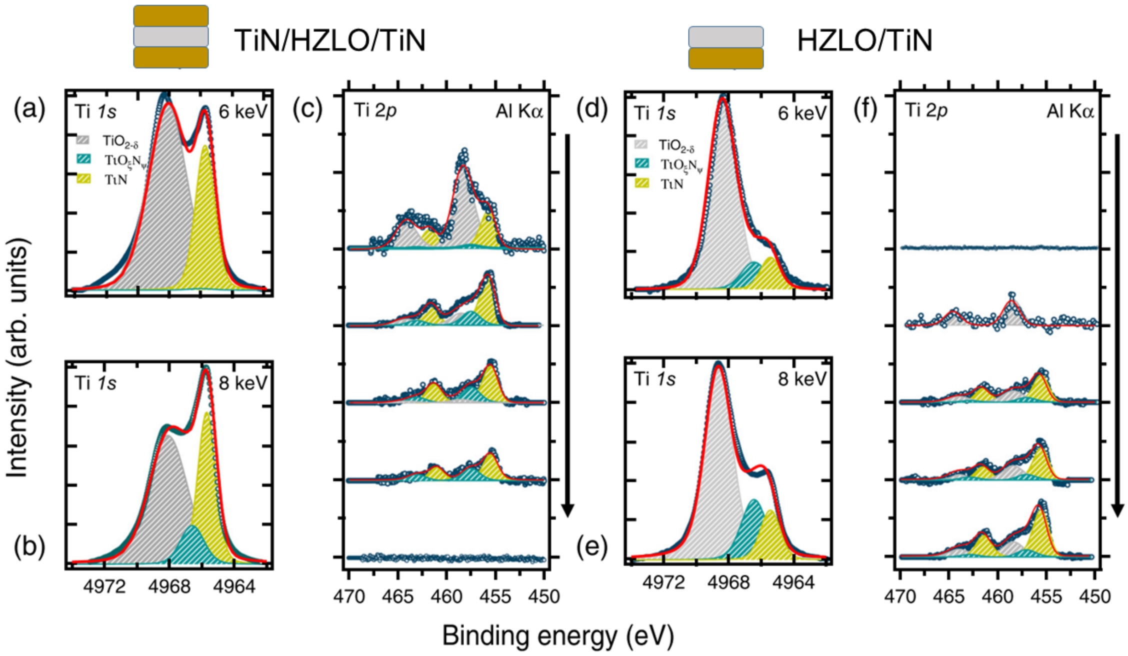

Figure 5.13: *HAXPES Ti 1s core level spectra of the TiN TE acquired with (a) 1.7 La mol% at* $6keV$ *and (b) at* $8keV$*. (c) XPS Ti 2p depth profiling of the TE with Ar*$^+$ *ion sputtering at 0.5 keV. HAXPES Ti 1s core level spectra of the TiN BE acquired through the bare film with 1.7 La mol% doping at (d)* $6keV$ *and (e) at* $8keV$*. (f) XPS Ti 2p depth profiling of the BE by Ar*$^+$ *ion sputtering time (direction of vertical arrow) at* $0.5kV$

Table 5.6: *Ti 1s core level spectra from the top electrode fitting results at 6 and 8 keV photon energy*

	$h\nu = 6keV$		$h\nu = 8keV$	
Component	FWHM(eV)	Area%	FWHM(eV)	Area%
TiN	1.3	31.4±0.07	1.3	39.8±0.03
$TiO_{\varsigma}N_y$	2.6	0.9±0.01	2.6	11.5±0.03
$TiO_{2-\delta}$	2.6	67.7±0.07	2.6	48.7±0.04

The increase in the intensity of the oxynitride phase at $8keV$ confirms that the $TiO_{\varsigma}N_y$ signal comes rather from the interface with the HZLO. In Fig. 5.13a, there is, in fact, a strongly attenuated TiON component at 6 keV (0.9%). Depth profiling using Ar$^+$ ion sputtering and laboratory XPS Ti 2*p* spectra is shown in Fig.5.13c. The results agree well with the HAXPES analyzes. The $TiO_{2-\delta}$ phase is only present at the TE surface, while at the interface with the HZLO (increasing sputtering time), Ti 2*p* shows only the metallic and the oxynitride phase. Sputtering can cause reduction, which would shift the oxide component to a position similar to $TiO_{\varsigma}N_y$; however, the depth dependence of the strength of this component in the N 1*s* spectra acquired at 6 and $8keV$ (shown in Fig.5.14) proves that the oxynitride component comes from the interface.

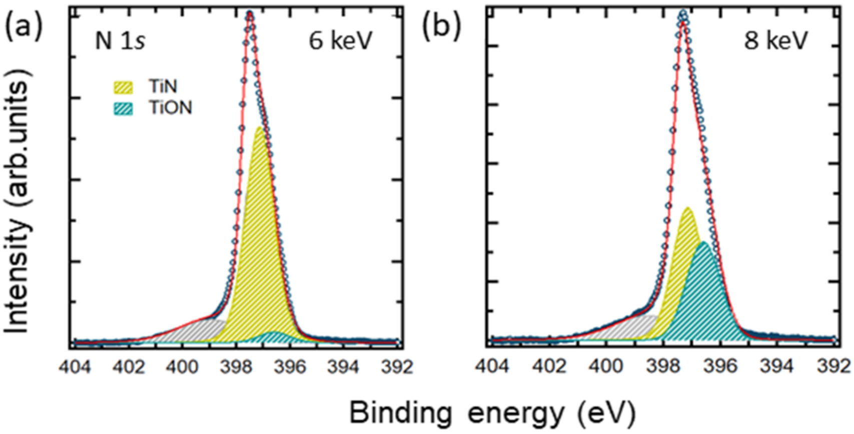

Figure 5.14: *N 1s core level recorded through the top electrode (a) at* $6keV$ *(b)* $8keV$

To analyze the interface with the BE, the HAXPES Ti 1*s* core level spectra were recorded through the bare film, i.e., without the TE. At $6keV$, the spectra are sensitive to the bottom interface, while at $8keV$, they are representative of the electrode bulk. The spectra are fitted with same parameters as the TE and are shown in Figs. 5.13d and e. The spectra are dominated by a $TiO_{2-\delta}$ phase. At 8 keV, the relative intensity of the latter decreases, while both $TiO_{\varsigma}N_y$ and TiN increase, suggesting the presence of an oxynitride below the $TiO_{2-\delta}$ layer. The depth profiling shown in Fig. 5.13f detects first a $TiO_{2-\delta}$ phase at 458.5 eV, followed by $TiO_{\varsigma}N_y$ and then TiN after further etching. Using the photoelectron attenuation function, a layer-by-layer model of the stack, and the HAXPES results at $8keV$, we calculated the thicknesses of the interface layers as follow:

$$d_{TiO_{\varsigma}N_y} = \lambda_{Ti} ln(\frac{Sexp^{\frac{d}{\lambda_{Ti}}} + 1}{S+1}) \tag{5.3}$$

$$d_{TiO_{2-\delta}} = -\lambda_{Ti} ln(\frac{S' + exp^{\frac{-d}{\lambda_{Ti}}}}{S+1}) \tag{5.4}$$

Where d is the electrode thickness, λ_{Ti} is the inelastic mean free path of Ti 1*s* photoelectrons assumed equal through all the layers, $S = I_{TiN}/I_{TiO_{\varsigma}N_y}$ and $S' = I_{TiO_{2-\delta}}/I_{TiN}$. The top interface layer thickness is 1.3±0.05 nm and the measured thicknesses of $TiO_{2-\delta}$ and $TiO_{\varsigma}N_y$ bottom interface layers were calculated to be 3.2nm and 0.5±0.05 nm, respectively. Figure.5.15a shows a schematic of the HZLO stack with the measured interface layers thicknesses. Cross sectional transmission electron microscopy (TEM) image of similar stack (W/TiN(BE)/HZO/TiN(TE)) prepared by ALD is shown in Figure.5.15b. Low La doping as it is the case in the analyzed capacitors, should not affect the interface chemistry. The image shows indeed a less sharper bottom interface than the top one. However, a complete oxidation at the bottom interface should in principle be noticeable by a change of the TiN structure to an amorphous or crystalline anatase or rutile phase (TiO_2 phase). However, this was not observed at the bottom interface, and is in agreement with our HAXPES and XPS results which suggest partial oxidation, a $TiO_{2-\delta}$ phase rather than a fully oxidized TiO_2 generally observed in $Ti2p_{3/2}$ spectra at 459.5-460 eV. The stoichiometry of this sub-oxide may differ depending on the ALD parameters since we suggest that this layer is may be formed due to transport in air to the ALD chamber and the initial oxygen pulses input during the first ALD steps. After TiN deposition, the sample was in fact exposed to air while moving the sample to the ALD chamber. If the formation of the double layer were due only to air exposure, then we would expect the same structure at the TE surface, which is not the case. This sub-oxide may also be conductive like the Ti_4O_7 *Magneli* phase forming conductive nanofilaments and exploited in TiO_2-based resistive memories[227]. An insulating TiO_2 interface layer would cause a higher λ_{eff} between the polarization and the electrode screening charges resulting in significant voltage drop and E_{dep}.

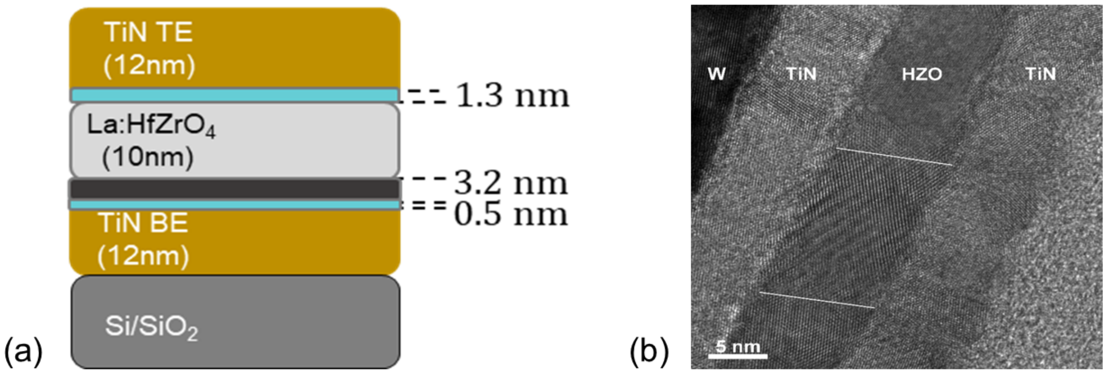

Figure 5.15: *(a) Schematic of the capacitor showing the derived asymmetric interface configuration and (b) a cross sectional TEM image of HZO capacitor grown by ALD with TiN electrodes showing a less sharper bottom interface. (The TEM image was provided by NIMP, Romania)*

5.3.3 Oxygen vacancies

Figure. 5.16 compares the Hf $3d_{5/2}$ core level of the capacitor structure for 1.7 and 2.7% La doping at $8keV$. The spectra are fitted with two components as for the Hf 4*f*. The high binding energy component at 1662.5 eV corresponds to stoichiometric Hf in HZO (Hf^{4+}) and the low binding energy one at 1660.5 eV to reduced hafnium (Hf^{3+}) due to electron transfer from adjacent V_O. The peaks were fitted with GL(70) line shapes, the energy separation was set to 2 eV and the FWHM of both components to 1.8 eV. The higher energy splitting and FWHM in addition to the higher Lorentzian character with respect to what used with Hf 4*f* discussed in chapter.4 are attributed to the different intrinsic broadening of d and f photoelectrons. These fitting parameters allow to obtain the best fitting to the experimental results. The percentage of reduced hafnium increases from 2.72±0.06

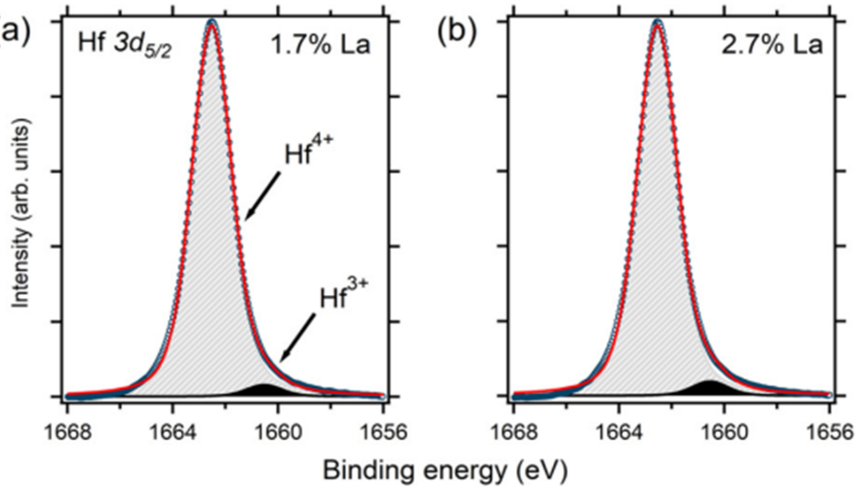

Figure 5.16: *Hf 3d$_{5/2}$ core level spectra acquired at $8keV$ through the TE for (a) 1.7 and (b) 2.7 mol% La doping*

to 3.36±0.07 when increasing La from 1.7 to 2.7 mol%,. The corresponding V_O concentrations are 1.5 and 1.9$\times 10^{20}$ cm^{-3}, respectively. Assuming that the La dopants are compensated by positively charged oxygen vacancies ($V_{\ddot{O}}$) , the 1 mol% ($\sim$8$\times 10^{19}$ cm^{-3}) difference in La doping between the two samples gave $\sim$4$\times$10^{19} cm^{-3} additional $V_{\ddot{O}}$. The results support therefore that two substitutional La cations are compensated by the formation of a new $V_{\ddot{O}}$, consistent with a fully ionically compensated defect. The results show also that $V_{\ddot{O}}$ increases from 1.5$\times 10^{20}$ (Fig. 5.17a) to 2.1$\times$10^{20} cm^{-3} (Fig. 5.17b) when decreasing the photon energy from 8 to 6 keV. This is consistent with a $V_{\ddot{O}}$ profile from the top interface into the film as found with laboratory-XPS measurements (chapter. 4). The TiN BE is oxidized and passivated, preventing thus oxygen scavenging of the first layers of HZLO. The TiN TE is however grown directly on the HZLO and can scavenge oxygen when annealing, leading to the formation of an oxynitride phase, the accumulation of $V_{\ddot{O}}$, and Hf reduction near the interface. The results are therefore in perfect agreement with the XPS results discussed in chapter. 4.

To investigate the effect of annealing on the V_O profiles, similar stacks were annealed at higher temperature of 800°C for 20s. The Hf 3$d_{5/2}$ at $6keV$ shows more reduced Hf relative to the sample annealed at 500°C (Fig. 5.18a and b), corresponding to an increase in V_O from 2.1 to 2.9$\times 10^{20}$ cm^{-3} . The Ti 1*s* of the TE and BE for a capacitor annealed at 800°C are also shown in Fig. 5.18c and d, respectively. The spectra show an increase in the intensity of the oxynitride component of the TE from 11.5±0.06 to 14.9± 0.05% whereas no significant difference at the BE with respect to the sample annealed at 500°C. This is consistent with the passivation state of the bottom electrode during the growth process. The intensity corresponding to the reduced Hf at $8keV$ after annealing does not change significantly, suggesting that the change in the V_O concentration occurs only near the TE and is correlated with the increased oxygen scavenging, also visible from the stronger oxynitride component. The calculated V_O concentrations from the discussed samples are summarized in Tab.5.7.

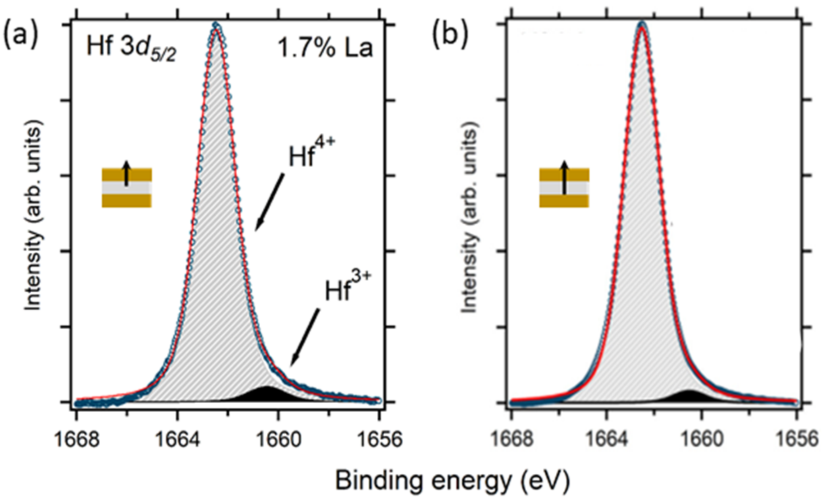

Figure 5.17: *Hf 3*$d_{5/2}$ *core level spectra acquired with 1.7 mol% La through the TE at (a)* 6 *(b)* $8keV$ *photon energies*

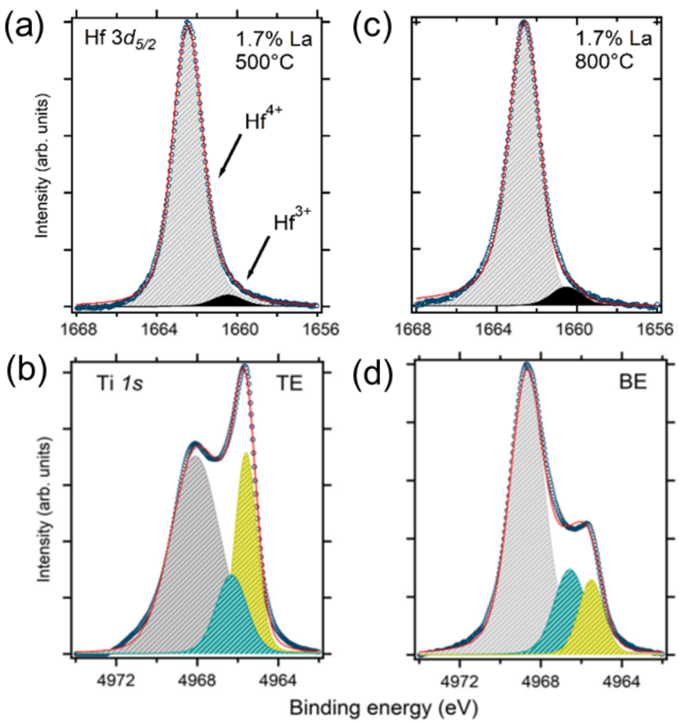

Figure 5.18: *(a) Hf 3*$d_{5/2}$ *core level spectra acquired with 1.7 mol% La through the TE at* $8keV$ *with* T_{RTA}*=500°C (1min) and (b)* T_{RTA}*= 800°C (20s). (c) Ti 1s of the TE and (d) the BE, both at* $8keV$ *with* T_{RTA}*=800 °C (20s)*

Table 5.7: V_O *concentration (×10*^{20} *cm*$^{-3}$*) calculated from the Hf 3*$d_{5/2}$ *spectra for 1.7 and 2.7% La doped samples at* $6keV$ *(top interface) and* $8keV$ *(bulk film)*

	T$_{RTA}$=500°C		T$_{RTA}$=800°C	
	6 keV	8 keV	6 keV	8 keV
1.7 % La	2.1	1.5	2.4	1.6
2.7 % La	2.1	1.9	2.5	1.9

5.4 HAXPES with applied bias

Device patterning

In this section, the effects of field cycling and polarization reversal in TiN/HZLO/TiN capacitors with an optimal La content, i.e 2.3 mol% were investigated using HAXPES with *in-situ* biasing. The samples are made by ALD at NamLab and described in Appendix. A.

For *operando* photoemission, the MFM structure has to be carefully designed. The starting point is a $(5 \times 5) mm^2$ full wafer plane sample. The BL15XU beamline offer photoemission end-station with a beam spot of 35 and 30μm in horizontal and vertical direction, respectively. In addition to that, intone must take into account the long tails of the beam profile. Furthermore, grazing X-ray incidence is better to promote the photoemission signal but at 5° incidence, the projected beam in horizontal direction is $\sim$400μm (35μm/sin(incidence angle)). On the other hand, with large electrodes (i.e 400μm), it is likely that defects inducing high leakage current, namely high conduction channels through grain boundaries, occur randomly for some capacitors. For these reasons, we chose to work with (100$\times$100) μm^2 capacitor area and to fabricate 96 of independent capacitors per sample to ensure that at least some of them have a low enough defect concentration for ferroelectric stability. In this case, signal from bare HZLO surface will make a strong contribution to the measured signal as the projected beam size is much larger than the device. Therefore, screening layers in the horizontal direction have to be added. These layers must be thick enough to suppress photoelectrons from bare surface, be chemically distinct from the capacitor structure, conductive in order to avoid charging effects but have no electrical contact with top electrode to allow biasing of only the capacitor. The next issue is to design a system, which can be electrically connected to the ultra-high vacuum manipulator through the sample holder. The thin top electrode cannot hold any wire and an intermediate stage has to be designed to allow an easy connection. This is done by the deposition of a thicker layer of metal, overlapping a small part of the top electrode of interest, and will serve as a connecting pad. It can be wired by micro-wiring to the metallic contacts available on the sample holder. However, it has to be also electrically separated from the bare ferroelectric layer to not disturb the electrical properties of the capacitor of interest. An intermediate, highly insulating, dielectric layer has to be inserted therefore between the pad and the ferroelectric to limit parasitic behaviors. The contacting pads and the screen layers are made of Ti(10nm)/Au(100nm) because of the good conduction properties, high adhesion to the TiN TE and excellent compatibility with micro-wiring. The intermediate dielectric layer used is 50 nm thick Al_2O_3 because of its highly insulating properties. The micro-fabrication processes have been done at NanoFab (CEA Saclay). They consist of the following steps:

(*i*) Patterning of devices using photolithography

After dehydratation at 155°C for $\sim$5 min and then cooling, the MFM full wafer sample is covered with a negative photoresist by spin coating. A negative photoresist is the one which becomes solid after exposure to light, on the contrary to positive photoresists. We used AZ nLof 2000 photoresist which is a polymer and the spin coating parameters were 60s at 4000rpm. This results in $\sim$2μm thick layer on the entire sample. After, a pre-bake at 110°C for 90s is used to drive off the photoresist solvent excess. After pre-baking, the photoresist is exposed to a pattern of intense light (λ=365nm/Dose=90mJ.cm^{-2}) using a μMLA Heidelberg maskless lithography instrument. The pattern was prepared using KLayout software providing GDS. extension file and consists of 96 100×100μm^2 capacitors and a big (1mm^2) TiN capacitor in one of the corners to serve as bottom electrode and provide an asymmetry needed to identify the devices locations. The exposure to light causes chemical changes that allows the exposed area to be hydrophilic, namely by polymer cross linking. A special solution, called "developer", is then used for the removal of the unexposed hydrophobic areas. Before developing, which is made using MF319 (based on Tetramethylammonium hydroxide) solution for 60s, the wafer is "hard-baked" (at 110°C for 90s) to make the photoresist a more durable protecting layer during developing.

(*ii*) Reactive ion etching

Reactive ion etching (RIE) is an RF sputtering process using chemically reactive species in addition to the Ar$^+$ ion beam etcher. It allows the removal of the TiN top electrode on the entire sample area expect from the protected capacitors by the cross-linked photoresist. The parameters for 12nm TiN etching are CF$_4$(20sccm)/Ar(10sccm) as the plasma gases and an etching time of 90s. The chamber pressure during etching is 5×10^{-2} mbar and the RF power is 50W. The remained photoresist on the capacitors is finally removed by a solution called remover. Remover 1165 (N-methyl-2-pyrrolidine) at 70°C for 30min was used.

(*iii*) Evaporation of Al$_2$O$_3$ insulating layer

A positive photoresist in this case is used to pattern the area where the insulator will be deposited. S1813 was used. A pre-bake at 115°C for 60s is performed and the lithography parameters are λ=365nm/dose=115mJ.cm^{-2}. The patterns consist of three 100×100μm^2 squares overlapping the TiN capacitors from 3 sides by 20μm. No hard baking is needed for positive photoresists. Developing in MF319 for 60s removes the exposed area. Finally, 50nm thick Al$_2$O$_3$ were deposited by electron beam evaporation using an MEB 450 e-gun PLASSYS instrument at a pressure of 10^{-7} mbar. The remaining photoresist is removed by lift-off using Technistrip NI555 solution.

(*iv*) Evaporation of metal layers (contacting pads and screening layers)

The same methodology as the previous step is used to deposit Ti(10 nm)/Au(100 nm) layers. Ti is used as an adhesion layer. For the contacting pads, the metal overlaps the TE. However, the screen layers are placed on the top of the insulating layers and not in contact with the TiN TE (far away by 30μm). The subsequent lift-off procedure of Au might actually be not reproducible. A lift-off layer (LOL 2000) was therefore spin coated before the positive photoresist coating in order to facilitate the lift–off which was ensured using 1165 remover solution at 70°C.

The final design is presented in Fig. 5.19, with an optical microscope image from 4 devices taken from the middle of the sample (left), a single device (top right) and a side schematic view of the device ready for introduction in any photoemission end-station.

Three capacitors were then cycled *ex-situ* to different cycling stages corresponding to pristine (1 cycle), woken-up (after 10^6 cycles) and fatigue (after 10^9 cycles) states. The polarization state was switched *in-situ*. Figure. 5.20a and b show a schematic of the device dedicated for HAXPES with *in-situ* bias and an en-

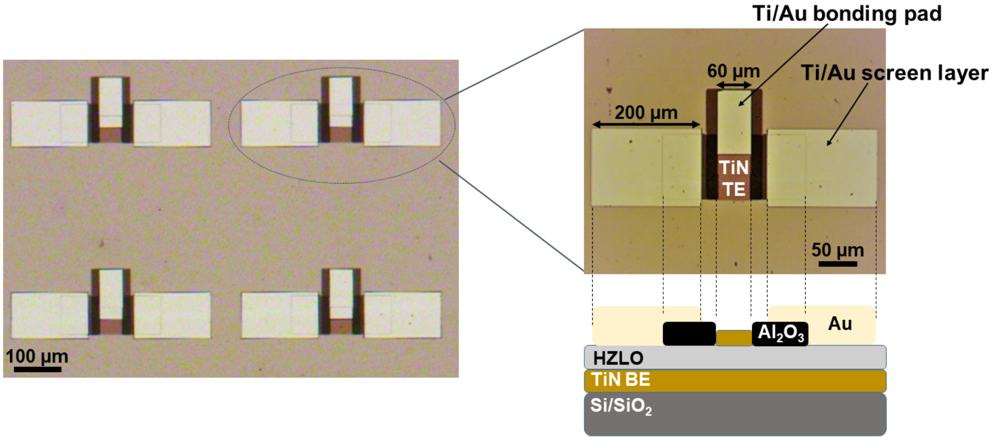

Figure 5.19: *(left) optical microscope image from 4 devices taken from the middle of the sample (right) a single device and a side schematic view*

durance plot obtained from the patterned devices, respectively. The latter shows the evolution of the memory window as a function of field cycling and the circles indicates the positions of the three capacitors presenting distinct cycling stages. An image of the mounted sample and the corresponding devices of interest are also shown in the inset of Fig. 5.20b. The devices of interest (their contacting pads) are connected to the gold contacts of the sample holder via Au micro-wires while the bottom electrode from the big square (submitted to breakdown) via silver paste. In all electrical measurements, the signal is applied to the TE while keeping the BE grounded.

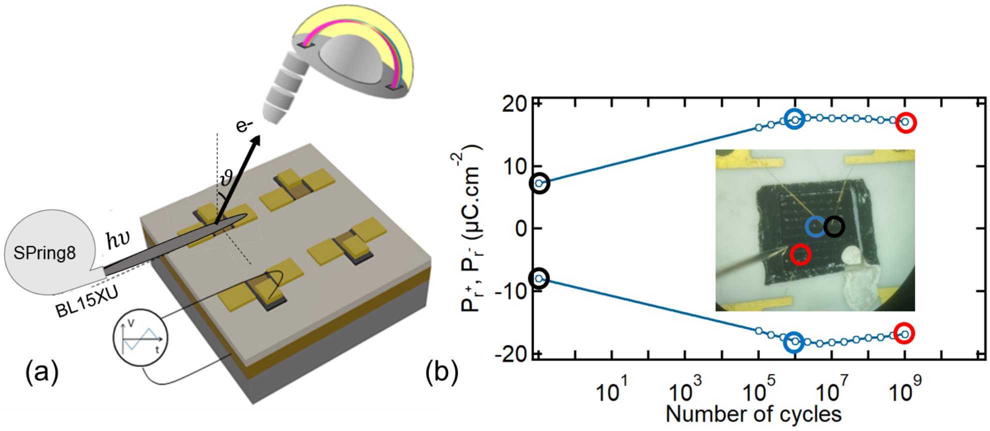

Figure 5.20: *Schematic of the sample for HAXPES with in-situ applied bias at the BL15XU beamline and (b) an endurance plot of a patterned device with an image of the mounted sample on the dedicated sample holder. The positions of the wired devices corresponding to pristine, woken-up and fatigue stages are also highlighted by black, blue and red circles, respectively*

5.4.1 Electrical characterization

The switching current curves ($I_s - V$), hysteresis loops ($P - V$), capacitance ($C - V$) and leakage current density ($J - V$) are given in Fig. 5.21a, b, c and d, respectively. The presence of double switching peaks in both bias polarities at the pristine state (black curve in Fig. 5.21a and c) suggests that the films have considerable domain pinning, which is either linked to charge trapping at $V_O^{\cdot\cdot}$ or to depolarization fields caused by non-polar phase portions. This results in a pinched hysteresis loop closer to an antiferroelectric-like behavior (Fig. 5.21b). After 10^6 cycles, the double switching peaks merge to a single peak with higher intensity resulting in the de-pinching of the hysteresis curve and the MW increases from 16 to 35 μC.cm^{-2} characteristic of significant wake-up behavior. Further cycling (at 10^9) slightly reduces the $2P_r$ value to 32 μC.cm^{-2}. Figure.5.21d shows the leakage current response from the three devices. The results show an increase of J on cycling. Table.5.8 summarizes the electrical properties of the discussed devices.

Table 5.8: The electrical properties of the devices of interest

	MW ($\mu C.cm^{-2}$)	$E_C(MV.cm^{-1})$	$\epsilon_{r,min}$	J@4V (A.cm^{-2})	J@-4V (A.cm^{-2})
Pristine	16	0.82	60	3.5×10^{-5}	1.2×10^{-4}
Woken-up	35	1.10	48	6×10^{-3}	3×10^{-3}
Fatigue	32	1.11	52	1×10^{-2}	2.5×10^{-2}

The relative permittivity values (ϵ_r) were extracted from the small signal capacitance measurements shown in Fig. 5.21c for a film thickness $d = 10nm$ and a capacitor area $A = 0.01mm^2$. However, the measured values do not correspond to the o-phase reported to be in the 25-35 range[144]. We attribute this to the parasitic capacitance induced by the insulating Al_2O_3 layer playing the role of additionnal capacitance in series to HZLO. The minimal $\epsilon_{r,min}$ outside the switching peaks regions (at ±3V) were added to Tab. 5.8. They represents only the overall dielectric contributions. The results show a decrease from 60 to 48 after wake-up. This can be assigned to an increased o-phase portion after wake-up as shown by Grimley *et al*[144] who reported a decrease from 33 to 27 after 10^5 cycles in TiN/Gd:HfO_2/TiN capacitors. Table. 5.8 gives also the J values at ±4V. The result indicate higher leakage current at negative bias applied to the TE with the pristine device, suggesting higher charge injection from the top interface. For the woken-up and fatigued capacitors, the leakage current is more symmetric.

The imprint behavior was also investigated. This was performed on a separate woken-up device after 10^6 cycles for easier visualization (one single switching peak) of eventual shifts related to imprint. The procedure is as follows: Two separate capacitors are first woken-up. Then, one is polarized toward the TE ($P\uparrow$) and the other toward the BE ($P\downarrow$). The sample is then baked at 85°C for a certain amount of time (up to 3hrs) using a hot plate (85°C is the standard for consumer electronics). After few minutes for cooling, the hysteresis loop is measured again using a single triangular pulse allowing to maintain the previous stored state after the measurement. The coercive voltage (V_c) shifts, resulting from imprint for a given polarization state, are thus recorded. Fig. 5.22a and b show the $I_s - V$ curves measured from the capacitors stored at $P\uparrow$ and $P\downarrow$, respectively. The V_c with $P\uparrow$ stored capacitor shifts in the positive direction while the shifts are in the negative direction with the opposite polarization stored state.

In the case of leaving the capacitor in $P\uparrow$ (applying a negative pulse at the TE before baking), positive and negative polarization charges are located at the top and bottom interfaces, respectively. Trapping of electrons at the top interface and possibly de-trapping at the bottom interface enhanced by thermal energy is a plausible mechanism for the observed shifts. The electron trapping at the top

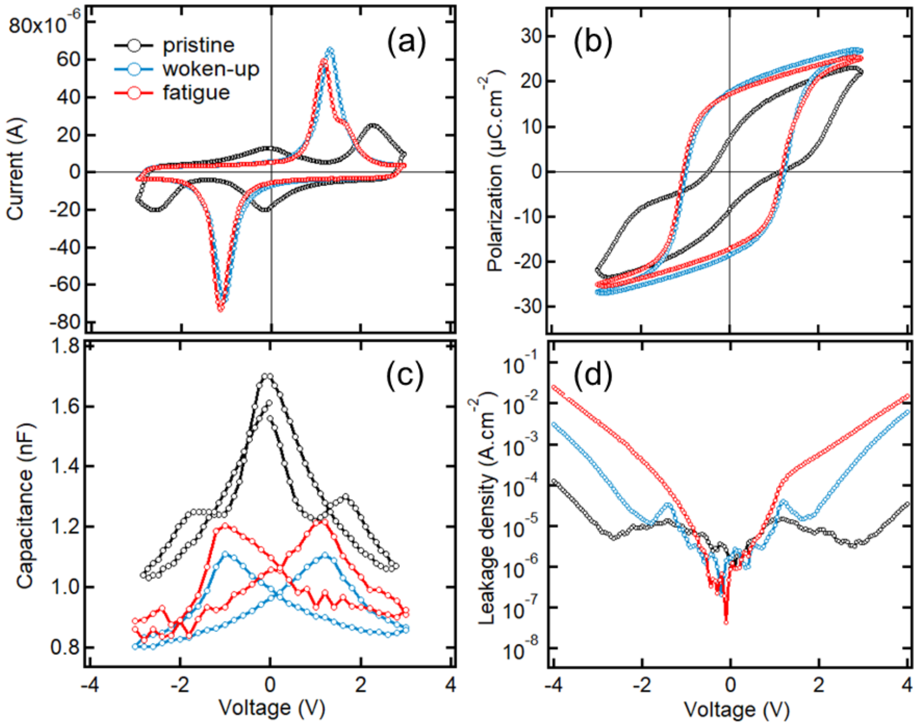

Figure 5.21: *(a) $I_s - V$ (b) $P - V$ (c) $C - V$ and (d) $J - V$ response from the discussed devices*

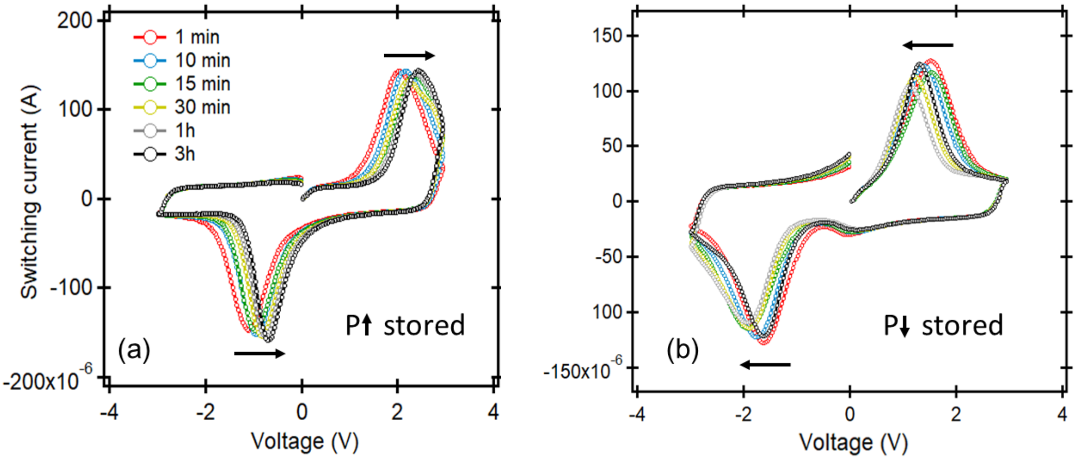

Figure 5.22: *$I_s - V$ curves as a function of baking time 85°C for (a) $P\uparrow$ and (b) $P\downarrow$ stored states measured from distinct woken-up capacitors*

interface creates a field in the same direction of the stored polarization and acts against the field to switch the polarization in the opposite direction. Hence, a higher switching bias is the result. The opposite trend is observed when samples are left in the $P\downarrow$ state where electron trapping is higher at the bottom interface. However, the shifts magnitudes are higher with the $P\uparrow$ state, suggesting higher electron trapping at the top interface and thus higher available trap sites. Figure. 5.23 shows the imprint shifts measured as $(V_C^+ - V_C^-)/2$ for both polarization states. After 3hrs of baking, the imprint reaches 0.8V (-0.8 MV.cm^{-1} pointing toward the top electrode) and -0.5V (0.5 MV.cm^{-1}) for $P\uparrow$ and $P\downarrow$, respectively. The extraoplated data for 10 years operation of a TiN/HZLO/TiN device gives an imprint magnitude of -1.4 and 0.9MV.cm^{-1}. The values are relatively high and very close to the coercive field of the ferroelectric. An oxygen vacancy engineering approach seems therefore to be essential to improve this aspect which highly impact the reliability of hafnia-based devices.

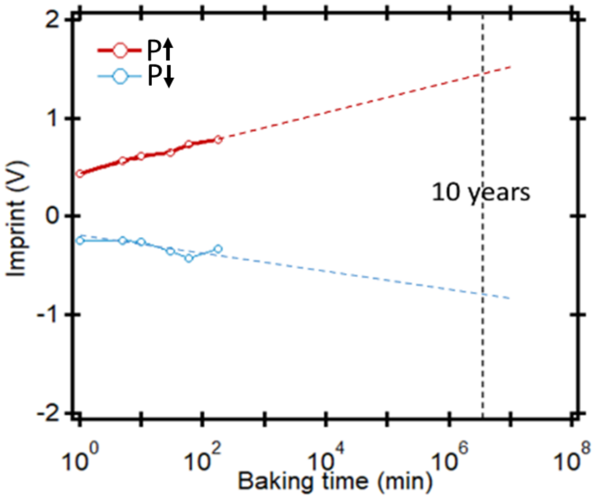

Figure 5.23: *Positive (red) and negative (blue) time-dependent imprint shifts measured at baking temperature of 85°C . The data are extrapolation for 10 years operation*

5.4.2 Effect of field cycling

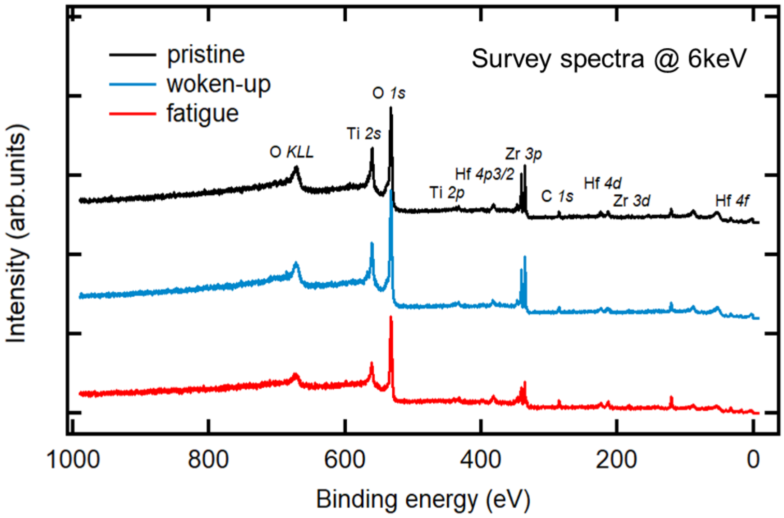

Figure 5.24: *Survey spectra from the discussed devices* $at h\nu = 6keV$

HAXPES measurements were first conducted on the as-received cycled capacitors without further poling. Two photon energies of 6 and $8keV$ are used. The overall energy resolution was 235 meV, verified by the Fermi cutoff of an Au film for both energies. Figure. 5.24 shows the survey spectra recorded at $h\nu = 6keV$ photon energy. All the core levels are present with negligible carbon contamination present mainly at the surface. Figure. 5.24 shows the recorded Hf 3$d_{5/2}$

spectra. The measured $I_{Hf^{3+}}/(I_{Hf^{3+}} + I_{Hf^{4+}})$ values are also included in the figures.

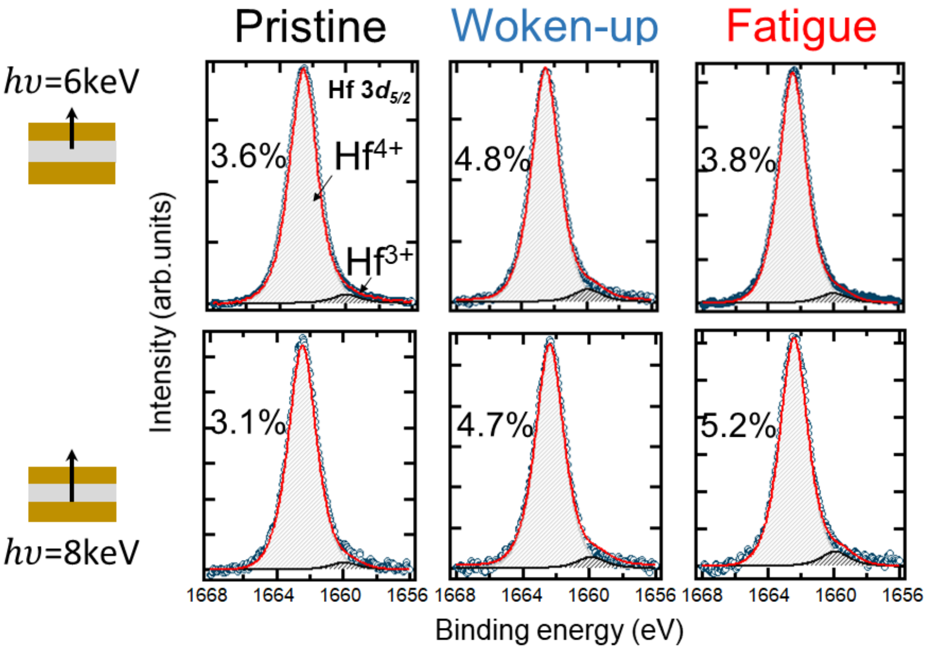

Figure 5.25: *Hf 3d$_{5/2}$ spectra recorded from the discussed devices at (top panel) $h\nu = 6keV$ and (bottom panel) at $h\nu = 8keV$*

Figure. 5.26 summarizes the derived V_O concentration for the three devices. First, the depth-dependent results of the pristine capacitor are consistent with higher V_O at the top interface. After wake-up, the V_O concentration near the top interface and the overall concentration along the film thickness increase. This may explain the increase in leakage current density in both polarities after 10^6. Similar results were obtained by Islamov *et al* when modelling the leakage current results of similar TiN/HZO/TiN capacitors with the phonon assisted tunneling mechanism (PAT) as discussed in chapter.2 (see Fig.2.17). In addition, Fig.5.26a shows that wake-up is accompagnied by an homogenisation of the V_O profile through the entire film thickness. Indeed, Pesic *et al* have reported a redistribution of V_O and a decrease of their asymmetric profile in the pristine state as the root cause of wake-up[140]. The results support this hypothesis. However, a redistribution of existing V_O would reduce their concentration at the top interface, where they are suspected initially to be present, after cycling. The results show rather an increase both at the interface and in the entire film. Generation of more V_O and their subsequent diffusion under millions of cycles imply the suppression of asymmetric charge trapping leading to reduction of imprint and significant domain depinning. Furthermore, a higher V_O amount can locally transform non polar crystallites to polar o-phase[144]. Further cycling results in a drop of the defect concentration at the top interface and the film bulk showed the highest values among the three capacitors. The leakage density from the fatigued device was also the highest. The origin of MW decrease is possibly due to increased domain wall pinning. Figure. 5.26b draws the averaged V_O density within the entire film (8 keV) and the memory window *vs* the number of working cycles. Our results suggest that the optimal V_O density in term of MW in these HZLO films is around

2.7×10^{20} cm^{-3}. The overall trend is in agreement with the values extracted from the PAT model used by Islamov *et al*[168]. The higher values we observe may stem from La doping since in their analyzes, undoped HZO was investigated. It sould be emphasized that the estimation method of V_O from the reduction state of Hf can also over estimate the actual vacancy concentration. First, the model assumes only the presence of double positively charged V_O. Second, reduction with electron transfer may also reduce the Zr cations decreasing thus the calculated V_O densities although this was not observable on the Zr core levels in our measurements.

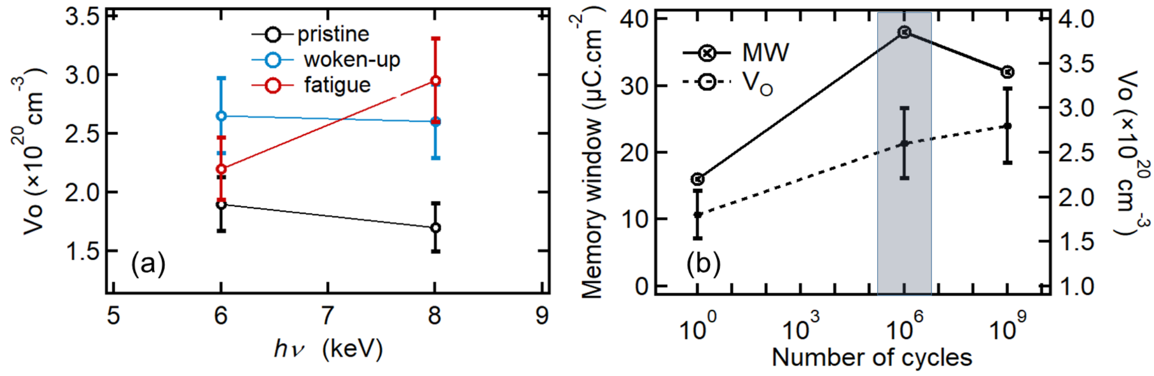

Figure 5.26: *(a) V_O values at two distinct probing depths as derived from the Hf 3d$_{5/2}$ spectra recorded from the discussed capacitors (b) Correlation between the MW and V_O density in HZLO-based capacitors showing the optimal V_O content allowing the highest MW*

5.4.3 Polarization-dependent band diagram

A triangular signal of ±3V and 10 μs duration is applied to the top electrode in order to switch the polarization and evaluate the effects on E_B shifts allowing the derivation of the polarization-dependent band alignement at interfaces. A KEYSIGHT 33512B function generator was used. Figure. 5.27 shows the bias induced displacements of the Hf 3*d*$_{5/2}$ and Zr 3*d* spectra recorded just after storing a $P\uparrow$ or $P\downarrow$ polarization state in the optimal woken-up device with the two photon energies. The top and bottom electrodes are grounded during the analyzes. Near the top interface, the spectra shift downwards (toward E_F) rigidly by 300 meV when switching from $P\uparrow$ to $P\downarrow$. At 8 keV, no change was noticeable and both core levels present the same E_B. The Ti 1*s* from the grounded top electrode is also included.

φ_{Bn} at the top and bottom interfaces are determined using the Kraut method adopted in chapter. 4. The reference energy separation between of Hf 3*d*$_{5/2}$ emission and the VBM is obtained from spectra recorded from bare HZLO areas. The VBM is obtained by linear extrapolation of the leading edge with the baseline as shown in Fig.5.28. This gives an energy separation of 1659.6 eV.

The exact position of the Hf 3*d*$_{5/2}$ peak at the top interface ($6keV$) is known for both polarization orientations (Fig.5.27). For the bottom interface, we assumed a linear electrostatic potential within the film and that the obtained E_B value at 8 keV is the mean value between the top and bottom interfaces. Thus, we estimated the E_B value at the bottom interface as 2E_B(8keV) - E_B(6keV). This

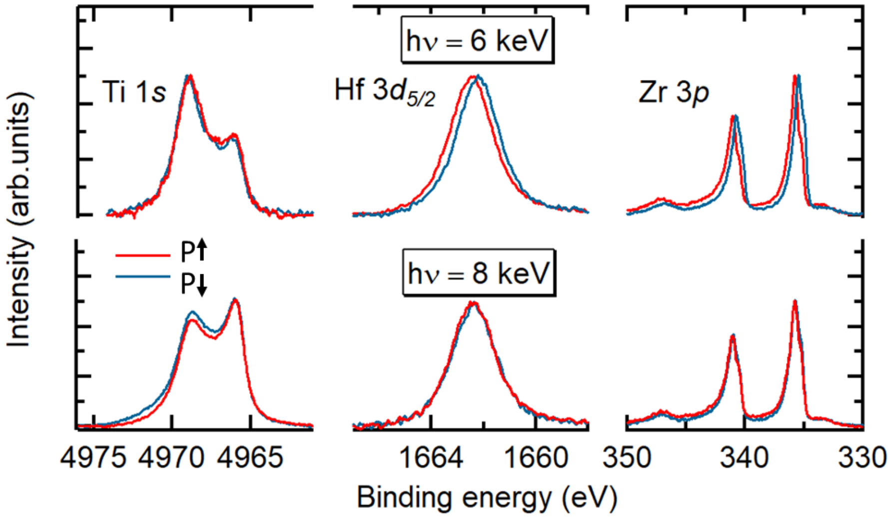

Figure 5.27: *Polarization induced band shift as detected using Hf 3d$_{5/2}$ and Zr 3d emission lines at* $6keV$ *(top) and* $8keV$ *(bottom) photon energies, respectively. The Ti 1s spectra are also included*

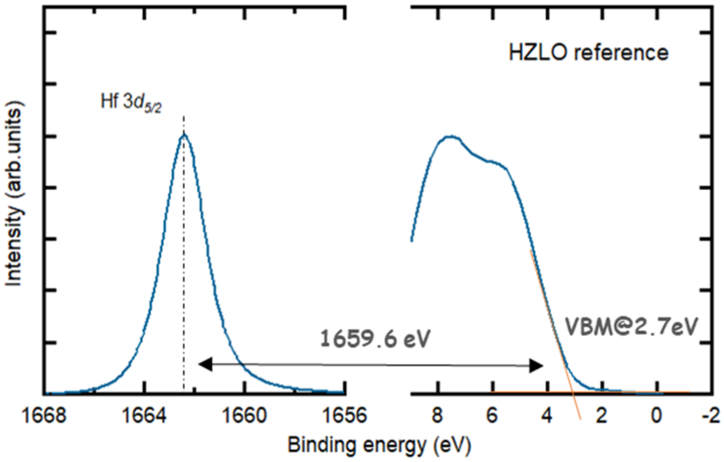

Figure 5.28: *The energy difference between the Hf 3d$_{5/2}$ emission and the VBM from bare HZLO area*

gives E_B values at the bottom interface of 1662.30. Using $E_g = 5.6eV$, the polarization-dependent band alignment is schematically shown in Fig.5.29. The obtained trap energy as measured from the 2.2 mol%La sample (Fig. 5.9) using the Poole-Frenkel mechanism of (~0.16 eV) was also added included in the schematic. The obtained φ_{Bn} values are 2.5 (2.7) and 2.8 (2.4) eV at the top (bottom) interface for P↑ and P↓ states, respectively. First, the SBH values at the top interfac is higher than found with undoped HZO (chapter. 4) corroborating the effect of La doping on upward band bending and the increase of the potential barrier height for electrons. Second, the electrostatic potential changes sign with polarization. Its direction is in accordance with previous derived band alignment using HAXPES upon ferroelectric switching in BaTiO$_3$-based capacitors[52]. At $P\uparrow$, the upward potential through the film suggests an internal field pointing toward the top electrode as observed by the imprint analyzes. However, the internal field magnitude with the P↓ state (400 kV.cm^{-1}) is higher with respect to the P↑ state (-200 kV.cm^{-1}) whereas the imprint analyzes showed that the imprint field is higher with the P↑

state. This may be due to low HAXPES sensitivity to the bottom interface preventing an accurate measurement of the barrier height at the bottom interface. In addition, the $\Delta\varphi_{Bn}$ at the top and bottom interfaces is 0.3 eV. This suggests that the high width of the sub-oxide layer (3.2nm) may be no so different from the thinner oxynitride layer at the top interface. Both provide similar screening efficiency of the polarization charges. Using P$_r$=0.35 C.m^{-2}, the λ_{eff} at the two interfaces was calculated to be 0.04Å. Finally, the measured φ_{Bn} values are very close to what reported by Matveyev *et al* using standing wave HAXPES experiment[228]. The technique allowed a more accurate mapping of the electrostatic potential. Based on their experimental results along with modeling, the authors also showed that charge depleted regions near the interfaces are present. The reported oxygen vacancy space charge concentration are however very close to the values reported in this work despite the lower measured SBHs in their case which can, again, be linked to the La doping in our case.

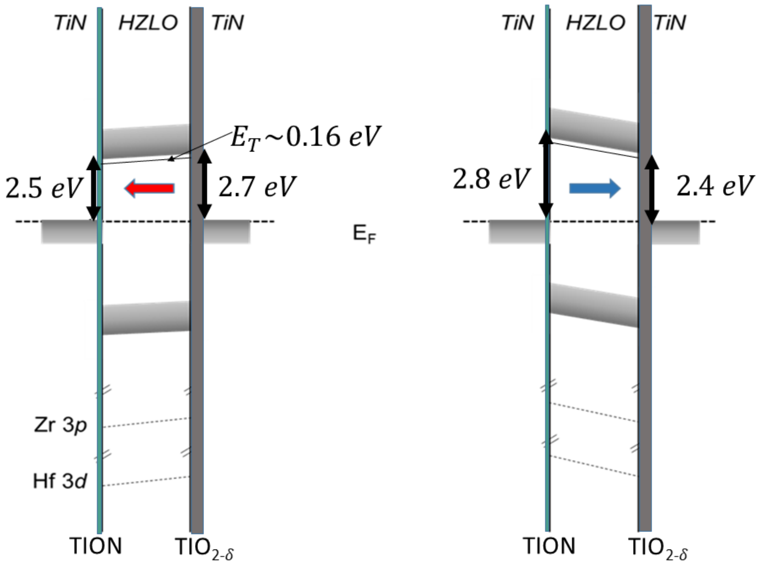

Figure 5.29: *Polarization-dependent band diagram of optimal HZLO-based capacitors taking into account the derived asymmetric interface configuration. The trap energy level associated to V_O is also included*

5.5 Conclusions

In conclusions, technologically relevant ferroelectric La doped HZO-based capacitors have been subjected to advanced characterization through soft and hard X-ray photoelectron spectroscopy, in addition to electrical measurements. The analyzes highlight the chemical and the electronic properties of the films following La doping, field cycling and polarization reversal. The XPS analyzes revealed an upward band bending toward E_F when increasing La doping, characteristic of p-type doping. However, the depth-dependent measurements of the Hf 4*f* suggested that this actually depends on the defective state of the HZO film and the chemical environment of the introduced La within the film. In oxygen-poor environment, La doping is ionically screened by available $V_O^{\cdot\cdot}$ while in oxygen-rich portions of the film, 2 La impurities induce a new $V_O^{\cdot\cdot}$ and the doping is n-type as further confirmed by HAXPES. La doping was also found to decrease the trap energy level associated to modeling. The leakage current decrease with La is therefore possibly by the combination of defect screening and the decrease of the latter concentration due to the extra oxygen provided when adding La_2O_3 layers during the growth process. The leakage current reduction with La is believed to be at the origin of the enhanced endurance with respect to undoped HZO films. HAXPES with a specific sample design was used to analyze the top and bottom interfaces separately, confirming an oxygen scavenging mainly by the top electrode due to the passivation of the bottom one during the film growth process. HAXPES with *in-situ* biasing was also performed. A correlation between the $V_O^{\cdot\cdot}$ densities derived from Hf3 $d_{5/2}$ spectra and the electrical characteristics was obtained. The results suggest that wake-up is due to generation, redistribution and homogenization of $V_O^{\cdot\cdot}$s along the film thickness with an appropriate concentration of 2.7$\times 10^{20}$cm^{-3}, allowing the optimal memory window of the device (35μC.cm^{-2}). Lower asymmetric charge trapping, domain depinning and local increase of the polar o-phase are the most possible consequences of the measured $V_O^{\cdot\cdot}$ profiles. The Schottky barrier height at both interfaces in optimal HZLO capacitor operation are 2.5 (2.7) and 2.8 (2.4) eV, at the top (bottom) interfaces and for $P\uparrow$ and $P\downarrow$ states, respectively. The distinct chemical interfaces did not affected the effective screening length of the polarization bound charges and the derived electrostatic potential changes sign upon polarization reversal and it is in agreement qualitatively with the imprint analysis.

If trivalent dopant has this tremendous effect on the device performance, chemically and electronically, what about tetravalent dopants like Si which is known to form very strong bonds with oxygen and to highly stabilize the t-phase? Within the framework of the 3ϵFERRO project, similar investigations have been therefore performed on Si implanted HfO_2 films which are already demonstrated in BEOL-compatible integration in 130 CMOS nodes[96, 125]. This will be the theme of next chapter.

Chapter 6

Oxygen vacancy engineering in Si implanted HfO_2-based capacitors

6.1 Introduction

Ferroelectricity in hafnia-based thin films was first discovered in Si:HfO_2 (HSO) and it was used for the fabrication of the world's first ferroelectric field effect transistors in 28 nm technology node[229]. Along with HZO, it is one of the preferred choices for application-oriented work[56]. HZO still present a higher interest mainly due to the much wider stoichiometry and crystallization temperature window to achieve a stable ferroelectric phase[230]. This is mainly due to the role of Si as a very efficient stabilizer of the tetragonal phase which partially closes the window for the stable orthorombic ferroelectric phase[231, 108]. Richter *et al*, concluded that the HSO system is a rather fragile system but factors such as V_O and surface energy can be used to optimize the ferroelectric response[231]. In terms of doping content, 1% effective doping was stated by different authors to be an optimal content[232, 233]. Depending on the application, the crystallization temperature has also to be taken into account. Because of its lower crystallization temperature, HZO is not suited for anneal temperatures up to 1000°C, as it is typically observed when the material needs to be deposited prior to the source/drain anneal of MOS transistors. Here, HSO can be a better choice if the stoichiometry of the film is well controlled. On the other hand, HZO is often favored for BEOL processing, thanks to the low crystallization temperature (~500°C).

Alternate deposition of SiO_2/HfO_2 layers with ALD is the most established growth technique but is expected to face limits for ultra-thin layers and to achieve precise and uniform dopant concentration. Si doping with ion implantation was found to be an excellent alternative[232]. The technique is production line compatible, ensures a high uniformity at wafer scale and offers large flexibility to achieve different Si molar fractions in HfO_2[96]. Within the 3ϵFERRO project, Francois *et al* have explored the integration of TiN/HSO/TiN capacitors in 130 nm CMOS node integration. In their work, the authors further demonstrate the use of a Nanosecond Laser Annealing (NLA) to crystallize the films which allows a spatially more precise annealing (see section. 2.3.2).

The objective of this study is to retrieve the role of oxygen vacancies in interface engineered capacitors made of ferroelectric, Si implanted HfO_2 (HSO). The first objective is to engineer the V_O density by varying a Ti intermediate layer thickness between the TiN top electrode and the ferroelectric film created by oxygen scavenging. The second is to investigate the effect of field cycling on the evolution of the V_O densities. The third objective is to determine the band alignment using HAXPES with *in-situ* biasing. Results are expected on migration and increase of oxygen vacancies (V_O) following cycling and polarization reversal to induce changes on the internal potential of the film due to different screening efficiency at interfaces. Finally, the pristine engineered V_O concentration induced by different intermediate Ti thicknesses are expected to allow correlation with the device performance in order to identify the optimal stack.

6.2 Experimental

Three full wafer metal-ferroelectric-metal (MFM) samples were prepared on Si substrates at CEA Leti (Grenoble, France). The stacks, going from the TEs, are as follows: (1) TiN(20 nm)/HSO(10 nm)/TiN(100 nm), (2) TiN(18 nm)/Ti(2 nm)/HSO/TiN and (3) TiN(10 nm)/Ti(10 nm)/HSO/TiN (Fig. 6.1). HfO_2 was grown using ALD. Then, 1% Si content was achieved using ion implantation performed right after HfO_2 deposition . Further details on the stacks fabrication can be found in Appendix. A.

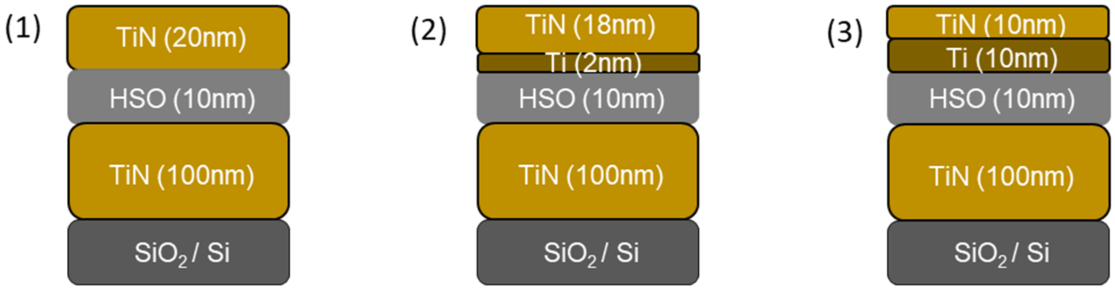

Figure 6.1: *Schematic of the analyzed capacitors*

Top electrodes were then patterned into 100×100 μm^2 devices through photolithography at the nanofabrication facility in CEA Saclay, NanoFab. Specific sample geometry with appropriate screening layers to allow analysis of a single capacitor in a similar way to the patterned HZLO-based capacitors detailed in the previous chapter was adopted. The same lithography steps were used. Floating Ti(10nm)/Au(100nm) pads overlapping the TEs were used for wire-bonding to allow bias application and grounded Ti(10nm)/Au(100nm) on the top of 50 nm thick Al_2O_3 are used to screen bare HfO_2 in horizontal direction and avoid charging effects. The incident X-ray beam is at 20° with respect to the sample surface making its projected size in that direction 250μm, i.e larger than the capacitor. Figure. 6.2 shows a top view optical micrograph images of the patterned devices on each of the three samples.

Samples were finally mounted on the sample holders dedicated for *in-situ* biasing application at the GALAXIES beamline. They present 13 Au electrical pins connected externally through UHV-compatible 13 miniature 50Ω coaxial cables connected to the sample holder's dedicated kit receiver situated on the UHV manipulator. The pins are connected once the sample holder is inserted in its receiver kit. Figure. 6.3a and b show a schematic and an image of the so-called

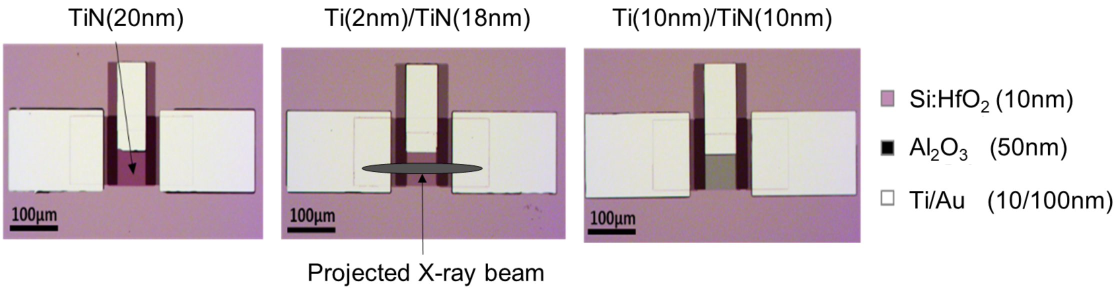

Figure 6.2: *Top view optical micrograph images of the final patterned devices on the three discussed samples. The color legend is given on the right of the figure*

SHOMEC13 sample holder and its corresponding receiver. The connected cables on the HAXPES manipulator at GALAXIES are shown in Fig. 6.3c. At the air side, the vacuum feedthroughs are labeled allowing the connection of the desired pins to an external pulse generator.

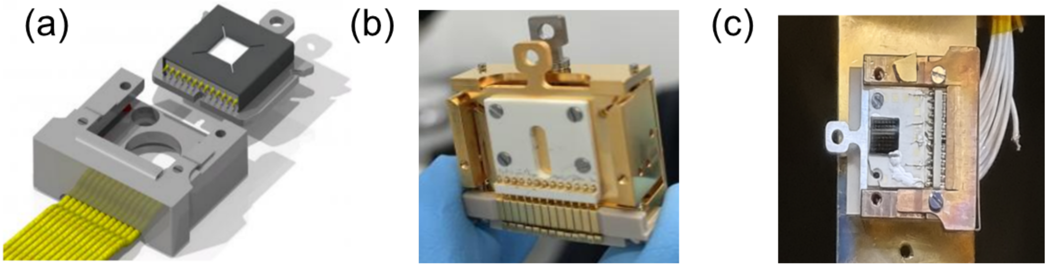

Figure 6.3: *(a) Schematic and (b) an image of the SHOMEC13 sample holder and its corresponding receiver UHV-compatible kit (c) The entire block when inserted in the manipulator of the HAXPES experiment at the GALAXIES beamline*

Several modifications were found to be necessary in order to allow reliable micro-wire bonding to the available pins. Figure. 6.4 shows the adopted approach. It consists in the addition of an intermediate bonding stage permanently connected on the alumina insulator block of the sample holder (white color in Fig. 6.3). 1 mm^2 pads made of 20nm Ti/100nm Au were deposited using electron beam evaporation. The 20 nm thick Ti is used to ensure a good adhesion of the Au to the alumina surface. The intermediate stage was connected using metallic wires fixed between the inner part of the pins and the 1 mm^2 Au pads using Sn soldering and conductive EpoteK at each side, respectively. Figure. 6.4 shows the modified sample holders with the new permanent intermediate stage. Devices of interest on the sample are then connected to the pins through micro-wire bonding to the corresponding Au pads.

Before introducing the samples in the UHV chamber of the GALAXIES beamline, pristine, woken-up and fatigue states were achieved by cycling three devices *ex-situ*. The cycling and DHM pulses are always applied to the top electrode while keeping the bottom electrode grounded. The connection to the bottom electrode was established through hard breakdown of the big capacitor present at the corner of each sample. The latter is then connected to one of the electrical pins via silver paste to a corresponding Au pad. Figure. 6.5 shows images from the

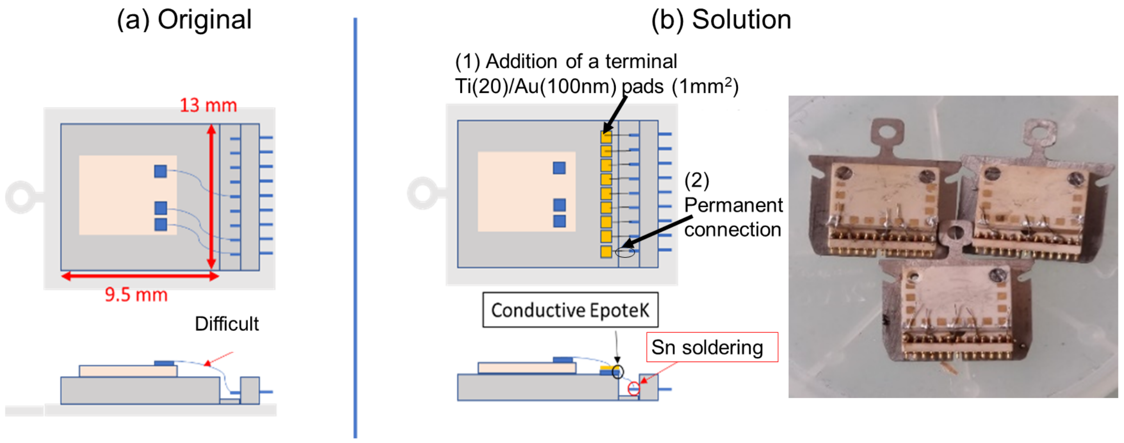

Figure 6.4: *(a) Schematic showing the encountered difficulty of microwire bonding directly on the electrical pins and (b) the adopted solution with the addition of a intermediate bonding stage (1 mm^2 Au pads) and the permanent pin connection*

mounted samples. The coloured circles indicate the position of the interested cycled devices and the connection of the bottom electrode via silver paste is also indicated by the black arrows.

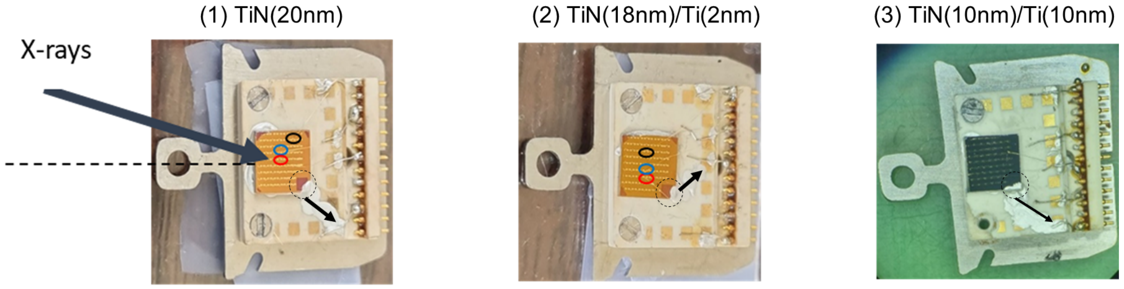

Figure 6.5: *Images of the mounted samples on the SHOMEC13 samples holders ready for HAXPES with in-situ applied bias at GALAXIES. The black, blue and red circles indicate the position of the pristine, woken-up and fatigued capacitors. The black arrows show the connection of the bottom electrode via silver paste*

6.3 Electrical characterization

First, different cycling pulse widths and amplitudes were tested to decide about the optimal cycling pulse characteristics. Figure. 6.6a compares the evolution of the memory window (MW) using rectangular pulses with voltage amplitudes ranging from 2 to 4V at a fixed pulse duration of 10μs. The results indicate that for the wake-up case, which corresponds to the increase of the MW, a higher promotion is achieved using higher voltages. However, the cycle to breakdown (CBD) number is on the other hand much lower. At 3V, a maximum CBD value of 10^6 is obtained while at 2 and 2.5V the device still in operation even after 10^8 cycles. The use of 2.5V was therefore chosen as an optimal pulse amplitude as it allows the visualization of a more considerable wake-up effect than 2V and a broader fatigue regime on the same device. Similarly, the pulse frequency was varied between

10 and 100kHz. The effect was checked on CBD using already woken-up devices as shown in Fig. 6.6b. At 100μs switching time, a CBD value of 10^7 was obtained. Lower switching times of 50 and 10μs allows as for them an endurance up to 10^8 cycles. However, at 10μs, the MW is higher than with 50μs after 10^8 cycles. The results shown in Fig. 6.6 are recorded from the sample without any Ti scavenging layer. The trend was also checked on the 2nm thick Ti sample and similar results were obtained. The optimal rectangular pulse characteristics for cycling was therefore chosen to be 2.5V amplitude and 10μs width. This is consistent with the results reported by Francois *et al* on the switching efficiency in similar HSO-based devices by varying similarly the pulse width and amplitude. On similar 100×100μm^2 capacitors, the same pulse characteristics, i.e 2.5V and 10μs are found to allow optimal efficiency[96]. At higher voltages and at lower switching speed, the ferroelectric domains present a higher response but the endurance is reduced resulting in significantly lower CBD.

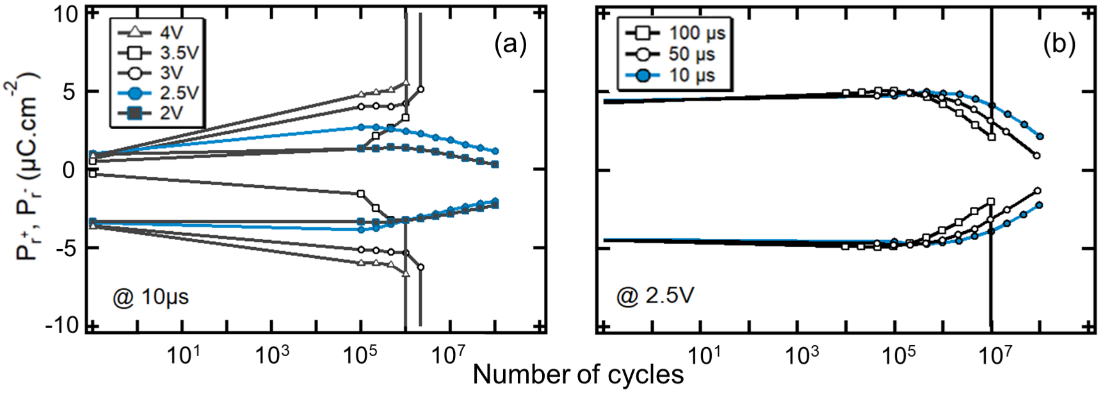

Figure 6.6: *(a) Cycling pulse amplitude and (b) pulse width effects on the field cycling behavior of TiN/HSO/TiN capacitors*

The I-V and P-V response from the samples are now addressed. Figure.6.7 shows the obtained results with the 0 and 2nm Ti samples. Three distinct cycling stages were used for each: Pristine (1 cycle), wake-up (10^5 cycles) and fatigue (10^8 cycles). Table. 6.1 summarizes the MW and the E_c values from each one of the capacitors.

Table 6.1: *The memory window and coercive field values from the three cycled capacitors on the 0 and 2 nm Ti samples*

		MW (μC.cm^{-2})	E_C (MV.cm^{-1})
0 Ti	Pristine	6	0.62
	Woken-up	13	1.24
	Fatigue	4	0.60
2nm Ti	Pristine	17	1.11
	Woken-up	30	1.45
	Fatigue	14	1.05

The sample without a Ti scavenging layer shows a pristine memory window of 6μC.cm^{-2}. Similar values are reported by François *et al*[232, 96]. With the addition of 2nm thick Ti layer between the ferroelectric layer and the TE, this increases to 17 μC.cm^{-2}. In both stacks, the pristine state shows a double current

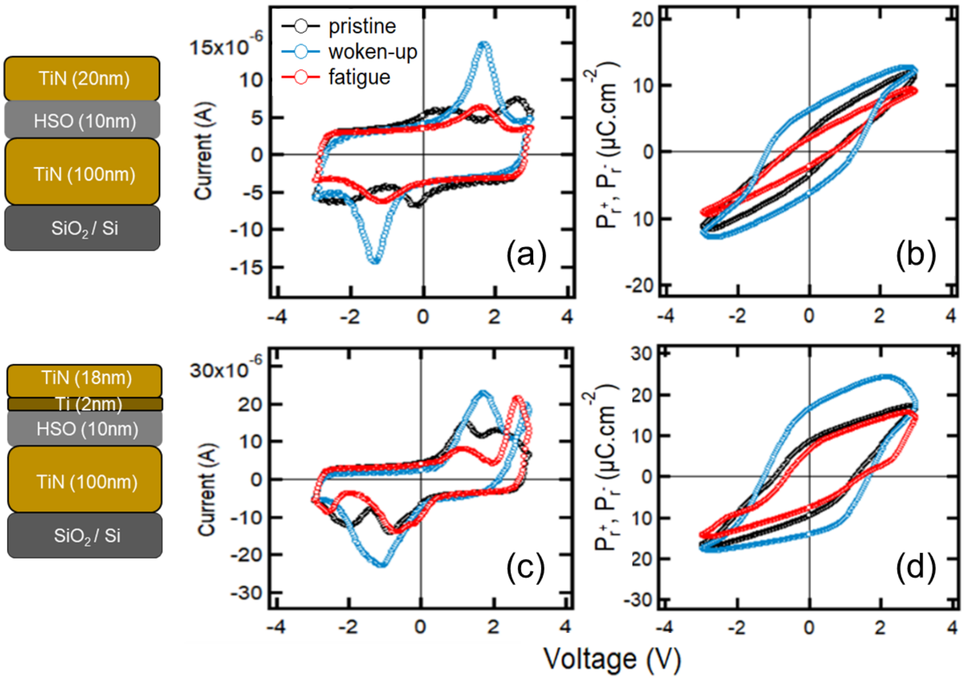

Figure 6.7: *I-V and the corresponding P-V curves respectively from (a,b) 0 Ti and (c,d) the 2 nm Ti scavenging layer thickness samples. DHM are recorded using ±3V/1kHz and cycling using ±2.5/100kHz pulses. The different cycling stages are highlighted using different colors*

peaks in both positive and negative bias direction which results in pinched hysteresis loops. After 10^5 cycles, the 2P$_r$ values increase from 6 to 13 and from 17 to 30μC.cm^{-2}, with respectively 0 and 2 nm Ti. This is characteristic of the wake-up behavior. Further cycling to 10^8 cycles, back reduces the MW to 4 (0 nm Ti) and 14μC.cm^{-2} (2 nm Ti). The E_c values, following the trend of the MW, are also higher in the devices prepared with 2nm Ti scavenging layer. With woken-up capacitors, E_c increases by $\sim$200 kV.cm^{-1}. In addition, the 2 nm Ti sample shows also more imprinted hysteresis loops toward positive bias direction. The two effects might be linked to a higher density of V_O induced by the scavenging layer. On one hand, higher V_O is beneficial in stabilizing higher orthorhombic phase which may explain the MW increase while on the other hand more V_O may further pin the domains increasing thus the E_c and the imprint behavior. The imprint field magnitude with the pristine capacitors are 50 (0 nm Ti) and 150 kV.cm^{-1} (2 nm Ti). Figure. 6.8 shows the I-V response from the 10 nm Ti sample. The current profile recorded from all the prepared devices showed the same leaky behavior. In order to check if this is in some how related to the lithography process, a mesa structure, was further prepared from the same stack and checked. A mesa structure means that the film outside the capacitor is etched until the Si substrate to avoid any possible leaky paths from the surrounding area[118]. With the initial HAXPES structure, the etching involves only the TE. The results are identical. A leaky behavior is always obtained using this stack. It seems therefore that this likely intrinsic to the sample due to the thick Ti scavenging layer resulting in important V_O densities and the creation of conductivity paths or by filamentary conductors as in resistive RAMs.

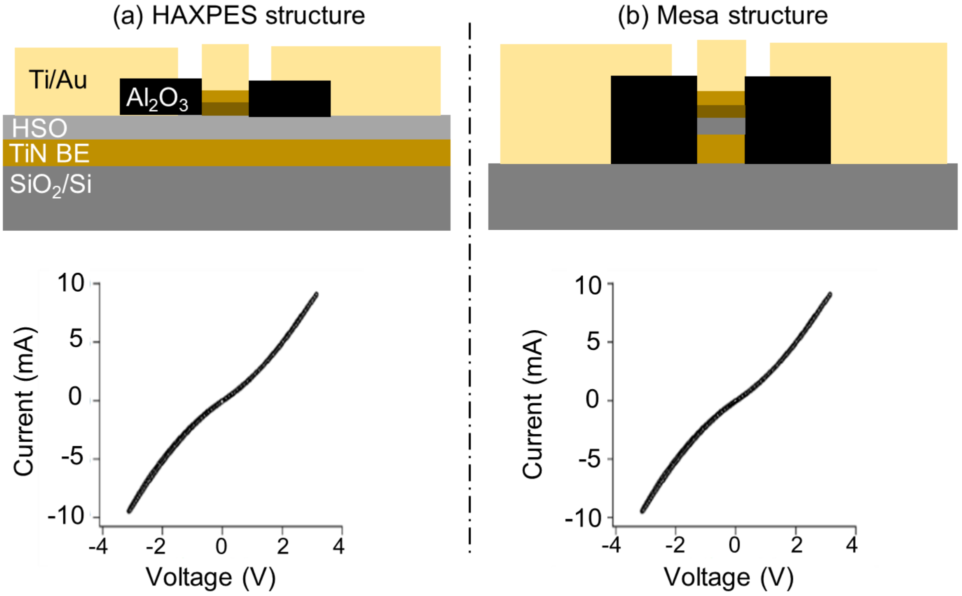

Figure 6.8: *(a) HAXPES and (b) mesa structure prepared from the 10nm Ti sample and the corresponding I-V response to a DHM pulse suggesting an intrinsic leakay behavior of the stack*

6.4 HAXPES results

Hard X-ray Photoelectron Spectroscopy (HAXPES) was carried out at room temperature using two photon energies of 7 and 9 keV at the GALAXIES beamline described in section. 3.3.3. The energy resolution was 160 and 190 meV for 7 and 9 keV, respectively. Figure. 6.9 presents the procedure used to find the exact coordinates of the cycled devices on the 5$\times$5mm^2 sample *in-situ*. First, Fig. 6.9a shows the different axes of the possible manipulator movements. The sample normal is in the plane of the paper. Rz corresponds to the rotation of the sample relative to the incident beam and thus defines the incident X-ray angle. tx represents the distance from the analyzer. The axes tz and ts represent movements in vertical and horizontal directions relative to the electron analyzer, respectively. The arrows indicate the direction of each movement. By fixing Rz and tx, the procedure consists of scanning the entire sample area following the tz and ts directions while acquiring specific core level lines (Hf 3$d_{5/2}$, Ti 1*s* and Au 4*f*) in order to map the sample devices. This allows the extraction of the profiles shown in Fig. 6.9c and d, which in turn enable to find the capacitor coordinates. Figure. 6.9b shows the lithography schematic of the 5$\times$5mm^2 sample with 61 patterned devices. The capacitors were labeled from 1s to 9s in vertical direction as there is 9 lines and from z1 to z7 in the horizontal direction. An increase of the ts position at fixed tz value corresponds to scanning from the right to the left side of the samples while an increase on the tz axis at a given ts value, corresponds to moving the sample down in a way that the first detected Ti peak corresponds to the last line of capacitors labelled 9s. Figure. 6.9c and d show the obtained core level profiles along ts and tz at fixed tz and ts values of 257.8 (4th line) and 227 mm (4th column), respectively. The obtained number of devices on each line and column is in accordance with the available devices. This allows to precisely determine the coordinates of the cycled capacitors.

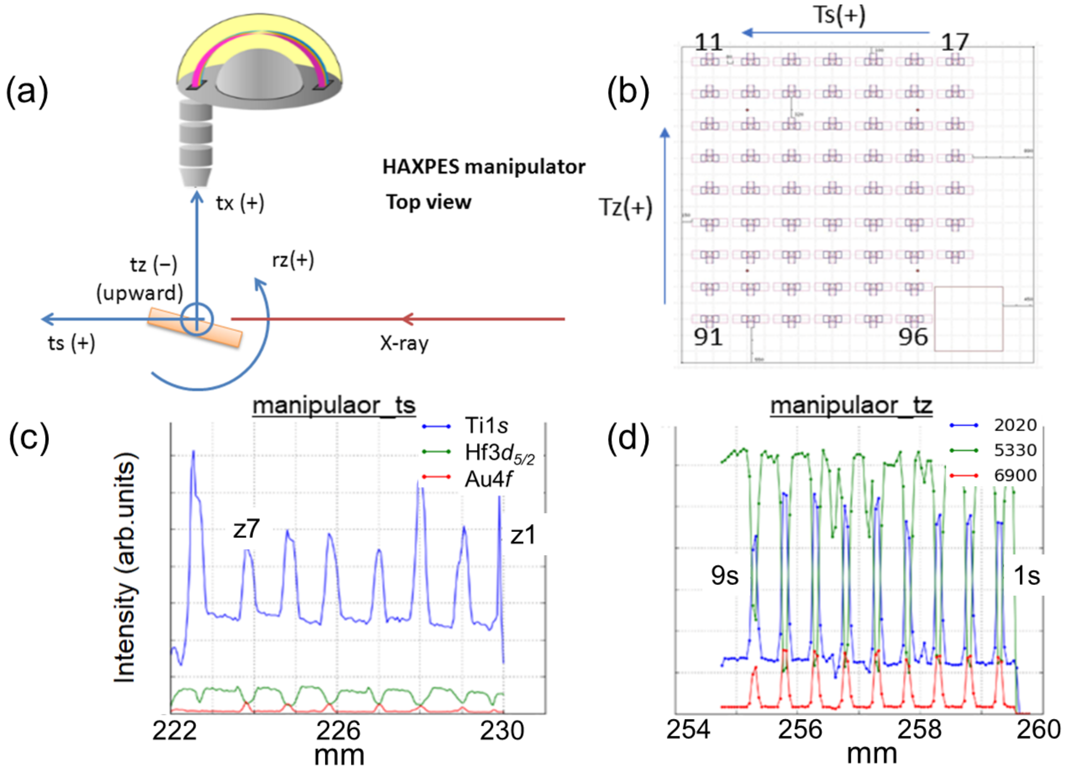

Figure 6.9: *(a) Schematic of the UHV-manipulator axes (b) a schematic of the patterned devices on 5×5mm*^{2} *sample (c and d) Specific core levels profiles along* ts *and* tz*, respectively*

Knowing the exact positions, the X-ray beam can be then directed thanks to the high precision of the manipulator. The survey spectra taken from the devices on each sample are presented in Fig. 6.10. The expected Hf, O, Ti and N core levels are clearly visible, no evidence for contamination.

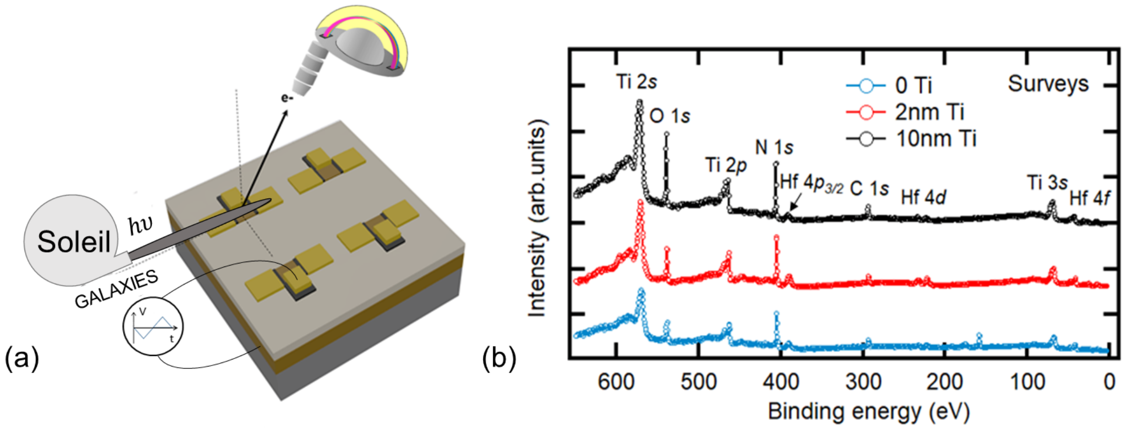

Figure 6.10: *(a) Schematic of the analyzed sample at the GALAXIES beamline and (b) survey spectra recorded at 9 keV from the 0, 2 and 10 nm Ti samples*

6.4.1 Effect of Ti scavenging layer on the as grown V_O distribution

To address the effect of additional Ti layer between the HSO and the TiN TE on the defect chemistry, Ti 1*s* and Hf 3$d_{5/2}$ core levels were recorded at 9 and 7 keV photon energies, respectively. The correspnding IMFPs using these energies are, respectively, $\sim$6 and 7.5 nm. Thus, this provides the best sensitivity to the interface chemistry while maintaining high signal. Figure. 6.11 show the results obtained from the pristine devices. First, the Ti 1*s* spectra reveal the presence of three components assigned to metallic TiN, an oxynitride phase (TiON) and to a suboxide phase (TiO$_X$) situated at BEs of 4965.5, 4966.5 and 4968.5, respectively. Comparison between these spectra indicates enhanced oxidation of the Ti when increasing the Ti layer thickness. The oxides (TiON and TiO$_x$) to the metal ratio evolves from 66.5, 73 and 81% when passing from 0, 2 and 10nm thick Ti, respectively. Both the TiN and the oxynitride phase decrease with increasing Ti. The TiON component is principally due to TiN oxidation at the interface. The addition of a Ti layer between TiN and the HfO$_2$, enhances the scavenging effect resulting in an increase of the TiO$_x$ rather than the TiON.

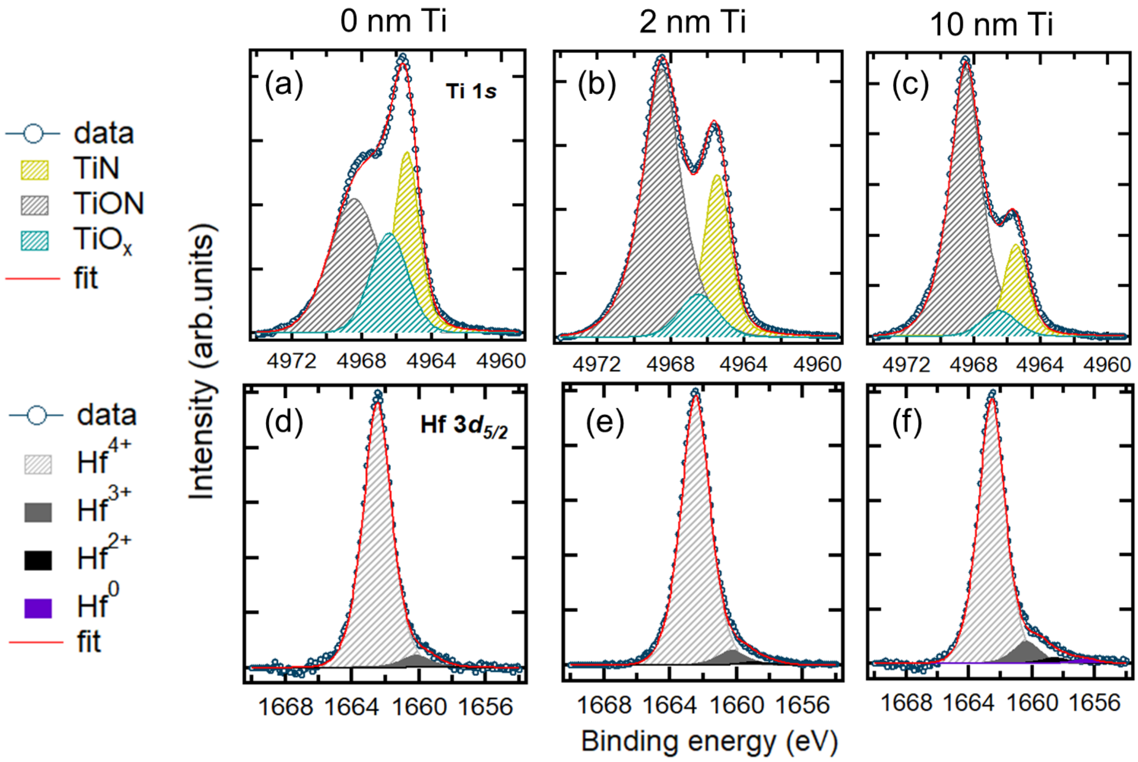

Figure 6.11: *(a,b,c) Ti 1s core level spectra at 9 keV and (d,e,f) Hf 3*$d_{5/2}$ *core level spectra recorded at 7 keV photon energy from the 0, 2 and 10 nm Ti samples, respectively*

The Hf 3$d_{5/2}$ spectra show in their turn a significant asymmetry toward low binding energies. This hints toward a significant reduction of the Hf cations. Similar asymmetry in Hf4*f* spectra recorded from HSO films by laboratory-XPS have already been reported[233]. The degree of asymmetry also increases with the Ti layer thickness. With no Ti interlayer, only a Hf^{3+} was detected at 2 eV from the stoichiometric peak which is situated at 1662.5eV. However, a better fitting is obtained by adding a second low E_B component in the case of 2nm Ti and even a third one with the 10nm thick Ti case. Higher reduction is consistent with a higher V_O amount at the interface. We attribute these componenets situated at 3.5 and 4.5 from the stoichiometric Hf^{4+} peak to Hf^{2+} and Hf^{0}, respectively. Giving that Hf^{2+} and Hf^{0} are reduced by 2 and 4 electrons, respectively, and that a V_O gives two electrons, the $V_O^{\cdot\cdot}$ concentration was derived from the reduced hafnium intensities as follows:

$$V_O^{\cdot\cdot}(\%) \sim \frac{1}{4}[\frac{1}{2}(\frac{I_{Hf^{3+}}}{I_{tot}}) + \frac{I_{Hf^{2+}}}{I_{tot}} + \frac{2I_{Hf^{0}}}{I_{tot}}] \tag{6.1}$$

The fitting results including the oxides to metal ratios derived from the Ti 1*s* spectra and the percentage of reduced hafnium with respect to the total Hf intensity in addition to the resulting $V_O^{\cdot\cdot}$ concentrations are shown in Table. 6.2. The table also includes the MW obtained from the pristine devices.

Table 6.2: *I_{oxides}/I_{TiN} (%), MW, the reduced Hf intensity (% of the total Hf intesnity) and the derived $V_O^{\cdot\cdot}$ concentration (in %)*

Ti layer (nm)	MW (μC.cm^{-2})	I_{oxides}/I_{TiN}	$I_{Hf^{3+}}$	$I_{Hf^{2+}}$	$I_{Hf^{0}}$	$V_O^{\cdot\cdot}$
0	6	66.5	4.3	-	-	0.54
2	17	73	5.1	1.0	-	0.89
10	leaky	81	7.4	1.9	1.4	2.1

A progressive increase in the oxygen vacancy was indeed found by increasing a scavenging layer at the interface. With 0, 2 and 10nm Ti, the $V_O^{\cdot\cdot}$ concentration is ~0.54, 0.89 and 2.1%, respectively. The increase of $V_O^{\cdot\cdot}$ from 0.54 to 0.89 my be behind the increased MW from 6 to 17 μC.cm^{-2}. Oxygen vacancies are known to stabilize the polar orthorhombic phase increasing the volume of switchable domains and thus increasing the 2P$_r$ value[144, 116]. The highest hafnium reduction is obtained with 10 nm Ti intermediate layer. The spectrum reveals even the presence of metallic hafnium (in purple) indicating enhanced oxygen scavenging and may behind the leaky, near ohmic, behavior of all the prepared capacitors on this sample with the HAXPES and mesa structures as shown in Fig. 6.8.

A controlled thickness of a Ti layer at interfaces seems therefore be a tool to control the oxygen scavenging and hence engineer the V_O density which in turn can be used to optimize the ferroelectric response of the device. Our results reveal that 2 nm thick Ti layer at the top interface is the optimal choice in HSO-based capacitors.

6.4.2 Effect of field cycling on V_O

The effect of field cycling on the overall V_O concentration was investigated by analyzing the HAXPES Hf 3$d_{5/2}$ spectra from the pristine, woken-up and fatigued devices at 9 keV, i.e representative of the entire film thickness. The IMFP of Hf 3$d_{5/2}$ using this energy is ~9.5 nm (3$\lambda \sim$ 28.5 nm). The results are shown in Fig. 6.12 and the obtained $V_O^{\cdot\cdot}$ concentrations (in %) are also included.

Figure. 6.13 plots the evolution of V_O concentration upon cycling. The result obtained from the as-grown device with the 10 nm Ti (not cycled due to the excessive leakage current) is also included and shows the highest V$_{O]}$ concentration.

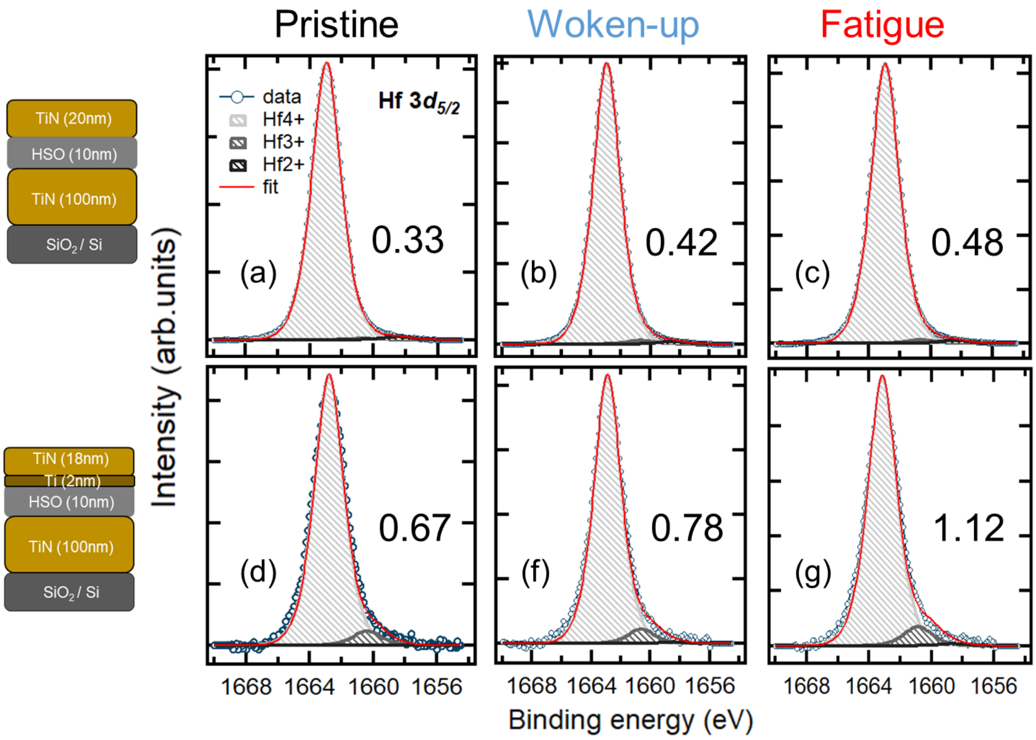

Figure 6.12: *Hf 3$d_{5/2}$ spectra recorded at $h\nu$=9keV from the pristine, woken-up and fatigued capacitors with the 0 and 2nm Ti samples*

After wake-up (for the 0 and 2 nm Ti samples), the V_O concentration increases in both samples which is consistent with the results obtained with HZLO-based capacitors. At the same time, the MW increases from 6 to 13 (0nm Ti) and from 17 to 30μC.cm^{-2} (2nm Ti). Generation of more V_O and their subsequent redistribution under repeated cycling is the most possible explanation of the increased vacancy value and the wake-up behavior. This depinches the domains (highly pinned at the pristine state) and increases the stability of the o-phase within local non-polar portions near the interface and within the bulk of the film. This redistribution and indirect field induced phase stabilization by the mean of V_O was already proposed to explain this phenomenon[144, 140]. A higher amount of V_O is also at the origin of fatigue (decrease of the MW) due to increased domain wall pinning[143]. This will continuously increase while cycling until hard breakdown occurrence. Our results suggest that a 2 nm Ti layer integrated into HSO-based capacitors allows broader MW than 0 nm Ti and the optimal V_O content in such device, corresponding to the average concentration across the film after wake-up, is around ~0.8% (2.4×10^{20} cm^{-3}).

6.4.3 Polarization-dependent band diagram

We now tackle the impact of polarization reversal on the interface electronic structure of the optimal devices (after wake-up) and specifically on the Schottky barrier height for electrons (φ_{Bn}) which highly impact the charge injection and the ferroelectric stability. Triangular pulse of ±3V amplitude and 1ms duration was applied to the top electrode to switch the polarization vector . A RIGOL DG3061A function

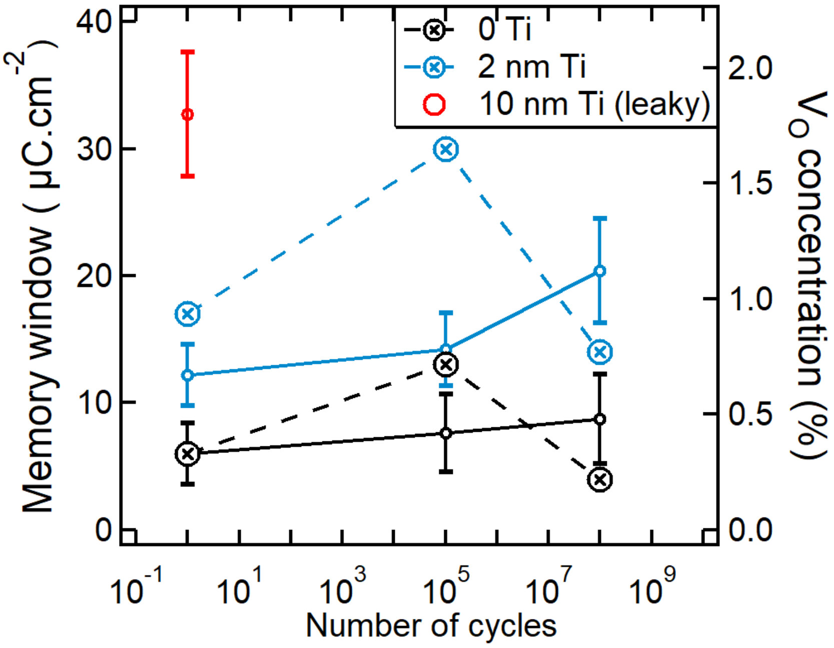

Figure 6.13: *Evolution of the MW and the averaged V_O concentration within the 10 nm films as a function of field cycling with 0 and 2nm Ti samlpes*

generator was used to provide such signal and the large amplitude signal is used to ensure no back-switching. After bias application, all pins are gounded to avoid charging effects or floating potentials which might induce additionnal shifts in the spectra. Table. 6.3 shows the measured E_B values of the Hf 3$d_{5/2}$ peaks for the P↑ (P↓) polarization states taken from the woken-up capacitors in both 0 and 2 nm Ti samples. Binding energies were calibrated relative to the metallic TiN component at 4965.5eV. Near the top interface, the Hf 3$d_{5/2}$ shifts downward in both samples by 100 meV towards E_F when switching from P↑ to P↓ state. At 9 keV, the E_B represents the average value along the film thickness and no change was noticeable upon polarization switching for the 0 nm Ti case whereas 150 meV downward shift is detected for the 2 nm Ti stack. With 10nm Ti, as all the devices are leaky, the analysis was done on a single device without poling but using the 2 photon energies. The obtained E_B values are 1664.10 (7 keV) and 1663.40 eV (9 keV).

Table 6.3: *Hf 3$d_{5/2}$ core level binding energies at P↑ and P↓ states from the 0 and 2nm Ti samples using 7 and 9 keV photon energies*

Ti layer (nm)	0 Ti		2nm Ti	
$h\nu$	7 keV	9keV	7keV	9keV
E$_B$ (P↑)	1662.50	1662.40	1662.70	1662.45
E$_B$ (P↓)	1662.40	1662.40	1662.60	1662.30

The binding energies values indicate that the Hf core level lines are in both samples closer to the E_F using 9 keV photon energy suggesting less n-type doping of the entire film with respect to the top interface. This is in accordance with the higher V_O concentration obtained at 7 keV (Fig. 6.11 and 6.13). The φ_{Bn} values at the top interface are calculated using the Kraut method using the binding energies at 7 keV shown in Tab. 6.3. The energy separation between the Hf emission and the valence band maximum (VBM) in bare HSO area was calculated to be 1659.3 eV (Hf 3$d_{5/2}$ at 1662.4 and the VBM at 3.1eV). For the determination of the φ_{Bn} value at the bottom interfaces, we first assume a linear electrostatic potential within the film and that the obtained E_B value at 9 keV are the mean value between the top and bottom interfaces. Thus, we estimated the E_B value at the bottom interface as (2E_B(9keV) - E_B(7keV)). This gives E_B values at the bottom interface of 1662.30 (P↑) and 1662.40(P↓) with the 0 Ti samples and 1662.20 (P↑) and 1662.00 (P↓) with the 2 nm Ti case. Finally, taking E_g=5.6eV, the band offset determination is straightforward. The band alignment diagrams of the three samples (after wake-up for 0 and 2nm Ti) are schematically shown in Fig. 6.14.

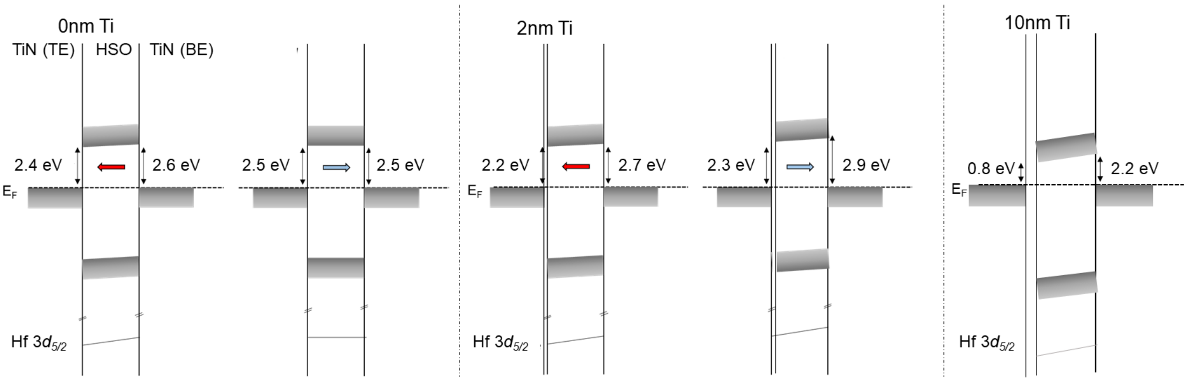

Figure 6.14: *Polarization-dependent band alignement from woken-up devices related to the 0 and 2 nm Ti samples in addition to the band diagram of a capacitor containing 10 nm Ti at the top interface*

First, the φ_{Bn} values without any Ti added layer, are in accordance with values obtained with HZLO/TiN interfaces. Adding 2nm Ti decreases the φ_{Bn} at the top interface by 0.2 eV for both polarization directions. This potential barrier decrease is possibly related to the higher V_O concentration near that interface. For all samples, φ_{Bn} is lower at the top interface than the bottom interface. This downward band bending hints toward a higher electron accumulation at the top interface. At the bottom interface, the φ_{Bn} decreases by of 0.1 eV upon polarization reversal with 0 nm Ti and increases by 0.2 eV with the 2nm Ti sample. As this band diagram is from woken-up devices, the initial higher V_O concentration and the subsequent redistribution with cycling in the 2 nm case may lead to different screening efficiency at the bottom interface with respect to the sample without Ti as observed at the top interface. In all cases, the two samples are functional as back to back Schottky diodes with an upward internal potential going deeper into the film. This would give an internal fiel pointing toward the top electrode as suggested by the positive imprinted hysteresis loops. The potential sign is also intendent of the polarization direction. In the case of 10nm Ti, a significant decrease of φ_{Bn} (0.8 eV) occurs mainly at the top engineered interface. This is mainly due to the higher V_O concentration found with this sample resulting in severe electron trapping and more steeper upward electrostatic potential within the insulator.

6.5 Conclusions

In conclusions, we have analyzed the chemical and electronic phenomena involved in the insertion of different Ti scavenging layer thicknesses between a TiN TE and a technologically relevant Si implanted $\mathrm{HfO_2}$-based ferroelectric capacitors annealed by BEOL-compatible nanosecond laser annealing. Hard X-ray photoelectron spectroscopy was used using two photon energies to conduct a non-destructive and depth-dependent investigations of the different effects. Specific attention was paid to produce specific geometry allowing analyzes of a single device with *in-situ* biasing conditions. First, increasing a Ti layer thickness induces higher oxidation of the electrode material and higher V_O densities due to the scavenging effect. This has a direct impact on the memory window of the device. With 0 and 2 nm Ti, we measured a V_O concentration of $\sim$0.5 and 0.9% which translates in an increased MW value at the pristine state from 6 to 17.cm^{-2}. With 10nm Ti, a metallic Hf signature was observed and a higher amount of V_O was derived ($\sim$2.1%). Devices made from this stack following different patterning strategies were all found to be leaky. The results indicate that 2nm Ti is an optimal choice to engineer the MW to an optimal value by means of V_O. Analysis of the field cycling effects indicates, in a similar way to the HZLO capacitors, that wake-up is accompanied by an increased amount of V_O within the film due to new generated ones at the beginning of cycling near the top interface and their subsequent redistribution under repeated cycles at releatively high fields (3MV.cm^{-1}). Finally, the polarization-dependent band alignment of the discussed samples in their optimal performance was investigated. A back to back schottky diodes functionality was derived with SBHs values close to that found with HZLO were obtained. This methodology allows the extraction of the electrostatic potential profile within the ferroelectric (even with just 2 points) and revealed that the latter does not change in sign with polarization and hints toward the presence of an internal field pointing toward the top electrode, also visible by the electrical characteristics.

Conclusions $\&$ perspectives

In conclusion, nanometer scale ferroelectric Hf$_x$Zr$_{1-x}$0$_2$ based capacitors show electrical performances which are highly dependent on different physico-chemical factors. TiN and W electrodes were found to induce different chemical and electronic effects at interfaces in pristine HZO-based capacitors. Under 600°C rapid thermal annealing temperature in N$_2$ atmosphere, the TiN top electrode scavenge more oxygen atoms than W thanks to the higher oxygen affinity. The measured V_O density at the first nanometers of the ferroelectric film are $\sim$3.4$\times$10^{20} and below 5$\times$10^{19} cm^{-3} with TiN and W electrodes, respectively. This increases the potential barrier height for electron transport (φ_{Bn}) at the interface from 2.05 to 2.30$\pm$0.3 eV. Higher annealing temperature at T$_{RTA}$=1000°C, increases the n-type doping at the top TiN/HZO interface and φ_{Bn} decreases to 1.83$\pm$0.3eV. Oxygen scavenging is found to occur mainly at the top interface, promoted by thermal energy resulting in $\sim$1nm oxynitride layer and oxygen-deficient HZO layer. At the bottom interface, HAXPES analyzes revealed, however, a thicker sub-oxide layer ($\sim$3nm) and lower V_O content. This sub-oxide layer was suggested to be the result of contact with air and the first oxygen pulses of the ALD-growth sequence. It passivates the electrode and acts as a diffusion barrier, impeding oxygen scavenging.

La doping in HZO-based capacitors have been subjected to advanced characterization through soft and hard X-ray photoelectron spectroscopy in addition to electrical measurements. XPS analysis revealed an upward band bending toward E_F when increasing La doping, characteristic of p-type doping. Negative La impurities and positively charged V_O are thus mutually screened. However, the depth-dependent XPS measurements suggested that this may be dependent on the defective state of the HZO film and the chemical environment of the introduced La. In oxygen-poor environment, La doping is ionically screened by available V_O and the overall V_O concentration drops thanks to the extra oxygen atoms provided by La$_2$O$_3$ layers during growth. In oxygen-rich portions of the film, 2 La impurities induce a new V_O site. In addition, La was found to decrease the trap energy level of positively charged V_O with respect to the conduction band minimum. The leakage current reduction induced by La seems to be linked rather to the screening of V_O impeding electron trapping and/or due to lower trap concentration. Thanks to the lower leakage current, La doped HZO-based capacitors present higher endurance cycling than the undoped case and are therefore very attractive for future eNVM applications. However, a higher wake-up number of cycles are needed ($\sim$10^6 cycles). HAXPES with *in-situ* biasing was performed to further evaluate the effects of field cycling and polarization reversal. A correlation between the V_O densities and the electrical characteristics was obtained. The results suggest that wake-up is due to generation, redistribution and homogenization of V_O along the film thickness. Lower asymmetric charge trapping, domain wall depinning and local increase of the polar orthorhombic phase fraction are the most possible consequences of the measured V_O profiles and the wake-up behavior. The optimal memory window of the device with 35μC.cm^{-2} is obtained at an averaged V_O density from the entire film thickness of $\sim$2.7$\times$10^{20} cm^{-3}. The φ_{Bn} at both interfaces in optimal TiN/La:HZO/TiN operation are 2.5 (2.7) and 2.8 (2.4$\pm$0.2) eV, at the top (bottom) interfaces and for P$\uparrow$ and P$\downarrow$ states, respectively. The distinct chemical interfaces did not affected the effective screening length of the polarization bound charges and the derived electrostatic potential profile is in qualitative agreement with the imprint fields detected from the hysteresis loops.

Similar HAXPES with *in-situ* bias were used to investigate the chemical and electronic phenomena involved in the insertion of varying Ti scavenging layer thickness between a TiN TE and another technologically relevant Si implanted HfO_2-based ferroelectric capacitors crystallized via BEOL-compatible nanosecond laser annealing. Increasing a Ti scavenging layer allowed to engineer the V_O density at the interface and within the film upon field cycling. This was found to have a direct impact on the memory window of the device. With 0 and 2 nm Ti, the measured V_O densities are of $\sim$2.4 and 4.3$\times$10^{20} cm^{-3} corresponding to a 2P$_r$ increase, at the pristine state, from 6 to 17μC.cm^{-2}, respectively. With 10nm Ti, a metallic Hf signature was observed and a higher amount of V_O was obtained resulting in a non-rectifying contact (nearly ohmic) with HfO_2. The result indicate that 2nm Ti is an optimal choice to engineer the memory window by the mean of V_O. Analyzes of the effect of cycling indicate, in a similar way to the HZLO capacitors, that both wake-up and fatigue are accompanied with an increased amount of V_O. The φ_{Bn} at both interfaces in optimal TiN/Ti(2nm)/Si implanted HfO_2/TiN capacitor operation are 2.2 (2.7) and 2.3 (2.9$\pm$0.2) eV, at the top (bottom) interfaces and for P$\uparrow$ and P$\downarrow$ states, respectively.

The exploitation of photoemission spectroscopy and microscopy techniques is further needed to provide a fully systematic evaluation of the ferroelectric, chemical and electronic properties of HfO_2 based films to be integrated into advanced technology nodes as the active element in non-volatile memory cells in addition to other promising ferroelectric materials for eNVM applications such as AlScN. During the synchrotron campaigns, the objectives of the thesis within the framework of the European project 3ϵFERRO, were focused on technologically aspects like the effects of field cycling and polarization reversal. However, further beamtimes could be devoted to study more accurately, for instance, the internal potential within these films by studying less parameters and focusing on obtaining higher density experimental points from different probing depths of the core level lines emission in order to accurately map band bending, oxygen vacancy concentration profiles and evaluate the chemistry of interface layers. Instead of varying photon energies, analyses can be performed at different emission angles. Standing-wave HAXPES can also be a perfect option as it allows the access to different probing depths and has already been reported with films for logic and memory applications. In our case, two experimental points allowed the derivation of φ_{Bn} at interfaces and to draw the potential within the insulator. In HZLO, the electrostatic potential changes sign, while it does not in Si implanted HfO_2 upon polarization reversal. More experimental points would allow the identification of the presence of depletion layers and the quantification of space charges by modeling the recorded rigid band shifts using Poisson equation providing further information on the ferroelectric film physics[234]. The derived space charge densities can be compared to the obtained results from the fitting procedures of core level spectra and the indirect calculation from the reduced cations signature. With the improvements of the growth techniques and the wider knowledge acquired with hafnia films, the stabilization of monocrystalline films would also allow dispersion measurements, which could give valuable information on V_O energies within the band gap and the overall electronic structure of the material. Time-resolved measurements are also needed to obtain closer insights on the mechanisms involved during the polarization switching.

Appendix A

Sample preparations and preliminary analyzes

A.1 TiN/$Hf_{0.5}Zr_{0.5}O_2$/TiN capacitors

The analyzed TiN/HZO/TiN capacitor samples discussed in section. 4.2 were provided by NamLab, Germany. The samples consist of planar capacitor structures deposited on p-type doped Si/SiO_2 substrate. The bottom TiN electrode is 9 nm thick with a RMS roughness of 0.7 nm. 10 nm thick $Hf_{0.5}Zr_{0.5}O_2$ (HZO) was grown by tomic Layer Deposition (ALD) in an Oxford Instruments OpAL ALD tool at $T_{deposition}$=300°C using Tetrakis(ethylmethylamido) hafnium (IV) $Hf(N(CH_3)(C_2H_5))_4]$ and $Zr[N(C_2H_5)CH_3]_4$ organic precursors for Hf and Zr, respectively, while ozone was used as an oxygen precursor. The HfO_2 and ZrO_2 layers were deposited at 1:1 cycle ratios to achieve $Hf_{0.5}Zr_{0.5}O_2$. A 2 nm thick TiN top electrode was then deposited. The bottom and top TiN electrodes were grown by physical vapor deposition (PVD) sputtering in a Bestec ultrahigh vacuum (UHV) sputter cluster at room temperature from a Ti target. Finally, in order to stabilize the polar o-phase (P*ca*2_1), the sample was annealed by rapid thermal annealing for 20s at T_{RTA}=600°C in N_2 atmosphere after the top electrode deposition. To check the effect of the annealing temperature, a further sample was crystallized with higher RTA temperature of 1000°C for 1s.

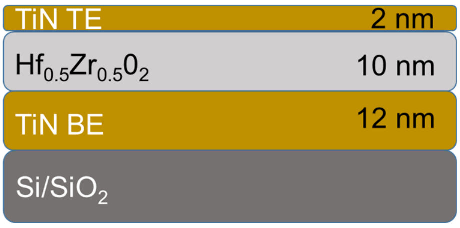

Figure A.1: *Schematic of the analyzed TiN/HZO/TiN capacitor samples analyzed in section. 4.2. Two RTA temperatures were used: 600°C for 20s and 1000°C for 1s both in N_2 atmosphere*

Conductive Atomic Force Microscopy (C-AFM) was used to qualify the uniformity of the used 2 nm TiN TE prior to the XPS analyzes and to verify that there are no pinholes and that the XPS will indeed probe only one single, buried interface between HZO and the top electrode. C-AFM experiments were done with a

Bruker microscope using an n-doped silicon tip coated with a thin layer of Pt/Ir in the contact mode. The current profile was measured by applying a constant bias between the conducting cantilever tip and a silver paste deposited on the surface of the electrode. The back plane of the sample was isolated in order to probe just the in-plane conductivity of the top electrode.

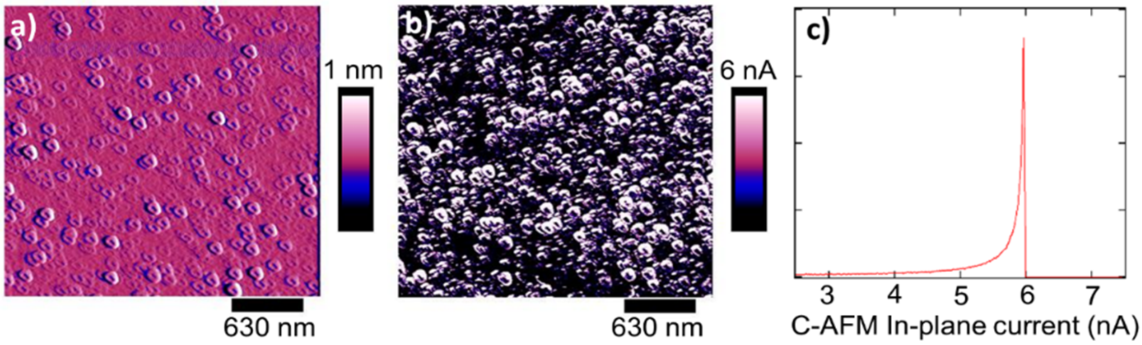

Figure A.2: *(a) Topography of the TiN top electrode surface, (b) C-AFM in-plane current profile of the TiN surface (3×3 μm^2 scan/U=15 mV), and (c) current histogram corresponding to (b)*

The topography and the in-plane current profile of the electrode surface shown in Fig. A.2a and b were acquired in a 3×3 μm^2 area with an applied bias of 15 mV for the current profile. First, the topography shows that the surface of the electrode is covered by 100 nm large structures with a roughness below 1 nm. The in-plane current profile map shows that the electrode is uniformly conductive with a maximum measured current of 6 nA as shown in Fig. A.2c. The current profile is correlated with the topography map.

Scanning electron microscopy (SEM) was performed in order to evaluate the grain size of the HZO film. For this purpose, the top electrode was removed using standard cleaning 1 (SC1) procedure followed by a HF treatment. The SC1 consists of a solution of $NH_4OH/H_2O_2/H_2O$ (1:2:50) with a contact time of 5 min at 50°C (for a 2 nm top electrode etching). The HF solution used was pure HF (5%), and the contact time was 20 min. SEM was done using a JEOL Gemini microscope in the secondary electron mode with an acceleration voltage of 3 kV and a work distance of 4.4 mm. Ti 2*p* core level spectra were also recorded to follow the evolution of the stack after these chemical treatments. Figure. A.3 shows the obtained SEM images and the Ti 2*p* XPS spectra after each cleaning. First, the SC1 treatment was shown to leave residual nanoparticles at the surface of the HZO as shown in Fig. A.3b. Analysis of the Ti 2*p* spectrum shows that these particles (diameter <10 nm) are TiO_2 (BE Ti 2$p_{3/2}$=459.1 eV)[206]. After HF treatment, there is no more Ti at the surface and the SEM image (Fig. A.3c) shows that the HF cleaning has removed the TiO_2 nanoparticles and that the film consist of uniform, fine grains. Giving H_2O_2 is an oxidant, the SC1, therefore, etch TiN by converting TiN to TiO_2 and later removal of the latter by HF. From the SEM image of bare HZO (Fig. A.3c), the average grain size was found to be 20-30 nm. This corresponds to the lateral size of these grains.

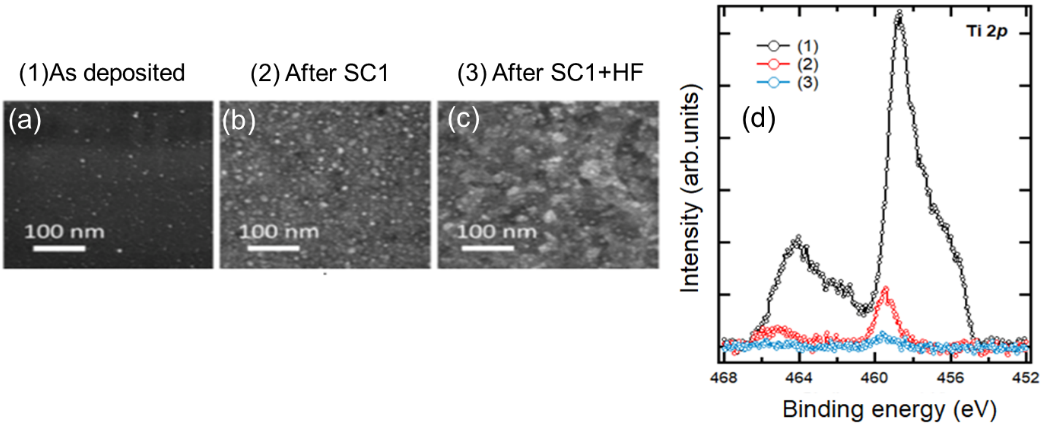

Figure A.3: *SEM images and XPS Ti 2p core level spectra from the as received TiN top electrode surface and after the SC1 and HF chemical treatments*

A.2 W/HZO/W capacitors

The W/HZO/W and HZO/W interfaces investigated in section. 4.3 are prepared by NamLab. MFM samples are used to study the top interface while for the bottom interface, we used samples without top electrode. Tungsten bottom and top electrodes were deposited using PVD sputtering at room temperature. The bottom electrode is 30nm thick and the thickness of the top electrode in the case of the capacitor structure is 13nm. HZO thin films were grown by ALD using an Oxford Instruments OpAL system at T_{dep}=300°C using tris(dimethylamido) cyclopentadienyl hafnium ($HfCp(NMe_2)_3$) and ($ZrCp(NMe_2)_3$) as Hf and Zr precursors, respectively. O_3 was used as an oxidant. The HZO thicknesses were 10 and 5nm for the capacitor and the samples without top electrode, respectively. The capacitor samples underwent an RTA annealing at 500°C for 20s. For the three discussed HZO/W(BE) samples, one was annealed at 600°C fro 20s, one without any annealing and an additional sample without annealing but subjected to 2min O_2 exposure prior to the HZO deposition.

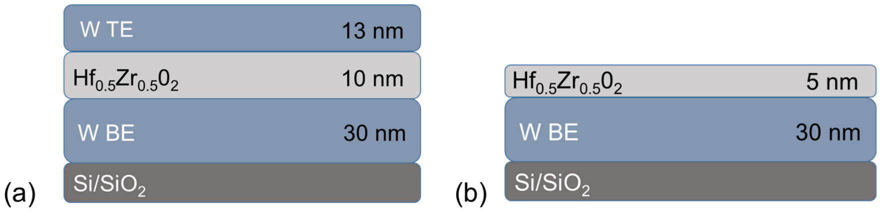

Figure A.4: *Schematic of the analyzed W/HZO/W and HZO/W samples analyzed in section. 4.3*

A.3 TiN/La doped HZO/TiN capacitors

TiN/La:$Hf_{0.5}Zr_{0.5}O_2$ (HZLO)/TiN capacitors discussed in chapter.5 were fabricated on (100) p-doped silicon substrates by NamLab as follows: 12 nm thick TiN bottom electrode (BE) was deposited using an Alliance Concept sputter tool at room temperature. 10 nm thick HZLO films were then deposited at $T_{deposition}$=280°C using an Oxford Instruments OpAL plasma ALD tool. $Hf[N(C_2H_5)CH_3]_4$, $Zr[N(C_2H_5)CH_3]_4$, and tris(isopropyl-cyclopentadienyl) lanthanum (La-$(iPrCp)_3$) were used as hafnium, zirconium, and lanthanum precursors, respectively. Oxygen plasma and H_2O were used as oxidants for the La_2O_3 and HZO growth, respectively. The La doping concentrations are 0, 2.2, 3.4 and 5.8 mol%, achieved by modulating the La/(Hf + Zr) ALD cycle ratios and growth rates accordingly. La_2O_3 was always deposited on top of an HZO under layer and La atoms were not uniformly distributed within the HZO film[115]. 12 nm thick top TiN electrode (TE) was deposited using the same processing conditions as the bottom electrode. Samples with top electrode were used for the HAXPES analysis. Crystallization annealing of these films was performed at 600°C for 20s in N_2 atmosphere.

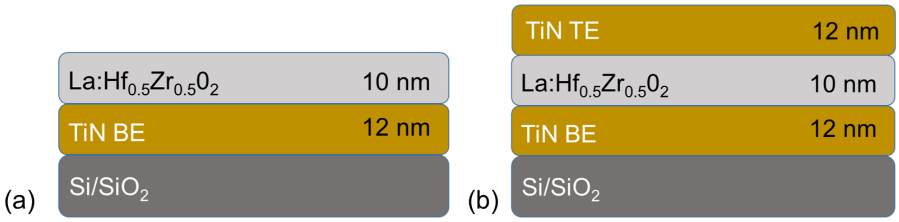

Figure A.5: *(a) Schematic of the analyzed La:HZO/TiN samples with XPS using 0, 2.2, 3.4 and 5.8mol%La doped bare HZO films and (section. 5.2.1) (b) the 12 nm TiN/La:HZO/TiN samples analyzed by HAXPES using 1.7 and 2.7 mol% La doping and T_{RTA} of 500°C and 800°C in section. 5.3.1 and using 2.3 mol% La/T_{RTA}=600°C in section. 5.4*

A.4 TiN/Ti/Si implanted HfO_2/TiN capacitors

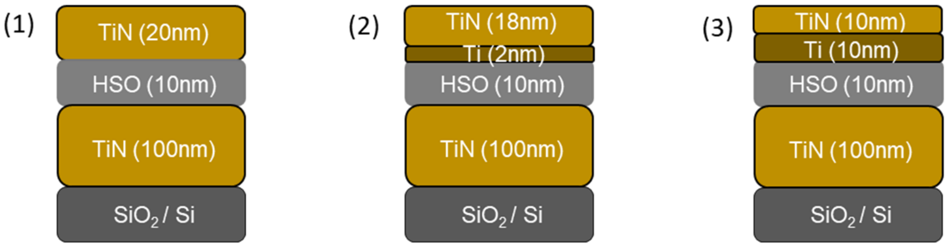

Figure A.6: *(a) Schematic of the analyzed TiN/Ti/HSO/TiN capacitors discussed in chapter. 6*

The TiN/Ti/Si implanted HfO_2(HSO)/TiN capacitors discussed in chapter. 6 were provided by CEA Leti. 10 nm thick HfO_2 films were deposited by ALD at $T_{deposition} = 300$°C and by using $HfCl_4$ and H_2O precursors. Deposition is performed in an ASM Polygon Pulsar chamber. Si doping was provided by ion implantation performed right after HfO_2 deposition, with an energy and a dose of 4 keV and $3\times10_{14}$ cm_2, respectively, corresponding to 1% Si effective concentration. TiN top and bottom bottom electrodes were deposited by PVD at 350°C. Prior to HfO_2 deposition, the 100 nm thick bottom electrode was planarized by chemical mechanical polishing (CMP) to decrease the TiN surface roughness down to 0.18nm RMS. The use top electrodes are 20 nm thick TiN, 18 nm TiN/2 nm Ti and 10 nm TiN/10 nm Ti.

Appendix B

Synchrotron-based X-PEEM experiments

We have studied the field cycling behaviour of microscopic TiN/Hf$_{0.5}$Zr$_{0.5}$O$_2$/TiN ferroelectric capacitors using soft X-ray photoemission electron microscopy (X-PEEM) at the Nanospectroscopy beamline at the Elettra synchrotron (Trieste, Italy) which combine X-ray spectroscopy with electron microscopy. It consists of state-of-the-art spectroscopic photoemission and low energy electron microscopy using an Elmitec LEEM III instrument[235].

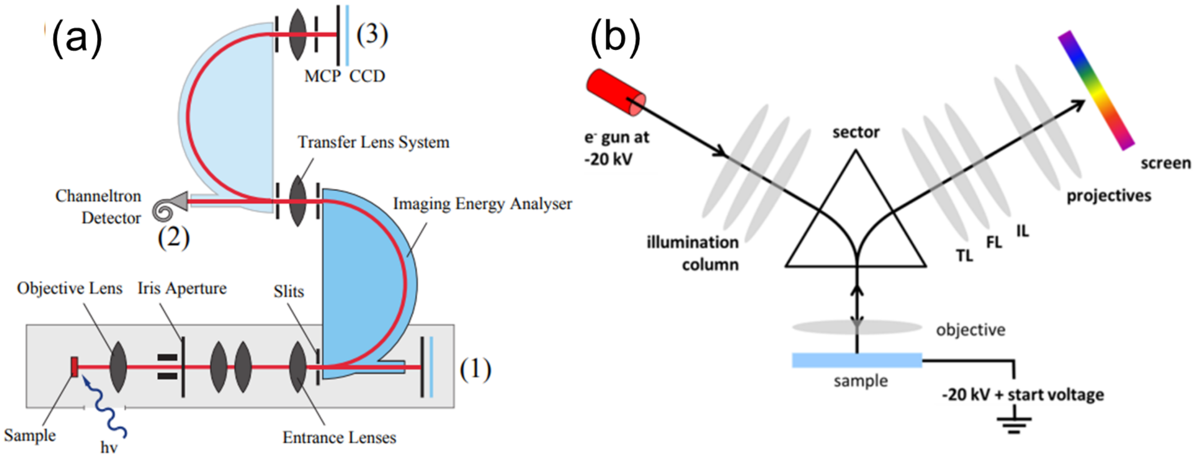

Figure B.1: *(a) Schematic of the NanoESCA analyzer used for photoemission electron microscopy (PEEM). It can operates in three modes: (1) direct PEEM, (2) micro-spectroscopy and (3) energy-filtered PEEM. (b) Schematic of low energy electron microscopy (LEEM) operation*

Figure. B.1a shows a schematic of the double hemispherical electron analyzer used to spatially resolve the photoelectrons in addition to their kinetic energy (photoemission electron microscopy, PEEM). The energy-filtered PEEM technique was used in Chapter. 4 using He I light source to measure the work function of TiN (I(x,y,E_k)). Figure. B.1b illustrates the basic principle of the low energy electron microscopy (LEEM) technique. It is composed of an illuminating column which focuses a monochromatic beam of electrons on the surface (few eV). Meanwhile, the sample is held at a potential of -20kV plus a given voltage called the start voltage. If the incident electrons have a kinetic energy below the surface potential of the sample, they are reflected. This case is referred as the mirror electron microscopy (MEM). Whith higher kinetic energy, electrons can penetrate the surface and interact with the sample and back-scattered. The measured electron intensity *vs* E_k curve are known as the reflectivity curve of the sample. The reflected and back-scattered electrons are then collected by the objective and a beam separator (sector in Fig. B.1b) permits the separation between the incident and imaging electrons. The Nanospectroscopy beamline combines PEEM and LEEM.

To reveal correlations between directly measured V_O concentration and field cycling behaviour, the capacitor structures must be free of excessive leakage current which would prevent cycling and polarization. We have chosen to study microscopic capacitors, 20$\times$30 μm^2 in size, much smaller than the capacitor sizes (100$\times$100 μm^2) studied with area averaged XPS[228]. We have therefore used the PEEM using soft synchrotron X-rays to quantify the V_O concentration near the TiN/HZO interface, as a function of field cycling and polarization state. LEEM is used to map the patterned devices on the sample.

Given the depth sensitivity of soft X-ray photoemission, the top electrode must be thin, $\sim$ 2-3 nm. After crystallization, it was thinned from 10 to 2 nm using 500 eV Ar$^+$ ion sputtering following an established protocol[236]. The XPS spectra acquired as a function of sputtering time are reported in Fig. B.2.

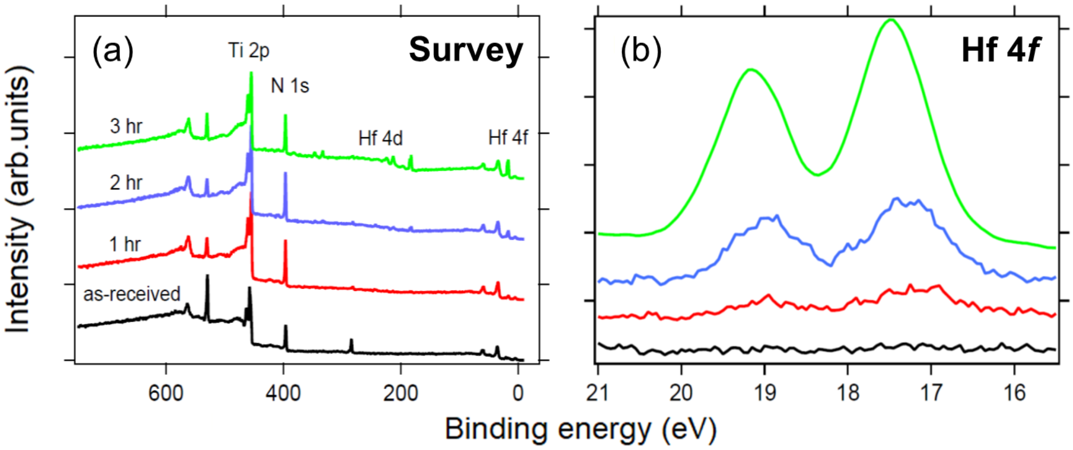

Figure B.2: *(a) XPS survey and (b) Hf 4f core level spectra as a function of top electrode sputtering time*

The XPS Hf 4*f* and 4*d* intensity increases steadily with sputtering time. In the as-received sample the 4*f* emission is completely extinguished by the 10 nm TiN electrode whereas after three hours sputtering the Hf 4*f* peaks are well-resolved with the expected weak reduced Hf component at lower binding energy, due to oxygen scavenging at the interface. As can be seen from the survey spectra, the Ti and N emission from the top electrode are still present after three hours sputtering, showing that the electrode has been thinned but not removed. Furthermore, there is no evidence for strong reduction and disorder which would be associated from sputtering of the HZO. From the strength of the Hf peak we can estimate the electrode thickness after 3h sputtering to be 2.5 nm[236]. The low energy Ar ions do not induce any chemical changes in the underlying HZO. Square TiN top electrodes with 20 $\times$30 μm^2 were patterned using previously calibrated reactive ion etching (RIE) and connected by Au interconnects, electrically insulated from the HZO layer by 50 nm thick Al_2O_3 mm long vias. A total of 32 capacitors were structured in the centre of the wafer as shown in Fig. B.3a and b. The best (in terms of low leakage current and high polarization) were identified for the cycling experiments. One week prior to the experiments capacitors were prepared in pristine (1 cycle), wake-up (10^6 cycles) and fatigue (10^8) states and left in P↑ and P↓.

Dynamic hysteresis measurements (DHM) and field cycling were performed with an Aixacct TF Analyzer 1000 ferrotester. Figure. B.3c shows the pulse train used to cycle and to measure the I-V curves. Rectangular cycling pulses with $\pm$3V amplitude and 10 μs period were used, thus cycling was done at 100 kHz making it possible to access the fatigue regime in a reasonable time. The DHM were done using $\pm$3V amplitude triangular pulses with 1 ms period. Figure B.3d shows the evolution of the remanent polarization, calculated from the time integrated I-V characteristic as a function of cycling. As expected for undoped, there is only modest wake-up for the HZO/TiN capacitors. A memory window > 40 μC/cm^2 persists up to 10^8 cycles, where the onset of fatigue and closing of the memory window becomes visible.

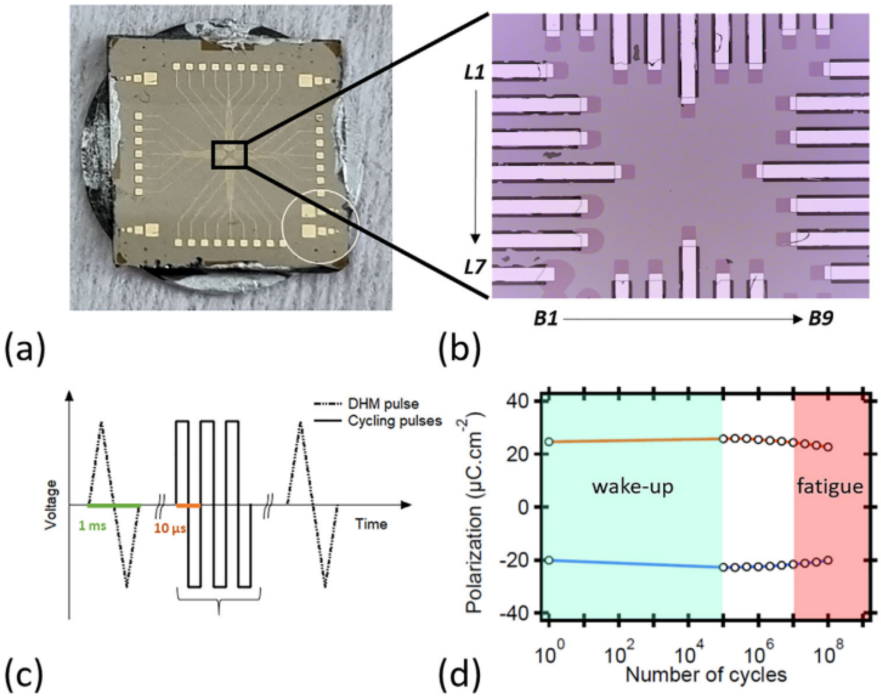

Figure B.3: *(a) Photograph of 5$\times$5 mm^2 sample after capacitor structuring and Au via deposition. The capacitors are in the black square at the centre of the sample, an optical micrograph is shown in (b). (c) pulse train used for the dynamical hysteresis measurements and the cycling. I-V curves are recorded after a second triangular pulse in order to ensure a well-defined initial state before switching. (d) Typical polarization endurance measured from one of the 20$\times$30 μm^2 capacitors in (b). Wake-up increases the remanent polarization by 10%. After 10^8 cycles, P_r is reduced to below 20 μC/cm^2, marking the onset of fatigue*

Figure. B.4 shows the switching peaks recorded in the I-V curves for (a) P↑ to P↓ and (b) P↓ to P↑ switches for the three cycling conditions, pristine (1 cycle), after wake-up (10^6 cycles) and fatigue onset (10^8 cycles). The imprint as a function of cycling is calculated from the voltage difference between the two peaks. For the pristine sample the imprint is +0.53 V whereas after wake-up and fatigue onset it is almost negligible, 0.02 and 0.07 V, suggesting an initial internal field, possibly due to the V_O concentration profile observed in as-received samples. The absence of imprint after 10^6 cycles is evidence for a field induced redistribution of the V_O. Note that the switching peaks are superimposed on a high dielectric current of $\sim 2\mu$A. This is due to the Au interconnects sputtered onto the Al_2O_3 vias which create an additional capacitance in parallel to the studied devices. Assuming dielectric constants 28 and 11.5 for HZO and Al_2O_3, respectively, and given the length of the interconnects (3600 μm), the expected dielectric current, calculated from $I_{dielectric}$ = C dV/dt, is 1.80 μA, very close to the measured value.

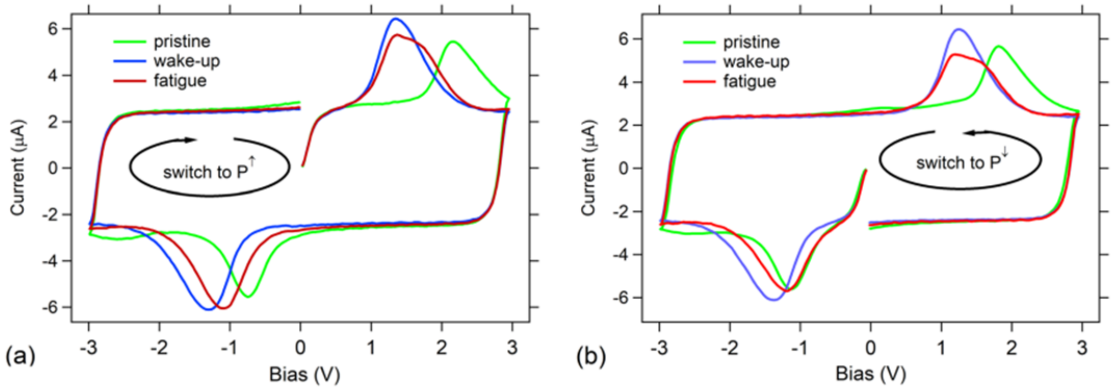

Figure B.4: *Switching peaks for (a) P↑ to P↓ and (b) P↓ to P↑ for the pristine (green), after wake-up (blue) and fatigue (red) states. The black arrows indicate the direction of the voltage ramp, applied to the top electrode. The switching peaks are superimposed on a dielectric current of $\sim$2 μA*

Rapid navigation across the sample to localize the capacitor structures was done using low energy electron microscopy (LEEM). A field of view of 40 μm was used which included the capacitor, an adjacent area of bare HZO and the gold contact pad for the Fermi level reference, see LEEM image in Fig. B.5. The photon energy was set to 670 eV, providing an inelastic mean free path of 1.4 nm as calculated using the TPP-2M algorithm, sufficient to mesure the local Hf chemistry in the vicinity (within $\sim$2 nm) of the top TiN/HZO interface. The Au 4*f* spectrum measured from the interconnect for each capacitor was used to calibrate the binding energy, obtained by a fit to the 4*f* core levels extracted from the image series. The Hf 4*f* spectra were acquired in a 12 eV window using 0.1 eV step in kinetic energy. To optimize statistics a 4$\times$4 binning and 30 s acquisition time per image was used. All images were divided by a flat field image acquired from a featureless part of the sample, to remove any artefacts due to detector inhomogeneities. The FWHM for the Hf 4f was fixed at 1.31 eV, the spin-orbit splitting 1.7 eV, the branching ratio 0.75. In addition, components representing the O and N 2*s* emission were included. The O 2s was centered at 22 eV and a FWHM of 2.5 eV while the N 2*s* was fixed at 1.7 eV lower binding energy with respect to the Hf 4$f_{7/2}$ and a FWHM of 1.79 eV. Thus the only free parameters were the 4$f_{7/2}$ binding energy and the relative intensity of the Hf^{4+} and Hf^{3+} emission.

Figure. B.6 shows the best fits to the Hf 4*f* spectra as a function of polarization for the pristine, after wake-up and fatigue onset cycling conditions. The N (blue) and O (pink) 2*s* core level positons are constrained as described above. In particular, by fixing the N 2*s* position degeneracy with the Hf^{3+} is avoided and the

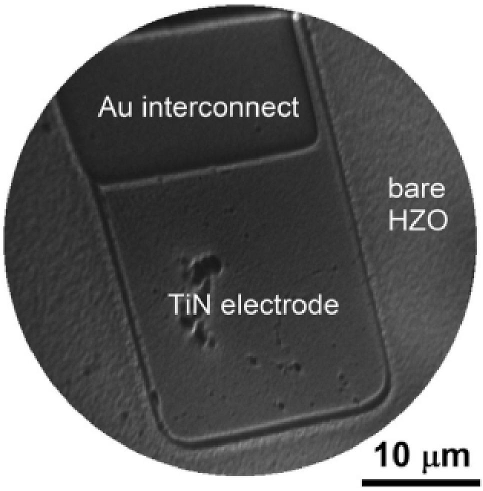

Figure B.5: *Low energy electron microscopy image of pristine capacitor in P↑ state, taken at a start voltage of 1.925 V, showing the thinned electrode, bare HZO and the Au interconnect. Field of view* $\sim$*40* μm

latter evolution with cycling can be followed. The only free parameters are the position of the Hf 4*f* manifold and the relative intensity of the Hf^{4+} (light grey) and Hf^{3+} (dark grey) components. As discussed, the spectra probe the first 2 nm of the HZO. Assuming that each V_O frees two electrons, given the $Hf_{0.5}Zr_{0.5}O_2$ stoichiometry, the V_O concentration as a percentage of the total oxygen content can be calculated as 1/8th of the Hf^{3+} relative intensity. The Hf^{3+} intensity in the first 2 nm of $HfZrO_4$ increases with cycling for capacitors measured in P↑ states. In the case of P↓ state, it first increases after wake-up but then decreases again with the onset of fatigue. We interpret this in terms of two competing mechanisms. Field cycling with ±3V peak AC voltage is sufficient to create new V_O[213]. In addition, the capacitors were left in a well defined polarization state P↑ or P↓ for one week before analysis. Positively charged oxygen vacancies ($V_O^{\cdot\cdot}$) will drift away from the top interface under the internal field in the P↑ state whereas they will accumulate near the top interface under the influence of the P↓ state. This would explain the monotonic increase in the Hf3+ intensity for P but the decrease in Hf^{3+} intensity and therefore V_O concentration at the onset of fatigue for the capacitor left in the P↑ state.

Figure. B.7 summarizes the key results of the X-PEEM analysis. The V_O concentration in the first 2 nm of HZO at the top interface is plotted in Fig. B.7a and the Schottky barrier for electrons in Fig. B.7b, both as a function of cycling. The V_O concentration increases linearly for the capacitors in P↓ state from 0.75 to 2.0% whereas for capacitors in P↑ it increases from 1.0 to 1.4% after 10^6 cycles before decreasing to 1.1% after 10^8 cycles. Thus, the V_O shows evidence for drift away from the top interface under the internal field set up by the P↑ polarization state. The reduction in the Schottky barrier is also consistent with the increase in V_O although the absolute barrier height is still sufficiently important to prevent any significant leakage. The continued high SBH even after the onset of fatigue suggests that hard breakdown is a local phenomenon due to the irreversible formation of conducting paths/filaments. One shortcoming of the experiment is the limited photon energy range available in soft X-ray PEEM making the complete V_O pro-

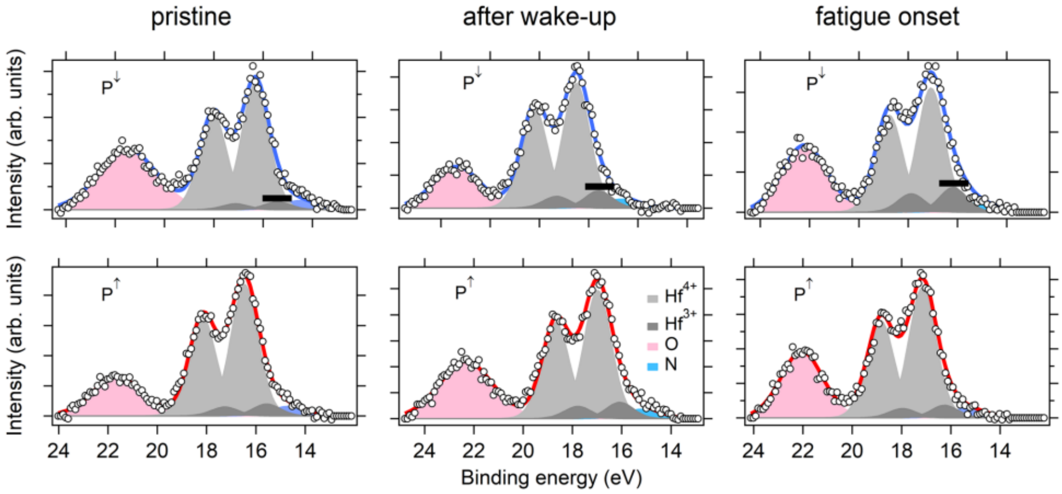

Figure B.6: *Hf 4f spectra and best fits for three cycling conditions pristine (1 cycle) after wake-up (10^6 cycles) and fatigue onset (10^8 cycles), with devices in to polarization states P↑ (top) and P↓ (bottom). The spectra are fitted with Hf^{4+} (light grey), Hf^{3+} (dark grey), N (blue) and O (pink) 2s*

file over the film thickness inaccessible. This could be solved by using hard X-ray excitation although the signal levels in spectromicroscopy become challenging. It would also be interesting to conduct the analysis to hard breakdown to study the interaction between overall V_O concentration and the probable filamentary breakdown mechanism.

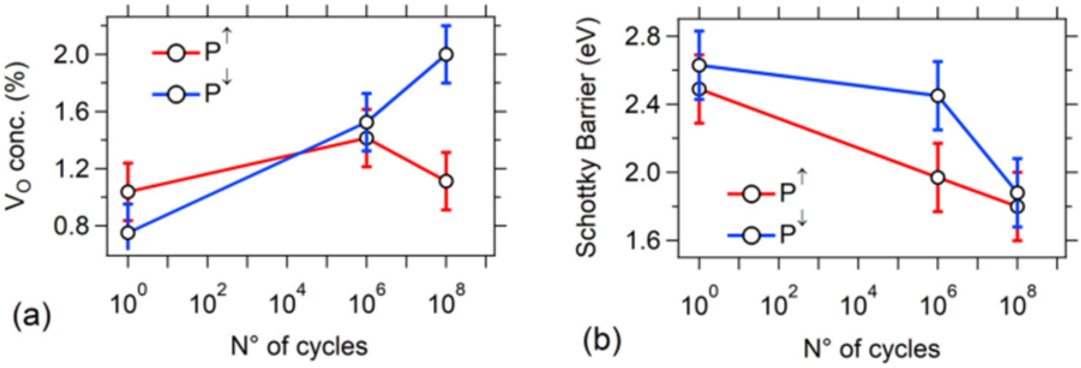

Figure B.7: *(a) V_O concentration in the first 2 nm of HZO at the top interface and (b) Schottky barrier for electrons as a function of cycling, measured in P↑ and P↓ polarization states*

In conclusion, we have used synchrotron radiation based X-PEEM to study the evolution of the V_O concentration in microscopic TiN/HZO/TiN capacitors with field cycling. The V_O concentration increases with cycling at ± 3 V peak AC and furthermore redistributes under the influence of the internal field set up by the polarization state. Upward pointing polarization causes oxygen vacancy drift depleting the concentration near the top interface, whereas downward polarization causes vacancy drift towards the top interface. The Schottky barrier height for electrons decreases systematically wth cycling, whatever the polarization state, consistent with an overall increase in oxygen vacancies with cycling. The creation of new V_O with cycling and field induced V_O drift have important consequences for both endurance and data retention in ferroelectric HZO-based NVMs.

French summary

Les films minces ferroélectriques à base de HfO$_2$ sont des candidats prometteurs pour les technologies de mémoire non volatile à haute densité telles que la mémoire à accès aléatoire ferroélectrique (FRAM) et les transistors à effet de champ ferroélectriques (FeFET). Ils peuvent surmonter les limitations d'intégration associées aux matériaux pérovskites conventionnels grâce aux faibles épaisseurs de films supportant la ferroélectricité, au conformité du dépôt avec la technique de déposition par couche atomique (ALD) et à la compatibilité avec la technologie CMOS. Les lacunes d'oxygène (V_O) jouent un rôle décisif dans la performance globale de dispositifs fabriqués avec ces systèmes attrayants. Le rôle de ces défauts ponctuels est souvent discuté par des calculs théoriques ou par des approches de modélisation des mesures électriques expérimentales.

En utilisant la haute sensibilité chimique et électronique des techniques de spectroscopie basées sur la photoémission, l'objectif de cette thèse est d'étudier et de corréler la réponse ferroélectrique optimisée dans des condensateurs à base de Hf$_x$Zr$_{1-x}$O$_2$ avec la variation des densités de V_O et les décalages des bandes électroniques. Tout d'abord, la chimie de l'interface électrode-ferroélectrique et l'effet de la température de recuit de cristallisation dans des empilements à base de TiN/Hf$_{0.5}$Zr$_{0.5}$O$_2$(HZO)/TiN et W/HZO/W ont été étudiés par la spectroscopie de photoélectrons induits par des rayons X (XPS). En utilisant des rayons X durs (HAXPES) avec le rayonnement synchrotron, des interfaces HZO/TiN enterrées plus profondément ainsi que les effets du dopage au La ont été évalués. En plus, un dispositif spécial a été conçu pour permettre des mesures HAXPES avec une polarisation appliquée *in-situ*. Des condensateurs technologiquement prometteurs à base de TiN/HZO dopé La/TiN et TiN/Ti/ HfO$_2$ implanté au Si/TiN ont été étudiés.

Les résultats révèlent que le TiN induit une concentration de V_O plus élevée que les électrodes de W avec des hauteurs de barrière de Schottky pour le transport d'électrons (φ_{Bn}) plus faibles en raison de la plus grande affinité du TiN pour l'oxygène. Les analyses HAXPES ont montré que le pompage d'oxygène se produit principalement avec l'électrode supérieure lors du recuit en raison de la passivation de l'électrode inférieure pendant les premières étapes du processus de croissance. La distribution asymétrique des V_O avec TiN entraîne un piégeage asymétrique d'électrons ce qui donne lieu à un champ interne. L'utilisation du W a permis l'amélioration de cet effet. Le dopage au La a montré que la charge négative induite par la substitution de Hf^{4+} par des impuretés La^{3+} est plutôt écrantée par des V_O chargés positivement. Dans des parties du film riches en oxygène, cela conduit à une augmentation de la concentration globale de V_O. En utilisant le mécanisme de Poole-Frenkel pour le transport des charges, le La induit aussi une diminution du niveau énergétique associée au V_O dans la bande

interdite vers des niveaux plus proche de la bande de conduction. Les études en fonction du cyclage ont permis quant à eux de prouver que le comportement de réveil est principalement dû à une augmentation de la concentration des V_O et leur redistribution d'une manière plus homogène dans le film. Le basculement de la polarisation in- situ a aussi permis d'évaluer les valeurs de φ_{Bn} dans les dispositifs optimales. Finalement, des analyses de spectro-microscopie X-PEEM ont été menés pour des investigations similaires sur des condensateurs de tailles micrométriques à base de TiN/HZO/TiN.

Ce travail présente une nouvelle étape vers la compréhension des sources et des effets de V_O dans les condensateurs à base de HfO_2 et souligne l'énorme potentiel des techniques basées sur la photoémission pour fournir des informations qualitatives et quantitatives nécessaires pour une meilleure optimisation.

Mots clés: Ferroélectricité, mémoires non volatiles, HfO_2 ferroélectrique, spectroscopie de photoémission (XPS, HAXPES), lacunes d'oxygène, alignement de bandes.

Bibliography

[1] J. Valasek. Piezo-electric and allied phenomena in Rochelle salt. *Physical Review*, 17(4):475–481, 1921.

[2] Ekhard K H Salje. Ferroelastic Materials. *Annual Review of Materials Research*, 42(1):265–283, 2012.

[3] Anne S. Zimmermann, Dennis Meier, and Manfred Fiebig. Ferroic nature of magnetic toroidal order. *Nature Communications*, 5:2–7, 2014.

[4] Lei Ding, Xianghan Xu, Harald O. Jeschke, Xiaojian Bai, Erxi Feng, Admasu Solomon Alemayehu, Jaewook Kim, Fei Ting Huang, Qiang Zhang, Xiaxin Ding, Neil Harrison, Vivien Zapf, Daniel Khomskii, Igor I. Mazin, Sang Wook Cheong, and Huibo Cao. Field-tunable toroidal moment in a chiral-lattice magnet. *Nature Communications*, 12(1):1–7, 2021.

[5] Georg Busch. How I discovered the ferroelectric properties of KH2PO4. *Ferroelectrics*, 71(1):43–47, 1987.

[6] A Von Hippel, R G Breckenridge, F G Chesley, and Laszlo Tisza. High ceramics.

[7] H. Kato and T. Fukuda. New insulating materials. *IEEE Transactions on Electrical Insulation*, EI-21(6):925–927, 1986.

[8] C.A. Randall, R.E. Newnham, and L.E. Cross. Hystory of the First Ferroelectric Oxide, BaTIO3. *Materials Research Institute*, pages 1–11, 1944.

[9] Gene H. Haertling. Ferroelectric Ceramics: History and Technology. *Ferroelectricity: The Fundamentals Collection*, 818:157–178, 2007.

[10] Single Micro, Nanowire Pyroelectric Nanogenerators, and Self-powered Temperature Sensors. Single Micro / Nanowire Pyroelectric. (9):8456–8461, 2012.

[11] Ding Zhang, Heting Wu, Chris R. Bowen, and Ya Yang. Recent Advances in Pyroelectric Materials and Applications. *Small*, 17(51):1–23, 2021.

[12] IEEE Standard on Piezoelectricity. *ANSI/IEEE Std 176-1987*, pages 0_1–, 1988.

[13] Jackeline Narvaez Morales. PhD Thesis: Flexoelectricity in Single Crystals. *Departament de Física*, PhD:109, 2016.

[14] Irene Arias, Gustau Catalan, and Pradeep Sharma. The emancipation of flexoelectricity. *Journal of Applied Physics*, 131(2):020401, 2022.

[15] R. D. Mindlin. Polarization gradient in elastic dielectrics. *International Journal of Solids and Structures*, 4(6):637–642, 1968.

[16] Gabriel L. Smith, Jeffrey S. Pulskamp, Luz M. Sanchez, Daniel M. Potrepka, Robert M. Proie, Tony G. Ivanov, Ryan Q. Rudy, William D. Nothwang, Sarah S. Bedair, Christopher D. Meyer, and Ronald G. Polcawich. PZT-based piezoelectric MEMS technology. *Journal of the American Ceramic Society*, 95(6):1777–1792, 2012.

[17] Karin M. Rabe, Matthew Dawber, Céline Lichtensteiger, Charles H. Ahn, and Jean-Marc Marc Triscone. Modern Physics of Ferroelectrics: Essential Background BT - Physics of Ferroelectrics: A Modern Perspective. *Topics in Applied Physics*, 105(2007):1–30, 2007.

[18] Massimiliano Stengel, Pablo Aguado-Puente, Nicola A. Spaldin, and Javier Junquera. Band alignment at metal/ferroelectric interfaces: Insights and artifacts from first principles. *Physical Review B - Condensed Matter and Materials Physics*, 83(23):1–27, 2011.

[19] Federico A. Rabuffetti and Richard L. Brutchey. Structural evolution of BaTiO 3 nanocrystals synthesized at room temperature. *Journal of the American Chemical Society*, 134(22):9475–9487, 2012.

[20] Brienne Johnson and Jacob L Jones. Chapter 2 - Structures, Phase Equilibria, and Properties of HfO2. In Uwe Schroeder, Cheol Seong Hwang, and Hiroshi Funakubo, editors, *Ferroelectricity in Doped Hafnium Oxide: Materials, Properties and Devices*, Woodhead Publishing Series in Electronic and Optical Materials, pages 25–45. Woodhead Publishing, 2019.

[21] LD Landau. Zh. eksp. teor. fiz. *JETP*, 7:19, 1937.

[22] A F Devonshire. XCVI. Theory of barium titanate. *The London, Edinburgh, and Dublin Philosophical Magazine and Journal of Science*, 40(309):1040–1063, 1949.

[23] R Comès, M Lambert, and A Guinier. Désordre linéaire dans les cristaux (cas du silicium, du quartz, et des pérovskites ferroélectriques). *Acta Crystallographica Section A*, 26(2):244–254, mar 1970.

[24] W Cochran. Crystal stability and the theory of ferroelectricity. *Advances in Physics*, 9(36):387–423, oct 1960.

[25] Raffaele Resta and David Vanderbilt. Chapter 02 Theory of Polarization: A Modern Approach. *Physics of Ferroelectrics*, 105/2007(Cm):31–68, 2007.

[26] Resta, R. Polarization as a Berry Phase. *Europhys. News*, 28(1):18–20, 1997.

[27] R. E. Cohen. Ref 25_ Ferroelectricity in Pv oxides. *Nature*, 358(July):136–138, 1992.

[28] Ph Ghosez, J. Michenaud, and X. Gonze. Dynamical atomic charges: The case of compounds. *Physical Review B - Condensed Matter and Materials Physics*, 58(10):6224–6240, 1998.

[29] G. Catalan, J. Seidel, R. Ramesh, and J. F. Scott. Domain wall nanoelectronics. *Reviews of Modern Physics*, 84(1):119–156, 2012.

[30] Z. Zhao, N. Barrett, Q. Wu, D. Martinotti, L. Tortech, R. Haumont, M. Pellen, and E. K.H. Salje. Interaction of low-energy electrons with surface polarity near ferroelastic domain boundaries. *Physical Review Materials*, 3(4):1–12, 2019.

[31] Junsoo Shin, Von Braun Nascimento, Grégory Geneste, John Rundgren, E. Ward Plummer, Brahim Dkhil, Sergei V. Kalinin, and Arthur P. Baddorf. Atomistic screening mechanism of ferroelectric surfaces: An in situ study of the polar phase in ultrathin BaTiO3 films exposed to H 2O. *Nano Letters*, 9(11):3720–3725, 2009.

[32] J L Wang, B Vilquin, and N Barrett. Screening of ferroelectric domains on BaTiO3(001) surface by ultraviolet photo-induced charge and dissociative water adsorption. *Applied Physics Letters*, 101(9):92902, 2012.

[33] S. V. Kalinin and D. A. Bonnell. Surface potential at surface-interface junctions in SrTiO3 bicrystals. *Physical Review B - Condensed Matter and Materials Physics*, 62(15):10419–10430, 2000.

[34] Sergei V. Kalinin and Dawn A. Bonnell. Screening phenomena on oxide surfaces and its implications for local electrostatic and transport measurements. *Nano Letters*, 4(4):555–560, 2004.

[35] Olivier Copie, Nicolas Chevalier, Gwenael Le Rhun, Cindy L. Rountree, Dominique Martinotti, Sara Gonzalez, Claire Mathieu, Olivier Renault, and Nicholas Barrett. Adsorbate Screening of Surface Charge of Microscopic Ferroelectric Domains in Sol-Gel PbZr0.2Ti0.8O3 Thin Films. *ACS Applied Materials and Interfaces*, 9(34):29311–29317, 2017.

[36] Samsung Advanced and Technology Sait. Surface-Functionalized Hafnia with Bespoke Ferroelectric Properties for Memory and Logic Applications. pages 326–329, 2021.

[37] L. Pintilie and M. Alexe. Metal-ferroelectric-metal heterostructures with Schottky contacts. I. Influence of the ferroelectric properties. *Journal of Applied Physics*, 98(12), 2005.

[38] L. Pintilie, I. Boerasu, M. J.M. Gomes, T. Zhao, R. Ramesh, and M. Alexe. Metal-ferroelectric-metal structures with Schottky contacts. II. Analysis of the experimental current-voltage and capacitance-voltage characteristics of Pb (Zr,Ti) O 3 thin films. *Journal of Applied Physics*, 98(12), 2005.

[39] General Principles, General Principles, L Ley, and L Ley. Photoemission in Solids. *New York*, 26:197, 1978.

[40] W Schottky. Zur Halbleitertheorie der Sperrschicht- und Spitzengleichrichter. *Zeitschrift für Physik*, 113(5):367–414, 1939.

[41] N F Mott. an Insulator or Semi-Conductor. 76(October):568–572, 1938.

[42] M Dawber, K M Rabe, and J F Scott. Physics of thin-film ferroelectric oxides. *Rev. Mod. Phys.*, 77(4):1083–1130, oct 2005.

[43] Raymond T. Tung. The physics and chemistry of the Schottky barrier height. *Applied Physics Reviews*, 1(1), 2014.

[44] John Bardeen. Surface states and rectification at a metal semi-conductor contact. *Physical Review*, 71(10):717–727, 1947.

[45] Graduate Texts. *Solid Surfaces, Interfaces and Thin Films*.

[46] Volker Heine. Theory of Surface States. *Phys. Rev.*, 138(6A):A1689—-A1696, 1965.

[47] W. Mönch. Role of virtual gap states and defects in metal-semiconductor contacts. *Physical Review Letters*, 58(12):1260–1263, 1987.

[48] *Metal-Semiconductor Contacts*, pages 134–196. John Wiley & Sons, Ltd, 2006.

[49] L. Pintilie, I. Vrejoiu, D. Hesse, G. LeRhun, and M. Alexe. Ferroelectric polarization-leakage current relation in high quality epitaxial Pb (Zr,Ti) O3 films. *Physical Review B - Condensed Matter and Materials Physics*, 75(10):1–14, 2007.

[50] Massimiliano Stengel, David Vanderbilt, and Nicola A. Spaldin. Enhancement of ferroelectricity at metal-oxide interfaces. *Nature Materials*, 8(5):392–397, 2009.

[51] E. Kröger, A. Petraru, A. Quer, R. Soni, M. Kalläne, N. A. Pertsev, H. Kohlstedt, and K. Rossnagel. In situ hard x-ray photoemission spectroscopy of barrier-height control at metal/PMN-PT interfaces. *Physical Review B*, 93(23):1–8, 2016.

[52] J. E. Rault, G. Agnus, T. Maroutian, V. Pillard, Ph Lecoeur, G. Niu, B. Vilquin, M. G. Silly, A. Bendounan, F. Sirotti, and N. Barrett. Interface electronic structure in a metal/ferroelectric heterostructure under applied bias. *Physical Review B - Condensed Matter and Materials Physics*, 87(15):1–8, 2013.

[53] James F Scott. *Basic Properties of RAMs (Random Access Memories)*, pages 23–51. Springer Berlin Heidelberg, Berlin, Heidelberg, 2000.

[54] Fjitsu Microelectronics. FRAM guide book. *Fujitsu*, 2008.

[55] Benchmarking of ferroelectric memories with respect to other new memory technologies. (780302):7–10, 2021.

[56] Min Hyuk Park, Young Hwan Lee, Thomas Mikolajick, Uwe Schroeder, and Cheol Seong Hwang. Review and perspective on ferroelectric HfO2-based thin films for memory applications. *MRS Communications*, pages 1–14, 2018.

[57] C. E. CURTIS, L. M. DONEY, and J. R. JOHNSON. Some Properties of Hafnium Oxide, Hafnium Silicate, Calcium Hafnate, and Hafnium Carbide. *Journal of the American Ceramic Society*, 37(10):458–465, 1954.

[58] J. Wang, H. P. Li, and R. Stevens. Hafnia and hafnia-toughened ceramics. *Journal of Materials Science*, 27(20):5397–5430, 1992.

[59] Kazuhide Matsumoto, Yoshiyasu Itoh, and Tsuneji Kameda. EB-PVD process and thermal properties of hafnia-based thermal barrier coating. *Science and Technology of Advanced Materials*, 4(2):153–158, 2003.

[60] Alexandra Navrotsky. Thermochemical insights into refractory ceramic materials based on oxides with large tetravalent cations. *Journal of Materials Chemistry*, 15(19):1883–1890, 2005.

[61] Xinyuan Zhao and David Vanderbilt. First-principles study of structural, vibrational, and lattice dielectric properties of hafnium oxide. *Physical Review B - Condensed Matter and Materials Physics*, 65(23):1–4, 2002.

[62] Marie C. Cheynet, Simone Pokrant, Frans D. Tichelaar, and Jean Luc Rouvìre. ystal structure and band gap determination of Hf O2Crms thin fil. *Journal of Applied Physics*, 101(5), 2007.

[63] G. D. Wilk, R. M. Wallace, and J. M. Anthony. High-κ gate dielectrics: Current status and materials properties considerations. *Journal of Applied Physics*, 89(10):5243–5275, 2001.

[64] Kazuyuki Tomida, Koji Kita, and Akira Toriumi. Dielectric constant enhancement due to Si incorporation into HfO 2. *Applied Physics Letters*, 89(14):2–5, 2006.

[65] Sergey V Ushakov, Crystalyn E Brown, and Alexandra Navrotsky. Effect of La and Y on Crystallization Temperatures of Hafnia and Zirconia. *Journal of Materials Research*, 19(3):693–696, 2004.

[66] Byoung Hun Lee, Laegu Kang, Wen Jie Qi, Renee Nieh, Yongjoo Jeon, Katsunori Onishi, and Jack C. Lee. Ultrathin hafnium oxide with low leakage and excellent reliability for alternative gate dielectric application. *Technical Digest - International Electron Devices Meeting*, pages 133–136, 1999.

[67] T. S. Böscke, J. Müller, D. Bräuhaus, U. Schröder, and U. Böttger. Ferroelectricity in hafnium oxide thin films. *Applied Physics Letters*, 99(10), 2011.

[68] J. M. Leger, A. Atouf, P. E. Tomaszewski, and A. S. Pereira. Pressure-induced phase transitions and volume changes in HfO2 up to 50 GPa. *Physical Review B*, 48(1):93–98, 1993.

[69] Osamu Ohtaka, Takamitsu Yamanaka, and Shoichi Kume. Synthesis and X-ray structural analysis by the rietveld method of orthorhombic hafnia. *Journal of the Ceramic Society of Japan. International ed.*, 99(9):810–811, 1991.

[70] Experimental Procedure. r I or O2. 75(March):844–847, 1991.

[71] A. Jayaraman, S. Y. Wang, S. K. Sharma, and L. C. Ming. Pressure-induced phase transformations in HfO2 to 50 GPa studied by Raman spectroscopy. *Physical Review B*, 48(13):9205–9211, 1993.

[72] Serge Desgreniers and Ken Lagarec. High-density ZrO2 and HfO2: Crystalline structures and equations of state . *Physical Review B*, 59(13):8467–8472, 1999.

[73] Julian Haines, Jean Michel Léger, Steve Hull, Jean Pierre Petitet, Altair S. Pereira, Claudio A. Perottoni, and João A.H. Da Jornada. Characterization of the cotunnite-type phases of zirconia and hafnia by neutron diffraction and raman spectroscopy. *Journal of the American Ceramic Society*, 80(7):1910–1914, 1997.

[74] H. Arashi, T. Yagi, S. Akimoto, and Y. Kudoh. New high-pressure phase of ZrO2 above 35 GPa. *Physical Review B*, 41(7):4309–4313, 1990.

[75] Xuhui Luo, Wei Zhou, Sergey V. Ushakov, Alexandra Navrotsky, and Alexander A. Demkov. Monoclinic to tetragonal transformations in hafnia and zirconia: A combined calorimetric and density functional study. *Physical Review B - Condensed Matter and Materials Physics*, 80(13):1–13, 2009.

[76] M H Asghar, F Placido, and S Naseem. P HYSICAL J OURNAL Characterization of reactively evaporated TiO 2 thin films as high. *European Physical JournalApplied Physics*, 184(3):177–184, 2006.

[77] Ronald C. Garvie. The occurrence of metastable tetragonal zirconia as a crystallite size effect. *Journal of Physical Chemistry*, 69(4):1238–1243, 1965.

[78] Chih Hsin Lu, Joan M. Raitano, Syed Khalid, Lihua Zhang, and Siu Wai Chan. Cubic phase stabilization in nanoparticles of hafnia-zirconia oxides: Particle-size and annealing environment effects. *Journal of Applied Physics*, 103(12), 2008.

[79] Bethany M. Hudak, Sean W. Depner, Gregory R. Waetzig, Anjana Talapatra, Raymundo Arroyave, Sarbajit Banerjee, and Beth S. Guiton. Real-time atomistic observation of structural phase transformations in individual hafnia nanorods. *Nature Communications*, 8(May):1–9, 2017.

[80] Michael Shandalov and Paul C. McIntyre. Size-dependent polymorphism in HfO2 nanotubes and nanoscale thin films. *Journal of Applied Physics*, 106(8):0–5, 2009.

[81] Dominik Fischer and Alfred Kersch. The effect of dopants on the dielectric constant of Hf O2 and Zr O2 from first principles. *Applied Physics Letters*, 92(1), 2008.

[82] Lili Zhao, Dong Hou, Tedi Marie Usher, Thanakorn Iamsasri, Chris M. Fancher, Jennifer S. Forrester, Toshikazu Nishida, Saeed Moghaddam, and Jacob L. Jones. Structure of 3 at.% and 9 at.% Si-doped HfO2 from combined refinement of X-ray and neutron diffraction patterns. *Journal of Alloys and Compounds*, 646:655–661, 2015.

[83] ROBERT RUH, H. J. GARRETT, R. F. DOMAGALA, and N. M. TALLAN. The Svstern Zirconia-Hafnia. *Journal of the American Ceramic Society*, 51(1):23–28, 1968.

[84] Erich H Kisi, Christopher J Howard, and Roderick J Hill. Crystal Structure of Orthorhombic Zirconia in Partially Stabilized Zirconia. *Journal of the American Ceramic Society*, 72(9):1757–1760, 1989.

[85] J. H. Choi, Y. Mao, and J. P. Chang. Development of hafnium based high-k materials - A review. *Materials Science and Engineering R: Reports*, 72(6):97–136, 2011.

[86] Takashi Ando. Ultimate Scaling of High-κ Gate Dielectrics: Higher-κ or Interfacial Layer Scavenging? pages 478–500, 2012.

[87] Demkov. *Material Fundamentals for Gate Dielectrics*, volume 53. 1989.

[88] T. Ando, M. M. Frank, K. Choi, C. Choi, J. Bruley, M. Hopstaken, M. Copel, E. Cartier, A. Kerber, A. Callegari, D. Lacey, S. Brown, Q. Yang, and V. Narayanan. Understanding mobility mechanisms in extremely scaled HfO2 (EOT 0.42 nm) using remote interfacial layer scavenging technique and V t-tuning dipoles with gate-first process. *Technical Digest - International Electron Devices Meeting, IEDM*, 2:423–426, 2009.

[89] Byoung Hun Lee, Laegu Kang, Renee Nieh, Wen Jie Qi, and Jack C. Lee. Thermal stability and electrical characteristics of ultrathin hafnium oxide gate dielectric reoxidized with rapid thermal annealing. *Applied Physics Letters*, 76(14):1926–1928, 2000.

[90] K Mistry, C Allen, C Auth, B Beattie, D Bergstrom, M Bost, M Brazier, M Buehler, A Cappellani, R Chau, C.-H. Choi, G Ding, K Fischer, T Ghani, R Grover, W Han, D Hanken, M Hattendorf, J He, J Hicks, R Huessner, D Ingerly, P Jain, R James, L Jong, S Joshi, C Kenyon, K Kuhn, K Lee, H Liu, J Maiz, B McIntyre, P Moon, J Neirynck, S Pae, C Parker, D Parsons, C Prasad, L Pipes, M Prince, P Ranade, T Reynolds, J Sandford, L Shifren, J Sebastian, J Seiple, D Simon, S Sivakumar, P Smith, C Thomas, T Troeger, P Vandervoorn, S Williams, and K Zawadzki. A 45nm Logic Technology with High-k+Metal Gate Transistors, Strained Silicon, 9 Cu Interconnect Layers, 193nm Dry Patterning, and 100% Pb-free Packaging. In *2007 IEEE International Electron Devices Meeting*, pages 247–250, 2007.

[91] T. S. Böscke, P. Y. Hung, P. D. Kirsch, M. A. Quevedo-Lopez, and R. Ramírez-Bon. Increasing permittivity in HfZrO thin films by surface manipulation. *Applied Physics Letters*, 95(5):2–5, 2009.

[92] Johannes Müller, Tim S. Böscke, Uwe Schröder, Stefan Mueller, Dennis Bräuhaus, Ulrich Böttger, Lothar Frey, and Thomas Mikolajick. Ferroelectricity in simple binary ZrO 2 and HfO 2. *Nano Letters*, 12(8):4318–4323, 2012.

[93] J. Müller, T. S. Böscke, D. Bräuhaus, U. Schröder, U. Böttger, J. Sundqvist, P. Kcher, T. Mikolajick, and L. Frey. Ferroelectric Zr0.5Hf0.5O2 thin films for nonvolatile memory applications. *Applied Physics Letters*, 99(11):0–3, 2011.

[94] Hideki Takeuchi, Amy Wung, Xin Sun, Roger T. Howe, and Tsu Jae King. Thermal budget limits of quarter-micrometer foundry CMOS for post-processing MEMS devices. *IEEE Transactions on Electron Devices*, 52(9):2081–2086, 2005.

[95] Jun Okuno, Takafumi Kunihiro, Kenta Konishi, Hideki Maemura, Yusuke Shute, Fumitaka Sugaya, Monica Materano, Tarek Ali, Kati Kuehnel, Konrad Seide, Uwe Schroeder, Thomas Mikolajick, Masanori Tsukamoto, and Taku Umebayashi. SoC compatible 1 T1 C FeRAM memory array based on ferroelectric Hf0.5Zr0.5O2. *Digest of Technical Papers - Symposium on VLSI Technology*, 2020-June:2020–2021, 2020.

[96] T. Francois, L. Grenouillet, J. Coignus, N. Vaxelaire, C. Carabasse, F. Aussenac, S. Chevalliez, S. Slesazeck, C. Richter, P. Chiquet, M. Bocquet, U. Schroeder, T. Mikolajick, F. Gaillard, and E. Nowak. Impact of area scaling on the ferroelectric properties of back-end of line compatible Hf0.5Zr0.5O2and Si:HfO2-based MFM capacitors. *Applied Physics Letters*, 118(6):0–5, 2021.

[97] Min Hyuk Park, Han Joon Kim, Yu Jin Kim, Taehwan Moon, and Cheol Seong Hwang. The effects of crystallographic orientation and strain of thin Hf 0.5Zr0.5O2 film on its ferroelectricity. *Applied Physics Letters*, 104(7):0–5, 2014.

[98] Yongsun Lee, Youngin Goh, Junghyeon Hwang, Dipjyoti Das, and Sanghun Jeon. The Influence of Top and Bottom Metal Electrodes on Ferroelectricity of Hafnia. *IEEE Transactions on Electron Devices*, 68(2):523–528, 2021.

[99] Seungyeol Oh, Hyungwoo Kim, Alireza Kashir, and Hyunsang Hwang. Effect of dead layers on the ferroelectric property of ultrathin HfZrOxfilm. *Applied Physics Letters*, 117(25), 2020.

[100] K. T. Chen, C. Y. Liao, C. Lo, H. Y. Chen, G. Y. Siang, S. Liu, S. C. Chang, M. H. Liao, S. T. Chang, and M. H. Lee. Improvement on Ferroelectricity and Endurance of Ultra-Thin HfZrO2 Capacitor with Molybdenum Capping Electrode. *2019 Electron Devices Technology and Manufacturing Conference, EDTM 2019*, pages 62–64, 2019.

[101] Fabian Ambriz-vargas, Gitanjali Kolhatkar, Maxime Broyer, Azza Hadj-youssef, Andranik Sarkissian, Reji Thomas, Carlos Gomez-ya, Marc A Gauthier, and Andreas Ruediger. A Complementary Metal Oxide Semiconductor Process-Compatible Ferroelectric Tunnel Junction. pages 3–9, 2017.

[102] Patrick D. Lomenzo, Qanit Takmeel, Chuanzhen Zhou, Chris M. Fancher, Eric Lambers, Nicholas G. Rudawski, Jacob L. Jones, Saeed Moghaddam, and Toshikazu Nishida. TaN interface properties and electric field cycling effects on ferroelectric Si-doped HfO2thin films. *Journal of Applied Physics*, 117(13):0–10, 2015.

[103] Yingfen Wei, Pavan Nukala, Mart Salverda, Sylvia Matzen, Hong Jian Zhao, Arnoud Everhardt, Graeme R Blake, Philippe Lecoeur, Bart J Kooi,

Jorge Íñiguez, Brahim Dkhil, and Beatriz Noheda. A rhombohedral ferroelectric phase in epitaxially-strained Hf0.5Zr0.5O2 thin films. *arXiv*, 3(001):1801.09008, 2018.

[104] Alireza Kashir, Hyungwoo Kim, and Hyunsang Hwang. Large remnant polarization in a wake-up free Hf0 . 5 Zr0 . 5 O2 ferroelectric film Large remnant polarization in a wake-up free Hf 0 . 5 Zr 0 . 5 O 2 ferroelectric film through bulk and interface engineering Alireza Kashir *, Hyung Woo Kim , Seungyeol Oh . (January):0–3, 2021.

[105] Ignasi Fina and Florencio Sánchez. Epitaxial Ferroelectric HfO2Films: Growth, Properties, and Devices. *ACS Applied Electronic Materials*, 3(4):1530–1549, 2021.

[106] L Brunet, C Fenouillet-Beranger, P Batude, S Beaurepaire, F Ponthenier, N Rambal, V Mazzocchi, J-B. Pin, P Acosta-Alba, S Kerdiles, P Besson, H Fontaine, T Lardin, F Fournel, V Larrey, F Mazen, V Balan, C Morales, C Guerin, V Jousseaume, X Federspiel, D Ney, X Garros, A Roman, D Scevola, P Perreau, F Kouemeni-Tchouake, L Arnaud, C Scibetta, S Chevalliez, F Aussenac, J Aubin, S Reboh, F Andrieu, S Maitrejean, and M Vinet. Breakthroughs in 3D Sequential technology. In *2018 IEEE International Electron Devices Meeting (IEDM)*, pages 7.2.1–7.2.4, 2018.

[107] M. H. Park, H. J. Kim, Y. J. Kim, T. Moon, K. D. Kim, Y. H. Lee, S. D. Hyun, and C. S. Hwang. Study on the internal field and conduction mechanism of atomic layer deposited ferroelectric Hf0.5Zr0.5O2 thin films. *Journal of Materials Chemistry C*, 3(24):6291–6300, 2015.

[108] Patrick D. Lomenzo, Qanit Takmeel, Saeed Moghaddam, and Toshikazu Nishida. Annealing behavior of ferroelectric Si-doped HfO2 thin films. *Thin Solid Films*, 615:139–144, 2016.

[109] J. Müller, U. Schröder, T. S. Böscke, I. Müller, U. Böttger, L. Wilde, J. Sundqvist, M. Lemberger, P. Kücher, T. Mikolajick, and L. Frey. Ferroelectricity in yttrium-doped hafnium oxide. *Journal of Applied Physics*, 110(11):1–6, 2011.

[110] Stefan Mueller, Johannes Mueller, Aarti Singh, Stefan Riedel, Jonas Sundqvist, Uwe Schroeder, and Thomas Mikolajick. Incipient ferroelectricity in Al-doped HfO 2 thin films. *Advanced Functional Materials*, 22(11):2412–2417, 2012.

[111] S. Mueller, C. Adelmann, A. Singh, S. Van Elshocht, U. Schroeder, and T. Mikolajick. Ferroelectricity in Gd-Doped HfO 2 Thin Films . *ECS Journal of Solid State Science and Technology*, 1(6):N123–N126, 2012.

[112] T. Schenk, S. Mueller, U. Schroeder, R. Materlik, A. Kersch, M. Popovici, C. Adelmann, S. Van Elshocht, and T. Mikolajick. Strontium doped hafnium oxide thin films: Wide process window for ferroelectric memories. *European Solid-State Device Research Conference*, pages 260–263, 2013.

[113] Uwe Schroeder, Claudia Richter, Min Hyuk Park, Tony Schenk, Milan Pešić, Michael Hoffmann, Franz P.G. Fengler, Darius Pohl, Bernd Rellinghaus, Chuanzhen Zhou, Ching Chang Chung, Jacob L. Jones, and Thomas Mikolajick. Lanthanum-Doped Hafnium Oxide: A Robust Ferroelectric Material. *Inorganic Chemistry*, 57(5):2752–2765, 2018.

[114] Uwe Schroeder, Ekaterina Yurchuk, Johannes Müller, Dominik Martin, Tony Schenk, Patrick Polakowski, Christoph Adelmann, Mihaela I. Popovici, Sergei V. Kalinin, and Thomas Mikolajick. Impact of different dopants on the switching properties of ferroelectric hafniumoxide. *Japanese Journal of Applied Physics*, 53(8 SPEC. ISSUE 1):2–7, 2014.

[115] Furqan Mehmood, Michael Hoffmann, Patrick D. Lomenzo, Claudia Richter, Monica Materano, Thomas Mikolajick, and Uwe Schroeder. Bulk Depolarization Fields as a Major Contributor to the Ferroelectric Reliability Performance in Lanthanum Doped Hf 0.5 Zr 0.5 O 2 Capacitors . *Advanced Materials Interfaces*, 1901180:1901180, 2019.

[116] Terence Mittmann, Monica Materano, Patrick D. Lomenzo, Min Hyuk Park, Igor Stolichnov, Matteo Cavalieri, Chuanzhen Zhou, Ching Chang Chung, Jacob L. Jones, Thomas Szyjka, Martina Müller, Alfred Kersch, Thomas Mikolajick, and Uwe Schroeder. Origin of Ferroelectric Phase in Undoped HfO2 Films Deposited by Sputtering. *Advanced Materials Interfaces*, 6(11):2–10, 2019.

[117] Y Zhou, Y K Zhang, Q Yang, J Jiang, P Fan, M Liao, and Y C Zhou. The effects of oxygen vacancies on ferroelectric phase transition of HfO2-based thin film from first-principle. *Computational Materials Science*, 167:143–150, 2019.

[118] Jordan Bouaziz, Pedro Rojo Romeo, Nicolas Baboux, and Bertrand Vilquin. Characterization of ferroelectric hafnium/zirconium oxide solid solutions deposited by reactive magnetron sputtering. *Journal of Vacuum Science & Technology B*, 37(2):021203, 2019.

[119] C. Zacharaki, P. Tsipas, S. Chaitoglou, S. Fragkos, M. Axiotis, A. Lagoyiannis, R. Negrea, L. Pintilie, and A. Dimoulas. Very large remanent polarization in ferroelectric Hf1-xZrxO2 grown on Ge substrates by plasma assisted atomic oxygen deposition. *Applied Physics Letters*, 114(11):0–5, 2019.

[120] Takao Shimizu, Tatsuhiko Yokouchi, Takahiro Oikawa, Takahisa Shiraishi, Takanori Kiguchi, Akihiro Akama, Toyohiko J. Konno, Alexei Gruverman, and Hiroshi Funakubo. Contribution of oxygen vacancies to the ferroelectric behavior of Hf0.5Zr0.5O2 thin films. *Applied Physics Letters*, 106(11):0–5, 2015.

[121] Sergej Starschich, David Griesche, Theodor Schneller, and Ulrich Böttger. Chemical Solution Deposition of Ferroelectric Hafnium Oxide for Future Lead Free Ferroelectric Devices. *ECS Journal of Solid State Science and Technology*, 4(12):P419–P423, 2015.

[122] Evelyn T Breyer and Stefan Slesazeck. Chapter 10.6 - Ferroelectric Devices for Logic in Memory. In Uwe Schroeder, Cheol Seong Hwang, and Hiroshi

Funakubo, editors, *Ferroelectricity in Doped Hafnium Oxide: Materials, Properties and Devices*, Woodhead Publishing Series in Electronic and Optical Materials, pages 495–513. Woodhead Publishing, 2019.

[123] J Rodriguez, K Remack, J Gertas, L Wang, C Zhou, K Boku, J Rodriguez-Latorre, K R Udayakumar, S Summerfelt, T Moise, D Kim, J Groat, J Eliason, M Depner, and F Chu. Reliability of Ferroelectric Random Access memory embedded within 130nm CMOS. In *2010 IEEE International Reliability Physics Symposium*, pages 750–758, 2010.

[124] J. Muller, T. S. Boscke, S. Muller, E. Yurchuk, P. Polakowski, J. Paul, D. Martin, T. Schenk, K. Khullar, A. Kersch, W. Weinreich, S. Riedel, K. Seidel, A. Kumar, T. M. Arruda, S. V. Kalinin, T. Schlosser, R. Boschke, R. Van Bentum, U. Schroder, and T. Mikolajick. Ferroelectric hafnium oxide: A CMOS-compatible and highly scalable approach to future ferroelectric memories. *Technical Digest - International Electron Devices Meeting, IEDM*, pages 280–283, 2013.

[125] T. Francois, J. Coignus, A. Makosiej, B. Giraud, C. Carabasse, J. Barbot, S. Martin, N. Castellani, T. Magis, H. Grampeix, S. Van Duijn, C. Mounet, P. Chiquet, U. Schroeder, S. Slesazeck, T. Mikolajick, E. Nowak, M. Bocquet, N. Barrett, F. Andrieu, and L. Grenouillet. High-Performance Operation and Solder Reflow Compatibility in BEOL-Integrated 16-Kb HfO₂: Si-Based 1T-1C FeRAM Arrays. *IEEE Transactions on Electron Devices*, pages 1–7, 2022.

[126] Halid Mulaosmanovic, Evelyn T Breyer, Stefan Dünkel, Sven Beyer, Thomas Mikolajick, and Stefan Slesazeck. Ferroelectric field-effect transistors based on {HfO}2: a review. *Nanotechnology*, 32(50):502002, sep 2021.

[127] K. Florent, M. Pesic, A. Subirats, K. Banerjee, S. Lavizzari, A. Arreghini, L. Di Piazza, G. Potoms, F. Sebaai, S. R.C. McMitchell, M. Popovici, G. Groeseneken, and J. Van Houdt. Vertical Ferroelectric HfO 2 FET based on 3-D NAND Architecture: Towards Dense Low-Power Memory. *Technical Digest - International Electron Devices Meeting, IEDM*, 2018-Decem:2.5.1–2.5.4, 2019.

[128] Kitae Lee, Jong Ho Bae, Sihyun Kim, Jong Ho Lee, Byung Gook Park, and Daewoong Kwon. Ferroelectric-Gate Field-Effect Transistor Memory with Recessed Channel. *IEEE Electron Device Letters*, 41(8):1201–1204, 2020.

[129] Shen Yang Lee, Han Wei Chen, Chiuan Huei Shen, Po Yi Kuo, Chun Chih Chung, Yu En Huang, Hsin Yu Chen, and Tien Sheng Chao. Effect of Seed Layer on Gate-All-Around Poly-Si Nanowire Negative-Capacitance FETs with MFMIS and MFIS Structures: Planar Capacitors to 3-D FETs. *IEEE Transactions on Electron Devices*, 67(2):711–716, 2020.

[130] Myungsoo Seo, Min Ho Kang, Seung Bae Jeon, Hagyoul Bae, Jae Hur, Byung Chul Jang, Seokjung Yun, Seongwoo Cho, Wu Kang Kim, Myung Su Kim, Kyu Man Hwang, Seungbum Hong, Sung Yool Choi, and Yang Kyu Choi. First demonstration of a logic-process compatible junctionless ferroelectric FinFET synapse for neuromorphic applications. *IEEE Electron Device Letters*, 39(9):1445–1448, 2018.

[131] Sayeef Salahuddin and Supriyo Datta. Use of negative capacitance to provide voltage amplification for low power nanoscale devices. *Nano Letters*, 8(2):405–410, 2008.

[132] Michael Hoffmann, Stefan Slesazeck, Uwe Schroeder, and Thomas Mikolajick. What's next for negative capacitance electronics? *Nature Electronics*, 3(9):504–506, 2020.

[133] Michael Hoffmann, Asif Islam Khan, Claudy Serrao, Zhongyuan Lu, Sayeef Salahuddin, Milan Pešić, Stefan Slesazeck, Uwe Schroeder, and Thomas Mikolajick. Ferroelectric negative capacitance domain dynamics. *Journal of Applied Physics*, 123(18), 2018.

[134] Z Krivokapic, U Rana, R Galatage, A Razavieh, A Aziz, J Liu, J Shi, H J Kim, R Sporer, C Serrao, A Busquet, P Polakowski, J Müller, W Kleemeier, A Jacob, D Brown, A Knorr, R Carter, and S Banna. 14nm Ferroelectric FinFET technology with steep subthreshold slope for ultra low power applications. In *2017 IEEE International Electron Devices Meeting (IEDM)*, pages 15.1.1–15.1.4, 2017.

[135] Vincent Garcia and Manuel Bibes. Ferroelectric tunnel junctions for information storage and processing. *Nature Communications*, 5:1–12, 2014.

[136] M. Ye Zhuravlev, R. F. Sabirianov, S. S. Jaswal, and E. Y. Tsymbal. Giant electroresistance in ferroelectric tunnel junctions. *Physical Review Letters*, 94(24):1–4, 2005.

[137] Bo Bo Tian, Yang Liu, Liu Fang Chen, Jian Lu Wang, Shuo Sun, Hong Shen, Jing Lan Sun, Guo Liang Yuan, Stéphane Fusil, Vincent Garcia, Brahim Dkhil, Xiang Jian Meng, and Jun Hao Chu. Space-charge Effect on Electroresistance in Metal-Ferroelectric-Metal capacitors. *Scientific Reports*, 5(December), 2015.

[138] Suraj S. Cheema, Nirmaan Shanker, Cheng Hsiang Hsu, Adhiraj Datar, Jongho Bae, Daewoong Kwon, and Sayeef Salahuddin. One Nanometer HfO2-Based Ferroelectric Tunnel Junctions on Silicon. *Advanced Electronic Materials*, 2100499:1–10, 2021.

[139] Hyun Jae Lee, Minseong Lee, Kyoungjun Lee, Jinhyeong Jo, Hyemi Yang, Yungyeom Kim, Seung Chul Chae, Umesh Waghmare, and Jun Hee Lee. Scale-free ferroelectricity induced by flat phonon bands in HfO2. *Science*, 369(6509):1343–1347, 2020.

[140] Milan Pešić, Franz Paul Gustav Fengler, Luca Larcher, Andrea Padovani, Tony Schenk, Everett D Grimley, Xiahan Sang, James M LeBeau, Stefan Slesazeck, Uwe Schroeder, and Thomas Mikolajick. Physical Mechanisms behind the Field-Cycling Behavior of HfO2-Based Ferroelectric Capacitors. *Advanced Functional Materials*, 26(25):4601–4612, 2016.

[141] Franz Fengler, Min Hyuk Park, Tony Schenk, Milan Pešić, and Uwe Schroeder. Chapter 9.2 - Field Cycling Behavior of Ferroelectric HfO2-Based Capacitors. In Uwe Schroeder, Cheol Seong Hwang, and Hiroshi Funakubo,

editors, *Ferroelectricity in Doped Hafnium Oxide: Materials, Properties and Devices*, Woodhead Publishing Series in Electronic and Optical Materials, pages 381–398. Woodhead Publishing, 2019.

[142] Tony Schenk, Michael Hoffmann, Johannes Ocker, Milan Pešić, Thomas Mikolajick, and Uwe Schroeder. Complex Internal Bias Fields in Ferroelectric Hafnium Oxide. *ACS Applied Materials & Interfaces*, 7(36):20224–20233, sep 2015.

[143] Lixin He and David Vanderbilt. First-principles study of oxygen-vacancy pinning of domain walls in PbTiO 3. (October):1–7, 2003.

[144] Everett D. Grimley, Tony Schenk, Xiahan Sang, Milan Pešić, Uwe Schroeder, Thomas Mikolajick, and James M. LeBeau. Structural Changes Underlying Field-Cycling Phenomena in Ferroelectric HfO2 Thin Films. *Advanced Electronic Materials*, 2(9), 2016.

[145] Franz P G Fengler, Robin Nigon, Paul Muralt, Everett D Grimley, Xiahan Sang, Violetta Sessi, Rico Hentschel, James M Lebeau, and Thomas Mikolajick. Analysis of Performance Instabilities of Hafnia-Based Ferroelectrics Using Modulus Spectroscopy and Thermally Stimulated Depolarization Currents. 1700547:1–11, 2018.

[146] Franz P.G. Fengler, Milan Pešić, Sergej Starschich, Theodor Schneller, Christopher Künneth, Ulrich Böttger, Halid Mulaosmanovic, Tony Schenk, Min Hyuk Park, Robin Nigon, Paul Muralt, Thomas Mikolajick, and Uwe Schroeder. Domain Pinning: Comparison of Hafnia and PZT Based Ferroelectrics. *Advanced Electronic Materials*, 3(4), 2017.

[147] Stefan Mueller, Johannes Muller, Uwe Schroeder, and Thomas Mikolajick. Reliability Characteristics of Ferroelectric Si:HfO_{2} Thin Films for Memory Applications. *IEEE Transactions on Device and Materials Reliability*, 13(1):93–97, 2013.

[148] Anna G. Chernikova and Andrey M. Markeev. Dynamic imprint recovery as an origin of the pulse width dependence of retention in Hf0.5Zr0.5O2-based capacitors. *Applied Physics Letters*, 119(3):0–7, 2021.

[149] Hao Jiang, Maruf A. Bhuiyan, Zhan Liu, and T. P. Ma. A Study of BEOL Processed Hf0.5Zr0.5O2-based Ferroelectric Capacitors and Their Potential for Automotive Applications. *2020 IEEE International Memory Workshop, IMW 2020 - Proceedings*, pages 5–8, 2020.

[150] Keum Do Kim, Young Hwan Lee, Taehong Gwon, Yu Jin Kim, Han Joon Kim, Taehwan Moon, Seung Dam Hyun, Hyeon Woo Park, Min Hyuk Park, and Cheol Seong Hwang. Scale-up and optimization of HfO2-ZrO2 solid solution thin films for the electrostatic supercapacitors. *Nano Energy*, 39(April):390–399, 2017.

[151] Min Hyuk Park, Dong Hyun Lee, Kun Yang, Ju Yong Park, Geun Taek Yu, Hyeon Woo Park, Monica Materano, Terence Mittmann, Patrick D.

Lomenzo, Thomas Mikolajick, Uwe Schroeder, and Cheol Seong Hwang. Review of defect chemistry in fluorite-structure ferroelectrics for future electronic devices. *Journal of Materials Chemistry C*, 8(31):10526–10550, 2020.

[152] Lutz Baumgarten, Thomas Szyjka, Terence Mittmann, Monica Materano, Yury Matveyev, Christoph Schlueter, Thomas Mikolajick, Uwe Schroeder, and Martina Müller. Impact of vacancies and impurities on ferroelectricity in PVD- And ALD-grown HfO2films. *Applied Physics Letters*, 118(3):0–6, 2021.

[153] M. H. Park, H. J. Kim, Y. J. Kim, T. Moon, K. D. Kim, Y. H. Lee, S. D. Hyun, and C. S. Hwang. Study on the internal field and conduction mechanism of atomic layer deposited ferroelectric Hf0.5Zr0.5O2 thin films. *Journal of Materials Chemistry C*, 3(24):6291–6300, 2015.

[154] Monica Materano, Patrick D. Lomenzo, Alfred Kersch, Min Hyuk Park, Thomas Mikolajick, and Uwe Schroeder. Interplay between oxygen defects and dopants: Effect on structure and performance of HfO2-based ferroelectrics. *Inorganic Chemistry Frontiers*, 8(10):2650–2672, 2021.

[155] Anastasia Chouprik, Dmitrii Negrov, Evgeny Y. Tsymbal, and Andrei Zenkevich. Defects in ferroelectric HfO2. *Nanoscale*, 13(27):11635–11678, 2021.

[156] K. Tse, D. Liu, K. Xiong, and J. Robertson. Oxygen vacancies in high-k oxides. *Microelectronic Engineering*, 84(9-10):2028–2031, 2007.

[157] Vladimir A. Gritsenko, Timofey V. Perevalov, and Damir R. Islamov. Electronic properties of hafnium oxide: A contribution from defects and traps. *Physics Reports*, 613:1–20, 2016.

[158] Hideki Takeuchi, Hiu Yung Wong, Daewon Ha, and Tsu Jae King. Impact of oxygen vacancies on high-κ gate stack engineering. *Technical Digest - International Electron Devices Meeting, IEDM*, (510):829–832, 2004.

[159] J. Müller, P. Polakowski, S. Mueller, and T. Mikolajick. Ferroelectric Hafnium Oxide Based Materials and Devices: Assessment of Current Status and Future Prospects. *ECS Journal of Solid State Science and Technology*, 4(5):N30–N35, 2015.

[160] D C Sekar, B Bateman, U Raghuram, S Bowyer, Y Bai, M Calarrudo, P Swab, J Wu, S Nguyen, N Mishra, R Meyer, M Kellam, B Haukness, C Chevallier, H Wu, H Qian, F Kreupl, and G Bronner. Technology and circuit optimization of resistive RAM for low-power, reproducible operation. In *2014 IEEE International Electron Devices Meeting*, pages 28.3.1–28.3.4, 2014.

[161] Yuri A Genenko, Julia Glaum, Michael J Hoffmann, and Karsten Albe. Mechanisms of aging and fatigue in ferroelectrics. *Materials Science and Engineering: B*, 192:52–82, 2015.

[162] N. Umezawa, K. Shiraishi, S. Sugino, A. Tachibana, K. Ohmori, K. Kakushima, H. Iwai, T. Chikyow, T. Ohno, Y. Nara, and K. Yamada. Suppression of oxygen vacancy formation in Hf-based high- k dielectrics by lanthanum incorporation. *Applied Physics Letters*, 91(13):132902–132905, 2007.

[163] Christoph Slouka, Theresa Kainz, Edvinas Navickas, Gregor Walch, Herbert Hutter, Klaus Reichmann, and Jürgen Fleig. The effect of acceptor and donor doping on oxygen vacancy concentrations in lead zirconate titanate (PZT). *Materials*, 9(11), 2016.

[164] V. A. Gritsenko and A. A. Gismatulin. Charge transport mechanism in La:HfO2. *Applied Physics Letters*, 117(14), 2020.

[165] Herbert Schroeder. Poole-Frenkel-effect as dominating current mechanism in thin oxide films - An illusion?! *Journal of Applied Physics*, 117(21), 2015.

[166] Roman R. Khakimov, Anna G. Chernikova, Yury Lebedinskii, Aleksandra A. Koroleva, and Andrey M. Markeev. Influence of the Annealing Temperature and Applied Electric Field on the Reliability of TiN/Hf0.5Zr0.5O2/TiN Capacitors. *ACS Applied Electronic Materials*, 2021.

[167] F Domengie, P Morin, and D Bauza. Modeling the dark current histogram induced by gold contamination in complementary-metal-oxide-semiconductor image sensors. *Journal of Applied Physics*, 118(2):24501, 2015.

[168] Damir R. Islamov, Vladimir A. Gritsenko, Timofey V. Perevalov, Vladimir A. Pustovarov, Oleg M. Orlov, Anna G. Chernikova, Andrey M. Markeev, Stefan Slesazeck, Uwe Schroeder, Thomas Mikolajick, and Gennadiy Ya Krasnikov. Identification of the nature of traps involved in the field cycling of Hf 0.5 Zr 0.5 O 2 -based ferroelectric thin films. *Acta Materialia*, 166:47–55, 2019.

[169] D.R. Islamov, A.G. Chernikova, M.G. Kozodaev, T.V. Perevalov, V.A. Gritsenko, O.M. Orlov, and A.V. Markeev. Leakage currents mechanism in thin films of ferroelectnc Hf<inf>0.5</inf>Zr<inf>0.5</inf>O<inf>2</inf>. *ECS Transactions*, 75(32):5–9, 2016.

[170] C. B. Sawyer and C. H. Tower. Rochelle salt as a dielectric. *Physical Review*, 35(3):269–273, 1930.

[171] T. Schenk, E. Yurchuk, S. Mueller, U. Schroeder, S. Starschich, U. Böttger, and T. Mikolajick. About the deformation of ferroelectric hystereses. *Applied Physics Reviews*, 1(4), 2014.

[172] Simon Martin, Nicolas Baboux, David Albertini, and Brice Gautier. A new technique based on current measurement for nanoscale ferroelectricity assessment: Nano-positive up negative down. *Review of Scientific Instruments*, 88(2), 2017.

[173] S D Traynor, T D Hadnagy, and L Kammerdiner. Capacitor test simulation of retention and imprint characteristics for ferroelectric memory operation. *Integrated Ferroelectrics*, 16(1-4):63–76, apr 1997.

[174] Ciaran J Brennan. Characterization and modelling of thin-film ferroelectric capacitors using C-V analysis. *Integrated Ferroelectrics*, 2(1-4):73–82, nov 1992.

[175] Alexander G. Shard. Practical guides for x-ray photoelectron spectroscopy: Quantitative XPS. *Journal of Vacuum Science & Technology A*, 38(4):041201, 2020.

[176] Baiqing Lv, Tian Qian, and Hong Ding. Angle-resolved photoemission spectroscopy and its application to topological materials. *Nature Reviews Physics*, 1(10):609–626, 2019.

[177] Alexandre Pancotti, Jiale Wang, Peixuan Chen, Ludovic Tortech, Cristian Mihail Teodorescu, Emmanouil Frantzeskakis, and Nicholas Barrett. X-ray photoelectron diffraction study of relaxation and rumpling of ferroelectric domains in BaTiO3(001). *Physical Review B - Condensed Matter and Materials Physics*, 87(18):1–10, 2013.

[178] A. Pancotti, T. C. Back, W. Hamouda, M. Lachheb, C. Lubin, P. Soukiassian, J. Boeckl, D. Dorsey, S. Mou, T. Asel, G. Geneste, and N. Barrett. Surface relaxation and rumpling of Sn-doped β-Ga2 O3(010). *Physical Review B*, 102(24):1–11, 2020.

[179] N. Barrett, J. E. Rault, J. L. Wang, C. Mathieu, A. Locatelli, T. O. Mentes, M. A. Niño, S. Fusil, M. Bibes, A. Barthélémy, D. Sando, W. Ren, S. Prosandeev, L. Bellaiche, B. Vilquin, A. Petraru, I. P. Krug, and C. M. Schneider. Full field electron spectromicroscopy applied to ferroelectric materials. *Journal of Applied Physics*, 113(18):0–13, 2013.

[180] J. E. Rault, G. Agnus, T. Maroutian, V. Pillard, Ph Lecoeur, G. Niu, B. Vilquin, M. G. Silly, A. Bendounan, F. Sirotti, and N. Barrett. Time-resolved photoemission spectroscopy on a metal/ferroelectric heterostructure. *Physical Review B - Condensed Matter and Materials Physics*, 88(15):2–7, 2013.

[181] H Hertz. Ueber einen Einfluss des ultravioletten Lichtes auf die electrische Entladung. *Annalen der Physik*, 267(8):983–1000, 1887.

[182] P Lenard. Ueber die lichtelektrische Wirkung. *Annalen der Physik*, 313(5):149–198, 1902.

[183] P Lenard. Ueber die lichtelektrische Wirkung. *Annalen der Physik*, 313(5):149–198, 1902.

[184] Kai Siegbahn. ESCA : atomic, molecular and solid state structure studied by means of electron spectroscopy. 1967.

[185] Carl Nordling, Evelyn Sokolowski, and Kai Siegbahn. Precision Method for Obtaining Absolute Values of Atomic Binding Energies. *Physical Review*, 105(5):1676–1677, 1957.

[186] J Cooper and R N Zare. Angular Distribution of Photoelectrons. *The Journal of Chemical Physics*, 48(2):942–943, 1968.

[187] J J Yeh and I Lindau. Copyright 0 1985 by Academic Press, Inc. *Atomic Data and Nuclear Data Tables*, 32(l):1–155, 1985.

[188] Aleksander Jablonski. Database of correction parameters for the elastic scattering effects in XPS. *Surface and Interface Analysis*, 23(1):29–37, 1995.

[189] S Tanuma and C J Powell. Electron Inelastic Mean Free Paths. 21(September 1993):165–176, 2000.

[190] George H. Major, Neal Fairley, Peter M. A. Sherwood, Matthew R. Linford, Jeff Terry, Vincent Fernandez, and Kateryna Artyushkova. Practical guide for curve fitting in x-ray photoelectron spectroscopy. *Journal of Vacuum Science & Technology A*, 38(6):061203, 2020.

[191] Mathieu Claire. Approche intégree " Spectroscopies electroniques et Calculs ab-initio d ' etats de cœur excitées " des modes d ' adsorption de l ' ammoniac et de diamines sur la surface Si (001). (001), 2009.

[192] S. Suzer, S. Sayan, M. M. Banaszak Holl, E. Garfunkel, Z. Hussain, and N. M. Hamdan. Soft x-ray photoemission studies of Hf oxidation. *Journal of Vacuum Science & Technology A: Vacuum, Surfaces, and Films*, 21(1):106–109, 2003.

[193] Takahiro HASHIMOTO, Peter AMANN, Anna REGOUTZ, Nick BARRETT, Louis F. J. PIPER, Wassim HAMOUDA, Olivier RENAULT, Marcus LUNDWALL, and Masatake MACHIDA. Laboratory-based hard x-ray photoelectron spectroscopy for fundamental and industrial research. *Vacuum and Surface Science*, 64:20180793, 11 2021.

[194] Charles S. Fadley. *Hard X-ray photoemission: An overview and future perspective*, volume 59. 2016.

[195] Z. Liu and H. Bluhm. Liquid/solid interfaces studied by ambient pressure HAXPES. *Springer Series in Surface Sciences*, 59:447–466, 2016.

[196] Keisuke Kobayashi. *HAXPES applications to advanced materials*, volume 59. 2016.

[197] M. B. Trzhaskovskaya, V. I. Nefedov, and V. G. Yarzhemsky. Photoelectron angular distribution parameters for elements Z = 55 to Z = 100 in the photoelectron energy range 100-5000 eV. *Atomic Data and Nuclear Data Tables*, 82(2):257–311, 2002.

[198] Settimio Mobilio, Federico Boscherini, and Carlo Meneghini. Synchrotron radiation: Basics, methods and applications. *Synchrotron Radiation: Basics, Methods and Applications*, pages 1–799, 2015.

[199] Julian Schwinger. On the Classical Radiation of Accelerated Electrons. *Phys. Rev.*, 75(12):1912–1925, 1949.

[200] D H Tomboulian and P L Hartman. Spectral and Angular Distribution of Ultraviolet Radiation from the 300-Mev Cornell Synchrotron. *Phys. Rev.*, 102(6):1423–1447, 1956.

[201] Settimio Mobilio, Federico Boscherini, and Carlo Meneghini. *Synchrotron radiation: Basics, methods and applications*. 2015.

[202] Shigenori Ueda, Yoshio Katsuya, Masahiko Tanaka, Hideki Yoshikawa, Yoshiyuki Yamashita, Satoshi Ishimaru, Yoshitaka Matsushita, and Keisuke Kobayashi. Present status of the NIMS contract beamline BL15XU at SPring-8. *AIP Conference Proceedings*, 1234(June):403–406, 2010.

[203] D. Céolin, J. M. Ablett, D. Prieur, T. Moreno, J. P. Rueff, T. Marchenko, L. Journel, R. Guillemin, B. Pilette, T. Marin, and M. Simon. Hard X-ray photoelectron spectroscopy on the GALAXIES beamline at the SOLEIL synchrotron. *Journal of Electron Spectroscopy and Related Phenomena*, 190(PART B):188–192, 2013.

[204] I. Milošv, H. -H Strehblow, B. Navinšek, and M. Metikoš-Huković. Electrochemical and thermal oxidation of TiN coatings studied by XPS. *Surface and Interface Analysis*, 23(7-8):529–539, 1995.

[205] E. O. Filatova, A. S. Konashuk, S. S. Sakhonenkov, A. A. Sokolov, and V. V. Afanas'ev. Re-distribution of oxygen at the interface between γ-Al2O3 and TiN. *Scientific Reports*, 7(1):1–14, 2017.

[206] Charles D. Wagner. NIST X-ray Photoelectron Spectrometry Database. *NIST Standard Reference Database 20, Version 4.1*, pages 1–76, 1991.

[207] M. Kazar Mendes, E. Martinez, A. Marty, M. Veillerot, Y. Yamashita, R. Gassilloud, M. Bernard, O. Renault, and N. Barrett. Forming mechanism of Te-based conductive-bridge memories. *Applied Surface Science*, 432:34–40, 2018.

[208] Yury Matveyev, Dmitry Negrov, Anna Chernikova, Yury Lebedinskii, Roman Kirtaev, Sergei Zarubin, Elena Suvorova, Andrei Gloskovskii, and Andrei Zenkevich. Effect of Polarization Reversal in Ferroelectric TiN/Hf0.5Zr0.5O2/TiN Devices on Electronic Conditions at Interfaces Studied in Operando by Hard X-ray Photoemission Spectroscopy. *ACS Applied Materials and Interfaces*, 9(49):43370–43376, 2017.

[209] C. Lenser, A. Köhl, M. Patt, C. M. Schneider, R. Waser, and R. Dittmann. Band alignment at memristive metal-oxide interfaces investigated by hard x-ray photoemission spectroscopy. *Physical Review B - Condensed Matter and Materials Physics*, 90(11):1–8, 2014.

[210] C. Morant, L. Galán, and J. M. Sanz. An XPS study of the initial stages of oxidation of hafnium. *Surface and Interface Analysis*, 16(1-12):304–308, 1990.

[211] Alexei Gruverman, Maksim Spiridonov, Sergei Zarubin, Maksim Kozodaev, Haidong Lu, Dmitrii Negrov, Elena Suvorova, Ohheum Bak, Andrei Zenkevich, Andrei Markeev, Anna Chernikova, and Pratyush Buragohain. Ultrathin Hf 0.5 Zr 0.5 O 2 Ferroelectric Films on Si . *ACS Applied Materials & Interfaces*, 8(11):7232–7237, 2016.

[212] C. Morant, J. M. Sanz, L. Galán, L. Soriano, and F. Rueda. An XPS study of the interaction of oxygen with zirconium. *Surface Science*, 218(2-3):331–345, 1989.

[213] F. P.G. Fengler, M. Hoffmann, S. Slesazeck, T. Mikolajick, and U. Schroeder. On the relationship between field cycling and imprint in ferroelectric Hf0.5Zr0.5O2. *Journal of Applied Physics*, 123(20):0–8, 2018.

[214] E. A. Kraut, R.W. Grant, J.R. Waldrop, and S.P. Kowalczyk. Precise Determination of the Valence-Band Edge in X Ray Photoemission Spectra. *Physical Review Letters*, 44(24):1620, 1980.

[215] Steven A. Vitale, Jakub Kedzierski, Paul Healey, Peter W. Wyatt, and Craig L. Keast. Work-function-tuned TiN metal gate FDSOI transistors for subthreshold operation. *IEEE Transactions on Electron Devices*, 58(2):419–426, 2011.

[216] F. Y. Xie, L. Gong, X. Liu, Y. T. Tao, W. H. Zhang, S. H. Chen, H. Meng, and J. Chen. XPS studies on surface reduction of tungsten oxide nanowire film by Ar + bombardment. *Journal of Electron Spectroscopy and Related Phenomena*, 185(3-4):112–118, 2012.

[217] Alenka Vesel, Miran Mozetič, and Marianne Balat-Pichelin. Sequential oxidation and reduction of tungsten/tungsten oxide. *Thin Solid Films*, 591:174–181, 2015.

[218] Yehan Tao, Oreste De Luca, Bhawan Singh, Aeilke J. Kamphuis, Juan Chen, Petra Rudolf, and Paolo P. Pescarmona. WO3–SiO2 nanomaterials synthesized using a novel template-free method in supercritical CO2 as heterogeneous catalysts for epoxidation with H2O2. *Materials Today Chemistry*, 18:100373, 2020.

[219] Roman Leitsmann, Florian Lazarevic, Ebrahim Nadimi, Rolf Öttking, Philipp Plänitz, and Elke Erben. Charge transition levels of oxygen, lanthanum, and fluorine related defect structures in bulk hafnium dioxide (HfO2): An ab initio investigation. *Journal of Applied Physics*, 117(24), 2015.

[220] Robin Materlik, Christopher Künneth, Max Falkowski, Thomas Mikolajick, and Alfred Kersch. Al-, Y-, and La-doping effects favoring intrinsic and field induced ferroelectricity in HfO2: A first principles study. *Journal of Applied Physics*, 123(16), 2018.

[221] M. F. Sunding, K. Hadidi, S. Diplas, O. M. Løvvik, T. E. Norby, and A. E. Gunnæs. XPS characterisation of in situ treated lanthanum oxide and hydroxide using tailored charge referencing and peak fitting procedures. *Journal of Electron Spectroscopy and Related Phenomena*, 184(7):399–409, 2011.

[222] D. F. Mullica, C. K.C. Lok, H. O. Perkins, and V. Young. X-ray photoelectron final-state screening in La(OH)3: A multiplet structural analysis. *Physical Review B*, 31(6):4039–4042, 1985.

[223] Anna G. Chernikova, Maxim G. Kozodaev, Dmitry V. Negrov, Evgeny V. Korostylev, Min Hyuk Park, Uwe Schroeder, Cheol Seong Hwang, and Andrey M. Markeev. Improved Ferroelectric Switching Endurance of La-Doped Hf 0.5 Zr 0.5 O 2 Thin Films. *ACS Applied Materials and Interfaces*, 10(3):2701–2708, 2018.

[224] Doo Seok Jeong, Hong Bae Park, and Cheol Seong Hwang. Reasons for obtaining an optical dielectric constant from the Poole-Frenkel conduction behavior of atomic-layer-deposited HfO2 films. *Applied Physics Letters*, 86(7):1–3, 2005.

[225] O. Renault, E. Martinez, C. Zborowski, J. Mann, R. Inoue, J. Newman, and K. Watanabe. Analysis of buried interfaces in multilayer device structures with hard XPS (HAXPES) using a CrKα source. *Surface and Interface Analysis*, 50(11):1158–1162, 2018.

[226] Benjamin Meunier, Eugénie Martinez, Raquel Rodriguez-Lamas, Dolors Pla, Mònica Burriel, Michel Boudard, Carmen Jiménez, Jean Pascal Rueff, and Olivier Renault. Resistive switching in a LaMnO3 + δ/TiN memory cell investigated by operando hard X-ray photoelectron spectroscopy. *Journal of Applied Physics*, 126(22), 2019.

[227] Deok Hwang Kwon, Kyung Min Kim, Jae Hyuck Jang, Jong Myeong Jeon, Min Hwan Lee, Gun Hwan Kim, Xiang Shu Li, Gyeong Su Park, Bora Lee, Seungwu Han, Miyoung Kim, and Cheol Seong Hwang. Atomic structure of conducting nanofilaments in TiO2 resistive switching memory. *Nature Nanotechnology*, 5(2):148–153, 2010.

[228] Yury Matveyev, Vitalii Mikheev, Dmitry Negrov, Sergei Zarubin, Abinash Kumar, Everett D. Grimley, James M. Lebeau, Andrei Gloskovskii, Evgeny Y. Tsymbal, and Andrei Zenkevich. Polarization-dependent electric potential distribution across nanoscale ferroelectric Hf0.5Zr0.5O2 in functional memory capacitors. *Nanoscale*, 11(42):19814–19822, 2019.

[229] J. Müller, E. Yurchuk, T. Schlösser, J. Paul, R. Hoffmann, S. Müller, D. Martin, S. Slesazeck, P. Polakowski, J. Sundqvist, M. Czernohorsky, K. Seidel, P. Kücher, R. Boschke, M. Trentzsch, K. Gebauer, U. Schröder, and T. Mikolajick. Ferroelectricity in HfO 2 enables nonvolatile data storage in 28 nm HKMG. *Digest of Technical Papers - Symposium on VLSI Technology*, pages 25–26, 2012.

[230] T. Ali, P. Polakowski, S. Riedel, T. Büttner, T. Kämpfe, M. Rudolph, B. Pätzold, K. Seidel, D. Löhr, R. Hoffmann, M. Czernohorsky, K. Kühnel, X. Thrun, N. Hanisch, P. Steinke, J. Calvo, and J. Müller. Silicon doped hafnium oxide (HSO) and hafnium zirconium oxide (HZO) based FeFET: A material relation to device physics. *Applied Physics Letters*, 112(22), 2018.

[231] Claudia Richter, Tony Schenk, Min Hyuk Park, Franziska A. Tscharntke, Everett D. Grimley, James M. LeBeau, Chuanzhen Zhou, Chris M. Fancher, Jacob L. Jones, Thomas Mikolajick, and Uwe Schroeder. Si Doped Hafnium Oxide—A “Fragile” Ferroelectric System. *Advanced Electronic Materials*, 3(10):1–12, 2017.

[232] T. Francois, J. Coignus, L. Grenouillet, M. Barlas, B. Bessif, N. Vaxelaire, H. Boutry, M. Coig, E. Vilain, N. Rambal, Y. Morand, J.M. Pedini, F. Mazen, E. Nowak, and F. Gaillard. Evaluation of Ferroelectricity in Si-implanted HfO₂ along Cycling. pages 203–204, 2020.

[233] Kyoungjun Lee, Kunwoo Park, Hyun Jae Lee, Myeong Seop Song, Kyu Cheol Lee, Jin Namkung, Jun Hee Lee, Jungwon Park, and Seung Chul Chae. Enhanced ferroelectric switching speed of Si-doped HfO2 thin film tailored by oxygen deficiency. *Scientific Reports*, 11(1):1–9, 2021.

[234] P. Catrou, S. Tricot, G. Delhaye, J. C. Le Breton, P. Turban, B. Lépine, and P. Schieffer. Effect of oxygen vacancies at the Fe/SrTiO3(001) interface: Schottky barrier and surface electron accumulation layer. *Physical Review B*, 98(11):1–12, 2018.

[235] M. Amati, A. Barinov, V. Feyer, L. Gregoratti, M. Al-Hada, A. Locatelli, T. O. Mentes, H. Sezen, C. M. Schneider, and M. Kiskinova. Photoelectron microscopy at Elettra: Recent advances and perspectives. *Journal of Electron Spectroscopy and Related Phenomena*, 224:59–67, 2018.

[236] W. Hamouda, A. Pancotti, C. Lubin, L. Tortech, C. Richter, T. Mikolajick, U. Schroeder, and N. Barrett. Physical chemistry of the TiN/Hf0.5Zr0.5O2 interface. *Journal of Applied Physics*, 127(6):0–9, 2020.

université
PARIS-SACLAY

ÉCOLE DOCTORALE
Physique en
Île-de-France (PIF)

Mots clés: Ferroélectricté, HfO_2, spectroscopie de photoémission (XPS, HAXPES), lacunes d'oxygènes, mémoire non-volatile

Résumé: Dans le cadre du projet européen H2020 3ϵFERRO, coordonné par le CEA, nous avons utilisé de nouveaux matériaux ferroélectriques à base de HfO_2, pour développer une technologie FRAM compétitive et versatile pour des applications de mémoires non-volatiles embarquées. La formation d'une couche d'interface entre le ferroélectrique et l'électrode est d'une importance capitale dans la performance ultime des dispositifs et représente un défi majeur pour l'ingénierie de ces nouveaux systèmes. Nous avons donc utilisé des techniques de caractérisation avancées, principalement la photoémission avec des rayons X tendres et durs du rayonnement synchrotron, pour décrire l'interface avec différentes électrodes ainsi que l'effet de dopage, du recuit et du cyclage et leurs conséquences sur l'alignement des bandes et la concentration de lacunes d'oxygène. Les résultats des études sur la chimie et la structure électronique ont conduit à une meilleure compréhension de l'influence des défauts et des interfaces sur la réponse ferroélectrique permettant ainsi l'optimisation des performances de différents dispositifs.

Keywords: Ferroelectricity, HfO_2, photemission spectroscopy (XPS, HAXPES), oxygen vacancies, non-volatile memories

Abstract: Within the framework of the European H2020 3ϵFERRO project, coordinated by the CEA, we have used new HfO_2-based ferroelectric materials to develop a competitive and versatile FRAM technology for embedded non-volatile memory applications. The formation of an interface layer between the ferroelectric and the electrode is of paramount importance in the ultimate performance of the devices and represents a major challenge in engineering these new systems. We have therefore used advanced characterization techniques, mainly photoemission spectroscopy techniques using soft and hard synchrotron X-rays, to describe the interface with different electrodes as well as the effect of doping, annealing and cycling and their consequences on band alignment and oxygen vacancy concentration. The results of the chemistry and the electronic structure led to a better understanding of the influence of defects and interfaces on the ferroelectric response allowing the optimization of the performance of different prototype devices.